Evolution du flux de matière, de l'architecture et de la rhéologie d'un prisme d'accrétion crustal (Dôme d'Orlica-Śnieżnik, Sudètes)

F. Chopin

UNIVERSITÉ DE STRASBOURG

Ecole et Observatoire des Sciences de la Terre

Université de Strasbourg
Ecole doctorale Sciences de la Terre et de l'Univers

THÈSE

Pour obtenir le grade de

DOCTEUR EN SCIENCES

Spécialité Sciences de la Terre et de l'Univers

de l'Université de Strasbourg

Par

Francis Chopin

Evolution du flux de matière, de l'architecture et de la rhéologie d'un prisme d'accrétion crustal (Dôme d'Orlica-Śnieżnik, Sudètes)

Soutenue publiquement le 30 septembre 2010
devant le jury composé de :

Prof. Hubert Whitechurch	Université de Strasbourg	Rapporteur
Prof. Michèl Ballèvre	Université de Rennes I	Rapporteur
Prof. Jean-Marc Lardeaux	Université de Nice-Sophia Antipolis	Rapporteur
Prof. Onno Oncken	GFZ Helmoltz Centre, Potsdam	Examinateur
Dr. Stanisław Mazur	GETECH, Leeds	Examinateur
Dr. Ondřej Lexa	Université Charles de Prague	Invité
Prof. Karel Schulmann	Université de Strasbourg	Directeur de thèse

Resumé

L'évolution du flux de matière, de l'architecture et de la rhéologie d'un prisme d'accrétion orogénique au cours du temps est abordée à l'aide d'une étude géologique multiméthode. Le dôme d'Orlica-Śnieżnik dans les Sudètes est situé au front d'un butoir rigide. La formation de ce dôme est expliquée par l'influx de croûte continentale felsique issue de la marge passive subductée jusqu'à 50-60km de profondeur dans un prisme d'accrétion d'échelle crustale. La racine ainsi formée comprend une croûte inférieure felsique avec quelques lentilles basiques partiellement fondues en profondeur et séparées de la croûte moyenne (metasédiments, metavolcanites) par une couche rigide d'orthogneiss peu déformée. Cette infrastructure rhéologiquement hétérogène résultant du remplissage du prisme est fortement remaniée au front du butoir par des plissements plurikilométriques de longueurs d'onde variables. Ceux-ci permettent des échanges verticaux aboutissant à l'exhumation des différents niveaux crustaux de l'infrastructure. La croissance du dôme par plissement au front du butoir s'achève par le décoiffement de la suprastructure associé à un amincissement ductile localisé et à un remplissage des bassins syn-orogéniques adjacents. Cette étude montre bien la formation et l'évolution conjuguée des différents niveaux crustaux en particulier lors de l'enfouissement le long de la zone de subduction au sein du prisme. Ici, la déformation dans les orthogneiss est très localisée et permet le transport passif de larges portions de roches peu déformées et rigides. Ceci est expliqué par un changement dans le mécanisme de recristallisation des roches quartzo feldspathiques d'un fluage- dislocation intense vers un glissement aux joints de grains. Ce changement est initié par la croissance de phases interstitielles dans les agrégats monominéraux. Ce type d'évolution dans un gradient prograde éclogitique est aussi observé dans les migmatites formant le cœur des anticlinaux proches du butoir. Ils permettent l'adoucissement rhéologique nécessaire au fluage dans le prisme d'accrétion crustal.

Mots clé : Flux de coin, dôme de gneiss, plissement crustal, rhéologie, microstructures, dôme d'Orlica-Śnieżnik

Abstract

Evolution of flow, framework and rheology of an orogenic accretionnary prism is assessed with a multi-method geological investigation. The Orlica-Śnieżnik Dome in the Sudetes is situated in front of a rigid indenter. Its structure is explained by an influx of felsic continental crust from the subducted passive margin until 50-60 km depth in a crustal scale accretionnary wedge. The incipient root is composed of lower crustal felsic material partially melted with smaller pieces of basic rocks. Structurally above it lies an intermediate level of weakly deformed augen orthogneiss and metasediments of the middle crust. This rheologicaly heterogeneous layered infrastructure due to burial flow is subsequently reworked in front of the rigid buttress, developing major two-scale wave-length crustal upright folds. It permits vertical material transfers between different crustal levels throughout the infrastructure that is responsible for the growing dome. It is achieved by the detachment of the suprastructure and localized ductile thinning on the top of the exhumed infrastructure. Topography is adjusted by infill of adjacent syn-orogenic basins. This study highlights the shared evolution of the different crustal levels, in particular during influx and burial along the subducting plate. Here, the deformation in orthogneisses bearing eclogites is very localized and allows to passively transport large pieces of weakly deformed orthogneiss into the apex of the corner. This localization is explained by a switch in the mode of recrystallisation from dislocation creep to grain boundary sliding diffusion creep which is chemically enhanced by high nucleation of interstitial phases in monomineralic aggregates. This evolution that appears in a prograde gradient until eclogitic facies in mylonitic orthogneisses leads to drastic reaction weakening and strain localization. This switch in mode of deformation is also observed in the anticline cored by migmatites in front of the butress during exhumation. It permits the weakening of the rocks that is necessary to explain flow in the whole felsic corner.

Keywords: Corner flow, gneiss domes, crustal scale buckle fold, microstructure, Orlica- Śnieżnik Dome

Remerciements

Alors que je m'apprêtais à quitter les terres strasbourgeoises, G. Manatschal, J.F. Ghienne et K. Schulmann me proposèrent de commencer une étude sur l'héritage structural et l'évolution tectonique, avec pour exemple la zone cisaillée de Méséta occidentale (Maroc). Je les remercie de m'avoir proposé ce sujet, même si au final il a été tout autre, car après avoir voyagé un temps dans les Carpates, mon sujet d'étude s'est finalement posé dans le massif d'Orlica-Śnieżnik (Sudètes, Massif de Bohême).

Pendant ces quatre années, Karel Schulmann a toujours su me guider, me faire partager ses idées et son expérience. Ondrej Lexa et Pavla Štípská m'ont aussi beaucoup appris, que ce soit sur le terrain, en pétrologie, ou en analyse microstructurale. Avec eux, j'ai été directement plongé dans les techniques modernes de géologie structurale et de modélisation pétrologique.

J'aimerais remercier tout particulièrement Jean-Emmanuel Martelat avec qui j'ai passé de nombreuses semaines sur le terrain, à l'EBSD, au microscope, en congrès, pendant la rédaction, etc. Son exceptionnelle disponibilité, sa facilité à transmettre ses connaissances, son immense soutien tout au long de la thèse font que plus qu'un collaborateur, il est réellement devenu pour moi un ami.

Merci aux membres du jury, MM. Jean-Marc Lardeaux, Michel Ballèvre, Stanislaw Mazur, Onno Oncken, Hubert Whitechurch, et Ondrej Lexa d'avoir bien voulu évaluer mon travail.

Travailler avec Karel Schulman m'a aussi permis de mettre un pied dans la mafia géologique tchèque : grâce à Vladimir Kusbach, Martin Racek, Martin Staněk, Petr Jeřábek, Honza Franěk, Pavlína Hasalová, Monika Košuličová, Suzanna Kratinová, Prokop Závada, Lenka Baratoux et Matěj Peč, j'ai pu survivre aux innombrables périples rencontrés pendant ma thèse. Merci pour l'aide que vous m'avez apportée depuis que je suis venu pour la première fois à Prague, en 2005. Merci aussi à Jaroslav Synek d'avoir dessiné les magnifiques blocs diagrammes.

Merci à Michel Corsini, Pavel Pitra et Jean-Bernard Edel qui ont chacun contribué à l'élaboration de ma thèse et ont éclairé chacun à leur manière une face de la chaîne varisque (terrain, datation, pétrologie, gravimétrie…).

Bien que mon manuscrit final ne comporte pas de chapitre sur le varisque marocain, je salue Mohamed El Houicha et Ahmed El Attari de la Faculté des Sciences d'El Jadida (Université Chouaib Doukali) pour leur aide dans les Rehamna.

Je ne saurais oublier les chercheurs et enseignants-chercheurs de la rue Blessig et en particulier Anne-Marie Karpoff, Gianreto Manatschal, Philippe Duringer et Yves Géraud. Je leur suis très reconnaissant d'avoir soutenu avec force les jeunes étudiants/thésards du labo, ces années à Strasbourg ont pour moi été un immense plaisir.

Je remercie vivement les techniciens, ingénieurs et personels administratifs de l'EOST: Betty Kieffer pour sa merveilleuse bibliothèque, Binta Mesmacque et Ghenima Bégriche pour leur talent administratif, Annie Bouzeghaia pour l'infographie, Gilles Morvan et Amélie Aubert pour les analyses à l'EBSD, Jean-Pierre Braun et Robert Thuizat pour l'accès au « laboratoire » de litholamellage et pour mes colorations à l'acide fluorhydrique, mais aussi Thomas Theye (microsonde, Freiburg), James Alibon (microsonde, Lausanne), Jakub Haluda (EBSD, Prague) pour leur aide technique.

Tous mes remerciements vont maintenant aux docteurs, doctorants, ou futurs doctorants que j'ai pu rencontrer :

Grâce à Bep la fripouille (Herr Mohn), j'ai toujours eu l'impression que ces quatre annnées de thèse n'étaient finalement qu'une comédie musicale, une aventure sans fin. Merci donc à mon co-bureau : pour ta voix exceptionnelle, ton humour décapant et tes répliques cultes. Bep, ma prochaine thèse, elle sera sur toi !

Sheldon Warden, Pierre Wawrzyniak (et Charlotte Thiérion de Monclin) et Zak Duputel (et Indrah Catapoulet!) : merci pour toutes ces séances Fantasms, Barbarella et autres Planet of the Apes arrosées de Meteor. Mais mon meilleur film de S-F, c'est vous!

Jérémy (le Loup !!!!!!!), merci pour tes nombreuses Jeremiades. Who knows, peut-être qu'on se retrouvera au détour d'un chemin (dans un fossé, en kangoo), ou dans le même labo (au litholamellage), au pire autour d'une Pilsner Urquell.

Herr Etienne Skrzypek, ce fut un plaisir pour moi de travailler avec une machine. Mister Humbert, merci pour toutes les soirées que tu es venu passer avec nous à Strasbourg et merci pour l'accueil à Cergy : c'est si beau ;-) Un grand merci à la génialissime MLB, pour sa bonne humeur et ses gags à répétitions: à conseiller à tous les laboratoires !

La thèse aurait aussi été tout autre sans mes amis du 3ième : José Luis Cobrette et Florence Guegounette. Merci pour le nouveau souffle que vous m'avez apporté à votre arrivée avec vos podiums et autres Coco Lobo! Et spéciale dédicace à la colloc' des dentelles et son fauteuil Emmanuelle !

Je n'oublierai pas Jojo & Doudou, le duo de choc de Blessig, toujours là pour donner vie au labo (La fête de Moustache! Tournoi Daniel Martina!) ni tous les autres doctorants Blessigois comme Thomas Court-jus, Flavie Flament, El Manu Masini, Moussa Abderamane, Suzon, Alexandriaaaaa, Mohamed Jati, Anne-Sophie, Emilie, Jonathan… ou les Descartiens Julia, Chloé, Maxime, Julien, Anthony, Elise, Aurore… ou le bisontin Emilien Oliot. Merci à tous pour votre aide ou votre bonne humeur!

Cette thèse est aussi l'aboutissement d'un parcours entamé avec les géologues de l'Xtrem stéphanois Lydérick France (Globule) et Fabien Deschamps (%#@!&). Nos routes scientifiques se sont depuis longtemps éloignées, vivement qu'elles se rejoignent un jour !

Merci à mes vieux amis Florian Murard, Mathieu Chardon, Guillaume Denisse, Mister Nelson Simões et toute la troupe du 177 (Stansmith, Metastaz, Mo…).

Enfin, rien n'aurait été possible sans le soutien indéfectible de ma merveilleuse famille. Mille mercis.

Mais la plus belle de mes découvertes, c'est bien toi, ma douce Delphine.

AVANT-PROPOS

Cette thèse est une étude multiéchelle structurale et pétrologique détaillée des mécanismes de flux de matière dans les prismes d'accrétions orogéniques et des dômes de gneiss associés. Elle a bénéficié du soutien de nombreux collaborateurs internes et externes en liaison avec le projet ANR « LFO in orogens » (06-1148784 pour K. Schulmann). Elle souligne l'importance des mécanismes d'enfouissement dans un système de flux de coin d'échelle crustale et de plissement au front du butoir permettant l'exhumation des roches de hauts degrés. Elle met en valeur le rôle de l'adoucissement rhéologique de la croûte tout au long de ces processus.

La zone d'étude est le dôme d'Orlica Snieznik (OSD) situé dans la partie nord-est de la chaîne varisque européenne (Sudètes Centrales), à la frontière entre la République Tchèque et la Pologne. D'une superficie d'environ 250km², il représente une portion de la racine orogénique moldanubo-lugienne exhumée au cours du carbonifère et offre un cadre privilégié permettant d'étudier l'évolution de l'architecture et de la rhéologie dans un prisme d'accrétion crustal.

Le **chapitre I** est un bref rappel des principaux modèles géodynamiques existant permettant l'enfouissement et exhumation de roches de hauts degrés métamorphiques. Une attention particulière est donnée au modèle de flux de coin et de formation des dômes de gneiss.

Le **chapitre II** vise à comprendre l'architecture du massif d'Orlica-Śnieżnik par une étude structurale et pétrographique détaillée combinée à une compilation des données géochronologiques et pétrologiques existantes. Pour cela, j'ai effectué quatre mois cumulés de travail sur le terrain afin d'identifier les structures de déformation dans toutes les lithologies, de les corréler à l'ensemble du dôme, et d'effectuer un échantillonnage ciblé afin de poursuivre l'étude pétrographique une fois de retour à Strasbourg. Il m'a ensuite été possible d'associer les nouveaux âges ^{40}Ar-^{39}Ar réalisées à l'Université de Nice Sophia-Antipolis par l'équipe de M. Corsini, avec l'aide d'E. Skrzypek et J. Lehmann (Université de strasbourg) à une nouvelle base de données géochronologiques et pétrologiques issue de la bibliographie. Enfin, l'étroite collaboration avec J.R. Dujardin pendant son stage de Master 2 sur la modélisation gravimétrique des Sudètes m'a permis d'avoir en main des données essentielles à la compréhension de l'évolution de cette partie de l'orogène. Ce chapitre est en préparation pour *Tectonics*.

De cette étude découle le **chapitre III**. Il se focalise sur une zone d'étude particulière où des niveaux crustaux différents (différence de pression d'une quinzaine de kilobars) sont aujourd'hui latéralement juxtaposés de seulement 5 km, et ce sans discontinuité structurale majeure. Une étude structurale détaillée combinée avec de nouvelles données pétrologiques en liaison avec les structures de déformation a permis de dessiner un modèle d'exhumation par plissements crustaux au front d'un butoir rigide. Pour ce chapitre, la modélisation a été confiée à P. Stipska, E.Skrzypek (Université de Strasbourg), P. Pitra (Université de Rennes I) et C. Bolinger (Université de Lilles). Ma connaissance de terrain du dôme, de la pétrographie régionale et des données bibliographiques ont été indispensables à l'élaboration du modèle dont est issu ce chapitre. Il sera soumis à *Journal of Metamorphic Geology*.

Le **chapitre IV** de cette thèse est une étude microstructurale et pétrologique d'un gradient de déformation témoin de l'enfouissement progressif de la croûte continentale dans le prisme d'accrétion. J'ai pu effectuer les analyses EBSD sur le microscope électronique TESCAN VEGA XMU récemment acquis par l'EOST alors que j'ai dû effectuer un déplacement à l'Université de Lausanne pour les analyses microsondes. Pendant ce travail, O.Lexa (Université Charles, Prague) m'a initié à l'utilisation de la boîte à outils Matlab PolyLX toolbox pour l'acquisition des données microstructurales quantitatives. L'interprétation de ces données s'est faite en étroite collaboration avec J.E. Martelat (Université de Grenoble). Enfin, cette étude est complétée par une modélisation pétrologique réalisée par P. Stipska (Université de Strasbourg) qui a été fort utile pour l'élaboration finale du modèle. Ce chapitre sera soumis à *Journal of Metamorphic Geology*.

Enfin, je reprends dans le **chapitre V** une partie des outils utilisés dans le chapitre précédent mais cette fois appliqués à une zone de déformation dans des migmatites situées dans un anticlinal migmatitique. J'ai pu aller au Service Géologique Tchèque pour l'acquisition des données EBSD. Ce chapitre a bénéficié des travaux de P. Pitra (Université de Rennes I) sur la modélisation pétrologique.

Après un chapitre de conlusion, sont présentés dans un chapitre annexe quelques bases sur les microstructures de déformation dans le domaine ductile.

L'ensemble de ces travaux a été présenté successivement à la conférence Mechanism of Variscan Orogeny (Orléans, 2007), au séminaire intensif Marie-Curie EURISPET (Paris, 2007), à la RST2008 (Nancy), à l'EGU 2009 (Wien, Autriche), à Granulite&Granulites2009 (Turnov, République Tchèque), à la DRT2009 (Liverpool, Angleterre), au séminaire CNRS Forstérite 2009 (Ariège) ainsi qu'aux congrès annuels organisés par l'Ecole Doctorale.

Ne sont pas présentés ici les résultats préliminaires obtenus par une étude structurale (6 semaines de terrain cumulés) et géochronologique (datations ^{40}Ar-^{39}Ar, un séjour à Géoscience Azur) du dôme métamorphique intracontinental du massif des Rehamna (Maroc) que j'ai effectués en collaboration avec J.F. Ghienne (CNRS, Strasbourg), M.Corsini (Université de Nice-Sophia Anipolis) et MM. M. El Houicha et M. El Attari (Faculté des Sciences et Techniques d'El Jadida). Bien que réalisé pendant ma thèse, cette étude est moins avancée que celle effectuée sur le dôme d'Orlica-Snieznik et n'apporte pas à ce stade d'éléments indispensables à la discussion. Toutefois, ces résultats sont disponibles sous forme de résumés (EGU2009, RST2010). Ce travail sera mis en valeur au cours de mon ATER qui débutera au 1er septembre 2010 à l'Université de Nice-Sophia Antipolis.

SOMMAIRE

Résumé - Abstract 3

Remerciements 5

Avant-Propos - Foreword (in french) 9

Sommaire 12

Chapitre I - INTRODUCTION (in french) 15

1. Modeles d'exhumation 16
2. Les dômes de gneiss 19
3. Zone d'etude et problematique 21

Chapitre II - MULTISTAGE SYN-CONVERGENT GROWTH AND COLLAPSE OF MANTLED GNEISS DOME (ORLICA ŚNIEŻNIK DOME, BOHEMIAN MASSIF) 25

1. Introduction 27
2. Tectonic setting 28
3. Geology of the Orlica-Śnieżnik Dome 30
- 3. 1. Lithology of the OSD core 30
- 3. 2. Lithology of the OSD mantle 30
- 3. 3. Metamorphism 32
- 3. 4. Existing U-Pb and Sm-Nd geochronology 34
- 3. 5. ^{40}Ar-^{39}Ar geochronology of the OSD core 36
- 3. 6. ^{40}Ar-^{39}Ar geochronology of the OSD mantle 37

4. Structural evolution 38
- 4. 1. Northern Domain (Rychlebské Hory and Góry Złote mountains) 39
- 4. 2. Central Domain (Krowiarki Mountains) 42
- 4. 3. Southern domain (Międzygórze and Králíky-Śnieżnik massifs) 42
- 4. 4. South-Western Domain (Góry Bysrzyckie and Orlické Hory mountains) 44
- 4. 5. Structures of the metamorphic mantle 46

5. Deformation and metamorphism 46
- 5. 1. D1 parageneses 47
- 5. 2. D2 parageneses 47
- 5. 3. D3 parageneses 49
- 5. 4. Metamorphic gradients during polyphase deformation 49

6. Deep structure of the OSD 51
- 6. 1. Gravity constraints 51
- 6. 2. Gravity modelling 52

7. Discussion 55
- 7. 1. Significance of D1 – formation of continental wedge 55
- 7. 2. Significance of D2 – folding due to indentation of wedge 56

7. 3. Flat S3 fabric – ductile thinning and collapse of folds 58
7. 4. Significance of distribution of isotherms and isograds 59
7. 5. The geodynamic model for growth of the OSD 60

Chapitre III - THE ROLE OF LARGE-SCALE FOLDING AND EROSION ON JUXTAPOSITION OF ECLOGITE AND MID-CRUSTAL ROCKS (ORLICA-ŚNIEŻNIK DOME, BOHEMIAN MASSIF) 69

1. Introduction 71
2. Geological setting 72
2. 1. Lithology and protoliths 72
2. 2. Previous structural studies 74
2. 3. Previous metamorphic and geochronological studies 74
3. Structural geology 76
3. 1. D1 deformation 76
3. 2. D2 deformation 78
3. 3. D3 deformation 80
4. Petrology 82
4. 1. Analytical procedures and abbreviations 82
4. 2. Eclogite and amphibolitized eclogite 83
4. 3. Metapelites 84
5. Mineral equilibria modelling 90
5. 1. Calculation methods 90
5. 2. Pseudosection for eclogite and amphibolitized eclogite 91
5. 3. Pseudosection for metapelite sample ES95D 95
6. Discussion and conclusions 94
6. 1. Tectonic significance of orogenic fabrics 94
6. 2. P-T-D paths 95
6. 3. Constraining the juxtaposition of eclogite and metapelites 97
6. 4. P−T−D evolution in the frame of existing orogenic models 104

Chapitre IV - PROGRADE DEFORMATION GRADIENT IN SUBDUCTED HP ORTHOGNEISS (ORLICA – ŚNIEŻNIK DOME, CENTRAL SUDETES): IMPLICATIONS FOR REACTION SOFTENING AND STRAIN LOCALISATION DURING CONTINENTAL SUBDUCTION 105

1. Introduction 108
2. Geololgical setting 109
3. Definition of structural types according to finite strain gradient 111
4. Whole rocks composition 112
5. Microstructural and petrological characteristics of rock types 114
5. 1. Type I: Augen gneiss 114
Type II: Banded orthogneiss gneiss 121
5. 2. Type III: Mylonitic gneiss 121
6. Petrological modelling 122

7. Quantitative microstructural analysis 124
7. 1. Grain size statistics and Crystal Size Distribution (CSD) 124
7. 2. Grain Shapes and Shape Preferred Orientation (SPO) 127
7. 3. Grain Contact Frequency (GCF) and Grain Boundary Preferred Orientation (GBPO) 128
8. Lattice Preferred Orientation (LPO) 130
8. 1. LPO of quartz 130
8. 2. LPO of Kfeldspar 132
9. Discussion 133
9. 1. Interpretation of deformation mechanisms and rheology of orthogneiss across finite strain gradient 133
9. 2. Open or close system? 135
9. 3. HP character of studied orthogneiss sequence 135
9. 4. Model of strain localisation and reaction weakening in a continental accretionnary wedge 136
10. Conclusion 138

Chapitre V - RHEOLOGY OF HIGH GRADE MIGMATITES DURING LATERAL SHORTENING AND ASSOCIATED EXHUMATION (ORLICA ŚNIEŻNIK DOME - BOHEMIAN MASSIF) 139

1. Introduction 141
2. Geological setting 141
3. Macroscopique description 144
4. Whole rock chemistery 145
5. Microstructural observetions and mineral chemistery 146
5. 1. Type I microstructures: ophtamitic migmatite 147
5. 2. Type II microstructures: schlieren migmatite 149
5. 3. Type III microstructures: nebulitic migmatite 152
6. Evidence of melting 152
7. Latice preffered orientation 154
7. 1. LPO of quartz 154
7. 2. LPO of K-feldspar 154
7. 3. LPO of plagioclase 156
8. Discussion 161
8. 1. Migmatite origin 156
8. 2. Significance of lattice preferred orientation and associated microstructures 157
8. 3. Correlation with adjacent units 157

Chapitre VI - GENERAL CONCLUSION (in french) 159

References 163

Annexe - Appendix (in french) 181

CHAPITRE I

La dynamique de la tectonique des plaques associée aux forces de gravité entraîne la confrontation de forces latérales et verticales lors de la formation d'une orogène qui se manifeste par l'épaississement de la croûte puis son retour à l'équilibre alors que les forces latérales ne supportent plus les forces gravitaires (Rey *et al.*, 2001; Gapais *et al.*, 2009). Le matériel accumulé constitue en profondeur la racine orogénique où l'on retrouve à priori les roches de plus haut degré enfouies pendant la subduction et l'accrétion de matériel entre les deux plaques tectoniques. Dans les orogènes phanérozoïques actuels sont exposés en surface la juxtaposition de niveaux crustaux montrant des styles structuraux et des évolutions métamorphiques contrastés (infrastructure et suprastructure, (infrastructure et suprastructure, voir Culshaw *et al.*, 2006). L'étude géologique détaillée de ces orogènes associée à des modélisations numériques et analogiques ont permis de proposer de nombreux modèles permettant d'expliquer comment les roches de l'infrastructure peuvent être exhumées, mise à l'affleurement au même niveau que la suprastructure (Platt, 1993; Ring *et al.*, 1999).

1. Modeles d'exhumation des roches métamorphiques de haut degre dans les orogenes de collision

Le premier groupe se focalise sur les roches exhumées à la suture, le long de la zone de subduction par remontée gravitaire (Chemenda *et al.*, 1995) ou flux chenalisé d'un matériel de faible viscosité (Beaumont *et al.*, 2001; Hodges *et al.*, 2001; Jamieson *et al.*, 2002; Jolivet *et al.*, 2005) pendant ou après la convergence (Fig. I-1). Dans ce cas, les roches ainsi exhumées par cisaillement simple au front du prisme d'accrétion enregistrent un enfouissement et une exhumation le long d'un géotherme souvent froid sensiblement proche de celui de la zone d'exhumation. Le flux ascendant est totalement découplé de la zone de subduction adjacente.

Le modèle de flux de coin dans les prismes d'accrétion (Cowan & Silling, 1978; Cloos,

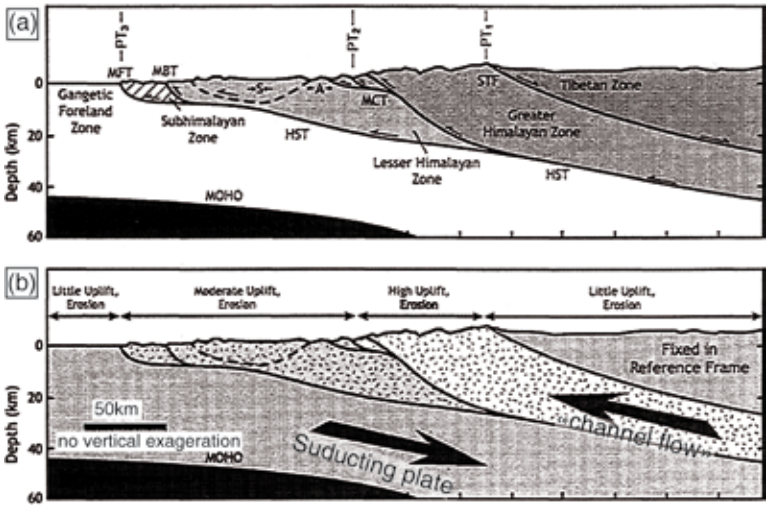

Fig. I- 1: (a) Coupe schématique à travers l'Himalaya et le plateau tibétain. (B) interprétation de l'architecture montrant le flux localisé en chenal le long de la zone de subduction (modifié d'après Hodges et al., 2001).

1982; Pavlis & Bruhn, 1983; Platt, 1993; Feehan & Brandon, 1999; Fig. I-2) est un modèle de flux de matière relativement ducile par enfouissement couplé le long de la zone de subduction suivie d'une exhumation par contraction verticale et/ou horizontale alors que le flux est bloqué par le butoir rigide (Platt, 1987, 1993; Allemand & Lardeaux, 1997; Plesch & Oncken, 1997; Ring et al., 1999).

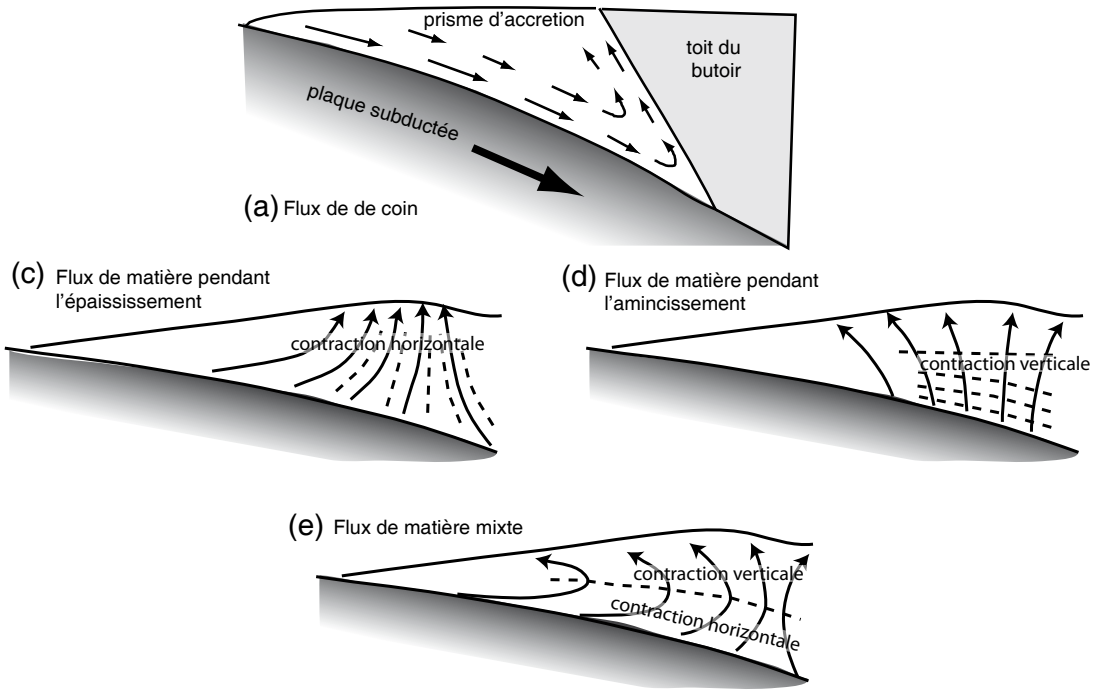

Fig. I- 2: Modèle de flux de flux de coin ("corner flow") dans un prisme d'accrétion. (a) Influx de matière dans la partie inférieure du prisme et exhumation à l'approche du butoir rigide (Platt, 1993). (b), (c), (d) Différents types de flux possibles proches du butoir en liaison avec l'épaississement (b), ou l'amincissement ductile (c) ou la conjonction de ces deux derniers types de flux (modifié d'après Feehan & Brandon, 1999; Ring et al., 1999). Les flèches indiquent les lignes de flux, les tiretés correspondent au clivage général attendu.

Le flux de matière est possible dans l'ensemble de l'orogène si on la considère comme un prisme d'accrétion d'échelle crustale (Buslov*, et al.*, 2001; Stöckhert & Gerya, 2005; Gerya & Stöckhert, 2006; Beaumont*, et al.*, 2009; Fig. I-3).L'exhumation des roches métamorphiques peut donc être distribuée sur une grande partie de la largeur du prisme ou bien être plus localisée au front du butoir.

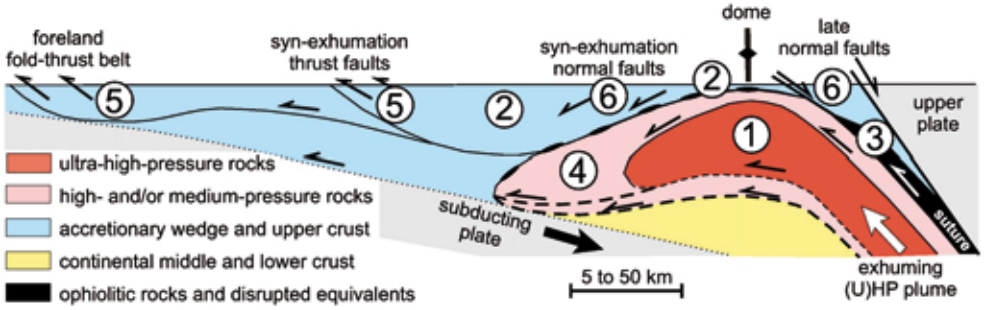

Fig. I- 3: Architecture d'un prisme d'accrétion d'échelle crustale d'après Beaumont et al. (2009). (1) dôme contenant des roches d'ultra haute pression surmontant des (2) roches de plus faible degré métamorphique. (3) Suture ophiolitique. (4) Nappe de moyenne à haute pression. (5) Nappes d'avant-pays. (6) Exhumation syntectonique le long de failles normales. La variation d'échelle souligne la taille variée des complexes d'ultra haute pression.

Elle peut être amplifié par les effets gravitaires. On peut observer un découplage entre les parties de l'infrastructure exhumées (où une déformation pervasive est observée) et les roches de la suprastructure où la déformation est plus localisée (failles normales, chevauchements). Si les deux blocs rigides limitant la zone d'épaississement présentent des limites abruptes, il peut alors se produire une extrusion verticale très efficace uniquement par cisaillement pur (Thompson *et al.*, 1997).

Le troisième groupe comprend l'exhumation par effondrement gravitaire extensif de la croûte orogénique épaissie (Dewey, 1988; Andersen & Fossen, 1993; Rey *et al.*, 2001; Vanderhaeghe & Teyssier, 2001; Teyssier & Whitney, 2002; Vanderhaeghe, 2009) qui entraîne le développement de « metamorphic core complex » et de dômes de gneiss le long de failles de détachements, après la convergence, bien que l'extension syn convergence soit aussi parfois observée. Là encore, on observe un fort découplage entre la suprastructure et l'infrastructure de l'orogène en cours de destruction (Fig. I-4). Les roches ainsi exhumées sont généralement les témoins de gradients géothermiques élevés issus de la maturité thermique de l'orogène.

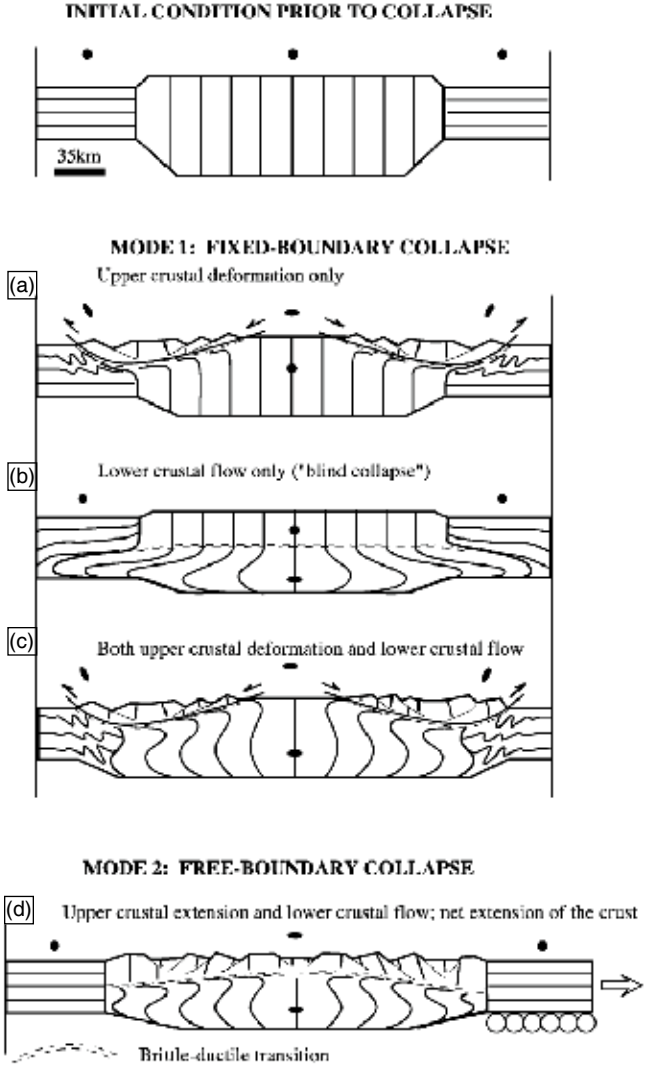

Fig. I- 4: Effondrement gravitaire d'une croûte épaissie d'après Rey et al. (2001). Par rééquilibrage dans (a) la suprastructure, (b) l'infrastructure ou (c) dans la croûte dans son ensemble (c). Le dernier modèle (d) permet l'extension de toute la structure (bords libres)

2. Les domes de gneiss

Les dômes de gneiss sont de larges structures constituées en majeures parties d'orthogneisses englobant des roches de haut degré métamorphique, généralement des migmatites associées à des granulites que l'on retrouve au sein des orogènes aussi bien à l'archéen qu'au phanérozoïque (Whitney *et al.*, 2004). Ces dômes sont généralement entourés de roches de plus faible degré métamorphique (« mantle gneiss dome ») et leur formation représente un rôle thermo-mécanique majeur responsable de l'échange de matière entre différents niveaux crustaux. Leur origine est discutée, elle est suivant les interprétations ou l'architecture considérée comme des structures extensives de type « metamorphic core complexe » (Brun & Van Den Driesshe, 1994), des structures de convergences par plissement crustal (Rolland *et al.*, 2001; Burg *et al.*, 2004) et extrusion (Štípská *et al.*, 2004) ou par des phénomènes de diapirisme (e.g. Lee *et al.*, 2000). La Figure I-5 présente d'une manière simple l'architecture de ces dômes et les gradients métamorphiques et structuraux qui en découlent.

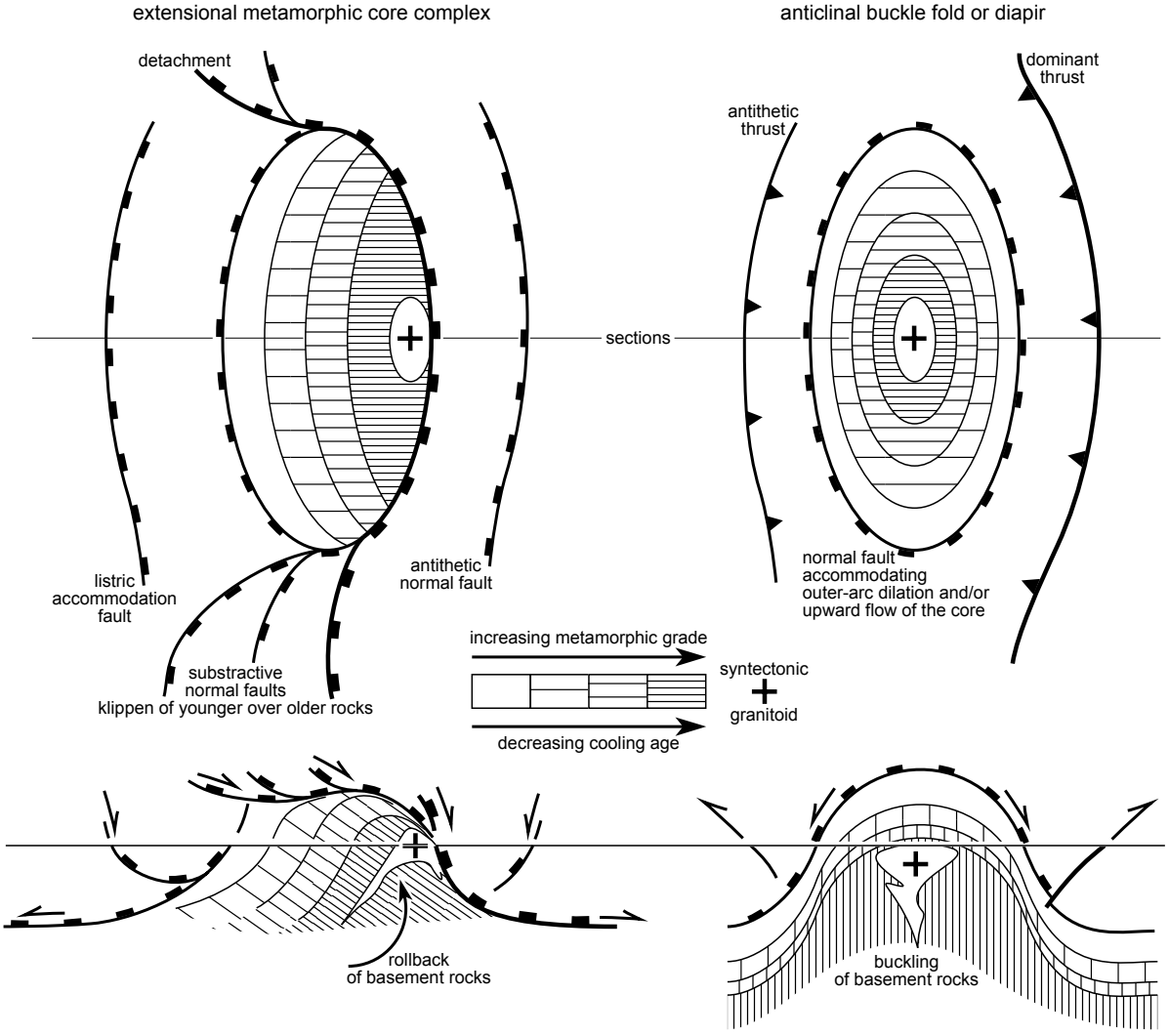

Fig. I- 5: Vue en carte (en haut) et en coupe (en bas) de la symétrie et de l'asymétrie qui caractérise les dômes formés par plissement (flambage) et diapir (à gauche) et par extension de type « metamophic core complex » (d'après Burg, et al. 2004).

Bien sûr, ces différents modèles peuvent être associés et il a été ainsi proposé des modèles d'ascension diapirique pendant l'extension ou la convergence (Vanderhaeghe, 1999; Lexa *et al.*, 2010), des modèles d'exhumation en système de transpression et transtension (Whitney *et al.*, 2007) ainsi que des modèles où l'on oppose au flux vertical un flux latéral chenalisé (Whitney et al., 2004). Ainsi, Burg *et al.* (2004) présente par exemple l'architecture attendue détaillée de dômes formés soit en système de convergence soit par diapirisme avec ou sans l'influence de l'érosion et de la suprastructure sus-jacente (Fig. I-6). Les structures résultantes sont contrastées d'un modèle à l'autre notamment au niveau du couplage entre l'infrastructure et la suprastructure et de la forme générale du dôme. Les mouvements verticaux qui en résultent sont associés à une fusion partielle intense qui peut précéder, être contemporaine ou suivre la formation du dôme et se manifester par la formation de migmatites ou de plutons granitiques. La fusion partielle associée à une baisse de la viscosité est souvent expliquée par la remontée quasi adiabatique du volume de roche felsique permettant de dépasser le solidus. D'autres facteurs comme la relaxation thermique ou la haute production de chaleur par accrétion de matériel felsique à forte radioactivité sont aussi proposés (e.g. Lexa *et al.*, 2010).

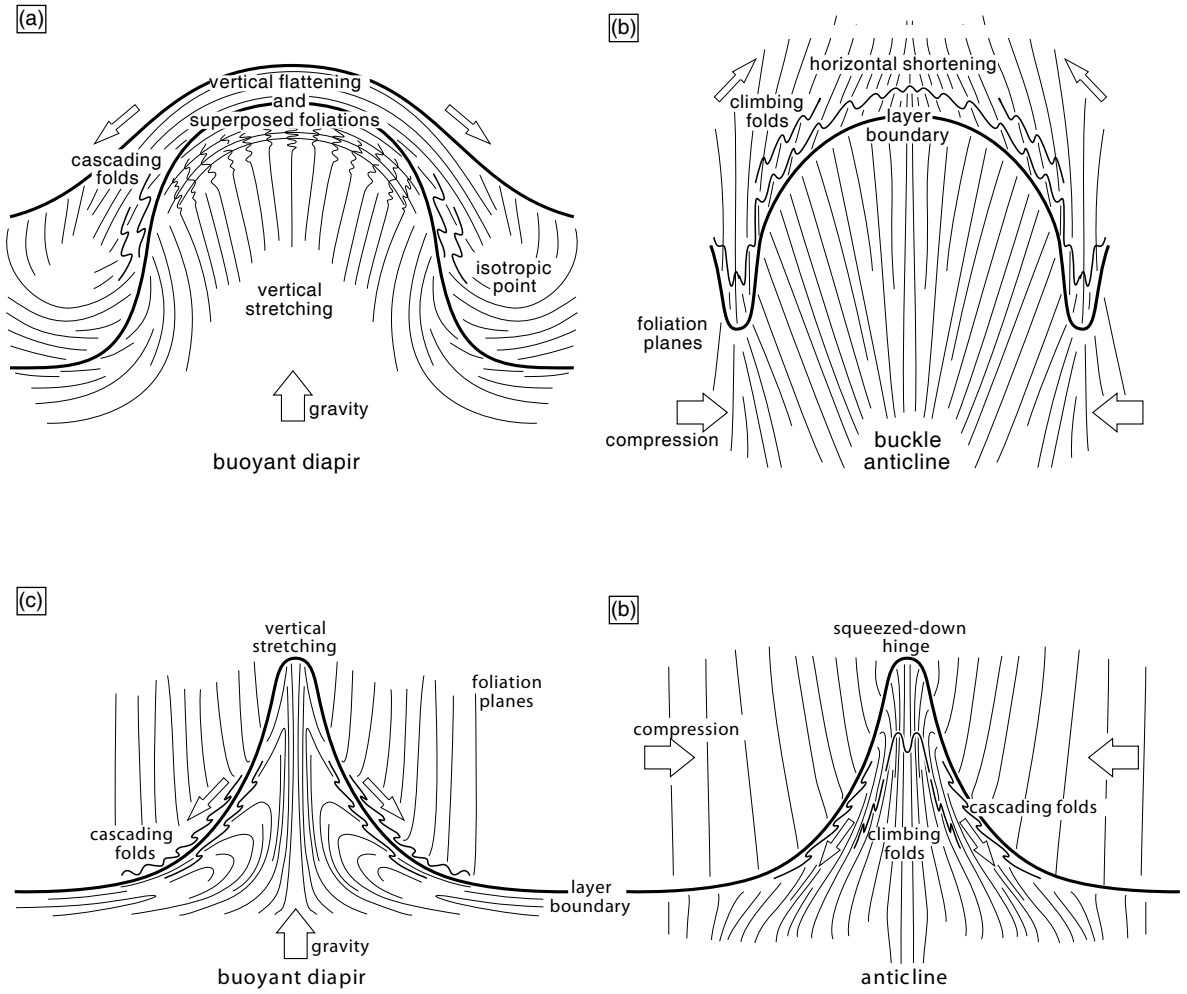

Fig. I- 6: Type de structures attendus dans des dômes de gneiss formés par (a) diapirisme ou (b) plissement. (c) et (d) montrent l'influence de l'érosion dans ces modèles d'exhumation (d'après Burg et al., 2004).

Il y a par conséquent de nombreux marqueurs permettant de différencier le mode d'exhumation des roches de haut degré comme la répartition géométrique des roches exhumées (le long de la suture, au sein du prisme d'accrétion, en bordure du butoir etc …), le type de structure (déformation localisée ou pervasive) et leur orientations (foliations métamorphiques plates, subverticales, failles de détachements), la forme des trajets PT (gradient de température, maturité thermique) et aux données géochronologiques (âges du métamorphisme, âge de refroidissement).

Les questions posées par les prismes d'accrétion orogénique et les dômes sont les suivantes:

Quel est l'évolution du flux de matière, de l'architecture et de la rhéologie au cours du temps ? Quel est l'influence de la convergence dans l'évolution de l'architecture par rapport à l'extension syn ou post orogénique, le diapirisme et l'érosion? Quel est le lien entre les déformations internes de l'infrastructure exhumée et la suprastructure (« mantle ») environnante ? Comment interpréter l'hétérogénéité des structures?

3. Zone d'etude et problematique

La chaîne varisque européenne (Matte *et al.*, 1990; Lardeaux *et al.*, 2001; Faure *et al.*, 2009) et plus particulièrement le massif de bohême (Schulmann *et al.*, 2009; Fig. I-7) pourrait représenter des structures de prisme d'accrétion d'échelle crustale, avec des zones d'exhumation localisées au front du prisme d'accrétion (saxo-thuringienne) et entre le butoir et (Brunia) l'ancienne structure d'arc (Teplá Barrandien) où l'on retrouve exhumée la racine orogénique (zone moldanubo-lugienne). Les études géophysiques associées au modèles numériques au Sud du massif de Bohême montrent que la formation de la racine orogénique moldanubiene se fait par sous-placage de croûte océanique et de larges portions de croûte continentale felsique de l'océan saxo-thuringien et de sa marge continentale passive (Guy *et al.* 2010; Lexa et al., in press). L'exhumation proche du butoir est réalisée par remontée diapirique des roches felsiques associée à la convergence continue dans le prisme (Lexa et al., in press) entraînant un plissement d'échelle crustal permettant l'exhumation des roches les plus profondes de la racine (Schulmann *et al.*, 2005; Racek *et al.*, 2006; Franěk *et al.*, 2010). L'exhumation se termine par un étalement latéral de la racine sur le butoir rigide (Racek et al., 2006). Ces études soulignent que de tels processus impliquent une faible résistance mécanique de l'infrastructure orogénique liée à la présence de roches partiellement fondues dans la racine (Zavada *et al.*, 2007; Hasalová *et al.*, 2008; Schulmann *et al.*, 2008).

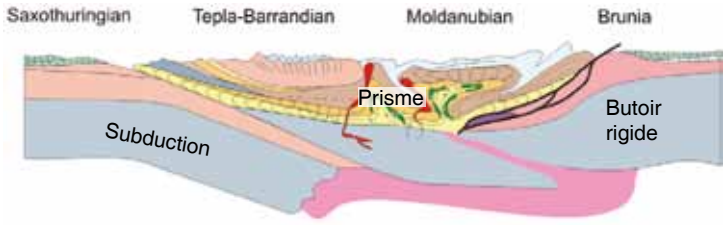

Fig. I- 7: Coupe interprétative à travers le massif de Bohême montrant les principales unités tectoniques sous la forme d'un prisme d'accrétion d'échelle crustale (d'après Schulmann, et al., 2009). Subduction de la zone Saxo-Thuringienne sous la suprastructure Teplá-Barrandienne et exhumation et étalement de la racine Moldanibienne sur le butoir rigide Brunia.

Dans ce volume est présentée une étude à grande échelle du dôme d'Orlica-Śnieżnik (OSD) situé au Nord-est du massif de Bohême, dans les Sudètes Centrales, à la frontière entre la République Tchèque et la Pologne. Situé en bordure du butoir orogénique, il présente une structure en dôme atypique, où l'on retrouve une alternance en bandes de metapelites du faciès amphibolite et d'orthogneiss variés au sein desquels sont exhumés des roches de haut degré métamorphique eclogites et HP-granulites (Don *et al.*, 2003). Ce dôme présente aussi de larges portions d'orthogneiss très peu déformés avec des zones très localisées de déformation. Cette configuration a été interprétée comme le résultat d'un plissement d'échelle kilométrique au sein du dôme (Dumicz, 1979; Don, 1982; Fig. I-8a) suggérant des échanges majeurs entre les différents niveaux crustaux (roches de haut degré, orthogneiss intermédiaires et métapélites sus-jacentes) permettant leur juxtaposition par convergence au front d'un butoir rigide (Štípská *et al.*, 2001; Štípská *et al.*, 2004; Pressler *et al.*, 2007; Skrzypek *et al.*, 2010b; Fig. I-8b).

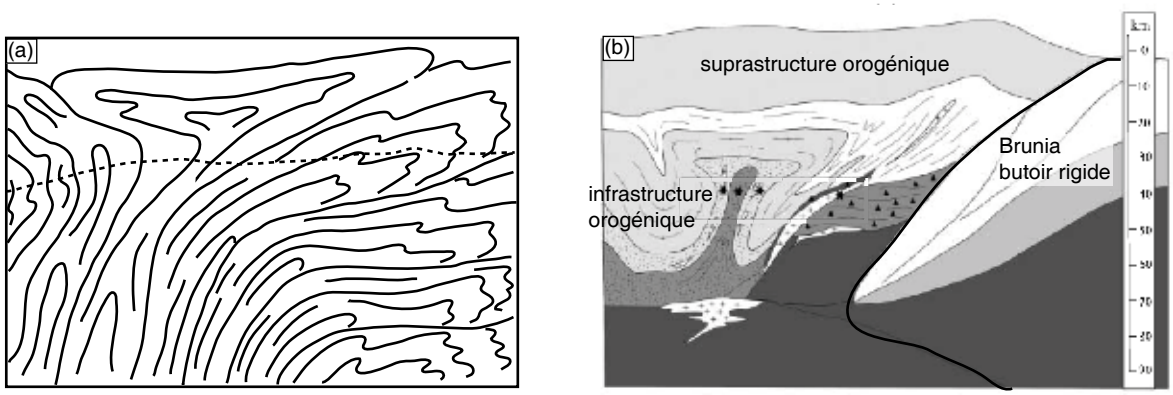

Fig. I- 8: (a) Structure et (b) modèle d'exhumation par plisssement et extrusion pour la bande granulitique du dôme d'Orlica-Śnieżnik située à cinq kilomètres du butoir rigide (Brunia) proposé par Dumicz (1979) et Štípská et al. (2004).

Les études sont limitées à une zone précise de l'OSD (Štípská *et al.*, 2004; Skrzypek, et al., 2010b) et ne prennent que peu ou mal en compte l'évolution polyphasée de l'orogène (Pressler *et al.*, 2007). De part son architecture, qui associe prisme orogénique et dôme de gneiss interne en bordure du butoir, il offre un cas exceptionnel où il est possible d'observer les différents niveaux crustaux de la racine (infrastructure) et des roches de plus faible degré environnantes (suprastructures). Ainsi, l'évolution du flux de matière, de la rhéologique et des mécanismes de déformation à l'échelle du dôme mais aussi à l'échelle du prisme (Sudètes) peuvent-elles être abordées depuis la formation de la racine, jusqu'à son exhumation à la surface.

Le **chapitre II** de cette étude vise ainsi à répondre aux questions suivantes: Comment interpréter à l'échelle du dôme la répartition des différents épisodes de déformation et métamorphiques associés en terme de convergence et de réponse gravitaire? Comment se répartissent ces structures dans l'espace et le temps? Quelle est aujourd'hui l'architecture en profondeur ? Y a-t-il un ou plusieurs dômes de gneiss? Comment évolue le système de sous-plaque de matériel felsique lors de la convergence à l'approche du butoir et comment s'exprime l'amincissement ductile et l'érosion au sein du prisme et finalement comment se comporte la suprastructure?

Ce modèle de flux de matière dans le prisme est étudié d'une façon plus détaillée dans le **chapitre III** où sont présentés les mécanismes d'enfouissement puis d'échanges de matière entre différents niveaux crustaux au front du prisme d'accrétion.

Les deux derniers chapitres permettent d'amener des réponses quant aux mécanismes de localisation de la déformation lors de l'enfouissement de la croûte continentale (**chapitre IV**) et de son exhumation dans les anticlinaux d'échelle crustale (**chapitre V**): quel est l'état rhéologique de la croûte felsique (orthogneiss) pendant son enfouissement et son exhumation ? Comment interpréter les changements des mécanismes de déformation associés aux variations texturales et pétrologiques?

Les résulats majeurs de ce travail sont finalement présentés dans le chapitre de conclusion.

CHAPITRE II

MULTISTAGE SYN-CONVERGENT GROWTH AND COLLAPSE OF MANTLED GNEISS DOME (ORLICA ŚNIEŻNIK DOME, BOHEMIAN MASSIF)

F. CHOPIN[1], K. SCHULMANN[1], E. SKRZYPEK[1], J.R. DUJARDIN[1], J. LEHMANN[2], J.E. MARTELAT[3], O.LEXA[2,4], M. CORSINI[5], J.B. EDEL[1],P. ŠTÍPSKÁ[1], P.PITRA[6]

[1]*Ecole et Observatoire des Sciences de la Terre, Institut de Physique du Globe – CNRS UMR 7516, Université de Strasbourg, 1 rue Blessig, F-67084, Strasbourg Cedex, France*

[2]*Czech Geological Survey, Klárov 3, CZ-11000, Prague, Czech Republic*

[3] *Laboratoire des Sciences de la Terre – CNRS UMR5570, Université de Lyon 1, F-69622, Villeurbanne, France*

[4]*Institute of Petrology and Structural Geology, Charles University, Albertov 6, CZ-12843 Prague, Czech Republic*

[5]*Geosciences Azur – CNRS UMR 6526, Université de Nice – Sophia Antipolis, Parc Valrose, F-06108 Nice, France*

[6]*Geosciences Rennes – CNRS UMR6118, Université Rennes 1, Campus de Beaulieu, F-35042 Rennes Cedex, France*

Key words: Mantled geniss dome, crustal folding, continental accretionary wedge, metamorphism and thermochronology, gravity modelling

Abstract

The Orlica-Śnieżnik dome shows polyphase structural and metamorphic history characterized by eastward influx of lower plate Cambro-Ordovician continental material bellow westerly upper plate Neoproterozoic crust. This event is manifested by development of flat fabrics related to HP-LT metamorphic gradient in orogenic lower crust and garnet-staurolite metamorphism in orogenic middle crust. Subsequent influx of continental crust creates thick felsic orogenic lower crust composed of HP granulites and HP partially molten gneisses. The orogenic wedge is next deformed by adjacent easterly continental indentor leading to multiscale folding of orogenic infrastructure. Folding is associated with further burial of orogenic middle crust in kilometre scale synforms and uplift of deep orogenic lower crust in antiforms. This stage continuously passes to crustal scale folding of the whole infrastructure responsible for uplift of continuously shortened smaller scale synforms and antiforms. This event leads to development of major cleavage system associated with metamorphic zonation increasing towards the large migmatitic dome to the east. While western part of wedge is cooled bellow argon blocking temperatures of micas the easterly migmatitic thermal dome remains hot and shows retarded cooling ages. Vertical growth of crustal dome is related to pure shear dominated ductile thinning followed by

major non-coaxial detachment fault zone and erosion of deep rocks leading to the development of sedimentary basin to the west. The Bouguer anomaly pattern shows that the felsic material was exchanged with orogenic suprastructre during growth of dome and sliding of orogenic suprastructure along large scale detachment.

1. Introduction

Orogenic processes imply interplay between lateral convergence and vertical gravitational forces resulting into distributed or pervasive homogeneous deformation in the crust (e.g. 2009) that can be achieved by juxtaposition of rocks that suffered different PTD paths, i.e. orogenic infra- and suprastructure (e.g. Culshaw *et al.*, 2006). The orogens are sites of thickening and burial of crust up to 70 km and development of topography reaching 5–6 km. The high topography results from thickening of buoyant crust and subsequent erosion bring deeper crustal levels to the surface and supply the sedimentary basin. Typical feature of ancient orogens is development of circular or elliptical structures containing high grade rocks in the core surrounded by sedimentary basins. The development of domes and basins is a sign of vertical movements in the crust (Brun, 1983) while thrusts and fold belts indicate horizontal movements and lateral shortening (Burg *et al.*, 2004). However, the vertical movements can be intimately associated with lateral channel flow producing highly asymmetric dome-like structures (Whitney *et al.*, 2004). The process of formation of classical gneiss domes associated with deep crustal channel flow was, successfully modeled by Beaumont *et al.* (2006) in areas of abandoned focused erosion.

Burg *et al.* (2004) discussed and modeled the interplay between gravity and tectonic forces in structuring the continental crust. These authors produced a phase diagrams discriminating several folding-diapirism modes as a result of relative contributions of gravity and compression during the growth of crustal scale buckle-anticlines and diapirs both submitted to instantaneous erosion. Finally, structural characteristics of matrix diapirism and folding is distinguished from detachment diapiric and folding modes when the system is submitted to instantaneous erosion.

The European Variscan belt shows geometry of continental accretionary wedge (Matte *et al.*, 1990; Lardeaux *et al.*, 2001; Faure *et al.*, 2009; Schulmann *et al.*, 2009). In the Bohemian massif, the structure of deep part of the orogen has been explained by allochthonous feeding of the wedge-shaped root by felsic rocks of the subducting continental plate (Guy *et al.*, 2010). Exhumation of orogenic lower crust is explained as a result of laterally forced gravitational overturns (Lexa *et al.*, 2010) and crustal scale folding (Štípská *et al.*, 2004; Franěk *et al.*, 2010; Skrzypek *et al.*, 2010b). Final increments of exhumation are controlled by lateral subsurface flow of extruded lower crust underneath rigid lid (Schulmann *et al.*, 2005; Schulmann *et al.*, 2008) similar to ductile thinning mode described e.g. by Koyi *et al.* (1999).

In this work we study crustal scale mantle gneiss dome, the Orlica-Śnieżnik Dome (OSD), where large bodies of orthogneiss are locally cored by high grade rocks like HP granu-

lites and eclogites. The large structure of the dome can be, at first approximation, interpreted as a classical mantled gneiss dome similar to crustal scale structures reported in other orogenic belts (Whitney *et al.*, 2004) . In this paper, we use large database of structural, petrological and geochronological data accompanied with crustal scale gravity modelling to propose a model of growth and decay of orogen scale gneiss dome. An attempt is made to distinguish the mode of crustal thickening from exhumation or burial of rocks in km scale antiforms and synforms and growth of large scale gneiss dome several tens kilometres in diameter. In order to evaluate the folding and diapiric modes of OSD formation we discuss the relative contribution of ductile thinning, development of large scale detachment and erosion associated with formation of adjacent sedimentary basins. This approach allows discussing in detail interplay between gravity of lateral shortening mode in formation of one of the largest gneiss dome of Variscan Europe.

2. Tectonic setting

The Sudetes form the easternmost part of the European Variscides (Fig. II-II-1) along the Czech and Polish border. The continental or oceanic affinity of tectonic units, their subdivision into terranes and correlation with other classical Variscan paleo-tectonic units defined by Suess (1926) and Kossmat (1927) are still debated (Cymerman *et al.*, 1997; Franke & Zelazniewicz, 2000; Kröner *et al.*, 2001; Mazur & Aleksandrowski, 2001; Mazur *et al.*, 2005; Mazur *et al.*, 2010). Nevertheless, a general template can be defined as follows: In the East Sudetes, from the NW to SE (Fig. II-1), and structurally from the bottom to the top occurs undeformed Neoproterozoic passive margin (Lusatian massif) of the Saxothuringian ocean with its syn- (late Cambrian – Early Ordovician) to post-rift par-autochtonous cover (Mazur *et al.*, 2006). These units are weakly (Izera Kowary Unit) to highly deformed at greenschist to blueschist facies conditions (South Karkonosze Unit, Smulikowski, 1995) during Late Silurian to Devonian subduction and Late Devonian to Carboniferous accretion (Maluski & Patoèka, 1997; Marheine *et al.*, 2002; Žáčková *et al.*, 2010). An obducted Ordovician oceanic crust that records Late Devonian blueschist and epidote amphibolite metamorphism locally occur in hangingwall of the par-autochthonous sequences (Rudawy Janowicke and Leszczyniec Unit, Mazur & Aleksandrowski, 2001). Because of protolith ages and LT-HP field metamorphic gradient, these units are supposed correspond to the Tepla/Saxothurigian suture (Mazur & Aleksandrowski, 2001; Žáčková *et al.*, 2010).

Farther to the SW, the Nové Město and Zabřeh Units as well as part of the unknown basement of the syn- to postorogenic Intra-Sudetic basin are supposed to represent the Teplá-Barrandian Neoroterozoic supra-crustal rocks (Mazur & Aleksandrowski, 2001; Mazur *et al.*, 2005). Both low grade units surround deep seated rocks of the Orlica Śnieżnik Dome. The dome is composed of amphibolites facies gneisses and relics of (U) HP rocks forming orogenic lower and middle crust. (U) HP metamorphic conditions have been attributed to the Devono-Carboniferous HP granulites and eclogites by many authors (Bakun-Czubarow, 1992; Bröcker

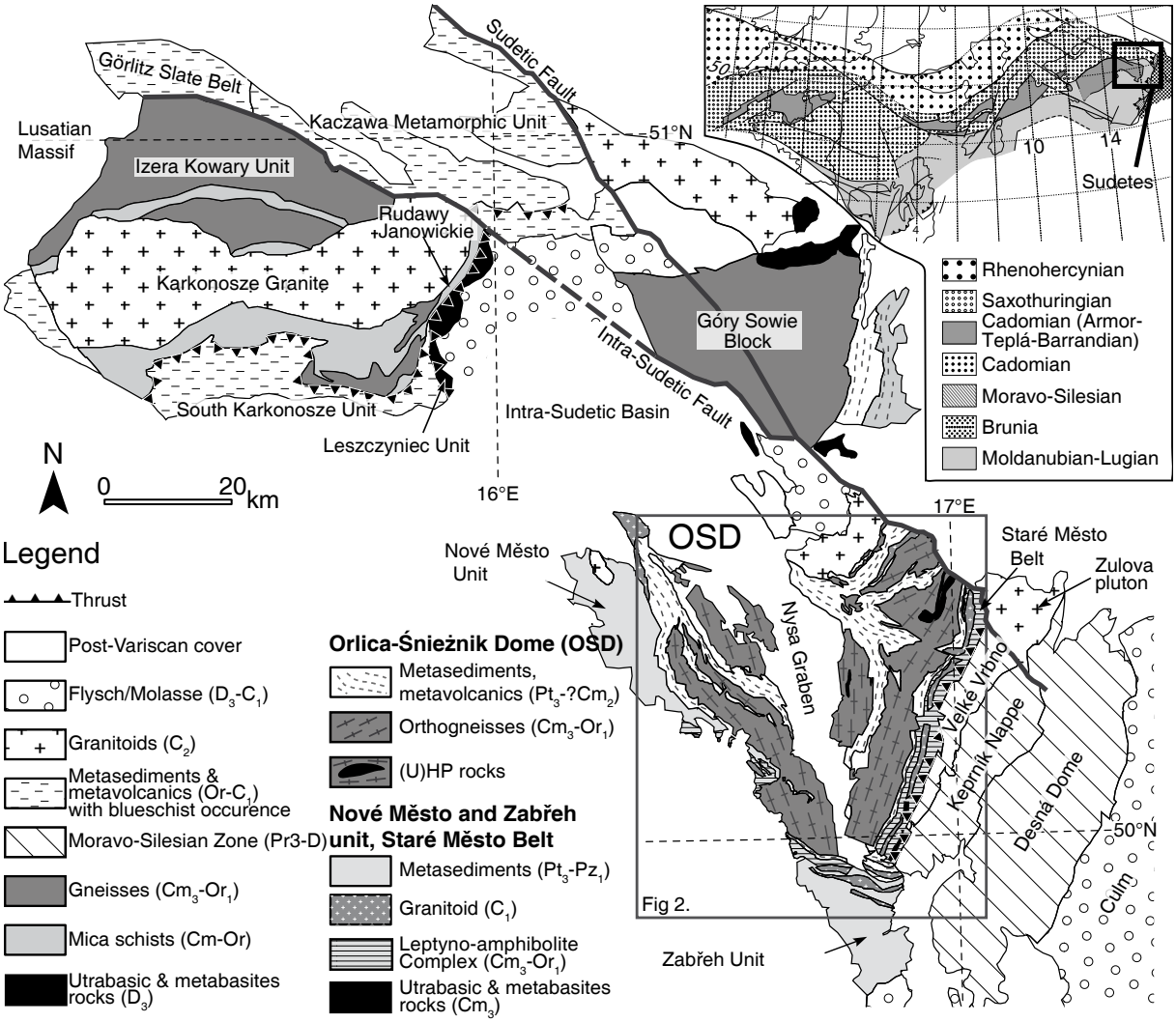

Fig. II-1: Simplified geological map of the Sudetes (modified after Aleksandrowski et al., 1997). Upper left inset depicts location of the study area within the Variscan belt of Europe (modified after Edel et al., 2003).

& Klemd, 1996; Klemd & Bröcker, 1999). The Orlica Śnieżnik Dome is juxtaposed to easterly Late Cambrian-Early Ordovician intracontinental rift of the Staré Město belt (Kröner *et al.*, 2000; Štípská *et al.*, 2001).

Easterly, Moravo-Silesian Zone consists of fragmented Neoproterozoic basement covered by Devonian sedimentary strata derived from Brunia continent and forming three successive units: the Velké Vrbno Unit, Keprník Nappe and the Desná Dome. All these units are tectonically imbricated and exhibit a Barrovian metamorphism ranging from kyanite zone in the west to chlorite zone in the east (Schulmann & Gayer, 2000; Štípská *et al.*, 2006; Košuličová & Štípská, 2007). The Brunia platform further east is covered by Devonian rift sequences and Early-Carboniferous Culm facies rocks.

3. Geology of the Orlica-Śnieżnik Dome

The studied area forms a 50x50 km V-Shape mantled gneiss dome called the Orlica-Śnieżnik Dome (OSD) which is rimmed by the low grade mantle rocks represented by the Nové Město unit in the west, the Zabřeh unit in the south and the Staré Město belt in the east (Fig. II-1).

3. 1. Lithology of the OSD core

The main outcrops of eclogites, surrounded by various orthogneiss types, are located in the area of Międzygórze massif or as isolated boudins scattered in other gneiss massif of the northeastern part of the OSD (Smulikowski, 1967). HP granulites are restrained in a NNE-SSW 1.5x8 km narrow and elongated belt in the north eastern part of the gneiss dome at the Rychleby-Złote range (Fig. II-2) where they form the core of a migmatitic gneiss complex (Kozłowski, 1961; Pouba *et al.*, 1985). Orthogneisses form the main lithological component of the OSD and they have been classically subdivided into two major groups: the augen to banded orthogneiss of the Śnieżnik group, and fine grained mylonitic to migmatic orthogneiss of the Gierałtów group (Fisher, 1936). The origin and mutual relation of both orthogneiss types are debated as regards age of protolith, intrusive and tectonic relationships and age of their deformation which ranges from Early to Late Palaeozoic (see Dumicz, 1964; Borkowska *et al.*, 1990; Don & Zelazniewicz, 1990). Lange *et al.* (2005b) propose that both main rock types result from the deformation of the same protolith and reflect variations in strain intensity only. The second most important lithology are metasedimentary formations alternating with gneisses (Fig. II-2). The Młynowiec monotonous and the Stronie varied formations are metamorphosed continuous volcano-sedimentary sequences (Jastrzębski *et al.*, 2010) mainly composed of paragneiss and metapelites intercalated with limestones (marbles and dolomites), quartzites, metarhyolites and amphibolites (Smulikowski, 1979; Don *et al.*, 2003).

3. 2. Lithology of the OSD mantle

To the East, the Staré Město belt (Fig. II-2) forms the boundary zone between the OSD and the Brunia microcontinent (Parry *et al.*, 1997; Štípská *et al.*, 2001; Lehmann, 2009). It forms a SSW-NNE trending belt (3 km wide and 45 km long) of Early Ordovician amphibolites, tonalitic gneiss, paragneiss and migmatites intruded by a granodioritic sill. This unit is interpreted as a relic of Early Ordovician intracontinental rift (Štípská *et al.*, 2001; Lexa *et al.*, 2005) . To the south occurs a weakly metamorphosed volcano-sedimentary Zabřeh unit of unknown age

Fig. II-2: Lithological map of the Orlica-Śnieżnik Dome (OSD) (modified afterDon et al., 2003; Żelaźniewicz et al., 2006 and geological maps from the Czech Geological Survey 1:25,000, 1:50,000 and the Polish Geological Institute 1:100,000). Abbreviations for eclogite localities are: mzg=Międzygórze, nw=Nowa Wieś, wj=Wójtówka, str=Strachocin, sg=Stary Gierałtów, b=Bielice, nm=Nowa Morawa. Inset shows the distinct structural domains: Northern Domain (Rychlebské Hory and Góry Złote Massifs), Central Domain (Krowiarki Mountains), Southern Domain (Międzygórze and Králíky-Śnieżnik Massifs) and Western Domain (Góry Bystrzyckie and Orlické Hory Massifs).

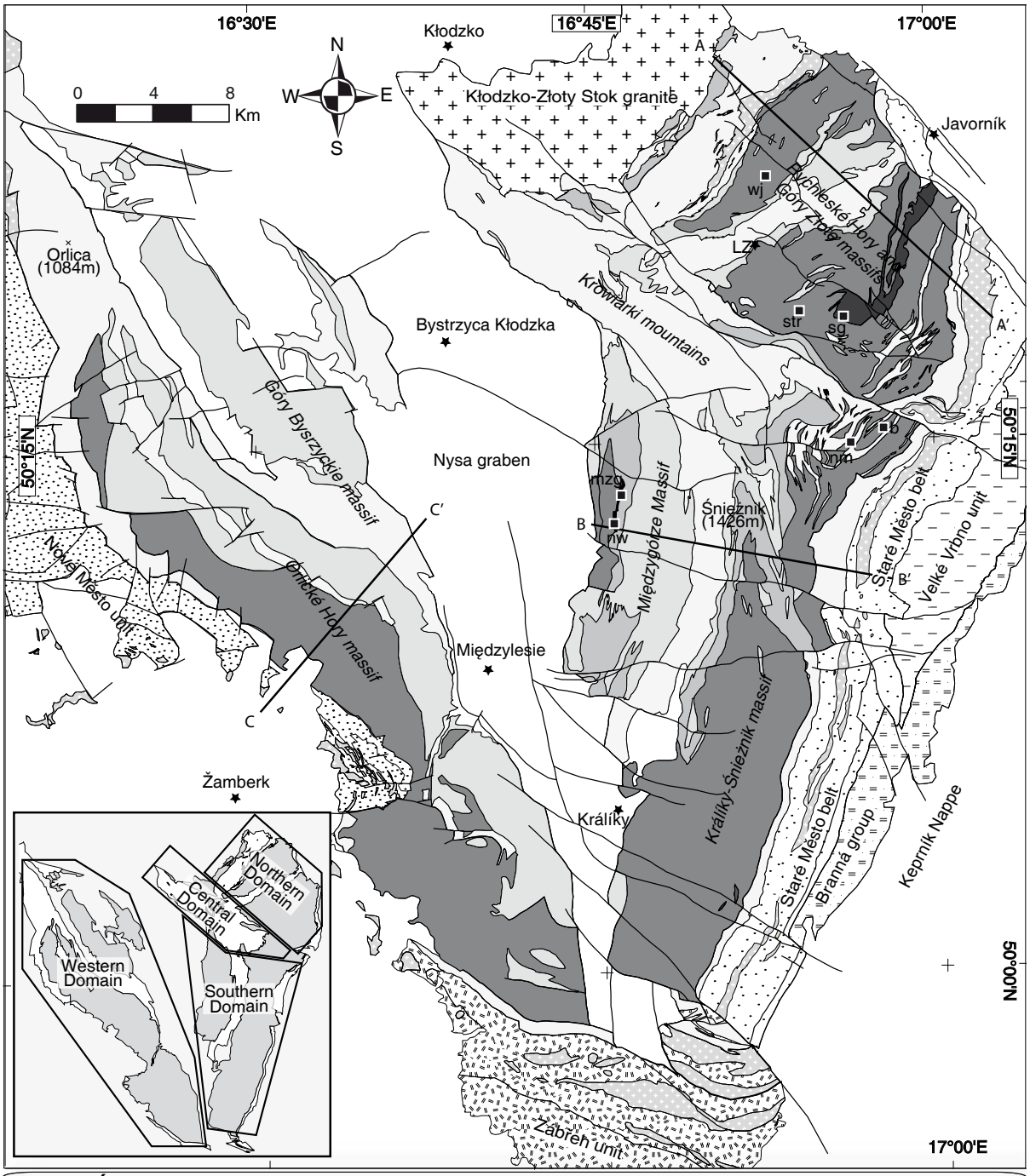
16°30'E
16°45'E
17°00'E
50°15'N
50°00'N
Kłodzko
Kłodzko-Złoty Stok granite
Javorník
Orlica (1084m)
Bystrzyca Kłodzka
Nysa graben
Śnieżnik (1426m)
Międzylesie
Žamberk
Králíky
Zábřeh unit
Nové Město unit
Orlické Hory massif
Góry Bystrzyckie massif
Międzygórze Massif
Králíky-Śnieżnik massif
Staré Město belt
Velké Vrbno unit
Keprník Nappe
Branná group
Krowiarki mountains
Góry Złotego massif
Western Domain
Northern Domain
Central Domain
Southern Domain
0 4 8 Km
N
S
W
E
A
A'
B
B'
C
C'
wj
LZ
str
sg
mzg
nw
Orlica-Śnieżnik Dome (OSD)
OSD mantle
Nové Město unit: undifferenciated metasediment & metavolcanite
Zábřeh unit: undifferenciated metasediment & metavolcanite
Staré Město belt: undifferenciated metabasite
OSD core
metasediment, metavolcanite
banded to augen orthogneiss
mylonitic orthogneiss
migmatitic orthogneiss
OSD (U)HP
granulite
eclogite, eclogite locality
granodiorite
Brunia
metagranite, metavolcanite metasediment
metasediment, metavolcanite
late variscan granite
Town

composed of mafic and felsic volcanics and metapelites unconformably overlaid by Early Carboniferous clastics sediments. This unit is intruded by numerous E-W trending steep granodirite sills (Lehmann, 2009; Verner *et al.*, 2009; Fig. II-2) . The Śnieżnik gneiss dome is rimmed from the west by low grade metapelites and basic volcanics of the Nové Město unit of probable Neo-Proterozoic age (Alexandrowski and Mazur, 2001). This unit is close to contact with the OSD also intruded by thick bodies of granodiorites and tonalites.

3. 3. Metamorphism

Eclogites reveal typical Omp-Phg-Grt-Ky-Rt mineral assemblage (Smulikowski, 1967; Smulikowski & Smulikowski, 1985) with possible pseudomorphoses after coesite in eclogites lenses of the Rychleské-Złote belt (Bakun-Czubarow, 1991, 1992) and in the area of Międzygórze and Bielice (Bröcker & Klemd, 1996). The estimated peak-metamorphic pressures range between 15 to 30 kbar at 600 to 800°C (Fig. II-3 & Table II-1). The retrograde metamorphism in amphibolite facies have been estimated at 6-12 kbar at 640-700°C (Fig. II-3

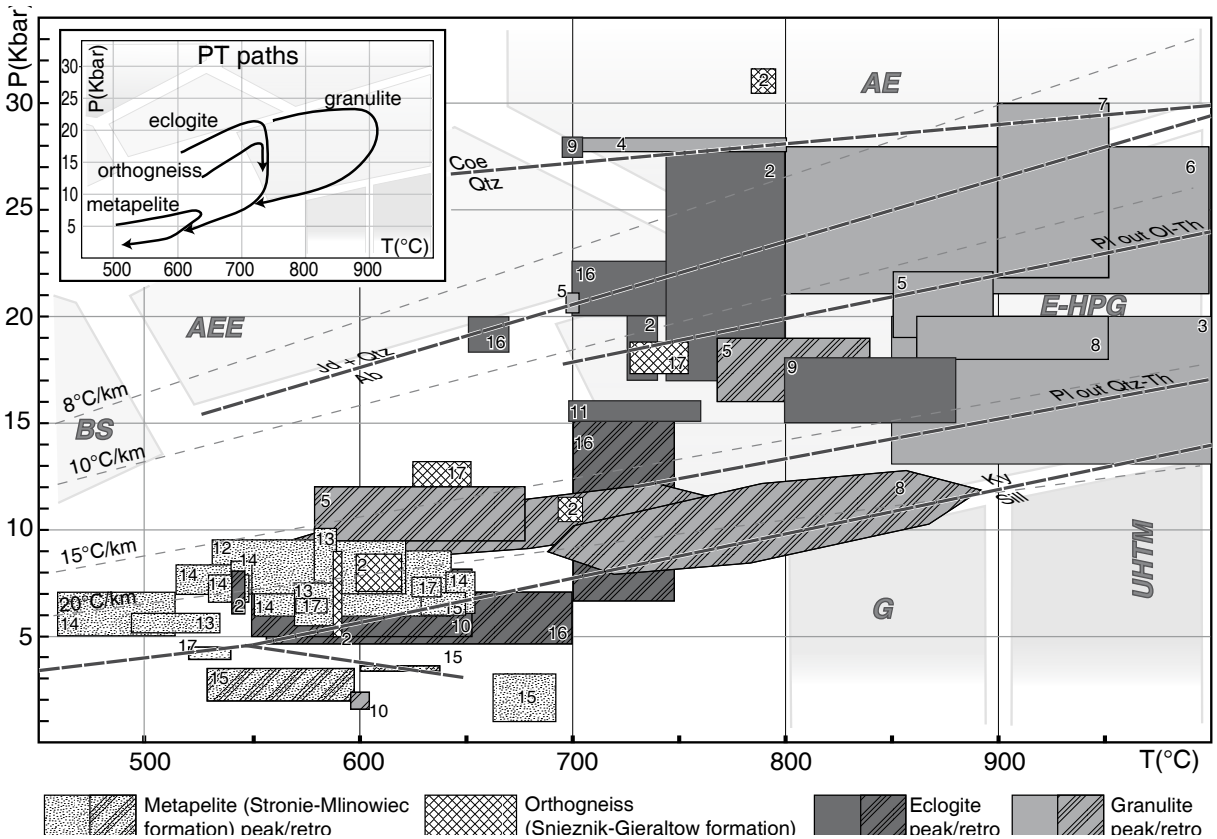

Fig. II-3: Compilation of existing P-T data for metapelite, orthogneiss, and (U)HP rocks in the OSD. Mean P-T paths are shown in the inset. Metamorphic high grades facies are after Brown (2007). BS: blueschist facies; AEE: amphibole-epidote eclogite facies; ALE: amphibole-lawsonite eclogite facies; LE: lawsonite eclogite facies; AE: amphibole eclogite facies; GS: greenschist facies; A: amphibolite facies; E-HPG: medium-temperature eclogite facies – high-pressure granulite metamorphism; G: granulite facies; UHTM: ultra-high-temperature metamorphic part of the granulite facies. References of P-T datas: (1) Kozlowska-Koch, 1973; (2) Bröcker & Klemb, 1996; (3) Pouba et al. 1985; (4) Bakun-Czubarow, 1992; (5) Steltenpohl et al. 1993; (6) Klemb & Bröcker, 1999; (7) Kryza et al. 1996; (8) Stipska et al. 2004; (9) Bakun-Czubarow, 1991; (10) Klemb et al. 1995; (11) Bakun-Czubarow, 1998; (12) Mazur et al. 2005; (13) Murtezi, 2006; (14) Jastrzebski, 2009; (15) Skrzypek et al. 2010; (16) Stipska et al. this volume; (17) Chopin et al. (this volume); (18) Smulikowski & Smulikowski, 1985.

Table II-1: Summary of published P-T data in the Orlica-Śnieżnik Dome, including results from this volume.. Abbreviations: N.D. (Northern Domain), C.D. (Central Domain), S.D. (Southern Domain), W.D. (Western Domain), see Figs II-2, 6 or 7.

Rock	P(kbar)	T(°C)	Interpr.	Reference
Orthogneiss				
S.D. & C.D.	5.5-6.5	550-650	Retrograde	(1) Kozłowska-Koch (1973)
S.D. & C.D.	31	790	UHP-Peak	(2) Bröcker & Klemb (1996)
S.D. & C.D.	11	700	UHP-Peak	(2) Bröcker & Klemb (1996)
S.D. & C.D.	7-9	600-620	Retrograde	(2) Bröcker & Klemb (1996)
S.D. & C.D.	4-9	600	Retrograde	(2) Bröcker & Klemb (1996)
S.D. (Międzygórze)	12	650	Prograde	(17) Chopin *et al.* (this volume)
S.D. (Międzygórze)	19	750	Retrograde	(17) Chopin *et al.* (this volume)
HP granulites				
N.D.	13-20	850-1000	HP-Peak	(3) Pouba et al. (1985)
N.D.	28	700-800	UHP-Peak	(4) Bakun-Czubarow (1992)
N.D.	20-21	700	Prograde	(5) Steltenpohl *et al.* (1993)
N.D.	19-22	850-900	HP-Peak	(5) Steltenpohl *et al.* (1993)
N.D.	16-19	770-840	Retrograde	(5) Steltenpohl *et al.* (1993)
N.D.	9.5-12.5	580-680	Retrograde	(5) Steltenpohl *et al.* (1993)
N.D. (Stary Gierałtów)	21-28	800-1000	UHP-Peak	(6) Klemb & Bröcker (1999)
N.D.	>22 (30)	>900	Peak	(7) Kryza *et al.* (1996)
N.D. (Čeverný Důl)	18	900	Peak	(8) Štípská *et al.* (2004)
N.D. (Čeverný Důl)	10	700	Retrograde	(8) Štípská *et al.* (2004)
Eclogites				
S.D. (Nowa Wieś)	-	560-620	Peak	(18) Smulikowski & Smulikowski (1985)
S.D. (Wojtowska)	-	560-620	Peak	(18) Smulikowski & Smulikowski (1985)
N.D.?	28	700 ?	UHP-Peak	(9) Bakun-Czubarow (1991)
N.D.?	15-18	800-880	Peak	(9) Bakun-Czubarow (1991)
S.D. & C.D.	5-8	550-650	Retrograde	(10) Klemd *et al.* (1995)
S.D. & C.D.	2	600	Retrograde	(10) Klemd *et al.* (1995)
S.D. & C.D.	2	200	Retrograde	(10) Klemd *et al.* (1995)
S.D. & C.D.	17-28	745-795	UHP-Peak	(2) Bröcker & Klemd (1996)
S.D. & C.D.	17-20	725-740	UHP-Peak	(2) Bröcker & Klemd (1996)
S.D. & C.D.	6-8	545	Retrograde	(2) Bröcker & Klemd (1996)
S.D. (Stary Gierałtów)	15-16	700-760	UHP-Peak	(11) Bakun-Czubarow (1998)
S.D. (Międzygórze)	22	720	HP-Peak	(16) Štípská *et al.* (this volume)
S.D. (Międzygórze)	10	700	Retrograde	(16) Štípská *et al.* (this volume)
S.D. (Międzygórze)	5	600	Retrograde	(16) Štípská *et al.* (this volume)
Metasediments (stronie Mlynowiec formations)				
W.D. (Zdobnice N)	2.2-6.5	250-400	Prograde	(12) Mazur *et al.* (2005)
W.D. (Zdobnice N and S)	6.9-9.6	535-623	Peak	(12) Mazur et al. (2005)
N.D. (Orlowiec)	7-10	580-590	Peak	(13) Murtezi (2006)
C.D. (Katy Bystrz.)	5.5-7.5	570-590	Peak	(13) Murtezi (2006)
W.D. (Gniewoszów)	5.2-6.1	495-540	Peak	(13) Murtezi (2006)
N.D. (Lądek Zdrój)	9-10	510	Peak P	(14) Jastrzębski (2009)
N.D. (Lądek Zdrój)	7-8	620	Peak T	(14) Jastrzębski (2009)
N.D. (Lądek Zdrój)	6-8	640-655	Peak T	(14) Jastrzębski (2009)

Table II-1 (continued)

C.D. (Stronie Slanskie)	5.7-9	555-640	Peak T	(14) Jastrzębski (2009)
C.D. (Romanovo)	7-8.3	515-545	Peak T	(14) Jastrzębski (2009)
E.D. (Gniewoszow)	5-7	460-515	Peak T	(14) Jastrzębski (2009)
N.D. (Javornik)	6-7	630-650	Peak P & T	(15) Skrzypek *et al.* (2010b)
N.D. (Javornik)	3.5	600-640	Retrograde	(15) Skrzypek *et al.* (2010b)
N.D. (Javornik)	2-3.5	530-600	Retrograde	(15) Skrzypek *et al.* (2010a)
S.D. (Marianskie Skaly)	5.5-7	550-600	Prograde	(16) Štípská *et al.* (this volume)
S.D. (Marianskie Skaly)	7-7.5	620-640	Peak P & T	(16) Štípská *et al.* (this volume)
S.D. (Marianskie Skaly)	4-4.5	520-540	Retrograde	(16) Štípská *et al.* (this volume)

& Table II-1), and 6-8kbar at 545°C (Fig. II-3 & Table II-1). Klemd *et al.* (1995) show that after amphibolites facies retrogression at 5-8kb and 550-650°C, eclogites from Międzygórze and Nowa Morawa area underwent an isothermal decompressional uplift until 2kb at 600°C and. Bröcker & Klemd (1996) argue also for (U)HP conditions of metamorphism for the Gierałtów gneiss juxtaposed to the eclogites of Międzygórze which finally retrograded at 4-9kbar for 550-650°C (Fig. II-3 & Table II-1). Mineralogical assemblage of HP granulites is made of Omp-Pl-Kfs-Grt-Qtz-Bt +/- Ttn, Ky and Rt (e.g. Štípská *et al.*, 2004). Pseudomorphoses of coesite have also been suggested in the Stary Gierałtów location (Klemd & Bröcker, 1999; Table II-1). Estimated peak-metamorphic pressures are the same as for previously described eclogites (15 to 30 kbar), but equilibrium temperature are higher ranging from 800 to 1000°C (Fig. II-3 & Table II-1). Late amphibolites facies retrogression is estimated to take place at 8-12 kbar and 580-720°C (Fig. II-3 & Table II-1).

Metapelites exhibit complex metamorphic evolution leading to the development of distinct mineral assemblages in the Barowian field gradient ranging from 5-9kb at 460-650°C for the prograde metamorphism (Fig. II-3 & Table II-1), and 2-3.5kb at 530-600°C for the retrogression (Fig. II-3 & Table II-1). The metapelites are characterized by mineral zonation ranging from the kyanite-sillimanite zone in the west and chlorite-biotite zone to the east (Jastrzębski, 2009). Both Nové Město and the Zabřeh Unit reveal narrow Barrovian zonation close to the OSD with metamorphic degree increasing towards the interior of the dome (Mazur *et al.*, 2005; Buriánek *et al.*, 2009).

3. 4. Existing U-Pb and Sm-Nd geochronology

Protolith ages of the (U)HP rocks are estimated at 473+/8Ma (U-Pb Shrimp zircon) for felsic granulites (Štípská *et al.*, 2004) and 460Ma for mafic granulites (U-Pb Shrimp Zircon, Lange *et al.*, 2005b) but theses ages of both eclogites and granulites are questioned by Bröcker et al. (2010) based on his detailed U-Pb Shrimp zircon analysis. Orthogneiss of the OSD yields Cambro-Ordovician protolith ages ranging from 510 to 490 Ma (Fig. II-4b & Appendix II- S1). Geochronology of detrital zircons demonstrated a continuous succession from middle Cambrian to early Ordovician of the Młynowiec & Stronie formations (Jastrzębski *et al.*, 2010).

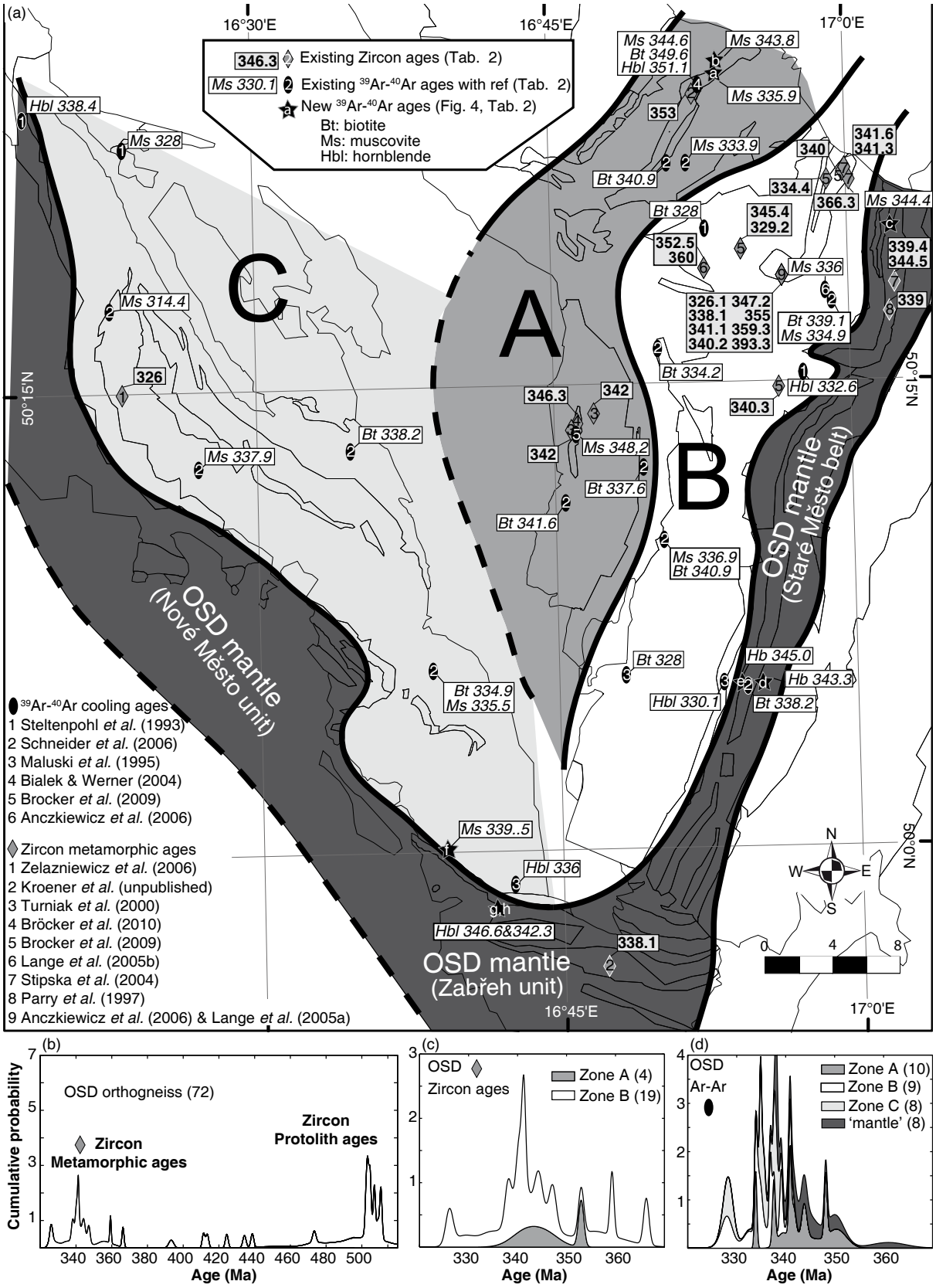

Fig. II-4: (a) Map showing new and existing geochronological data. Metamorphic zircon ages (diamonds) and $^{40}Ar/^{39}Ar$ cooling ages (ellipses, Fig. II-5) are distinguished. (b), (c) and (d) Probability curves of ages histograms for: (b) protolith and metamorphic zircon ages from orthogneiss of the OSD core (c), variscan metamorphic zircon ages from zones A and B of the OSD core, (d) 40Ar/39Ar ages across OSD core and mantle.

Consequently, these authors proposed that Cambro-Ordovician intrusion of Śnieżnik protolith is contemporaneous with deposition of Stronie and Młynowiec volcano-sedimentary formation during Late Cadomian rifting.

The metamorphic U-Pb zircon ages from the HP granulite belt are highly dispersed and range from 326 to 393Ma with a pronounced peak at 340Ma (Fig. II-4a,c & Appendix II-S1). This corroborates with highly scattered Sm/Nd metamorphic ages 320-357Ma (Appendix II- S1) and U-Pb metamorphic zircon ages 330 to 366Ma from adjacent migmatites (Fig. II-4a & Appendix II- S1). The Devono – Carboniferous age, 386 to 354Ma of granulite belt and adjacent paragneiss is also suggested by Lu-Hf and Sm/Nd data on garnets (Appendix II- S1). Existing zircon metamorphic ages from eclogites and orthogneiss of the Miedzygórze massif (Fig. II-4a,c) are clustered around a ~340Ma peak (Appendix II- S1) similarly to metamorphic ages of surrounding gneiss (Appendix II- S1). Eclogite boudins (Fig. II-4a & Nm, B localities in Fig. II-2) in the NE part of the dome yield U-Pb zircon and Nd-Sm ages ranging between 340 and 330 Ma (Appendix II- S1). The granodiorites rimming the OSD core yield uniform age distribution clustering around 340 Ma (Fig. II-4a & Appendix II- S1) while the granite sill intruding the internal units of the OSD in the NW (Javornik granite) yield U-Pb zircon age 351 Ma (Fig. II-4a & Appendix II- S1).

3. 5. ^{40}Ar-^{39}Ar geochronology of the OSD core

There is an extensive database of ^{40}Ar-^{39}Ar ages (Appendix II- S1) showing that most of cooling ages cluster in between 335 and 340 Ma which was completed in the frame of this study. Analytical procedure is shown in Appendix II- whereas localisation of samples and corresponding ^{40}Ar/^{39}Ar step-release spectra are presented in Fig. II-4 and Fig. II-5, respectively. ^{40}Ar/^{39}Ar analytical methods details of dating results are shown in Appendix II- S2 and 3 respectively.

There is no systematic distribution of ^{40}Ar-^{39}Ar ages with different blocking temperature (Hbl – 500°C, Mu – 400°C, Bt – 320°C) suggesting that the large portions of crust passed through different isotherms rapidly. It is namely the northeastern part of the OSD which is lacking ^{40}Ar-^{39}Ar data apart of unpublished ages of Białek & Werner (2004). Two samples were collected from metapelites of the Stronie formation, at 300 meters (JL14A) and a few meters (JL 11A) NW from the contact with the Javornik magmatic intrusion (Figs II-4a & 5a,b, Table II-3). The sample JL14A contains quartz, biotite, muscovite and opaque minerals whereas the sample JL11A is composed of quartz, biotite, muscovite, garnet and opaque minerals. In both samples the steep metamorphic foliation is defined by alternation of quartz layers with micas rich layers. These two sample yielded muscovite plateau age of 343.8±1.1 Ma and 335.9±2.54 Ma, respectively. The ca. 344 Ma age overlaps within error the muscovite and hornblende cooling ages from the adjacent granitoid (Appendix II- S1).

New ^{40}Ar-^{39}Ar data complete the cooling age map of the OSD (Fig. II-4a) and detailed inspection of cooling ages shows that the internal part of the OSD can be divided into three

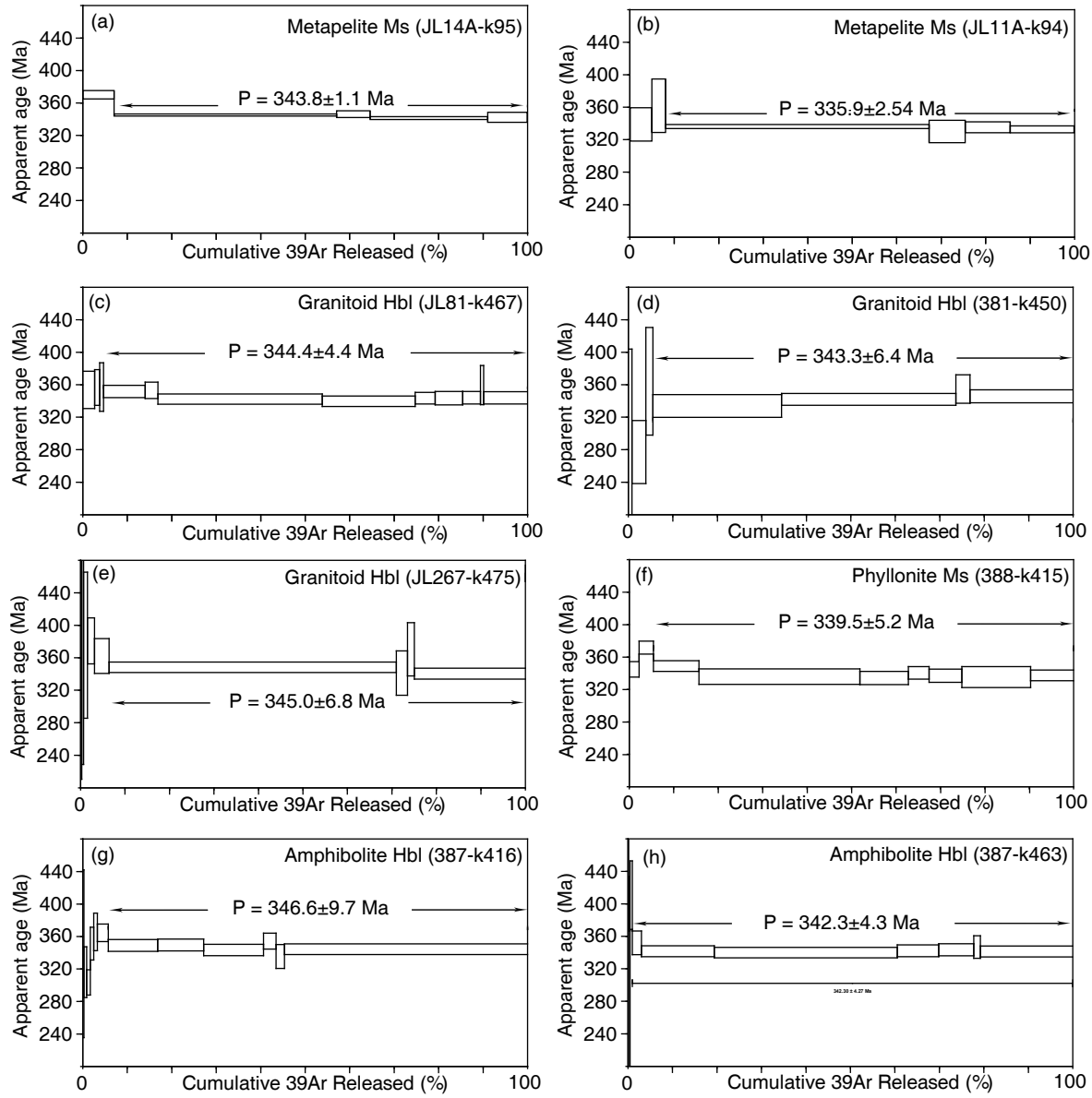

Fig. II-5: *$^{40}Ar/^{39}Ar$ age spectra as a function of released 39Ar on muscovite (Ms) and hornblende (Hbl) single grains in samples from the Orlica-Śnieżnik Dome. Rock type, and analyzed mineral are given together with sample name and analytical reference (in brackets). Location of samples is shown in Fig. II-4 (stars). The error boxes of each step are at the 2 σ level. Error of the plateau ages is given at the 2 σ level. Ages were calculated using the ArArCalc program (Koppers, 2002). MSWD for plateau ages are indicated.*

distinct domains: 1) Domain A located in the core and NW part of the OSD reveals ^{40}Ar-^{39}Ar cooling ages on hornblende, biotite and muscovite that show maximum ages in between 340 to 350Ma (Appendix II- S1). 2) Migmatitic and granulitic Domain B exhibits commonly younger cooling ages ranging from 330 to 340Ma (Appendix II- S1). 3) Domain C covers western flank of the OSD and it is characterized by 330 – 340Ma cooling ages (Appendix II- S1).

3. 6. ^{40}Ar-^{39}Ar geochronology of the OSD mantle

Three samples were collected from the northern (JL81) and the central parts (JL267, 381) of the Staré Město granodiorite intrusion (Figs II-4a & 5c-e, Table II-3). These three samples

are coarse grained granodiorite composed of plagioclase, quartz, K-feldspar, biotite and hornblende. The rock displays a magmatic to solid state fabric defined by the orientation of individual hornblende and biotite minerals as well as continuous aggregates of quartz. The granodiorite fabrics are completely concordant with those of the OSD gneisses in the hanginwall (Štípská *et al.*, 2001). The samples gave hornblende plateau ages of 344.4±4.4 Ma, 343.3±6.4 Ma and 345.0±6.8 Ma, respectively. Theses ages are similar to magmatic zircon ages in the whole granodiorite (340-345Ma, Fig. II-4a & Appendix II- S1) and can be interpreted as contemporaneous with crystallization and cooling under the blocking temperature of the Ar system in hornblende. Hornblende ages are slightly older than that of migmatitic gneiss intruded by granodiorite sill (^{40}Ar-^{39}Ar on biotite, 338.2±0.5Ma, Tab 2).

The southern part of the OSD mantle, the Zabřeh Unit provided two new plateau ages. Sample 388 (Fig. II-4f & Table II-3) was taken at the boundary zone between the south western part of the OSD and the Zabřeh unit. The rock is represented by highly sheared mylonitic amphibolite which exhibits penetrative flat foliation with numerous shear bands. This sample consists of fine grained amphibole, recrystallized plagioclase and biotite and gives a hornblende plateau age of 339.5±5.2Ma. Finally, sample 387 (Fig. II-4g,h & Table II-3) is an amphibolite from the northern part of the Zabřeh unit. The rock is of coarse grained hornblende and plagioclase. Two amphiboles from this sample yields plateau ages of 346±9.7 and 342±4.3Ma.

The systematic ^{40}Ar-^{39}Ar study of the OSD allowed discriminating fourth zone with specific cooling history. The mantle rocks show systematically older cooling ages compared to zones B and C of the OSD core but similar mean cooling age of 340Ma as the zone A.

4. Structural evolution

Three main deformation events (D1, D2 and D3) are developed in the OSD with variable intensity and geometry (Figs II-6- 9). The early D1 deformation is rarely preserved and it is responsible for the formation of flat lying foliation in all structural levels. The D2 deformation produces N-S, SW-NE trending anticlines cored by highly deformed orthogneisses and (U)HP rocks alternating with synclines cored with metapelites of the Stronie and Młynowiec formations. The last D3 deformation is associated with development of recumbent folds reworking both steep S1 and S2 foliations. The OSD orthogneiss gneissosity developed during D1 event from Ordovician porphyric granite protolith that had undergone several generations of heterogeneous Variscan deformations. As a result of recurrent reworking of the granite protolith originated all types of Śnieżnik and Gierałtów orthogneiss varieties that have been described in previous works: augen, banded and mylonitic orthogneiss (mylonitic microstructural trend) and augen (ophtalmitic) to stromatitic, and finally nebulitic migmatite (migmatitic microstructural trend). The geometries and degree of development of S1, S2 and S3 fabrics are highly variable in the studied area and therefore the OSD has been divided into four structural domains (Fig. II-6, inset): the northern domain covering the Rychlebské Hory and Góry Złote mountains, the

central domain covering Krowiarki mountains, the southern domain including Międzygórze and Králíky-Śnieżnik massifs and the western domain occurring at the Góry Bysrzyckie and the Orlické Hory mountains. Geometrical and kinematical relationships between structural fabrics of the OSD core and the OSD mantle units are also discussed.

4. 1. Northern Domain (Rychlebské Hory and Góry Złote mountains)

The northern domain is located between the Kłodzko-Złoty Stok granite in the NW and the Staré Město belt in the SE and consists of two synclines cored with metapelites of the Stronie group and two anticlines cored with orthogneiss and HP granulites (Fig. II-2). In the NW occurs large steep and open syncline formed by metapelites and quartzites. Syntectonic body of Carboniferous granite sill (~350Ma) is emplaced along the SE limb of the megafold. The syncline structure is dominated by S1 metamorphic schistosity of metapelites which is only gently affected by open to tight upright F2 folds. Steep S2 cleavage (Fig. II-8b) and S1 foliation along megafold limbs are locally reworked by NE gently to moderately plunging open and recumbent F3 folds and S3 crenulation cleavage. Sub-solidus and magmatic foliations of the granite sill at the SE border of the syncline is coherent with S2 fabric in metapelites, and it is moderately reworked by D3 deformation. Cross-cutting relationships between granite veins and S2 cleavage suggest that the granite is emplaced syn-tectonically with D2 deformation.

Further southeast occurs an anticline cored by migmatite and mylonitic Gierałtów orthogneiss and mantled by coarse Śnieżnik augen gneisses. Here, ubiquitous steep S2 gneissosity is related to intense flattening of feldspar porphyroclasts in augen gneiss variety and by stromatitic layering and schlierens in migmatitic orthogneisses. It is intensely transposed by S3 crenulations cleavage. The degree of D3 deformation is progressively increasing towards SE. Large close to isoclinal upright syncline cored by Stronie formation metasediments further southeast is dominated by steeply dipping S2 foliation defined by compositional layering defined by alternations of amphibolite, schist and quartzite bands and by typical metapelites schistosity. The S2 fabric in many places is intensely reworked by close to isoclinal F3 folds and moderately dipping penetrative schistosity S3.

The south-easternmost gneiss dominated anticline is cored by narrow belt of granulites surrounded by migmatites and augen to banded orthogneiss. Relics of S1 migmatitic fabrics were identified at the SE border of the granulite belt (Štípská *et al.*, 2004) suggesting that the partial melting was associated already with D1 event (Fig. II-8b). Within the granulite belt, both relics of mafic S1 layering and the S2 developed during HP-HT event as shown by syn-D2 growth of omphacite, plagioclase and garnet (Štípská *et al.*, 2004). In migmatites the S1 fabric is generally transposed into a NE-SW trending steep S2 foliation which is coeval with partial melting (Figs II-6 & 9a). D2 structures are heterogeneously reworked by recumbent, decimetre to metre scale, F3 folds and gently dipping amphibolite facies S3 foliations sometimes injected by granitic melt (Fig. II-8c).

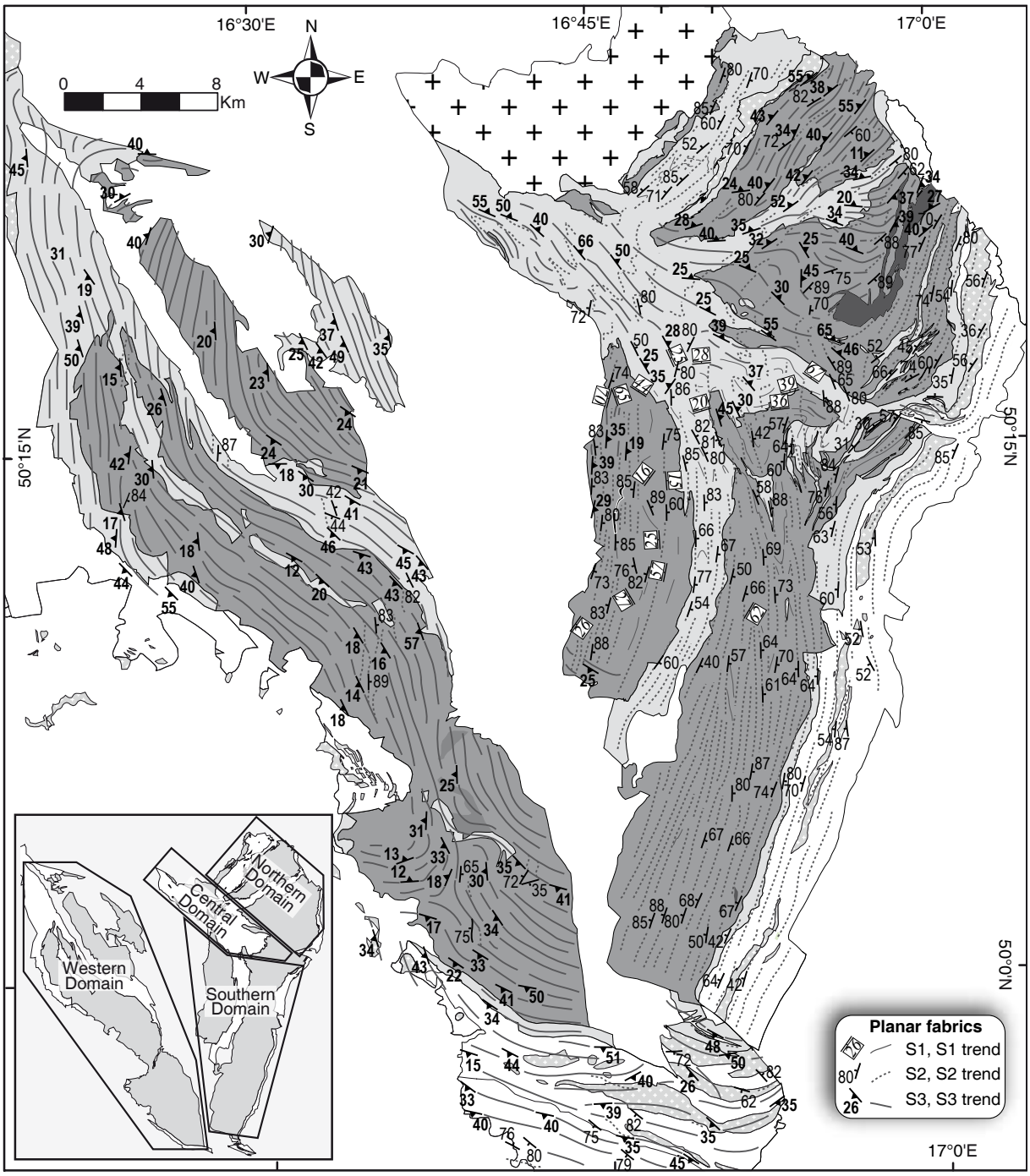

Fig. II-6: Structural map of planar fabrics in the OSD showing repartition and interaction between the early flat S1, the steep S2, and the gently dipping S3 fabrics. Locations of cross sections are indicated. Inset show the distinct structural domains.

The S2 foliation is always steep and NE-SW striking along the whole cross-section (Figs II-6, 8a,b & 9a). West of granulitic core, the axial planes of F3 folds are gently dipping to the SE while at the east they are dipping to the NW thereby forming positive fan like structure around the granulite belt (Figs II-6 & 9). The intensity of D3 is highest in metapelites north-west of the granulite belt and progressively decreases towards NW. The intersection of S2 and S3 fabrics is forming strong NE-SW trending subhorizontal L3 lineation parallel to hinges

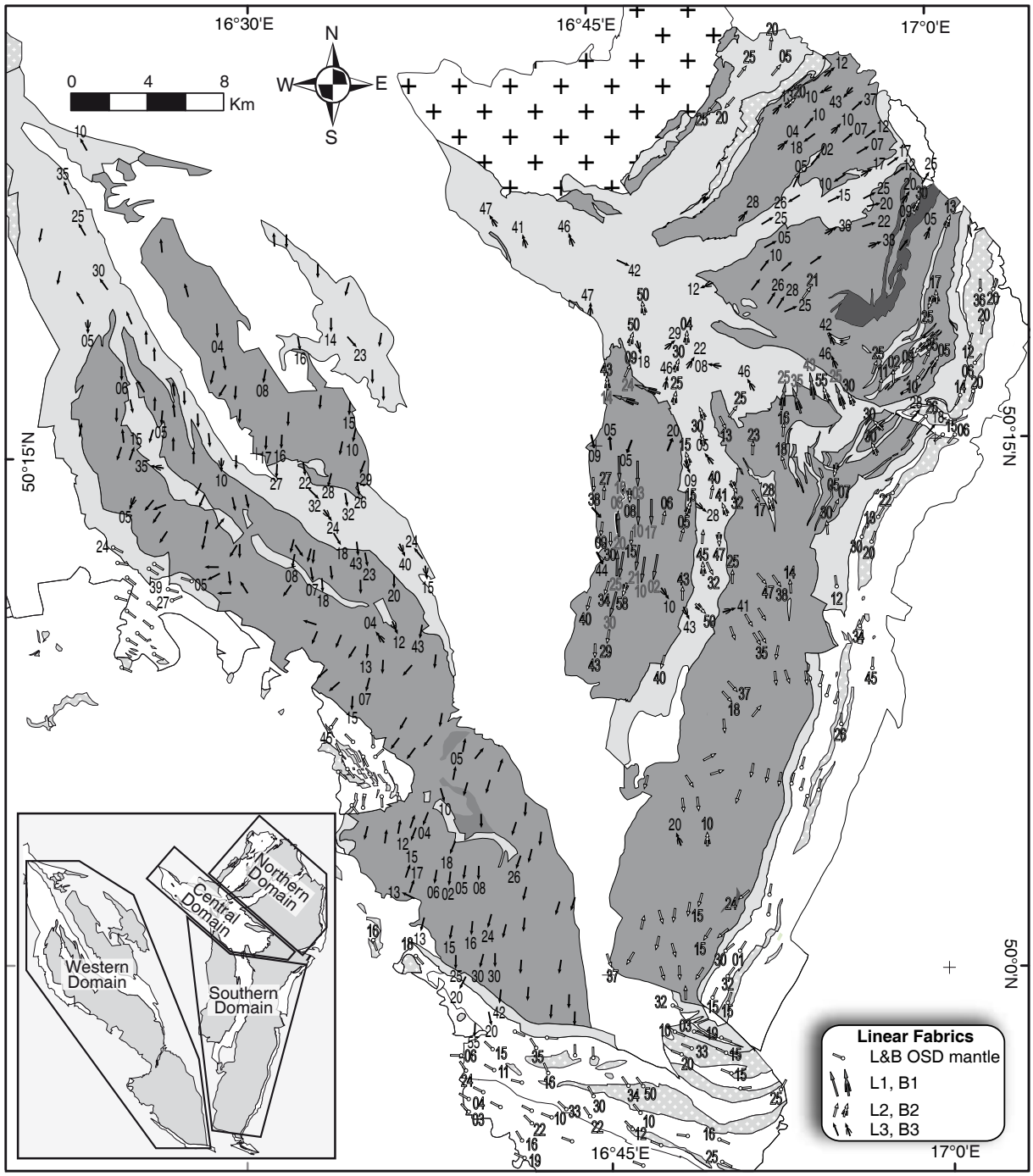

Fig. II-7: Structural map of linear fabrics (lineations and fold axes) in the OSD. Inset show the distinct structural domains. Linear fabrics without plunging datas are from Prikril et al., 1998 and Fajst, 1976. Datas from Zabřeh unit and Staré Město belt are from Lehmann (2009).

of F3 recumbent folds (Fig. II-7). Previous studies of Štípská *et al.* (2001; 2004), Lexa *et al.* (2005) and Baratoux *et al.* (2005) shown that the eastern flank of the granulite-gneiss anticline is obliquely thrust over the Ordovician Staré Město belt during D3 event (Fig. II-9a). Here, the thrusting is associated with ductile deformation and high temperature recrystallization of Ordovician gabbro located above the Carboniferous granodiorite sill emplaced at 7 kbar depth (Štípská *et al.*, 2001; Baratoux *et al.*, 2005).

4. 2. Central Domain (Krowiarki Mountains)

The prominent structure affecting metasediments of the Stronie and Młynowiec formations is represented by tight to isoclinal, NW-SE trending F3 folds (Fig. II-8d,e) with axial planes moderately dipping to the NE, parallel to S3 cleavage and schistosity (Fig. II-6). Rarely preserved S2 foliation is steeply to moderately dipping to the W or NW. It is more or less continuous with SW-NE striking S2 fabric in the north and with N-S striking S2 foliation in the south (Fig. II-6). In the easternmost part of the central domain which is dominated by Młynowiec formation and adjacent migmatitic gneisses the intensity of D3 decreases dramatically so that the D1 and D2 structures are well preserved. The D2 deformation is manifested by F2 upright to moderately inclined close to tight folds refolding S1 and F1 structures. In some places even the relics of composite S0-S1 fabrics are preserved.

4. 3. Southern domain (Międzygórze and Králíky-Śnieżnik massifs)

The Międzygórze massif (Fig. II-2) is formed by a belt of augen-gneiss and migmatites west from the N-S trending eclogite lineament. The earliest S1 foliation of stromatitic to nebulitic migmatites is highly transposed into a steep S2 migmatitic foliation which is in turn heterogeneously reworked by late moderately east dipping S3 mylonitic to migmatitic cleavage. East of the eclogitic lineament, the D1 structures differs in metamorphic conditions being almost unaffected by later deformations (Figs II-6 & 9b). Consequently, this is the only area in the OSD allowing to study in detail the geometry and kinematics of D1 deep seated tectonites. Here, the slightly to almost undeformed augengneiss is progressively (at metre scale) transformed into banded to mylonitic orthogneiss with subhorizontal foliation and N-S trending mineral lineation defined by elongation of feldspar porhyroclasts (Fig. II-8f). Augengneiss reveals excellent indicators of top to the north sense of shear defined by well developed sigma porphyroclasts and north dipping shear bands. These rocks show also close to isoclinal mildly non-cylindrical folds that locally evolve into typical highly non-cylindrical sheath folds with N-S oriented noses. The S1 layering is heterogeneously reworked by subsequent D2 deformation which is intensely developed at the eastern side of the eclogite lineament (Figs II-6 & 9b). The D2 is manifested by asymmetric steep open of metre to kilometre scale folds with locally developed penetrative

Fig. II-8: Field photographs showing deformation structures in the Northern, Central, Southern and Western Domains. (a) Penetrative subvertical S2 mylonitic fabric (Skrzynka- Złoty Stok area, 800m WNW of the Jawornik Wielki hill). (b) Steep S2 cleavage with relics of S1 phlebitic fabric (E of granulite belt, Kresowy stream, 1400m NW of Bielice). (c) Early stromatitic fabric S2 slightly reworked by D3 deformation stage. New leucosomes are injected in F3 fold axial plane (750m E of granulite belt, close to Červený Důl). (d) Tight recumbent F3 fold in marble (Krzyżnik quarry, 1600m SSW of Stronie Śląskie). (e) Moderately NE-dipping S3 foliation in metapelite (2000m SE of Żelazno). (f) Gradual transition from augen to banded/mylonitic orthogneiss (Międzygórze, 500m E of eclogite lens). (g) Early flat-lying augen gneiss planar fabric slightly reworked by steep S2 cleavage (Goworówka stream, 3300m E of Goworówka). (h) Relics of S1 stromatitic fabric transposed into S2 steep migmatitic cleavage (Malá Morava stream, 1500m N of Sklené). (i) Open F3 fold reworking early steep S2 fabric in metapelites (600m N of Neratov). (j) Early stromatitic to phlebitic S2 migmatite moderately transposed by S3 flat-lying fabric (Zemská Brána, 3600m NE of Klášterec nad Orlicí).

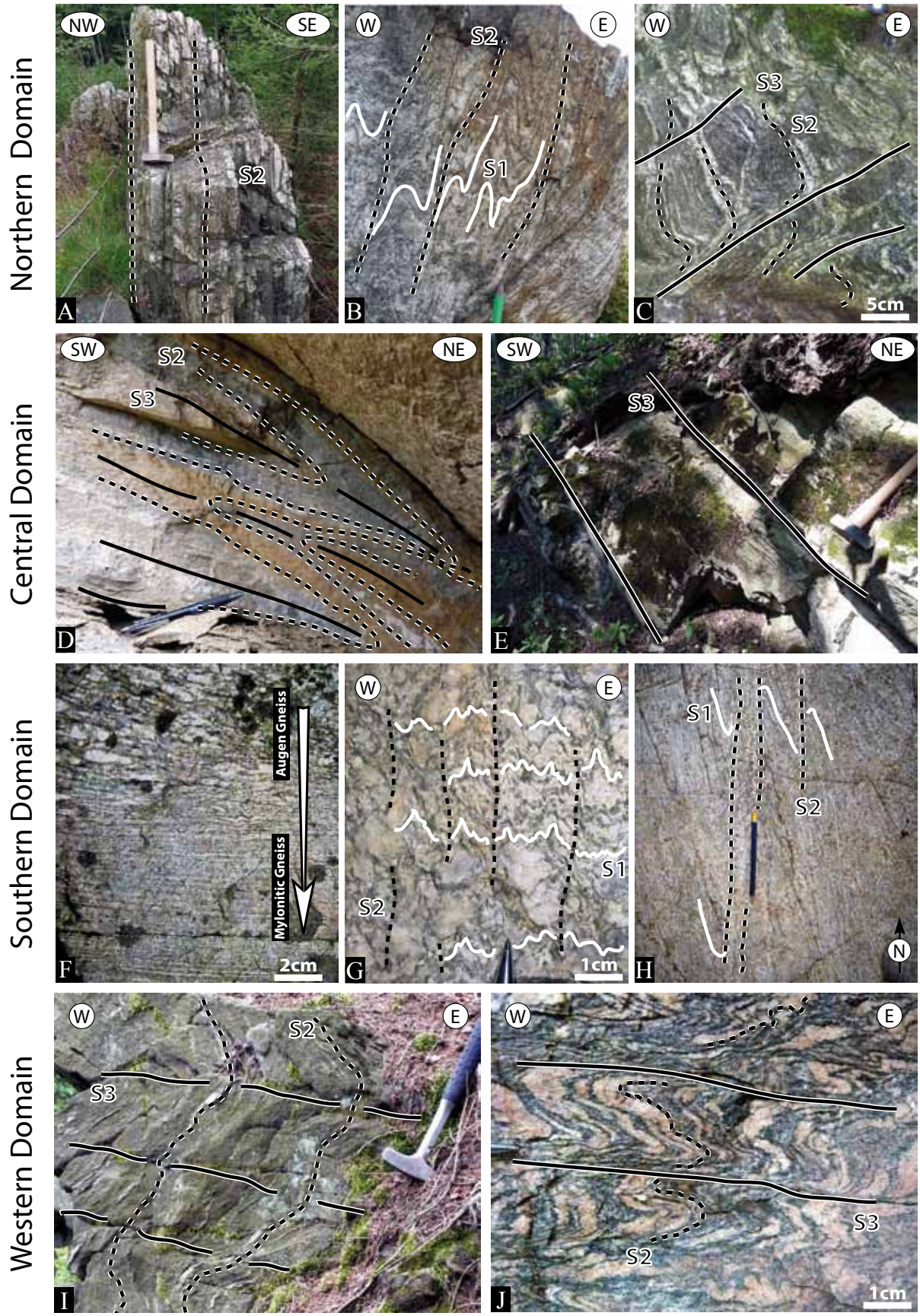
Northern Domain
Central Domain
Southern Domain
Western Domain
NW
SE
W
E
S2
S1
S3
5cm
SW
NE
Augen Gneiss
Mylonitic Gneiss
2cm
1cm
N
A
B
C
D
E
F
G
H
I
J

N-S striking steep crenulation cleavage (Fig. II-8g) leading to the development of a second generation of mylonitic gneiss. The S2 is only rarely affected by close to isoclinal gently inclined to recumbent F3 folds.

Further east, the D1 dominated structural domain is juxtaposed to a steeply inclined east vergent syncline (Fig. II-9b) formed by Stronie metapelites (Don, 1982). Here, well preserved penetrative S1 metamorphic fabric is deformed by close to isoclinal F2 upright fold progressively passing into new N-S striking S2 metamorphic foliation. The F2 folds hinges are gently to moderately plunging to the north or to the south (Fig. II-7). Weak and late S3 flat crenulation cleavage marked by growth of chlorite forms typical mullion structures parallel to N-S trending L3 lineation.

To the east in the area of the Králíky-Śnieżnik massif appear augen and banded orthogneiss and migmatites. Here, the dominant foliation S2 is reworking previously deformed migmatites. This is reflected by steep transition from augen/ophtalmitic to nebulitic migmatite via stromatitic varieties commonly associated with injection of granitic leucosome parallel to S2 foliation (Fig. II-8h). This N-S foliation bears weak sub-horizontal to moderately south S-SE plunging mineral lineation and form an upright negative structural fan which is concordant with the main S2-3 fabric in the adjacent Staré Město Belt (Štípská *et al.*, 2001; Lexa *et al.*, 2005) defined by high temperature mylonitic metagabbros and Carboniferous syntectonic sill (Figs. 7 & 9b).

4. 4. Western Domain (Góry Bysrzyckie and Orlické Hory mountains)

In this structural domain alternations of orthogneiss and metapelite belts are exposed similarly to central and northern areas (Fig. II-2). The dominant fabric is represented by gently to moderately W-SSW dipping S3 foliation trending parallel to the lithological boundaries. In augen gneiss, only the S3 flat lying planar fabric is generally present marked by rare deformation gradients from augen to banded gneiss. This foliation bears strong lineation plunging gently to moderately to the south. In these rocks, no relic of S1 fabrics were found but locally in migmatitic varieties, N-S trending steep S2 foliation is preserved (Fig. II-6). In metapelites the dominant structure is penetrative and crenulation cleavage S3 marked by growth of chlorite. This foliation is associated with rare open to tight F3 folds (Fig. II-8i) refolding S2 metamorphic fabric. In the migmatite domain, gradual transitions from augen gneiss to mylonitic or nebulitic migmatic are common in S2 foliation isoclinally folded by F3 folds. These recumbent folds are accompanied with S3 cleavage (Fig. II-8i) associated with axial planar leucosomes. F3 folds and axial leucosomes rework already partially molten gneiss and form N-S trending L3 lineation. Přikryl *et al.* (1996) recognized also main N-S trending linear fabric made of elongated Qtz aggregates recrystallized at low/middle temperature. In addition, Murtezi (2006) in metapelites and Přikryl *et al.* (1996) in orthogneisses recognized a gently to moderately ESE plunging lineation showing high temperature textures defined by recrystallization of feldspars.

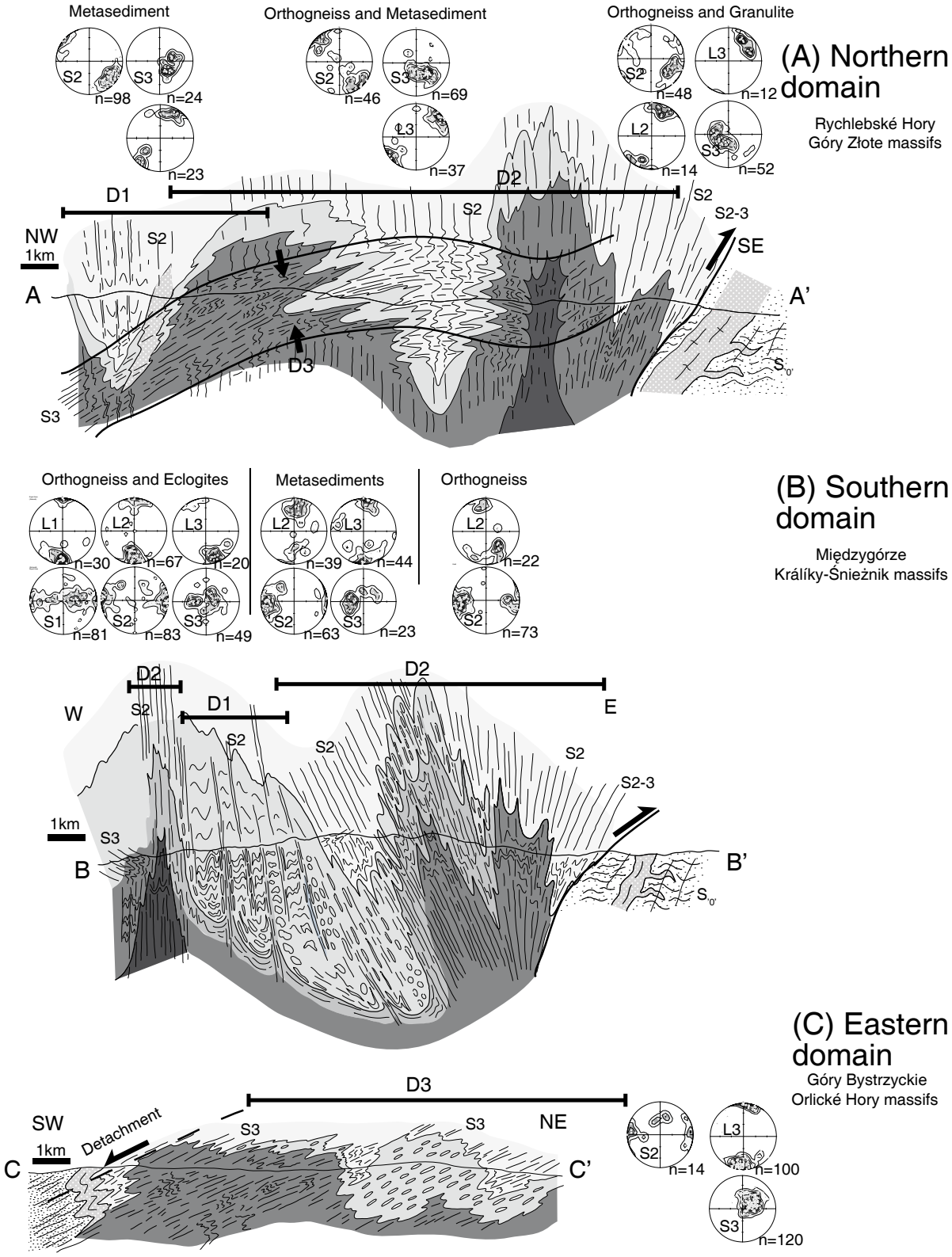

Fig. II-9: Interpretative geological cross sections (a) A-A' throughout the Northern domain, (b) B-B' throughout the Southern domain and (c) C-C' throughout the Western domain (see Figs II-2, 6 & 7 for the locations). Stereonets show equal-area, lower-hemisphere projections of planar and linear structures.

4. 5. Structures of the metamorphic mantle

The Nové Město and Zábřeh formations rim the southwestern margin of the core of the OSD. These formations also reveal a polyphase structural evolution marked by dominant S1 foliation trending parallel to the margin of the OSD. This early greenschist facies fabric is in the Nové Město Unit associated by asymmetric F2 folding and other kinematic indicators suggesting WSW directed compression (Mazur *et al.*, 2005). These units reveal intense reworking by W to SW gently dipping S3 cleavage which is progressively passing to mylonitic D3 fabric towards the boundary with orthogneiss of the OSD core. Here a number of kinematic senses of shear criteria indicating top to the SW normal shearing were observed. Characteristic feature of mantle units is a mineral and intersection lineations rimming the southern OSD margins at high angle to the lineation of the OSD core (Fajst, 1976). The existence of almost perpendicular linear fabrics of the gneiss core and its metamorphic rim was interpreted as a "structural un-conformity" reflecting different mode of emplacement of mainly gneissic core and its metasedimentary mantle (Pauk, 1953; Fajst, 1976). This L3 lineation is well developed in granodiorite sills that reveal intense NW-SE trending constrictional fabric interpreted as a result of deformation overprint (Lehmann, 2009).

The eastern border of the OSD is rimmed by third "mantle" unit, the Staré Město belt. Here, the oldest fabric is horizontal and generally interpreted as Cambro-Ordovician in age. This S1 foliation developed at granulite to amphibolite facies conditions. The second deformation affects this early fabric producing steep NE-SW trending folds, shear zones and penetrative amphibolite facies foliations. This deformation operated along the whole eastern margin of the OSD which at depth of ~6 – 7kbar (Štípská *et al.*, 2004; Baratoux *et al.*, 2005; Lexa *et al.*, 2005).

Towards Carboniferous granodiorite sill this fabric becomes more penetrative and associated with high temperature recrystallization (Baratoux *et al.*, 2005). Because of 340 Ma age of granodiorite intrusion, this D2 deformation is considered as Carboniferous in age (Parry *et al.*, 1997; Štípská *et al.*, 2001). Numerous senses of shear indicators developed in sheared gabbros and progressively cooled granodiorite suggest that D2 deformation developed during dextral transpression parallel to OSD margin. The D3 deformation is manifested by greenschist facies dextral shear zones that were interpreted as a result of kinematic continuum from D2 high temperature shearing (Štípská *et al.*, 2001).

5. Deformation and metamorphism

In several metapelitic belts, crystallization-deformation relationships have been examined in order to link the growth of metamorphic minerals with the successive macroscopic fabrics described above (Fig. II-10). A spatial correlation of all these microstructural observations is then used to reveal the dominant metamorphic regime of distinct areas from the OSD (Fig. II-11).

5. 1. D1 parageneses

Because of the successive tectonic overprints, relics of D1 are scarce and therefore access to metamorphic records associated with this deformation event is restricted to few samples from the Northern and Southern structural Domains. To the SE of the Northern Domain, (Skrzypek *et al.*, 2010a) reported prograde garnet growth up to 5kbar/550°C in the S1 fabric whereas to the NW, the microfolded garnet- and staurolite-rich S1 layering indicate that the metamorphic conditions reached the Grt–St stability field in the same foliation (Fig. II-11a). In the Southern Domain, microstructural evidences point to the occurrence of Grt–St assemblage in the S1 fabric (Fig. II-10e) and led Štípská et al. (this volume) to propose a prograde evolution to ~ 6kbar/580°C during D1 deformation.

5. 2. D2 parageneses

Metamorphic minerals growing in S2 foliation are better observed since this fabric is commonly well-preserved across the OSD. A prolonged prograde evolution was reported towards the sillimanite stability field in the NW part (Fig. II-10a) and kyanite field in the SE part of the Northern Domain (Fig. II-10b). Here, based on a Grt–St–Ky paragenesis developed parallel to S2 fabric, peak conditions of 7 kbar/630 °C related to the end of D2 deformation were estimated (Skrzypek *et al.*, 2010b). Therefore, peak conditions for the NW part of the valley, where staurolite decomposes into the assemblage Grt–Sil–Bt, should lie below the ky/sill transition, i. e. below ~ 6 kbar. In contrast, metapelites of the northern synform are characterized by syn-D2 mineral assemblage reflecting pressure and temperature decrease (Skrzypek *et al.*, 2010a). In the Central Domain, folded relics of metamorphic minerals indicate prograde metamorphism towards variable peak assemblages (Fig. II-11b). From NW to SE, a Grt–Cld paragenesis is followed by Grt–Sil (Fig. II-10c) and finally by a Grt–St–Ky assemblage (Fig. II-10d) that was also observed by Jastrzebski (2009) who proposed peak conditions of 9-10 kbar/510°C achieved in the vertical fabric. This view is supported by kyanite occurrence in the vertical foliation farther to the E, in the Młynowiec formation (Fig. II-11b). In the Southern Domain, a second generation of both garnet and staurolite (Fig. II-10e) parallel to S2 indicates prograde metamorphism up to ~ 7.5 kbar/630°C in the steep fabric (Štípská *et al.*, this volume). However, chlorite blastesis parallel to S2 foliation suggests that retrograde metamorphism down to 5 kbar (Fig. II-10b) also occurred during this deformation event. In the south-eastern part of the Western domain, garnet hosts chloritoid inclusions is in equilibrium with staurolite and elongated kyanite (Fig. II-10h) in the matrix. Both garnet inclusion trails and mineral elongation are parallel to S2 fabric and therefore point to a prograde evolution from the Grt–Cld to the Grt–St–Ky stability field during D2 in this area (Fig. II-11b).

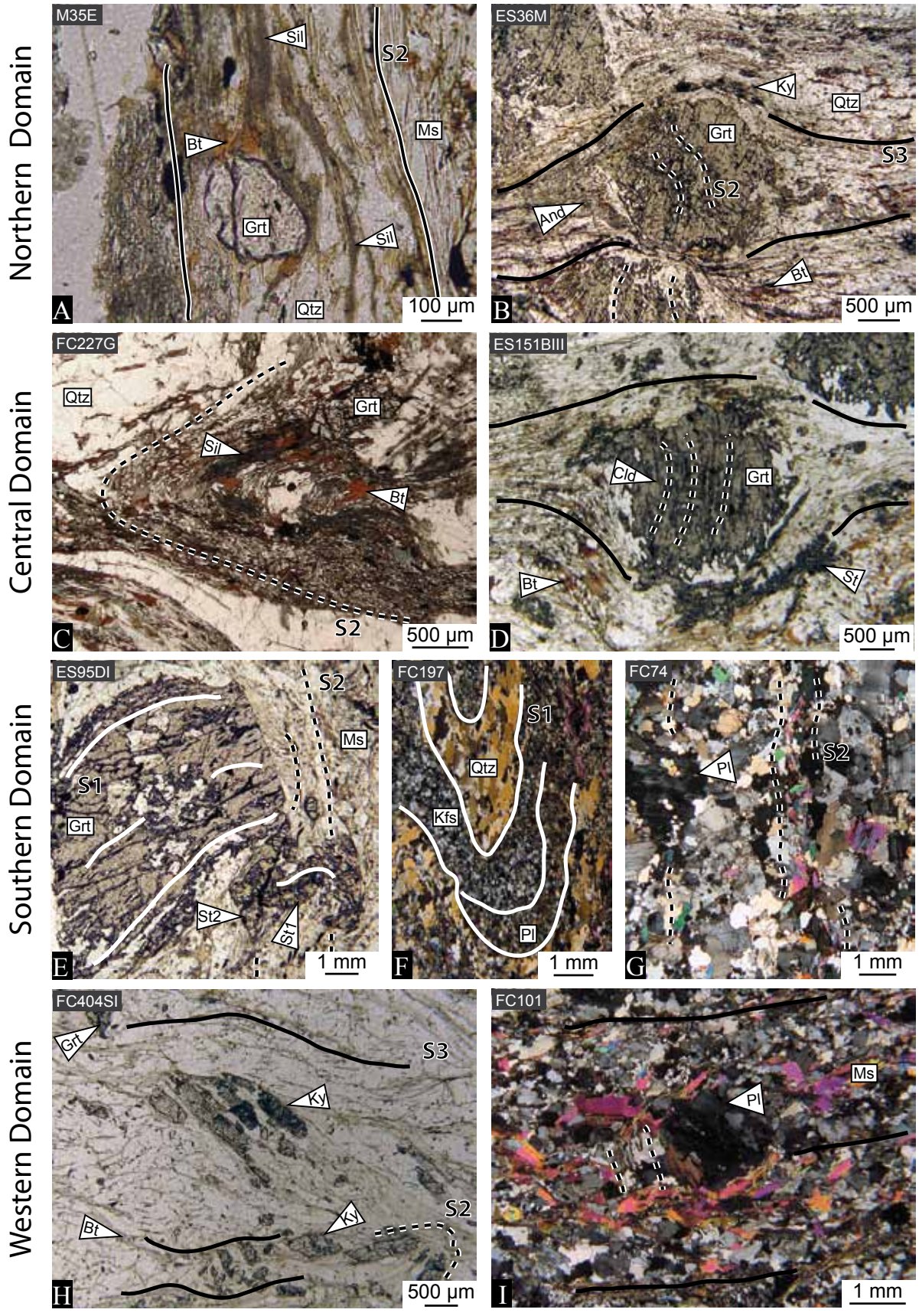
Northern Domain
Central Domain
Southern Domain
Western Domain
M35E
Sil
S2
Ms
Bt
Grt
Sil
Qtz
100 µm
A
ES36M
Ky
Qtz
Grt
S3
S2
And
Bt
500 µm
B
FC227G
Qtz
Grt
Sil
Bt
S2
500 µm
C
ES151BIII
Cld
Grt
Bt
St
500 µm
D
ES95DI
S2
Ms
S1
Grt
St2
St
1 mm
E
FC197
S1
Qtz
Kfs
Pl
1 mm
F
FC74
Pl
S2
1 mm
G
FC404SI
Grt
S3
Ky
Bt
Ky
S2
500 µm
H
FC101
Ms
Pl
1 mm
I

5. 3. D3 parageneses

Even if the D3 tectonic overprint is heterogenous, it is possible to distinguish which phases grew during this event, except the NW part of the Northern Domain where S3 is weak. In the SE valley of the Northern Domain, garnet is retrogressed and kyanite is successively replaced by sillimanite and andalusite oriented parallel to S3 foliation (Fig. II-10b). This retrograde path was constrained at 2-3 kbar/560-620°C (Skrzypek *et al.*, 2010b). In the north-western and central parts of the Central Domain, metamorphism associated with D3 deformation is deduced from chlorite growth after garnet (Fig. II-11c), while to the SE, sillimanite replacing staurolite is also observed. Consequently, the whole Central Domain shows retrograde conditions during D3 and in the SE area, Jastrzebski (2009) proposed decreasing P-T conditions from 7-8 kbar/620°C to ~ 4 kbar/500°C for the flat-lying fabric. In the Southern Domain, chlorite develops in the axial plane of F3 microfolds and is not in equilibrium with garnet any more. The resulting P-T path during D3 is therefore the continuation of a retrograde evolution (Fig. II-11c) towards temperatures lower than 550°C (Štípská *et al.*, this volume). In the Western domain, chlorite is abundant in garnet pressure shadows of D3 deformation indicating that metamorphic peak is followed by a decrease in both pressure and temperature during the formation of S3 foliation (Fig. II-11c).

5. 4. Metamorphic gradients during polyphase deformation

With the help of key relationships described above, sampled metapelites have been investigated to produce metamorphic isograds. In addition mineral parageneses are combined with existing P-T-D data to qualitatively constrain the P-T regime of each macroscopic fabric, while field observations and lithological maps (Don *et al.*, 2003; Żelaźniewicz *et al.*, 2006) were used to assess the extent of anatexis in orthogneisses (Figs II-10 & 11).

Few observations in metapelites indicate that D1 deformation is generally associated with both prograde metamorphism with only small P-T differences between different parts of the Stronie formation (Fig. II-11a,c). However, the underlying Śnieżnik protolith shows a marked contrast (Fig. II-11a). While partial melting occurs around the granulite belt, along the eastern boundary of the OSD and to the west of the eclogite lineament, orthogneiss located to the east of the eclogite shows dominant mylonitic transition (Fig. II-8f).

Fig. II-10: Photomicrographs illustrating relationships between metamorphic minerals and microstructures in metapelites and orthogneisses for the Northern, Central, Southern and Western domain. (a) Sillimanite in penetrative S2 cleavage (Skrzynka- Złoty Stok area, Muflon hill). (b) Garnet with inclusion trails oblique to the external S3, andalusite-bearing foliation. Relics of kyanite are present next to garnet (Zálesí). (c) Sillimanite and garnet in S2 foliation reworked by F3 close fold (Wapnisko hill, 3700m E of Stronie Śląskie). (d) Garnet with inclusion trails (chloritoid and ilmenite) oblique to the external S3 foliation. Folded staurolite aggretate is visible in the matrix (Janowiec hill, 3300m SSW of Stronie Śląskie). (e) Garnet with inclusion trails oblique to the external S2 foliation. Two generations of staurolite are visible (Mariánskie Skały, 4600m ESE of Międzygórze). (f) Laminated orthogneiss reworked by tight upright F2 fold (Goworówka stream, 3300m E of Goworówka town). (g) S2 nebulitic fabric in migmatite (Morava stream, S of Malá Morava). (h) Kyanite crystals oblique to the late S3 cleavage (Vrchní Orlice, 3000m S of Neratov). (i) Rigid plagioclase porphyroclast in a flat-lying migmatitic matrix (Jablonné nad Orlicí).

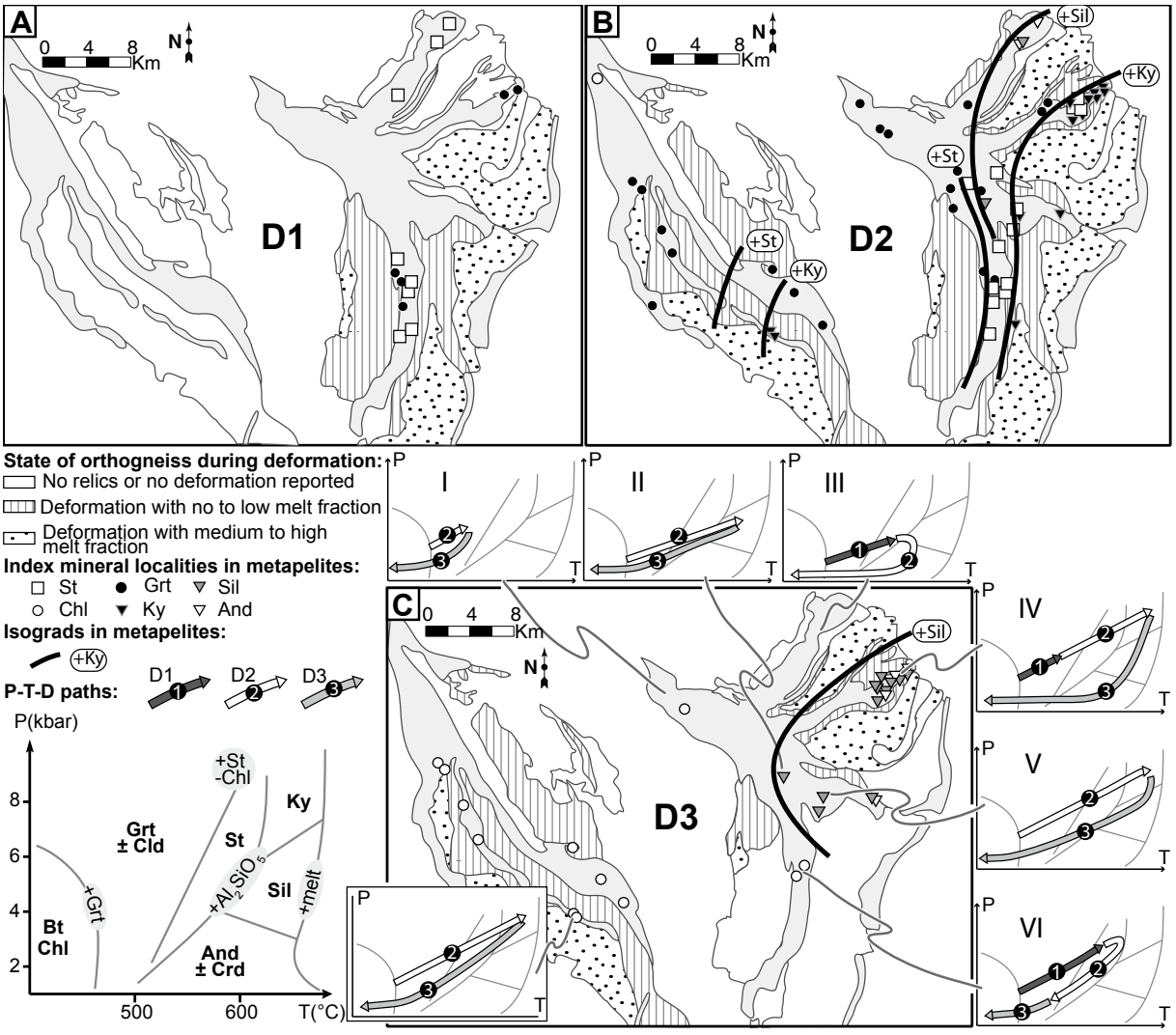

Fig. II-11: (a), (b), (c) Metamorphic maps showing occurrence of sTable II-mineral with isograds in metasediments and deformation state of orthogneiss during D1, D2 and D3 tectono-metamorphic events respectively. Insets I to VI show approximative P-T-D paths deduced from crystallization-deformation relationships in metapelites (exemplified in Fig. II-10) Mineral stability fields have been drawn using pseudosections of Skrzypek et al. (2010a, b).

In most metasedimentary synclines, D2 deformation can be associated with a continuous progression of metamorphism towards contrasted peak conditions (Fig. II-11b,c). While parageneses from belts located next to high-grade bodies document a prograde evolution reaching kyanite grade, metapelites occurring farther preserve only lower grade assemblages. Important feature is retrograde PT evolution during D2 in two synclines. This is associated with rather flat HT-LP prograde field gradients for PT path 2 and 3 in Fig. II-11 and steeper MT-MP gradients for paths 4, 5; 6 in Fig. II-11. The resulting metamorphic isograds define a concentric pattern showing decreasing pressure and temperature away from a granulitic anticline (Fig. II-11b). During D2 stage, all orthogneiss bodies are subsequently deformed under the same thermal regime that prevailed during D1 event, i.e. hot migmatitic orthogneisses are dominant to the east of the OSD (Fig. II-10g) whereas lower temperature domains (Fig. II-10f) with limited zones of anatexis are present around the eclogite and in the western Domain (Fig. II-11b).

In the Stronie formation, S3 foliation always develops under retrograde conditions, but

associated with a varying thermal regime. Around the granulite belt, sillimanite and andalusite occurrences (Fig. II-10b) suggest the persistence of a high temperature conditions compared to the rest of the OSD where D3 takes place in the chlorite stability field (Fig. II-11c). In the same way, deformation in the orthogneiss around the granulites is mostly associated to partial melting while in the Southern Domain, local weak D3 deformation appears to be at solid or sub-solidus state. In the western domain, limited syn-D3 partial melting occurs as well.

6. Deep structure of the OSD

Czech Geological Survey and LIAG (Leibniz Institut für Angewandte Geophysik) databases were used to compile the gravity map (Fig. II-12b) using surveys by Polanský and Škvor (1975), Ibrmajer (1981), Plaumann (1983, 1987). The geographic reference of the stations is the UTM coordinate system and the gravity is referred to the IGSN71 system (International Gravity Standardization Net 1971). The average density of gravimetric stations is 4-6 per km2 and the Bouguer anomaly map was obtained using a density of 2.67 g/cm3 for corrections.

6. 1. Gravity constraints

The Bouguer anomalies range from -50 mGal to 5 mGal (Fig. II-12) and four principal SW-NE trending anomalies were identified in the Western Sudetes: (1) In the north-west, a gravity low is associated with low density rocks identified at the surface as late Carboniferous granitic plutons and Neoproterozoic metagranites. This domain corresponds to the SE Lusatian massif and Karkonosze granite (Fig. II-12). (2) To the SE, belt of gravity high corresponds to high and medium density amphibolites and HP rocks of the Rudawy Janowickie and Lescenecz Units, unknown basement of the Intrasudetic basin and Nowa Ruda gabbro massif. This belt constitutes the prolongation of high density anomaly of the northern rim of the Tepla-Barrandian domain, which is identified as a belt of HP rocks and ulrabasics of the Marianske Lazne complex affinity (Guy *et al.*, 2010) (3) In the centre of studied profile occurs a large gravity low associated with low density rocks, essentially composed of Śnieżnik and Gierałtów orthogneiss and metasediments of the Stronie formation of the OSD. To the southwest the low is less pronounced and coincide with surface exposures of the Nové Město and Zabřeh formations. Both moderate and pronounced gravity lows are in a NE prolongation of similar gravity structure identified in the Moldanubian domain to the south (Fig. II-12) (4) In the south-east a large gravity high appears and it is correlated with high density rocks of the Pan-African Brunia basement (Brunovistulicum of Dudek (1980) and the eastern part of the Silesian domain. In contrast to similar profiles in the SW (Schulmann *et al.*, 2008; Guy *et al.*, 2010), the western part of Silesian basement rocks does not coincide with Brunia type gravity high but with a NE-SW trending belt of gravity low. This anomaly is traditionally interpreted as a result of high proportion of Proterozoic orthogneiss in the Keprnik nappe and a large Carboniferous pluton underplating these gneis-

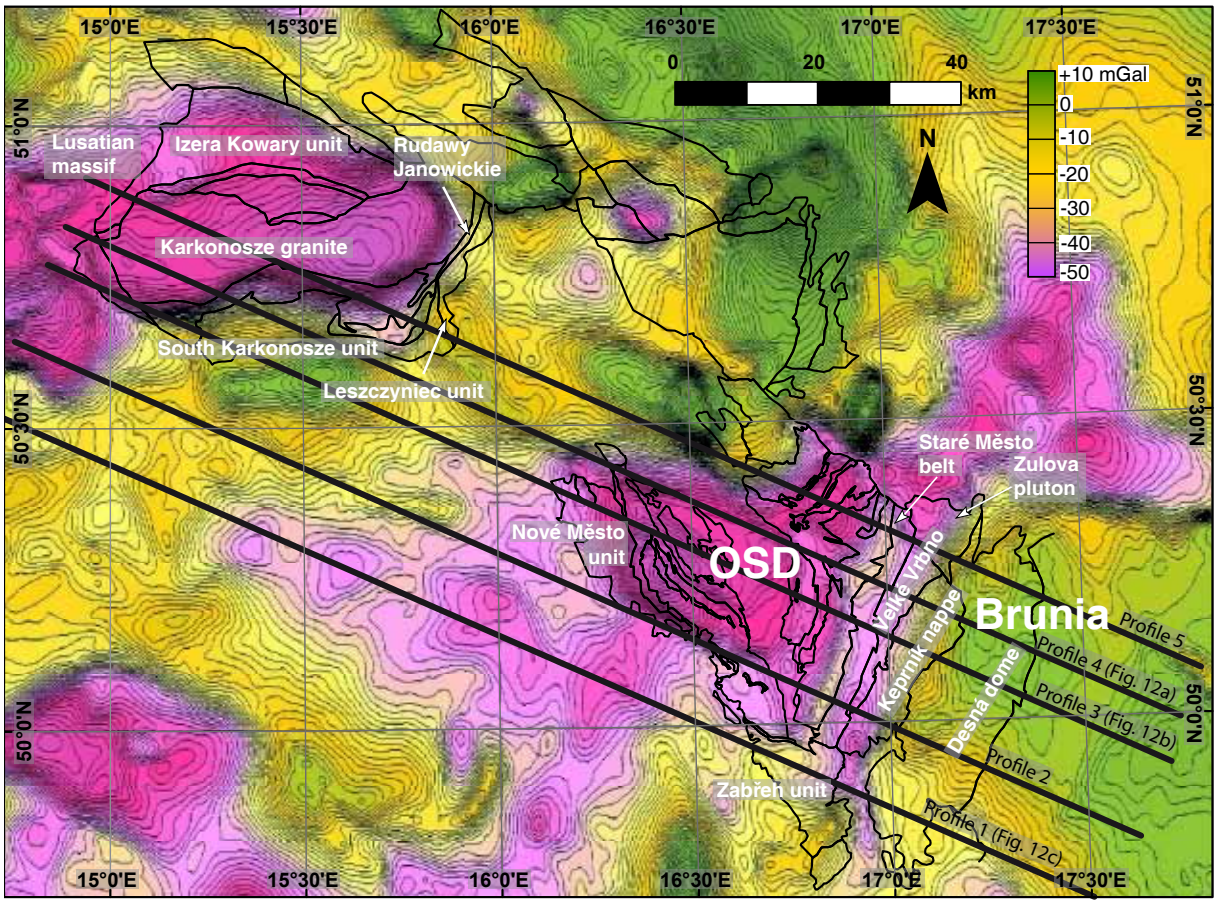

Fig. II-12: Bouguer anomalies map. Main lithological boundaries (see Fig. II-1) are represented by black lines. The 5 profiles (black lines) used for gravity modeling cover the entire Sudetic Massif.

sic units (Rychtár & Rybák., 1987). The geographic boundary between the OSD and Brunia is marked by narrow NE-SW trending belt of gravity high corresponding to surface exposure of amphibolites, gabbros and granodiorites of the Staré Město belt.

6. 2. Gravity modelling

The objective of this work is to estimate the spatial distribution of major tectonic contacts and volumes of the continental crust at depth. In order to image the deep structure of Western Sudetes, a 3D gravity model was computed. Five, ~250 km long and ~20 km spaced profiles were drawn perpendicular to the NE-SW striking gravity gradients. Therefore the model is limited to a maximum depth of 45 km and the 20 km average spacing between profiles exclude modelling of small anomalies. The irregular spacing was adopted in order to avoid that the sections are not influenced by NW-SE trending transucrrent faults which represent major deep rooted discontinuities in West Sudetes.

The density assignments take into account measurements from previous works of Ondra and Hanák (1984) and Švancara and Chlupáčová (1994). According to Ondra and Hanák (1984) granitic rocks of the Moldanubian/Lugian domain show densities in the range 2.63 to 2.70 g.cm-3. For paragneiss of the Moldanubian domain (here Stronie formation), the densities are higher, between 2.70 and 2.80 g.cm-3. A density of 2.67 g.cm-3 is attributed to the high

grade gneiss (Śnieżnik and Gierałtów) forming the core of the OSD. Concerning rocks of Nové Město and Zabřeh formations, densities reported for Tepla-Barrandian domain were used according to Hrouda & Chlupáčová (1993), i.e. densities range from 2.75 g.cm-3 for metasediements and 2.9 g.cm-3 for metabasites. Density values for Bruno-Vistulian microcontinent take into account a Neoproterozoic age of this domain, outcrop geology and conceptual model of Finger *et al.* (2000) and Guy *et al.* (2010). Consequently, we propose a stratified crustal model marked by mafic lower crust with a density of 2.9 g.cm-3 and a middle crust with 2.8 g.cm-3. The Žulova pluton was modelled using density of 2.65g.cm-3.

Seismic high angle refraction-reflection experiments in Sudetes region (Majdański *et al.*, 2007) are used to depict the depth of the MOHO in the region in question. The published map of MOHO depth (Majdański *et al.*, 2007) show small variations in the range of 32 to 34 km in the area of Lusatian to Lugian domains and corresponding to alternations of three low and high NW-SE trending gravity anomalies. The major variation in Moho depth occurs only in between Lugian and Brunia which exhibit higher depth values of 36 – 37 km. This suggests that the gravity signal in the NW and central parts of studied domains correspond to density variations within crust.

The main features in the scale of 250 km long profiles are four major high wavelength anomalies represented by large gravity low to the NW, important gravity high in the centre and gravity low to the SE and, in the SE the gravity high of Brunia. The most representative gravity section is the profile 3 which is not influenced by NW-SE trending transcurrent faults. In order to discuss 3D model we present also profiles 1 and 4 (Fig. II-13). The north-western gravity low corresponds to Lusitanian massif. This gravity low is associated with a large body of low density 2.65 g/cm-3 material ~5 km thick which reflects mainly the Karkonosze granite but probably also Neoproterozic and Ordovician orthogneisses. Several profiles show increasing gravity to the NW behind the Karkonosze pluton gravity low which is modelled by intermediate density values typical for Saxothuringian Neoproterozoic rocks. The gravity high to the SE is composed of two sub-maxima. The most important one is located to the NW and it is modeled by two attached SW gently dipping bodies with a high density of 2.9 g/cm-3. The north-western dense body corresponds to the accretion prism containing blue schist facies rocks of Rudawy Janowickie Unit formed during subduction of the Saxothuringian ocean beneath the upper plate Tepla-Barrandian domain. The south-eastern dense body represents Ordovician basalts and gabbros forming the Tepla-Barrandian lower crust. This latter structure plunges under moderate angle beneath a 2 to 8 km thick Barrandian crust represented by the Nové Město formation with a mean density of 2.75 g/cm-3. High accumulation of Nové Město sediments is responsible for the relative gravity low compared to the NW peak. The second peak in the SE corresponds to presence of amphibolites and other mafic rocks appearing along margins of the Tepla-Barrandian domain. Further SE, the Lugian gravity low is mainly due to the presence of thick masses of Śnieżnik and Gierałtów orthogneisses of the OSD with a density ~2.67 g/cm-3. In order to complete the negative anomaly to the NW the felsic low density material is prolonged beneath

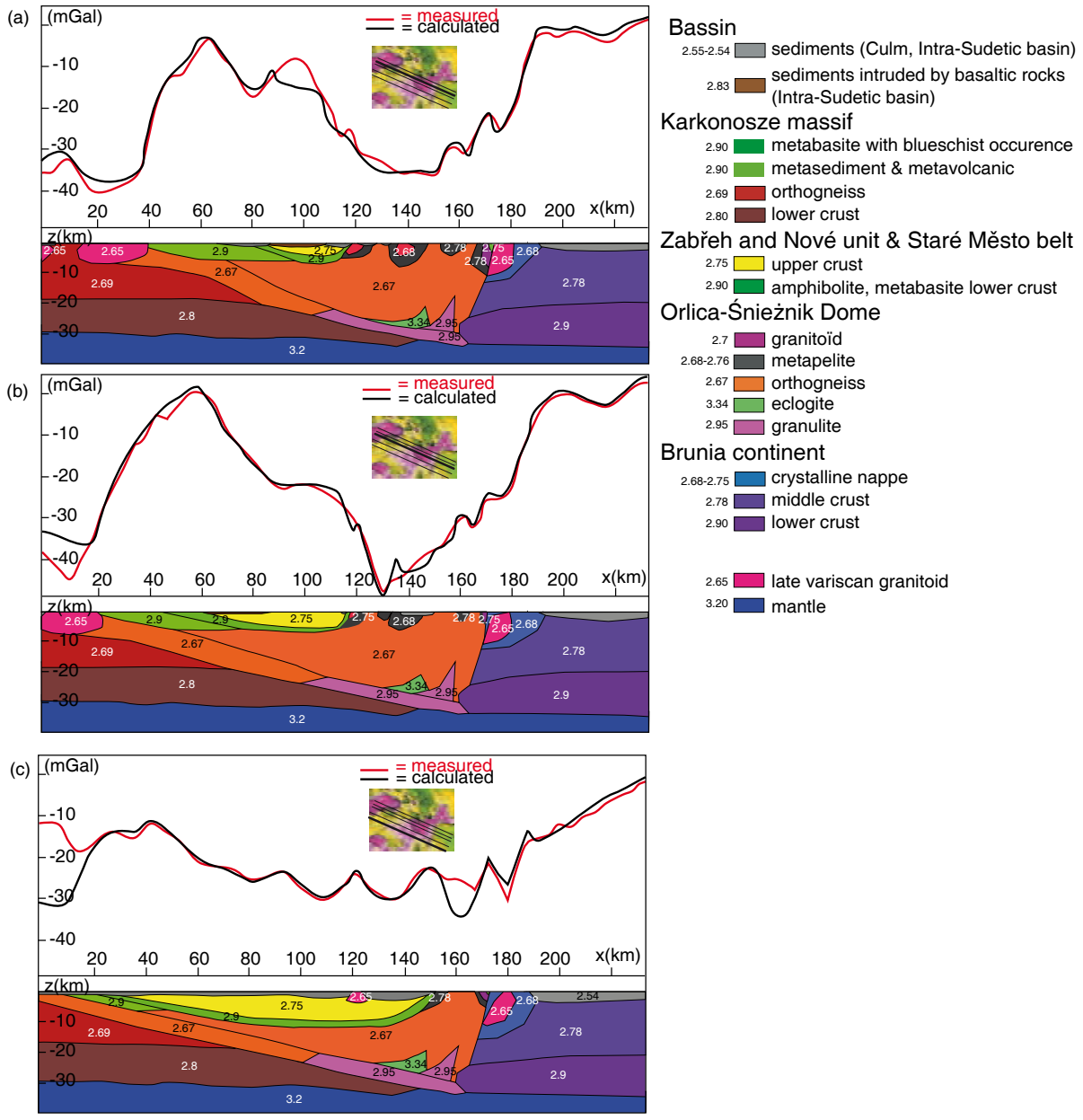

Fig. II-13: Representative modelled profiles. Location of each profile is indicated. (a) Profile N°1. (b) Profile N°3. (c) Profile N°4. Density in the legend is in g.cm-3.

Tepla-Barrandian rocks in mid-crustal depths. This low density material is outcropping in the NW as Ordovician orthogneisses intruded by granites of the Karkonosze massif at the eastern margin of the Lusatian domain. Underneath the thickest felsic crustal bulge, in a depth of 20 to 30 km, we expect the presence of high density eclogites and granulites similar to those exhumed in the core of the OSD. Such a presence of high density rocks at the bottom of thick felsic root is required to counterbalance the exceptionally low density felsic material above. In addition, the high frequency anomalies superposed on the main gravity low are modelled as shallow synclines of Stronie metasediments. Local gravity high at the eastern border of the Śnieżnik massif low roughly coincides with the trend of the gabbros and amphibolites of the Staré Město belt. The slight shift of the anomaly to the west is explained by general westward dip of this

belt to several kilometres depth. The southernmost negative gravity anomaly corresponds to the granite body of the Zulova pluton 8 to 10 km thick underplating orthogneiss dominated nappes of the Silesian domain. Finally, large gravity high in the east is modelled as a Brunia continent using intermediate densities of the middle crust and high densities of the lower crust according to tectonic model of Finger *et al.* (2000). The steep gradient between the OSD and the Brunia basement is modelled as a very steep tectonic boundary typical for the contact of Brunia continent with westerly orogenic root.

7. Discussion

Structural, geochronogical and geophysical study of the Orlica Śnieżnik Dome allowed reconstructing and modelling the tectonic and geodynamic evolution of the continental accretionary wedge and grow of the OSDduring Early Carboniferous convergence.

7. 1. Significance of D1 – formation of continental wedge

The D1 fabric marked by strong deformation gradient is best preserved in the Międzygórze area of the Southern Domain where it reaches eclogite facies conditions 21kbar at 650°C in mafic and 19kbar at 750°C in felsic lithologies (Chopin *et al.*, this volume; Štípská *et al.*, this volume). In addition, relics of S1 were equilibrated at 18-20 kbar at 800°C in intermediate and mafic granulites of the Rychlebské Hory area (Štípská *et al.*, 2004). The mylonitic and migmatitic orthogneiss "the Gierałtów gneiss" are separated from structurally higher metasediments by variably thick layer of "Śnieżnik" augen gneiss. The metasediments of the Stronie and Młynowiec formations reveal relatively well preserved S1 fabric in the Central structural domain and in the large synform at the NW termination of the northern domain. In other places the S1 is preserved in garnet porphyroblasts from ubiquitous D2 deformation. It is always associated with prograde metamorphic evolution of metasediments up to 7kbar at 500°C. Therefore, there is a major pressure break between both gneissic and meta-sedimentary lithologies in range of 10 – 12 kbar allowing to characterize the Gierałtów gneisses and associated granulites and eclogites as orogenic lower crust in agreement to definition of (Schulmann *et al.*, 2005; Schulmann *et al.*, 2008). The metasediments can be regarded as orogenic middle crust and the Śnieżnik augen orthogneiss forms a transitional layer separating both lower and middle crustal levels. In contrast to other regions of the Bohemian massif (e.g. Franěk *et al.*, 2010) the S1 is a prograde flat fabric related to the burial of the crust which allows interpreting the D1 deformation as a result of influx of crustal material into the continental wedge (Plesch & Oncken, 1999).

In the western domain of the OSD the D1 related fabrics are only poorly preserved with exception of ESE-WNW trending lineations (Přikryl *et al.*, 1996; Murtezi, 2006). The L1 lineation is parallel to ESE-WNW trending alternations of gneisses and metapelites which may

imply that such a crustal structure is of D1 origin. This pattern can to result from horizontal section of large scale sheath folds developed during ESE directed flat simple shear as it is observed in other places in the world (e.g. Forbes *et al.*, 2004; Culshaw, 2005). The orientation of linear fabrics corroborates the kinematics of D1 deformation in the Nové Město supracrustal unit in the hangingwall of Orlické Hory section (Mazur *et al.*, 2005) and also the stretching direction in supracrustal Kłodzko massif (Kadziałko-Hofmokl *et al.*, 2004). However, in the central part of the dome the D1 linear fabrics and associated kinematical criteria suggest top to the north shearing parallel to the boundary of Brunia continent. The generalized N-S stretching of the OSD core led Pressler *et al.* (2007) to propose a model of constriction perpendicular to main tectonic transport. Such an orthogonal flow of material in crustal wedges is difficult to explain but is reported from several orogens (e.g. Indares *et al.*, 2000; Jeřábek *et al.*, 2008) . These authors suggest that orogen-parallel stretching, perpendicular to thrusting may occur within the rheologically weaker units bounded by strong thrust sheets. However, this model is applicable only if the synconvergent orogen-parallel stretching is compensated by extrusion of weakly constrained lateral foreland (Seyferth & Henk, 2004).

7. 2. Significance of D2 – steep folding due to indentation of wedge

The D2 deformation is characterized by development of N-S to NNE-SSW trending antiformal structures cored by orogenic lower crust formed either by migmatites, HP-HT granulites and migmatites or eclogite bearing HP orthogneiss in the eastern and central parts of the dome. These antiforms are alternating with meta-sedimentary steep synforms cored by orogenic middle crust. In the western domain the large scale N-S directed folds are not developed. However, the remnants of vertical S1 fabric and the L3 intersection lineation are generally oriented N-S suggesting that the S1 was also refolded by steep F2 folds but in significantly smaller scale than in the east. The main feature of the D2 deformation is the steep N-S to NE-SW trending steep axial planar cleavage developed essentially in the migmatitic orthogneiss and the granulitic core of the southern and eastern domains as well as in adjacent synforms while in the western domain the S2 is hardly present. In general, the D2 shows clear deformation gradient decreasing from the east to the west marked by decrease of fold wavelength and amplitude towards west. The S2 cleavage reveals the same patterns and its intensity is gradually decreasing to the west as shown in schematic cross sections (Fig. II-9a,b) and block-diagram (Fig. II-14).

The general distribution of D2 deformation can be interpreted in terms of progressive indentation of the Orlica- Śnieżnik wedge from the east by a continental promontory. Such a strain distribution was successfully modelled by Jezek *et al.* (2002) and Lexa *et al.* (2003) in front of an oblique indenter. However, this model generated finite strain pattern in front of indeting plate without folding. Bott and Dean (1973) and Blay *et al.* (1977) proposed a model of progressive deformation and stress transfer across a visco-elastic plate leading in progressive fold amplification away from the indenter as the early folds lock up and harden during progres-

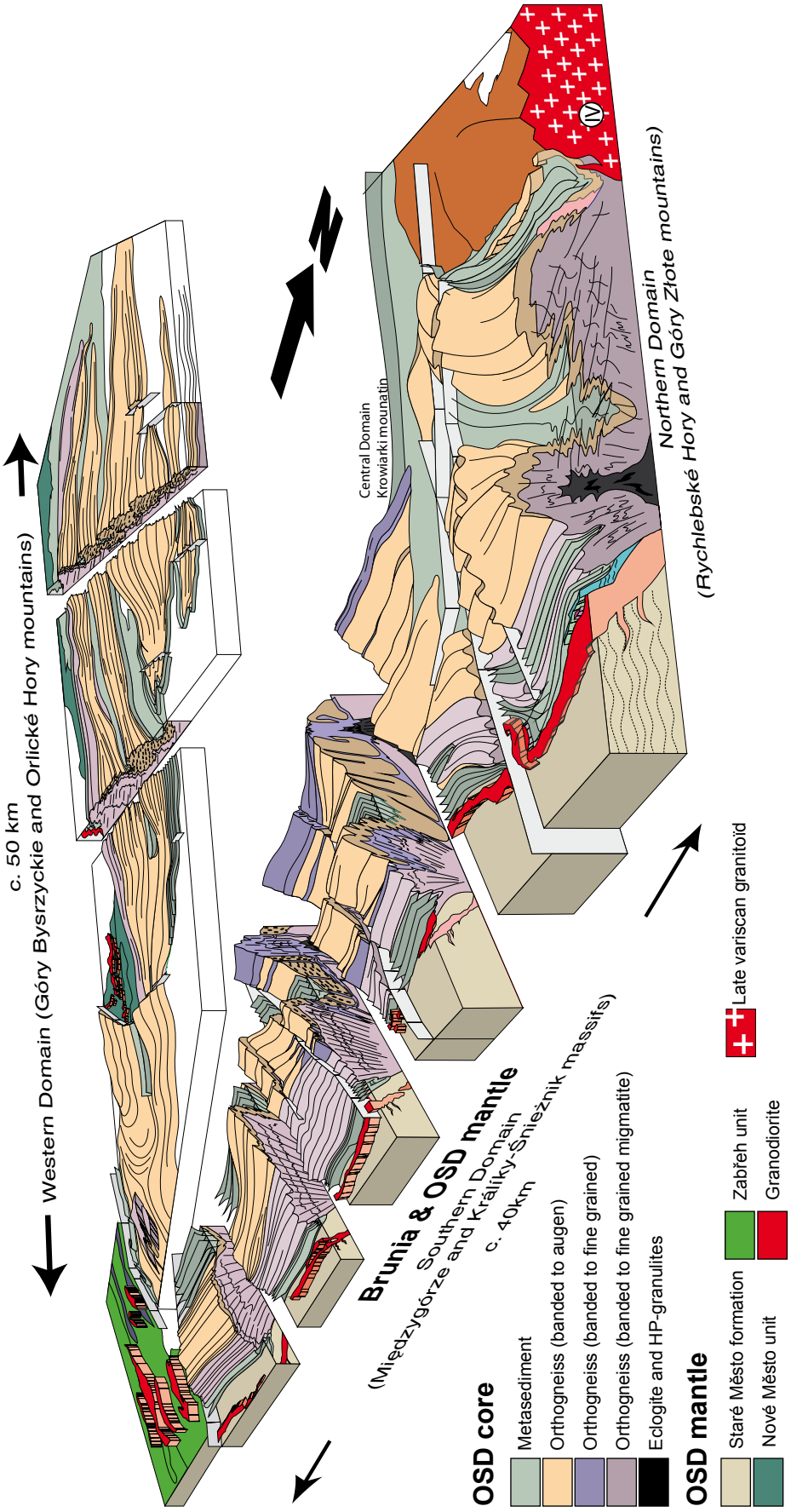

Fig. II-14: Block-diagram of the Orlica-Śnieżnik Dome. See text for discussion.

sive shortening. Post-buckle flattening was responsible for continuous passive amplification of folds close to indenting plate related to development of above mentioned cleavage front.

The structural observations from supracrustal Nové Město unit partially share deformation with underlying infrastructure, while easterly Staré Město belt shows dextral transpression which is unknown in the core of the units of the OSD.

7. 3. Flat S3 fabric – ductile thinning and collapse of folds

The latest deformation is expressed by horizontal to gently inclined fabric that is generally reworking the whole western structural domain of the Orlica Śnieżnik dome (Figs II-9c & 14). This rather flat and SW to S dipping foliation is transposing all previous structures and in particular steep S2 anisotropy or S1 foliation verticalized by F2 folding. S3 foliation is developed at amphibolites facies conditions which intensifies towards the boundary of the OSD core and mantle units. Here, greenschist facies ultramylonites occur marked by extreme grain size reduction and presence of numerous top to the SW or S sense of shear indicators. Therefore, the last increments of D3 deformation have character of major crustal detachment along which the mantle of the OSD units slid down from the core of the gneiss dome. In conclusion, the early high temperature vertical shortening was predominantly coaxial and reflected ductile thinning mode which progressively evolved towards greenschist facies non-coaxial detachment.

Many authors proposed a top to the north oriented shearing related to D3 event in the area of Orlicke Hory and Gory Bystrzyckie massif (Żelaźniewicz, 1988; Přikryl *et al.*, 1996; Cymerman, 1997; Murtezi, 2006). Conflicting kinematic observations can be explained by dominantly pure shear vertical shortening which may lead to heterogeneous opposite shearing (Gapais & Cobbold, 1987). Conflicting sense of shear criteria can also originate during vertical shortening of N-S trending vertical anisotropy, which in oblique section can produce opposite and false sense of shear indicators like shear bands and asymmetrical porphyroclasts (Lexa *et al.*, 2004; Cosgrove, 2007).

The second large flat D3 pure shear dominated shear zone is developed in the Northern Domain (Figs II-9a & 14). It is represented by flat fabric underlined by HT-LP mineral assemblage like gently dipping to the north – northwest. This 500 metres wide zone separates the D2 deformation dominated high grade rocks in the SE from the medium grade rocks in the NW. Here, the verticalized S1 fabric is affected by gentle vertical shortening producing crenulations and intersection lineation on steep NNE-SSW trending steep surfaces. This geometrical disposition led a range of authors to propose an existence of "apparent" dextral shearing along so called "Skrzynka" shear zone (e.g. Cymerman, 1997; Murtezi, 2006).

To sum it up, the D3 deformation leads to almost symmetrical collapse of vertical S2 anistropy in the SW, S and northern part of the OSD while the western part of the dome is collapsing (Fig. II-14). In classical orogenic wedge terminology, the vertical shortening results from ductile thinning of progressively growing crustal wedge (Feehan & Brandon, 1999; Ring

& Brandon, 1999). However, the ductile thinning followed by development of detachment can be also typical feature of growing crustal dome by gravity (Burg *et al.*, 2004).

The orogenic suprastructure of Zabřeh and Nové Město Units reveal strong deformation at the bottom of the system in continuity of detachment related deformations along the OSD core-mantle boundary. In contrast, the eastern Staré Město belt continues to be deformed in greenschist facies dextral transpression at this stage underlying the difference between compressive eastern and collapsing SW and N parts of the OSD.

7. 4. Significance of distribution of isotherms and isograds

The variations in PT trends in relation to D2 deformation fabrics reported in Fig. II-11 cannot be explained by simple tectonic scenario of gravity redistribution (e.g. Vanderhaeghe & Teyssier, 2001) . The global thermal structure of orogenic lower and middle crust indicates formation of large thermal dome in the east of the OSD and the trend of M2 isograds suggests their steep dip more or less parallel to the S2 cleavage trend. Variable prograde PT gradients can be explained by different position of the sample with respect to the axis of the diapiric dome (Warren & Ellis, 1996). However, the diapiric mode would produce contrasting fabrics in the apical part of dome (horizontal foliation) and in marginal synclines (vertical fabrics) which is not recorded in our study. Therefore, we suggest that the eastern migmatitic dome is a major crustal fold which brings the heat in the system during D2. Skrzypek *et al.* (2010b) explains the prograde syn-D2 evolution as a result of progressive burial of middle crustal rocks along large scale cusp-like synform (PT path IV in Fig. II-11). In contrast, Štípská *et al.* (this volume) propose that the retrograde syn-D2 metamorphic evolution results from folding of small scale wavelength synform above an inflexion point of large 20 km half-wavelength migmatitic antiform (PT path VI in Fig. II-11) . The retrograde syn-D2 evolution of the western synform of the northern domain (PT path III in Fig. II-11) can be explained in the same way. In conclusion, there is a first small half-wavelength folding (~4-5 Km) which is followed by large crustal scale folding that generates complex variations in prograde and retrograde D2 PT evolution developed along slightly different field gradients.

D3 related metamorphism shows considerable thermal variations as well. In the north, the thinning related fabrics reveal almost isobaric decompression from 7 to 3 kbars. It is the only area where the orogenic lower crust reveals persistent partial melting during vertical thinning. In contrast the ductile thinning related fabrics in the western domain reveal rapid loos of pressure and temperature with incipient partial melting. In conclusion, it can be seen in Fig. II-11 that the high temperature conditions persisted in the northern part of the dome during the process of ductile thinning (Skrzypek *et al.*, 2010a, b). In contrast the central and southern parts show rapid decompression and cooling characteristic for detachment systems.

There are two possibilities to explain age distribution reported in the cooling age map in Fig. II-4: 1) the earlier cooled areas have been exhumed before the younger ones or 2) the dif-

ferences result from thermal effect of the migmatitic dome imposing differential cooling history in the west and east. The former option can be ruled out due to presence of syn-D2 sillimanite isograd in the early cooled areas represented by western syncline of the northern domain and the Międzygórze massif. This means that during D2 small-scale folding these areas were located around the isotherm 600°C. Therefore, the exhumation of the whole system started during the large wavelength crustal scale folding at round 350 – 340 Ma when the western and central parts of the dome crossed 350 – 400°C isotherm. This model corroborates the cooling ages of the OSD mantle rocks which confirm that the orogenic suprastructure reached 500 and 320°C isotherms at around 340 – 350 Ma. In the east, the large migmatitic dome advectes heat closer to the surface and cooled longer compared to more westerly located areas. The growth of large wavelength anticline is coeval with ductile thinning and detachment related D3 fabrics which show the same younger cooling ages in the western structural domain. This is probably due to high degree of syn-D3 recrystallization, which may be responsible for entire resetting of argon isotopic system. Soon after, the deep seated rocks reached the surface so that large portion of apical part of dome started to be eroded. The erosion of the OSD core is proposed by Teisseyre (1968, 1975) and Dziedzic and Teisseyre (1990) to explain influx of sediments into Intrasudetic basin.

7. 5. The geodynamic model for growth of the OSD

The gravity model presented in this study shows that the large scale gravity low coincides with the geographic position of the OSD. The gravity modelling led us to develop a crustal scale model of OSD structure which suggests that the whole core of the dome is formed by felsic gneisses of Śnieżnik and Gieraltów type (Fig. II-15). The orogenic suprastructure coincides with major gravity high in the west and south of the OSD. The 3D image of present day OSD structure allows proposing that the low density anomaly result from major and crustal scale exchange of dense material forming the orogenic suprastructure with light and felsic material of orogenic infrastructure. The distribution of light gneiss material preserves still a coin-like shape which is probably inherited from the carboniferous period of the formation of continental wedge.

In order to explain the geophysical crustal scale and local scale features of the OSD we propose a schematic evolutionary model of the formation of the continental wedge and the OSD origin. The first stage is related to eastward Devonian subduction of Ordovician oceanic domain and obduction of the accretionary wedge over the eastern passive margin of the Nepotroterozoic Saxothuringian domain (Fig. II-16a). This event continuously passes to continental underthrusting of Saxothuringian continental passive margin dominated by Cambro-Ordovician granitoids and sedimentary basins underneath the upper plate rocks represented by Cambro-Ordovician mafic lower crust of the Staré Město belt type and overlying Neoproterozoic sequences of the Zabřeh and Nove Město Units (Fig. II-16b). The oceanic and continental subduction is

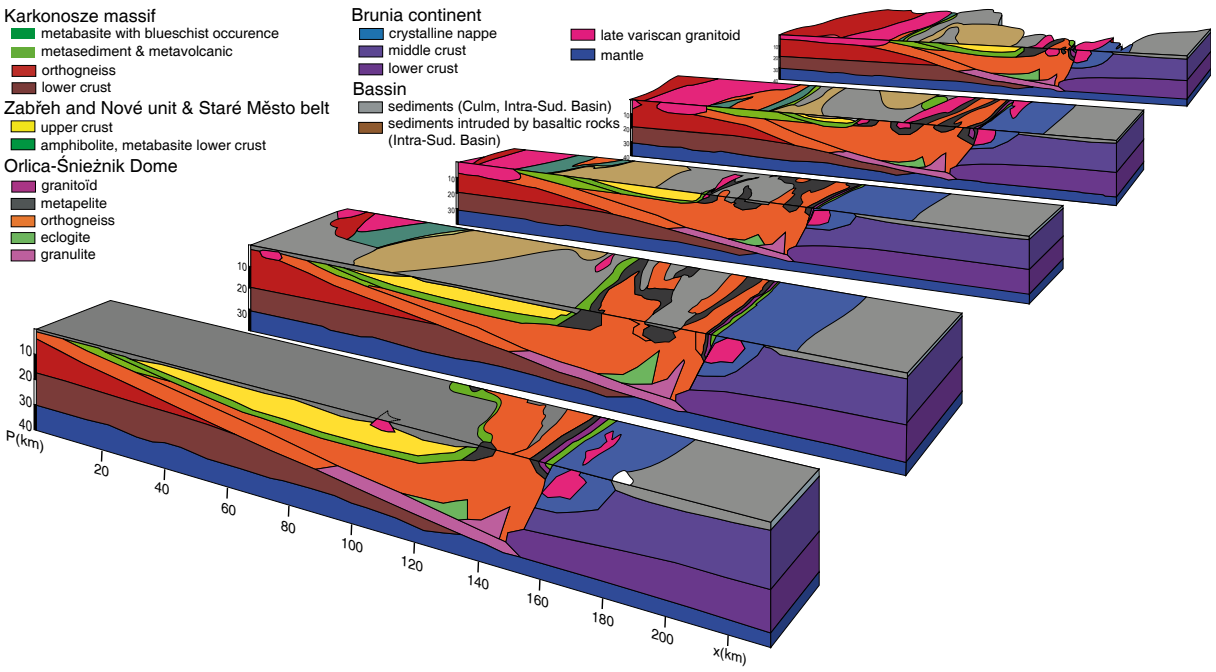

Fig. II-15: 3D geological interpretation of the modelled gravity sections from Fig. II-12. Legend same as Fig. 13.

responsible for development of eclogite facies rocks and HP-LT metamorphic gradient in adjacent orthogneiss today appearing in the Miedzygórze area. Continuous underthrusting of the continental crust is responsible for progressive underplating of early HP rock assemblage by felsic and intermediate rocks which were converted partly in HP granulites, associated kyanite bearing gneisses and migmatites which form today easternmost part of the OSD (Fig. II-16c). Folding deforms the orogenic middle crust and underlying gneisses due to buttressing effect of the advancing Brunia promontory (Fig. II-16d). This is followed by progressive growth of larger – crustal scale folds affecting the whole orogenic infrastructure. This event is inevitably related to ductile thinning of exhumed portions of crust followed by development of major detachment and unroofing of central part of the OSD (Fig. II-16e). The orogenic suprastructure slid down from growing crustal dome possibly leading to further expulsion of low viscosity felsic crust into the core of the dome. The massif erosion is a necessary element to explain the PT evolution and thermochronology of the OSD related to crustal folding. As discussed by Štípská *et al.* (this volume) it is the rapid erosion of vertically elevated rocks which allows to forms synclines and anticlines showing exhumation paths. According to Burg *et al.* (2004), the growth of the dome accompanied by instantaneous erosion leads to development of cascading folds which are observed both in the supra and infrastructure close to detachment. In our case study the limit between orogenic supra and infrastructure locally migrated deeper in the crust thanks to multiscale evolution of the dome. It is the building history of the crustal stratification during formation of crustal wedge and two scale folding pattern which control complex evolution of the Dome which does not entirely fit any classical model presented in literature.

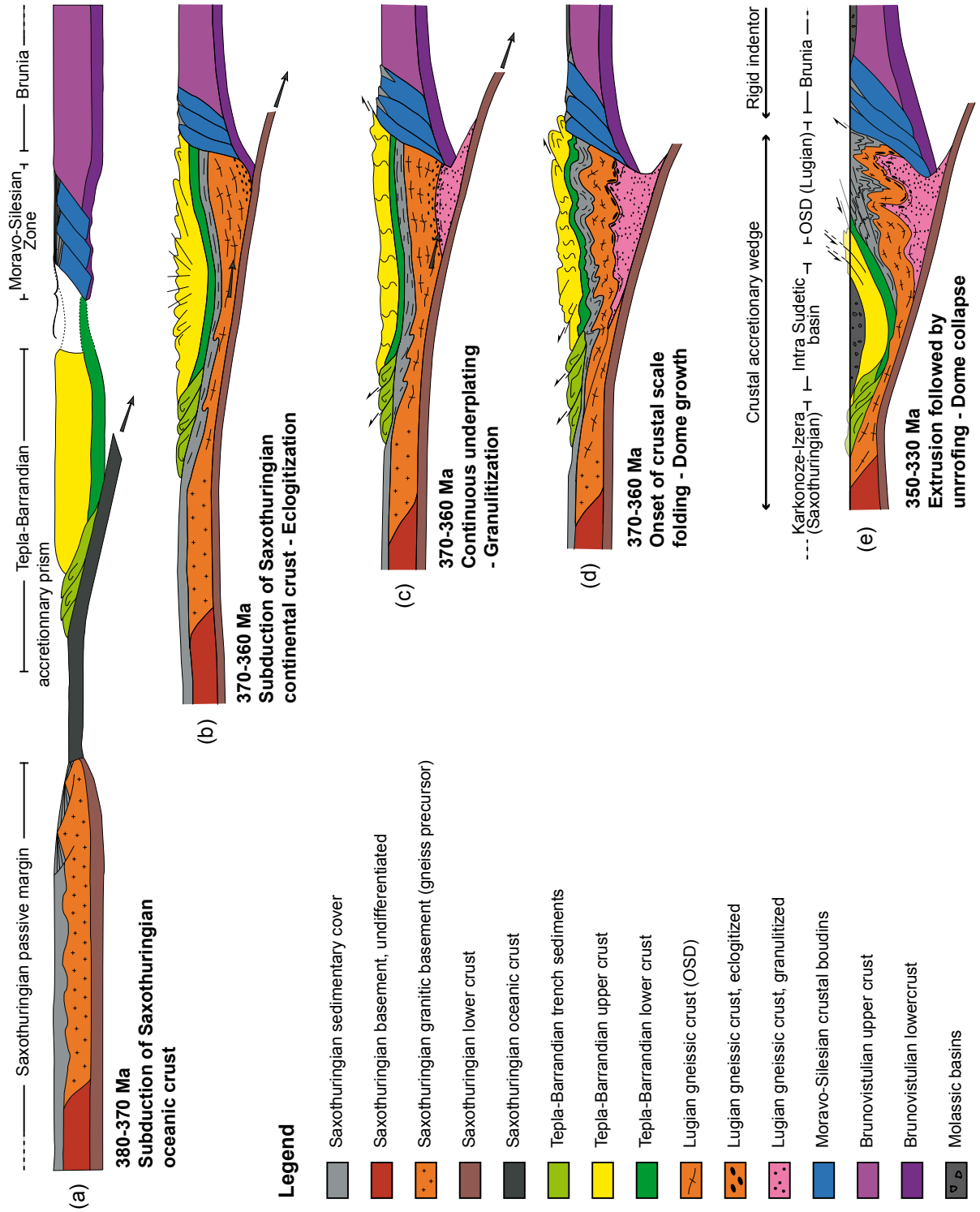

Fig. II-16: Idealized model of evolution of the Orlica-Śnieżnik Dome in frame of the Sudetes. See text for discussion

Acknowledgements

Financial support of the French National Grant Agency (06-1148784 to K. Schulmann) is acknowledged. We thank Jaroslav Synek for drawing Figs II-14.

Appendix

Appensix S1: Appendix II- S1: Summary of published isotopic ages related to metamorphism in the Orlica-Śnieżnik Dome. $^{40}Ar/^{39}Ar$ plateau ages of this study are included. Abbreviations: N.D. (Northern Domain), C.D. (Central Domain), S.D. (Southern Domain), W.D. (Western domain), Z.U. (Zabreh Unit), S.T. (Staré Mesto formation).

Loc.	Rock type	Age (Ma)	**Type of analysis**	**Interpretation**	**Reference**
Protolith OSD CORE U-Pb & Pb-Pb					
N.D.	mafic granulite	794 ± 120	U-Pb total grain (Zrn)	inherited age	Anczkiewicz *et al.* (2007)
N.D.	leucosome	*c.*450 ± 20	U-Pb in-situ (Zrn)	inherited age	Bröcker *et al.* (2009)
N.D.	leucosome	*c.* 470 ± 30	U-Pb in-situ (Zrn)	inherited age	Bröcker *et al.* (2009)
N.D.	leucosome	*c.* 480 ± 20	U-Pb in-situ (Zrn)	inherited age	Bröcker *et al.* (2009)
N.D.	intermediate granulite	477 ± 7	U-Pb in-situ (Zrn)	magmatic age	Bröcker *et al.* 2010
S.D.	eclogite	506 ± 6	U-Pb in-situ (Zrn)	magmatic age	Bröcker *et al.* 2010
N.D.	mafic granulite	509 ± 9	U-Pb in-situ (Zrn)	magmatic age	Bröcker *et al.* 2010
W.D.	metapelite	505 ± 24	U-Pb in-situ (Zrn)	magmatic age	Gordon *et al.* (2005)
S.D.	orthogneiss	504,9 ± 1	Pb-Pb total grain (Zrn)	magmatic age	Kröner *et al.* (2000)
S.D.	orthogneiss	510,8 ± 1,3	Pb-Pb total grain (Zrn)	magmatic age	Kröner *et al.* (2000)
W.D.	orthogneiss	502,9 ± 1,2	Pb-Pb total grain (Zrn)	magmatic age	Kröner *et al.* (2001)
W.D.	orthogneiss	503 ± 15	Pb-Pb total grain (Zrn)	magmatic age	Kröner *et al.* (2001)
W.D.	orthogneiss	503,2 ± 1	Pb-Pb total grain (Zrn)	magmatic age	Kröner *et al.* (2001)
W.D.	orthogneiss	503,5 ± 1,1	Pb-Pb total grain (Zrn)	magmatic age	Kröner *et al.* (2001)
W.D.	orthogneiss	504 ± 52	Pb-Pb total grain (Zrn)	magmatic age	Kröner *et al.* (2001)
W.D.	orthogneiss	504,6 ± 1,2	Pb-Pb total grain (Zrn)	magmatic age	Kröner *et al.* (2001)
W.D.	orthogneiss	507,1 ± 1,3	Pb-Pb total grain (Zrn)	magmatic age	Kröner *et al.* (2001)
W.D.	orthogneiss	509 ± 1,3	Pb-Pb total grain (Zrn)	magmatic age	Kröner *et al.* (2001)
W.D.	orthogneiss	510 ± 24	Pb-Pb total grain (Zrn)	magmatic age	Kröner *et al.* (2001)
W.D.	orthogneiss	510 ± 37	Pb-Pb total grain (Zrn)	magmatic age	Kröner *et al.* (2001)
W.D.	orthogneiss	510,5 ± 1,1	Pb-Pb total grain (Zrn)	magmatic age	Kröner *et al.* (2001)
S.D.	orthogneiss	510,8 ± 1,3	Pb-Pb total grain (Zrn)	magmatic age	Kröner *et al.* (2001)
S.D.	orthogneiss	512 ± 11	Pb-Pb total grain (Zrn)	magmatic age	Kröner *et al.* (2001)
W.D.	orthogneiss	564 ± 15	Pb-Pb total grain (Zrn)	magmatic age	Kröner *et al.* (2001)
W.D.	metavolcanite	656 ± 18	Pb-Pb total grain (Zrn)	magmatic age	Kröner *et al.* (2001)
W.D.	metavolcanite	674 ± 23	Pb-Pb total grain (Zrn)	magmatic age	Kröner *et al.* (2001)
W.D.	orthogneiss	692 ± 2,5	Pb-Pb total grain (Zrn)	magmatic age	Kröner *et al.* (2001)
W.D.	orthogneiss	782 ± 23	Pb-Pb total grain (Zrn)	inherited age	Kröner *et al.* (2001)
W.D.	orthogneiss	826 ± 11	Pb-Pb total grain (Zrn)	inherited age	Kröner *et al.* (2001)
W.D.	orthogneiss	867 ± 1,1	Pb-Pb total grain (Zrn)	inherited age	Kröner *et al.* (2001)
W.D.	orthogneiss	1184 ± 1,5	Pb-Pb total grain (Zrn)	inherited age	Kröner *et al.* (2001)
W.D.	metavolcanite	1240 ± 8	Pb-Pb total grain (Zrn)	inherited age	Kröner *et al.* (2001)

W.D. orthogneiss	1298 ± 10	Pb-Pb total grain (Zrn)	inherited age	Kröner *et al.* (2001)
W.D. orthogneiss	1372 ± 5	Pb-Pb total grain (Zrn)	inherited age	Kröner *et al.* (2001)
W.D. metavolcanite	1939 ± 5	Pb-Pb total grain (Zrn)	inherited age	Kröner *et al.* (2001)
N.D. felsic granulite	393,3 ± 2,8	U-Pb total grain (Zrn)	magmatic age	Lange *et al.* (2005a)
N.D. mafic granulite	411,4 ± 1,5	U-Pb total grain (Zrn)	magmatic age	Lange *et al.* (2005a)
N.D. mafic granulite	413,5 ± 1,6	U-Pb total grain (Zrn)	magmatic age	Lange *et al.* (2005a)
N.D. leucosome	424,4 ± 1,6	U-Pb total grain (Zrn)	magmatic age	Lange *et al.* (2005b)
N.D. leucosome	434,3 ± 1,8	U-Pb total grain (Zrn)	magmatic age	Lange *et al.* (2005b)
N.D. leucosome	438,7 ± 1,6	U-Pb total grain (Zrn)	magmatic age	Lange *et al.* (2005b)
N.D. leucosome	473,4 ± 1,9	U-Pb total grain (Zrn)	magmatic age	Lange *et al.* (2005b)
N.D. leucosome	499,5 ± 27,5	U-Pb in-situ (Zrn)	magmatic age	Lange *et al.* (2005b)
S.D. Gieraltow gneiss	501,0 ± 1,0	Pb-Pb total grain (Zrn)	magmatic age	Mazur *et al.* (2010)
S.D. Śnieżnik gneiss	500,2 ± 1,0	Pb-Pb total grain (Zrn)	magmatic age	Mazur *et al.* (2010)
W.D. Śnieżnik gneiss	503,5 ± 1,0	Pb-Pb total grain (Zrn)	magmatic age	Mazur *et al.* (2010)
S.D. undefined	488 ± 47	U-Pb total grain (Zrn)	magmatic age	Oliver *et al.* (1993)
S.D. undefined	504 ± 3	U-Pb total grain (Zrn)	magmatic age	Oliver *et al.* (1993)
N.D. felsic granulite	473 ± 8	U-Pb in-situ (Zrn)	magmatic age	Štípská *et al.* (2004)
N.D. metapelite	504,3 ± 1	Pb-Pb total grain (Zrn)	magmatic age	Štípská *et al.* (2004)
N.D. metapelite	507,1 ± 1	Pb-Pb total grain (Zrn)	magmatic age	Štípská *et al.* (2004)
S.D. Gieraltow gneiss	495 ± 14	U-Pb in-situ (Zrn)	magmatic age	Turniak *et al.* (2000)
S.D. Śnieżnik gneiss	495 ± 7	U-Pb in-situ (Zrn)	magmatic age	Turniak *et al.* (2000)
S.D. Śnieżnik gneiss	534 ± 14,1	U-Pb in-situ (Zrn)	magmatic age	Turniak *et al.* (2000)
S.D. Gieraltow gneiss	535 ± 5	U-Pb in-situ (Zrn)	magmatic age	Turniak *et al.* (2000)
W.D. migmatitic orthogneiss	484,8 ± 12	U-Pb in-situ (Zrn)	metamorphic age	Żelaźniewicz *et al.* (2006)
Protolith OSD CORE Rb-Sr				
N.D. Gieraltow gneiss	464 ± 18	Rb-Sr (WR)	cooling age	Borkowska *et al.* (1990)
N.D. Śnieżnik gneiss	540 ± 50	Rb-Sr (WR)	unknown	van Breemen *et al.* (1982)
S.D. Śnieżnik gneiss	395 ± 35	Rb-Sr (WR)	cooling age	Borkowska *et al.* (1990)
Metamorphic OSD CORE Rb-Sr				
N.D. mafic granulite	344,3 ± 1,5	U-Pb total grain (Zrn)	metamorphic age	Anczkiewicz *et al.* (2007)
N.D. Leucosome	329,2 ± 4,5	U-Pb in-situ (Zrn)	metamorphic age	Bröcker *et al.* (2009)
N.D. Leucosome	334,4 ± 4	U-Pb in-situ (Zrn)	metamorphic age	Bröcker *et al.* (2009)
N.D. Leucosome	340 ± 5,1	U-Pb in-situ (Zrn)	metamorphic age	Bröcker *et al.* (2009)
C.D. eclogite	340,3 ± 4,1	U-Pb in-situ (Zrn)	metamorphic age	Bröcker *et al.* (2009)
N.D. Leucosome	345,4 ± 4,5	U-Pb in-situ (Zrn)	metamorphic age	Bröcker *et al.* (2009)
S.D. eclogite	346,3 ± 5,2	U-Pb in-situ (Zrn)	metamorphic age	Bröcker *et al.* (2010)
N.D. felsic granulite	326,1 ± 1,5	U-Pb total grain (Zrn)	metamorphic age	Lange *et al.* (2005a)
N.D. felsic granulite	338,1 ± 1,3	U-Pb total grain (Zrn)	metamorphic age	Lange *et al.* (2005a)
N.D. mafic granulite	340,2 ± 1,2	U-Pb total grain (Zrn)	metamorphic age	Lange *et al.* (2005a)
N.D. mafic granulite	341,1 ± 1,3	U-Pb total grain (Zrn)	metamorphic age	Lange *et al.* (2005)a
N.D. felsic granulite	347,2 ± 1,4	U-Pb total grain (Zrn)	magmatic age	Lange *et al.* (2005)a
N.D. mafic granulite	355 ± 6	U-Pb in-situ (Zrn)	magmatic age	Lange *et al.* (2005)a
N.D. mafic granulite	359,3 ± 0,8	U-Pb total grain (Zrn)	metamorphic age	Lange *et al.* (2005)a
N.D. leucosome	352,5 ± 11,5	U-Pb in-situ (Zrn)	metamorphic age	Lange *et al.* (2005)b
N.D. leucosome	360 ± 8,2	U-Pb total grain (Zrn)	magmatic age	Lange *et al.* (2005)b
N.D. felsic granulite	341,3 ± 0,7	Pb-Pb total grain (Zrn)	metamorphic age	Štípská *et al.* (2004)

N.D. felsic granulite	341,6 ± 4,7	U-Pb in-situ (Zrn)	metamorphic age	Štípská *et al.* (2004)
N.D. leucosome	366,3 ± 1,1	Pb-Pb total grain (Zrn)	magmatic age	Štípská *et al.* (2004)
S.D. Gieraltow gneiss	342 ± 6	U-Pb in-situ (Zrn)	metamorphic age	Turniak *et al.* (2000)
S.D. Śnieżnik gneiss	342 ± 6	U-Pb in-situ (Zrn)	metamorphic age	Turniak *et al.* (2000)
W.D. Syenite	326 ± 3	U-Pb in-situ (Zrn)	magmatic age	Żelaźniewicz *et al.* (2006)
Metamorphic OSD CORE Lu-Hf				
N.D. felsic granulite	386,6 ± 4,9	Lu-Hf (Grt)	prograde metam.	Anczkiewicz et al. (2007)
N.D. mafic granulite	373,8 ± 4	Lu-Hf (Grt)	metamorphic age	Anczkiewicz et al. (2007)
N.D. metapelite	354,2 ± 3,3	Lu-Hf (Grt)	unknown	Anczkiewicz et al. (2007)
Metamorphic OSD CORE Sm-Nd				
N.D. mafic granulite	340,1 ± 4,1	Sm-Nd (Grt)	metamorphic age	Anczkiewicz *et al.* (2007)
N.D. felsic granulite	320,5 ± 3	Sm-Nd (Grt)	unknown	Anczkiewicz *et al.* (2007)
N.D. metapelite	381,2 ± 6,7	Sm-Nd (Grt)	metamorphic age	Anczkiewicz *et al.* (2007)
S.D. eclogite	352,2 ± 3,3	Sm-Nd (Grt)	metamorphic age	Bröcker et al. (2009)
C.D. eclogite	329 ± 6	Sm-Nd (WR)	cooling age	Brueckner *et al.* (1991)
C.D. eclogite	341 ± 7	Sm-Nd (WR)	cooling age	Brueckner *et al.* (1991)
S.D. eclogite	337 ± 4	Sm-Nd (WR)	cooling age	Brueckner *et al.* (1991)
N.D. mafic granulite	352 ± 4	Sm-Nd (WR)	cooling age	Brueckner *et al.* (1991)
C.D. metapelite	346,5 ± 4,4	Sm-Nd (Grt)	metamorphic age	Jastrzębski (2008)
C.D. metapelite	329,7 ± 4,6	Sm-Nd (WR)	metamorphic age	Jastrzębski (2008)
N.D. mafic granulite	351 ± 10	Sm-Nd (WR)	cooling age	Lange *et al.* (2005a)
N.D. mafic granulite	357 ± 10	Sm-Nd (WR)	cooling age	Lange *et al.* (2005a)
N.D. felsic granulite	337 ± 4	Sm-Nd (WR)	cooling age	Lange *et al.* (2005a)
Metamorphic OSD CORE Th-Pb				
W.D. metapelite	352 ± 5	Th-Pb (Mnz)	cooling age	Gordon *et al.* (2005)
W.D. metapelite	295 ± 4	Th-Pb (Mnz)	cooling age	Gordon *et al.* (2005)
W.D. orthogneiss	372 ± 8	Th-Pb (Mnz)	cooling age	Gordon *et al.* (2005)
W.D. orthogneiss	343 ± 7	Th-Pb (Mnz)	cooling age	Gordon *et al.* (2005)
Metamorphic/Cooling OSD CORE Rb-Sr				
S.D. Śnieżnik gneiss	335 ± 5	Rb-Sr (Ms)	cooling age	Borkowska *et al.* (1990)
S.D. Gieraltow gneiss	321,1 ± 3,2	Rb-Sr (Bt)	metamorphic age	Bröcker *et al.* (2009)
S.D. Śnieżnik gneiss	321,6 ± 3,2	Rb-Sr (Bt)	cooling age	Bröcker *et al.* (2009)
S.D. Gieraltow gneiss	323,5 ± 3,2	Rb-Sr (Bt)	cooling age	Bröcker *et al.* (2009)
S.D. eclogite	327,3 ± 4,1	Rb-Sr (Ms)	cooling age	Bröcker *et al.* (2009)
S.D. Śnieżnik gneiss	329,6 ± 3,2	Rb-Sr (Bt)	metamorphic age	Bröcker *et al.* (2009)
S.D. eclogite	330,9 ± 4,9	Rb-Sr (Ms)	metamorphic age	Bröcker *et al.* (2009)
S.D. eclogite	331,3 ± 6,5	Rb-Sr (Ms)	metamorphic age	Bröcker *et al.* (2009)
S.D. eclogite	335,5 ± 5,2	Rb-Sr (Ms)	metamorphic age	Bröcker *et al.* (2009)
S.D. Gieraltow gneiss	336,5 ± 4,1	Rb-Sr (Ms)	metamorphic age	Bröcker *et al.* (2009)
S.D. paragneiss	337,3 ± 3,6	Rb-Sr (Ms)	metamorphic age	Bröcker *et al.* (2009)
S.D. eclogite	346,3 ± 4,2	Rb-Sr (Ms)	metamorphic age	Bröcker *et al.* (2009)
S.D. eclogite	355,2 ± 6,7	Rb-Sr (Ms)	metamorphic age	Bröcker *et al.* (2009)
S.D. Śnieżnik gneiss	278,8 ± 2,8	Rb-Sr (Bt)	unknown	Bröcker *et al.* (2009)
S.D. orthogneiss	328,6 ± 4,4	Rb-Sr (Bt)	cooling age	Lange *et al.* (2002)
S.D. orthogneiss	337,4 ± 2,3	Rb-Sr (Ms)	cooling age	Lange *et al.* (2002)
N.D. Gieraltow gneiss	318,7 ± 3,2	Rb-Sr (Bt)	cooling age	Lange *et al.* (2005b)

N.D. Gieraltow gneiss	318,9 ± 3,2	Rb-Sr (Bt)	cooling age	Lange *et al.* (2005b)
N.D. Gieraltow gneiss	327,3 ± 3,3	Rb-Sr (Bt)	cooling age	Lange *et al.* (2005b)
S.D. Gieraltow gneiss	329,8 ± 3,4	Rb-Sr (Bt)	cooling age	Lange *et al.* (2005b)
C.D. Gieraltow gneiss	330,4 ± 3,5	Rb-Sr (Ms)	cooling age	Lange *et al.* (2005b)
N.D. Śnieżnik gneiss	330,4 ± 3,4	Rb-Sr (Bt)	cooling age	Lange *et al.* (2005b)
S.D. Śnieżnik gneiss	331,3 ± 3,3	Rb-Sr (Bt)	cooling age	Lange *et al.* (2005b)
S.D. Gieraltow gneiss	331,3 ± 3,4	Rb-Sr (Bt)	cooling age	Lange *et al.* (2005b)
S.D. Śnieżnik gneiss	332 ± 3,4	Rb-Sr (Bt)	cooling age	Lange *et al.* (2005b)
N.D. Śnieżnik gneiss	333,5 ± 3,5	Rb-Sr (Ms)	cooling age	Lange *et al.* (2005b)
S.D. Śnieżnik gneiss	333,8 ± 3,4	Rb-Sr (Bt)	cooling age	Lange *et al.* (2005b)
N.D. Gieraltow gneiss	334,1 ± 3,5	Rb-Sr (Ms)	cooling age	Lange *et al.* (2005b)
N.D. Gieraltow gneiss	334,1 ± 3,5	Rb-Sr (Ms)	cooling age	Lange *et al.* (2005b)
S.D. Śnieżnik gneiss	336,1 ± 3,5	Rb-Sr (Ms)	cooling age	Lange *et al.* (2005b)
S.D. Śnieżnik gneiss	336,3 ± 3,5	Rb-Sr (Ms)	cooling age	Lange *et al.* (2005b)
N.D. Gieraltow gneiss	336,8 ± 3,6	Rb-Sr (Ms)	cooling age	Lange *et al.* (2005b)
N.D. Gieraltow gneiss	336,9 ± 3,4	Rb-Sr (Bt)	cooling age	Lange *et al.* (2005b)
S.D. Śnieżnik gneiss	339,6 ± 3,9	Rb-Sr (Ms)	cooling age	Lange *et al.* (2005b)
N.D. Gieraltow gneiss	339,9 ± 3,8	Rb-Sr (Ms)	cooling age	Lange *et al.* (2005b)
S.D. Śnieżnik gneiss	341,6 ± 3,7	Rb-Sr (Ms)	cooling age	Lange *et al.* (2005b)
Metamorphic/ Cooling OSD CORE Ar-Ar				
N.D. metapelite	336 ± 2,1	Ar-Ar (Ms)	cooling age	Anczkiewicz *et al.* (2007)
S.D. eclogite	348,2 ± 0,6	Ar-Ar (Ms)	metamorphic age	Bröcker *et al.* (2009)
S.D. eclogite	388,4 ± 1	Ar-Ar (Ms)	extraneous Ar	Bröcker *et al.* (2009)
S.D. migmatitic orthogneiss	313,2 ± 3	Ar-Ar (Ms)	cooling age	Maluski *et al.* (1995)
S.D. migmatitic orthogneiss	328 ± 3	Ar-Ar (Bt)	cooling age	Maluski *et al.* (1995)
W.D. migmatitic orthogneiss	336 ± 3,2	Ar-Ar (Hb)	cooling age	Maluski *et al.* (1995)
S.D. orthogneiss	340,9 ± 0,9	Ar-Ar (Bt)	cooling age	Schneider *et al.* (2006)
S.D. orthogneiss	336,9 ± 0,5	Ar-Ar (Ms)	cooling age	Schneider *et al.* (2006)
S.D. orthogneiss	341,6 ± 1,1	Ar-Ar (Bt)	cooling age	Schneider *et al.* (2006)
W.D. metapelite	338,2 ± 0,9	Ar-Ar (Bt)	cooling age	Schneider *et al.* (2006)
W.D. orthogneiss	334,9 ± 0,4	Ar-Ar (Bt)	cooling age	Schneider *et al.* (2006)
W.D. orthogneiss	335,5 ± 0,8	Ar-Ar (Ms)	cooling age	Schneider *et al.* (2006)
W.D. orthogneiss	337,9 ± 0,7	Ar-Ar (Ms)	cooling age	Schneider *et al.* (2006)
W.D. metapelite	314,4 ± 0,8	Ar-Ar (Ms)	cooling age	Schneider *et al.* (2006)
N.D. orthogneiss	340,9 ± 0,5	Ar-Ar (Ms)	cooling age	Schneider *et al.* (2006)
N.D. Śnieżnik gneiss	333,9 ± 0,5	Ar-Ar (Bt)	cooling age	Schneider *et al.* (2006)
N.D. orthogneiss	339,1 ± 0,6	Ar-Ar (Bt)	cooling age	Schneider *et al.* (2006)
N.D. metapelite	334,9 ± 0,9	Ar-Ar (Ms)	cooling age	Schneider *et al.* (2006)
S.D. orthogneiss	337,6 ± 0,6	Ar-Ar (Bt)	cooling age	Schneider *et al.* (2006)
C.D. orthogneiss	334,2 ± 0,8	Ar-Ar (Bt)	cooling age	Schneider *et al.* (2006)
C.D. eclogite	332,6 ± 2,3	Ar-Ar (Hb)	cooling age	Steltenpohl *et al.* (1993)
W.D. mylonitic gneiss	328 ± 1,7	Ar-Ar (Ms)	cooling age	Steltenpohl *et al.* (1993)
W.D. mylonitic gneiss	328,8 ± 1,7	Ar-Ar (Ms)	cooling age	Steltenpohl *et al.* (1993)
W.D. amphibolite	338,4 ± 4,5	Ar-Ar (Hb)	cooling age	Steltenpohl *et al.*. (1993)
N.D. Śnieżnik gneiss	328 ± 2	Ar-Ar (Bt)	cooling age	Steltenpohl *et al.* (1993)
W.D. metapelite	339,5 ± 5,2	Ar-Ar (Ms)	cooling age	This study

N.D. metapelite	339,5 ± 2,54	Ar-Ar (Ms)	cooling age	This study
N.D. metapelite	343,8 ± 1,1	Ar-Ar (Ms)	cooling age	This study
Granitoid OSD CORE				
N.D. syntectonic granitoid	353 ± 1,1	Pb-Pb total grain (Zrn)	magmatic age	Kröner *et al.* unpublished
N.D. syntectonic granitoid	351,1 ± 3,7	Ar-Ar (Hbl)	cooling age	Białek & Werner (2004)
N.D. syntectonic granitoid	349,6 ± 3,8	Ar-Ar (Bt)	cooling age	Białek & Werner (2004)
N.D. syntectonic granitoid	344,6 ± 3,8	Ar-Ar (Ms)	cooling age	Białek & Werner (2004)
OSD MANTLE				
S.M. amphibolite	500.5 ± 0.6	U-Pb total grain (Zrn)	metamorphic age	Parry *et al.* (1997)
S.M. amphibolite	505 ± 6	U-Pb total grain (Zrn)	magmatic age	Parry *et al.* (1997)
S.M. metapelite	522.5 ± 1	Pb-Pb total grain (Zrn)	magmatic age	Kröner *et al.* (2000)
S.M. leptyno-amphibolite	503.4 ± 1	Pb-Pb total grain (Zrn)	magmatic age	Kröner *et al.* (2000)
S.M. metapelite	504 ± 12	Pb-Pb total grain (Zrn)	magmatic age	Kröner *et al.* (2000)
S.M. metapelite	503.4 ± 1	Pb-Pb total grain (Zrn)	magmatic age	Kröner *et al.* (2000)
S.M. trondhjemite gneiss	504 ± 4	Pb-Pb total grain (Zrn)	magmatic age	Kröner *et al.* (2000)
S.M. trondhjemite gneiss	503.2 ± 1	Pb-Pb total grain (Zrn)	magmatic age	Kröner *et al.* (2000)
S.M. leucosome	684 ± 6	Pb-Pb total grain (Zrn)	magmatic age	Kröner *et al.* (2000)
S.M. leucosome	641 ± 4	Pb-Pb total grain (Zrn)	magmatic age	Kröner *et al.* (2000)
S.M. leucosome	502.1 ± 1	Pb-Pb total grain (Zrn)	magmatic age	Kröner *et al.* (2000)
S.M. gneiss	502.5 ± 1	Pb-Pb total grain (Zrn)	magmatic age	Kröner *et al.* (2000)
S.M. leucosome	501.8 ± 1	Pb-Pb total grain (Zrn)	magmatic age	Kröner *et al.* (2000)
S.M. metapelite	507 ± 7	U-Pb in-situ (Zrn)	metamorphic age	Kröner *et al.* (2000)
S.M. metapelite	551 ± 9	U-Pb in-situ (Zrn)	magmatic age	Kröner *et al.* (2000)
S.M. metapelite	609 ± 10	U-Pb in-situ (Zrn)	magmatic age	Kröner *et al.* (2000)
S.M. gneiss	684.5 ± 0.9	Pb-Pb total grain (Zrn)	magmatic age	Kröner *et al.* (2000)
S.M. gneiss	504.1 ± 1	Pb-Pb total grain (Zrn)	magmatic age	Kröner *et al.*. (2000)
S.M. gneiss	333 ± 4	Th-Pb (Mnz)	cooling age	Gordon *et al.* (2005)
S.M. gneiss	315 ± 4	Th-Pb (Mnz)	cooling age	Gordon *et al.* (2005)
S.M. gneiss	334 ± 5	Th-Pb (Mnz)	cooling age	Gordon *et al.* (2005)
S.M. migmatitic orthogneiss	330.1 ± 3.4	Ar-Ar (Hbl)	cooling age	Maluski *et al.* (1995)
S.M. gneiss	338.2 ± 0.5	Ar-Ar (Bt)	cooling age	Schneider *et al.* (2006)
Z.U. amphibolite	342.3 ± 4.3	Ar-Ar (Hbl)	cooling age	This study
Z.U. amphibolite	346.6 ± 9.7	Ar-Ar (Hbl)	cooling age	This study
Z.U. syntectonic granitoid	338,1 ± 1,3	Pb-Pb total grain (Zrn)	magmatic age	Kröner et al. unpublished
S.M. syntectonic granitoid	339 ± 7	Pb-Pb total grain (Zrn)	magmatic age	Parry *et al.* (1997)
S.M. syntectonic granitoid	339,4 ± 1,1	Pb-Pb total grain (Zrn)	magmatic age	Štípská *et al.* (2004)
S.M. syntectonic granitoid	344,5 ± 1,1	Pb-Pb total grain (Zrn)	magmatic age	Štípská *et al.* (2004)
S.M. syntectonic granitoid	344.4 ± 4.4	Ar-Ar (Hbl)	cooling age	This study
S.M. syntectonic granitoid	343.3 ± 6.4	Ar-Ar (Hbl)	cooling age	This study
S.M. syntectonic granitoid	345 ± 6.8	Ar-Ar (Hbl)	cooling age	This study

Appensix S2: 40Ar/39Ar analytical methods

Mineral separates were classically obtained after crushing and handpicking of single grains ranging from 0.5 to 1 mm under a binocular microscope. The mineral were repeatedly cleaned ultrasonically in distilled water. The crystals were co-irradiated for 30 h in the nuclear reactor at the McMaster University in Hamilton (Canada), in position 5c, along with Hb3gr hornblende monitor (1072 Ma; Turner *et al.* 1971). $^{40}Ar/^{39}Ar$ analyses were performed at Geoazur laboratory. Eight mineral were heated with a CO_2 Synrad laser. The gas was purified in a stainless and glass extraction line using two Al–Zr getters (working at 400 °C and ambient temperature, respectively) and a liquid nitrogen cold trap. Isotopic measurements were performed with a VG3600 mass spectrometer and a Daly-photomultiplier system. Blank measurements were obtained before and after every three sample run. The correction factors for interfering isotopes correspond to $(^{39}Ar/^{37}Ar)_{Ca} = (7.30 \pm 0.28) \times 10^{-4}$; $(^{36}Ar/^{37}Ar)_{Ca} = (2.82 \pm 0.03) \times 10^{-4}$ and $(^{40}Ar/^{39}Ar)_{K} = (2.97 \pm 0.06) \times 10^{-2}$. Ages were calculated using the decay constants of Steiger & Jager (1977) and the air $^{40}Ar/^{36}Ar$ ratio of 298.56 ± 0.1% (at 1s) (Lee *et al.*, 2006). *J*- values range from 0.0035309 ± 0.0000177 (= 0.5% at 1s) to 0.0035312 ± 0.0000177 (=0.5% at 1s). Mass discrimination values range from 1.00474 to 1.00738 ± 1% (1s) per dalton (atomic mass unit). The criteria for defining plateau ages were as follows: 1) a plateau age should contain at least 70% of released ^{39}Ar; 2) there should be at least three successive steps in the plateau; and 3) the integrated age of the plateau should agree with each apparent age of twhe plateau within a 1s error confidence interval.

CHAPITRE III

THE ROLE OF LARGE-SCALE FOLDING AND EROSION ON JUXTAPOSITION OF ECLOGITE AND MID-CRUSTAL ROCKS (ORLICA-ŚNIEŻNIK DOME, BOHEMIAN MASSIF)

P. ŠTÍPSKÁ[1], F. CHOPIN[1], E. SKRZYPEK[1], K. SCHULMANN[1], O.LEXA[2,3], P.PITRA[4], J.E. MARTELAT[5], C. BOLINGER[6]

[1]*Ecole et Observatoire des Sciences de la Terre, Institut de Physique du Globe – CNRS UMR 7516, Université de Strasbourg, 1 rue Blessig, F-67084 Strasbourg Cedex, France*

[2]*Institute of Petrology and Structural Geology, Charles University, Albertov 6, CZ-12843 Praha, Czech Republic*

[3]*Czech Geological Survey, Klárov 3, 110 00, Praha, Czech Republic*

[4]*Geosciences Rennes – CNRS UMR6118, Université Rennes 1, Campus de Beaulieu, F-35042 Rennes Cedex, France*

[5] *Laboratoire des Sciences de la Terre – CNRS UMR5570, Université de Lyon 1, F-69622, Villeurbanne, France*

[6]*Unité Matériaux et Transformations – CNRS UMR8207, Université Lille 1, Bât. C6, F-59655 Villeneuve d'Ascq, France*

Short title: Eclogite and mid-crustal rocks juxtaposition

Key words: Śnieżnik eclogite, Thermocalc modelling, crustal scale folding, structures and metamorphism

Abstract

PT evolution of eclogites was compared with that of medium grade metapelite juxtaposed by crustal folding in a mutual distance of 5 km. Both types of rocks reveal flat orogenic influx related fabrics marked by 22 kbar at 720°C peak conditions for eclogites and 6 kbar at 550 - 600°C for metapelites. Kilometre scale steep folding produced steep retrograde amphibolites facies fabrics (10kbar at 700°C) in eclogites and prograde mineral assemblage (7kbar at 650°C) in metaplites. Finally, both rocks were exhumed along steep foliation to shallow crustal depth corresponding to PT conditions of 4.5 kbar at 500°C where flat ductile thinning related foliation originate. This evolution is explained partly by exhumation of eclogites and burial of metapelites associated with kilometer scale folding. These folds are interpreted as parasitic folds with respect to large migmatite dome-like antiform with half wavelength of 10 km. Eclogite bearing orthogneiss antiform and metapelite synform were located above inflection point of large scale migmatite fold which is responsible for their joint exhumation during ongoing shortening. The joint exhumation path associated with loss of pressure and temperature is explained by efficient

erosion at the top of the system which brought the zero temperature boundary conditions closer to vertically elevated rocks. The folding of originally flat anisotropy at the thickened crustal roots is considered as a first order exhumation mechanism of deep seated rocks in hot orogens of Variscan type.

1. Introduction

Orogenic belts are sites of common tectonic emplacement of (U)HP rocks at middle and upper crustal depth (Duchene *et al.*, 1997). The way how the (U)HP rocks and mid-crustal rocks become juxtaposed is critically dependent on the exhumation mechanism, i.e. on the mode of vertical elevation of rocks during regional convergence or extension. The most commonly reported kinematic model in a convergent setting is displacement of deeply subducted rocks above lower pressure rocks along a crustal scale thrust (e.g. Chemenda *et al.*, 2000; Jolivet *et al.*, 2005). Crustal-scale folding is another convergent kinematic model that may explain tectonic juxtaposition of high- and low-pressure rocks (Burg *et al.*, 1998; Burg *et al.*, 2004). In extensional setting, emplacement of (U)HP rocks into middle to upper crustal levels may occur along a deep-seated extensional fault zone following a subduction event (e.g. Andersen & Fossen, 1993).

Advent of analogue and numerical orogenic-scale models offered mechanical and dynamic explanation of burial and exhumation of rocks along convergent boundaries (Platt, 1987), which may lead to a close juxtaposition of high- and low-pressure rocks. A first group of models involves corner flow circulation of rocks above a downgoing plate in front of a rigid buttress (Platt, 1993; Allemand & Lardeaux, 1997; Gerya & Stöckhert, 2006), or above a gently inclined upper plate boundary (Beaumont *et al.*, 2001; Beaumont *et al.*, 2006). A second group of models is based on gravity-driven exhumation and redistribution of deeply buried material. The most typical example are crustal-scale "diapiric" domes (e.g. Gerya *et al.*, 2002; Gerya *et al.*, 2004), which may be enhanced by lateral forces leading to mixed diapiric and folding mechanisms (Burg *et al.*, 2004; Lexa *et al.*, 2011). Another example is horizontal spreading of a rebounded lower crust beneath a rigid orogenic lid (Koyi *et al.*, 1999).

Each model should be associated with a typical succession of structures and typical P−T paths related to the movement of rocks in individual crustal levels. Therefore, in order to correlate one of the above models or their combination with the tectono-metamorphic evolution of an orogen, information about structural, petrological and geochronological evolutions of the orogenic lower, middle and upper crust is needed. Structural geology can compare successions of deformation fabrics from different crustal levels in order to explore mechanical coupling or decoupling between the lower and upper crust during orogeny. Structural investigations may also show whether the juxtaposition of high- and low-pressure rocks results from tectonic movements related to orogenesis or with late to post-orogenic faulting or shearing. Petrology provides additional information about vertical displacements and thermal evolution of rocks

during orogeny. Establishing P−T paths of individual rocks allows relating these rocks to different crustal levels and demonstrating their shared or unshared metamorphic histories (Racek *et al.*, 2006; Štípská *et al.*, 2006; Štípská *et al.*, 2008). Combination of structural and petrological information into P−T−d paths allows determining burial and/or exhumation character of individual fabrics. It also allows correlation of relative horizontal and vertical displacements of rocks from different crustal levels during an orogenic cycle.

The polyphase structural and petrological evolution of lower crustal eclogite, felsic orthogneiss and adjacent mid-crustal metasediments is described in this work. The structural succession and associated metamorphic evolution of these rocks is evaluated in order to characterize burial and exhumation related fabrics in two contrasting crustal levels during the Variscan orogeny. Comparison of the P−T−d paths of the eclogite and the metapelite allows discussing fabrics and deformation processes that are responsible for the close juxtaposition of the lower and the mid-crustal rocks. Finally, the structural and P−T records of the individual fabrics are discussed in the frame of the kinematic and dynamic models introduced above.

2. GEOLOGICAL SETTING

The Orlica-Śnieżnik dome (OSD) is located in the easternmost part of the Bohemian Massif (Fig. III-1). It is interpreted as part of the orogenic root of the Moldanubian-Lugian zone (e.g. Schulmann *et al.*, 2009) bordered to the east by the Staré Město formation, a remnant of a Late Cambrian intracontinental rift (Parry *et al.*, 1997; Kröner *et al.*, 2000; Štípská *et al.*, 2001; Lexa *et al.*, 2005), and the Moravo-Silesian zone, a deformed and metamorphosed part of the Neoproterozoic Brunovistulian (Brunia) microcontinent (Schulmann & Gayer, 2000; Štípská *et al.*, 2006; Košuličová & Štípská, 2007). The south-western and southern part of the OSD are surrounded by low grade rocks of the Nové Město and the Zábřeh formations interpreted as the upper orogenic crust (Mazur *et al.*, 2005; Schulmann *et al.*, 2008).

2. 1. Lithology and protolith ages

The OSD (Fig. III-1) is dominated by felsic orthogneiss, locally containing lenses of (U)HP rocks (eclogite and granulite), alternating with generally N−S trending belts of the volcanosedimentary Młynowiec-Stronie formation (Don *et al.*, 2003). The felsic orthogneisses are traditionally subdivided into two main types (Fig. III-2): an augen and banded variety (the Śnieżnik type) and a fine-grained and/or migmatitic variety (the Gierałtów type) (Don *et al.*, 1990). Several authors suggest that both types result from variable reworking of the same porphyritic granite (Turniak *et al.*, 2000; Lange *et al.*, 2002; Lange *et al.*, 2005b) although this view is questioned by other authors (Żelaźniewicz *et al.*, 2006). The fine-grained and migmatitic Gierałtów types are volumetrically more abundant around the eclogite and granulite occurrences. Eclogitic bodies form a 3 km long N−S trending belt in the area of the Międzygórze town (Fig. III-2),

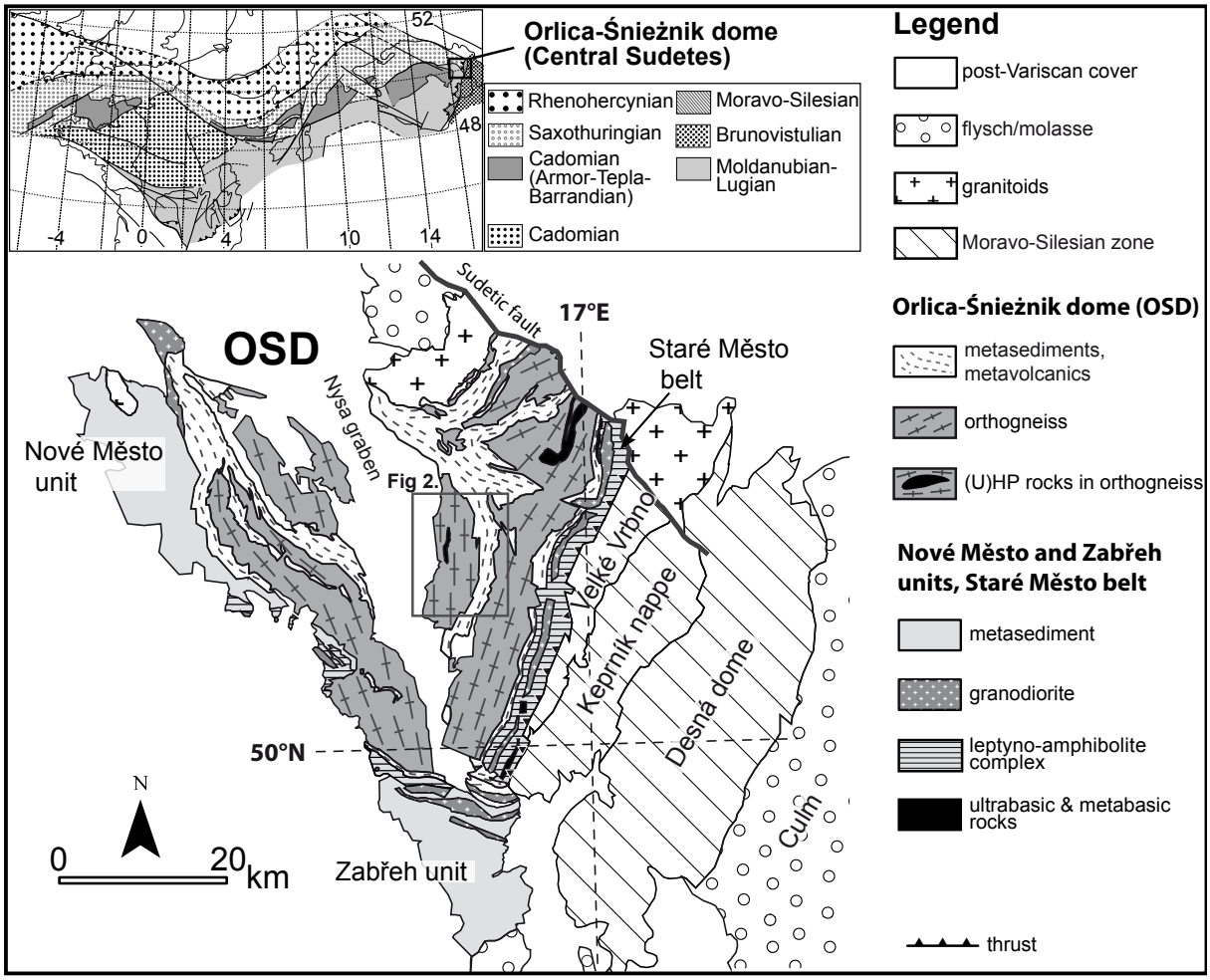

Fig. III-1: Geological map of the Orlica-Śnieżnik dome (OSD) (modified after Aleksandrowski et al., 1997; Don et al., 2003; Żelaźniewicz et al., 2006). Location of the study area (Fig. III-2) is indicated. Upper left inset shows position of the study area in the framework of the European Variscides (modified after Edel, 2003).

and occur as scattered lenses or loose blocks in the felsic orthogneiss mainly in the eastern and central parts of the OSD (Smulikowski, 1967). High-pressure basic and felsic granulites are restricted to a NNE−SSW trending 12 km long belt to the northeast (Pouba *et al.*, 1985; Štípská *et al.*, 2004). The metasedimentary unit is subdivided into the Młynowiec formation comprising plagioclase paragneiss and micaschist, and the Stronie formation composed of micaschist, paragneiss, quartzite, marble, amphibolite and acid volcanic rocks (Don *et al.*, 1990).

Zircon dating of both felsic orthogneiss varieties spans between 490 and 520 Ma, which is interpreted as the emplacement of the granitic precursor (Oliver *et al.*, 1993; Kröner *et al.*, 2000; Turniak *et al.*, 2000; Kröner *et al.*, 2001; Štípská *et al.*, 2004; Lange *et al.*, 2005b; Bröcker *et al.*, 2009). Sedimentation of the Młynowiec formation is older than 530 Ma (Jastrzębski *et al.*, 2010) and the Stronie sediments and volcanics are deposited between 520−470 Ma (Kröner *et al.*, 2000; Jastrzębski *et al.*, 2010). Despite the difficulties to determine the protolith ages of (U)HP rocks in the OSD (Bröcker *et al.*, 2010), they are probably older than 470 Ma (Štípská *et al.*, 2004; Lange *et al.*, 2005a; Bröcker *et al.*, 2010).

2. 2. Previous structural studies

Structural studies focused mainly on the explanation of the generally N−S trending alternation of metasediments and felsic orthogneisses, cored in places by the (U)HP rocks. A succession of three major deformation events was recognized: an early shallow-dipping metamorphic foliation was followed by upright folding and development of a new metamorphic foliation, and subsequently reworked by folds with shallow-dipping to subhorizontal axial planes and associated cleavage (Don, 1964; Dumicz, 1979; Don, 1982; Don *et al.*, 1990; Štípská *et al.*, 2004; Jastrzębski, 2009; Skrzypek *et al.*, 2011b).

2. 3. Previous metamorphic and geochronological studies

Detailed petrography and occurrences of the eclogite types is given in Smulikowski (1967). Based on possible pseudomorphs after coesite and thermobarometry, several authors suggested pressures above 27 kbar for the eclogite (Bröcker & Klemd, 1996) and granulite (Bakun-Czubarow, 1992; Klemd & Bröcker, 1999), while other authors proposed maximum pressures of about 18−22 kbar for granulite (Steltenpohl *et al.*, 1993; Štípská *et al.*, 2004). Peak temperature is estimated at 700−800 °C for the eclogite (Bröcker & Klemd, 1996) and 800−1000 °C for the granulite (Pouba *et al.*, 1985; Bakun-Czubarow, 1992; Steltenpohl *et al.*, 1993; Kryza *et al.*, 1996; Klemd & Bröcker, 1999; Štípská *et al.*, 2004; Bröcker *et al.*, 2010). The retrograde evolution in the eclogite is estimated to lie at 4−9 kbar and 550−650 °C (Bröcker & Klemd, 1996), and is also constrained by fluid inclusion study that shows isothermal decompression from 8 kbar to 3 kbar at 600 °C, followed by almost isobaric cooling to 200 °C (Klemd *et al.*, 1995). Retrogression in the granulite is estimated between 9.5−12.5 kbar at 560−680 °C (Steltenpohl *et al.*, 1993) and 10 kbar at 700−800 °C (Štípská *et al.*, 2004).

Lu−Hf ages on garnet and U−Pb zircon ages clustering between 360 and 380 Ma are reported, but their geological meaning is questioned in terms of incomplete resetting (Anczkiewicz *et al.*, 2007; Bröcker *et al.*, 2010). In contrast, Sm−Nd data on whole-rock and garnet, and U−Pb geochronology on zircon bracket the age of (U)HP metamorphism between 350 and 330 Ma (Brueckner *et al.*, 1991; Klemd & Bröcker, 1999; Štípská *et al.*, 2004; Lange *et al.*, 2005a; Bröcker *et al.*, 2010). This is confirmed by the trace element characteristics of metamorphic zircon suggesting contemporaneous crystallization with garnet and indicating that zircon dates the (U)HP event and not a middle pressure overprint (Bröcker *et al.*, 2010). 40Ar−39Ar cooling ages range between 340 and 350 Ma around the Międzygórze eclogite belt (Schneider *et al.*, 2006; Bröcker *et al.*, 2009) and between 330 and 340 Ma around the granulite belt (Steltenpohl *et al.*, 1993; Schneider *et al.*, 2006; Bröcker *et al.*, 2009).

Metamorphic studies of metapelites in the OSD are commonly linked with deciphering the relationships between the structures and the degree of metamorphism (Jastrzębski, 2005; Mazur *et al.*, 2005; Murtezi, 2006; Jastrzębski, 2009; Skrzypek *et al.*, 2011b). The first record of prograde metamorphism is connected with the early shallow-dipping fabric (Skrzy-

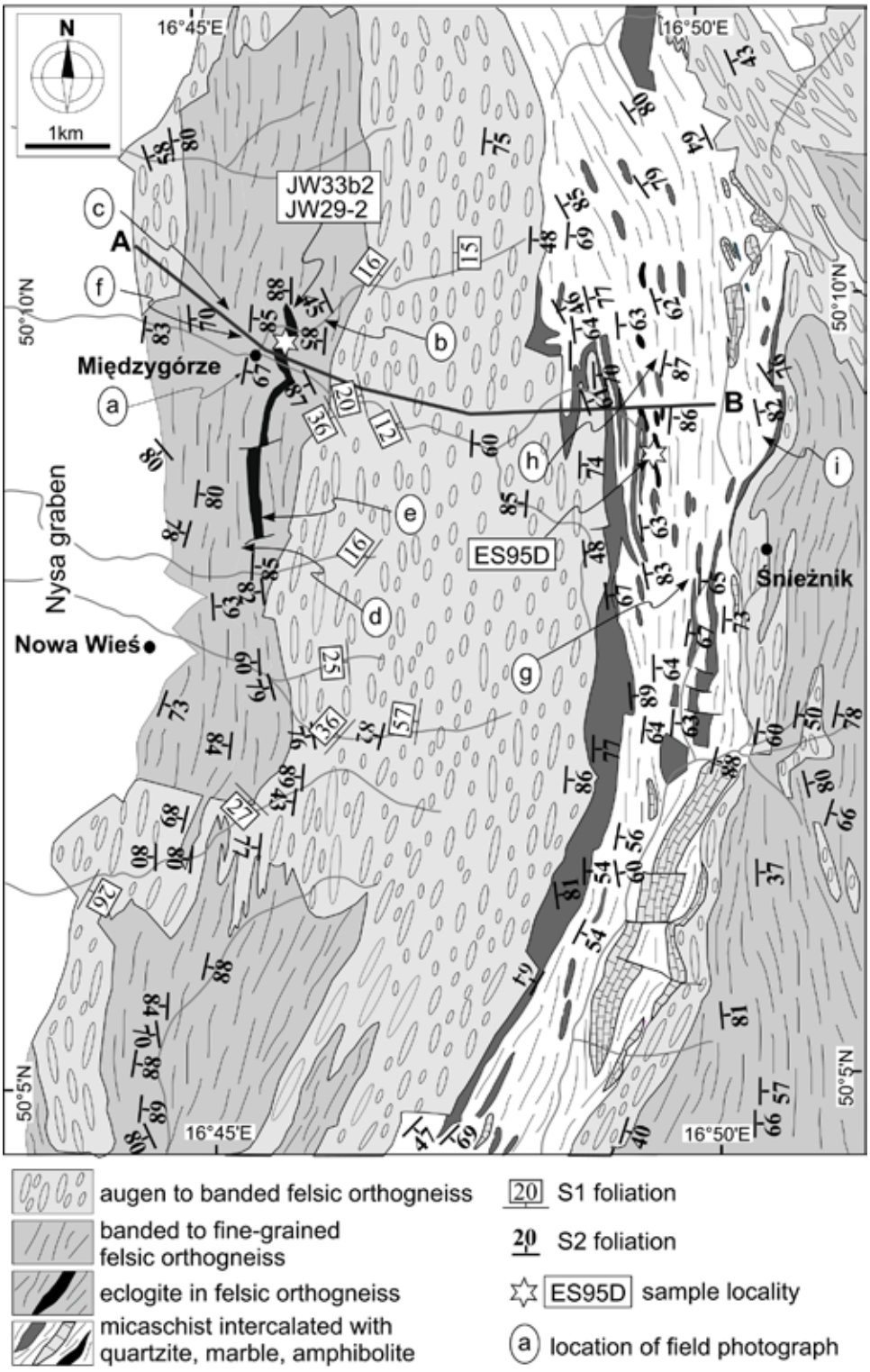

Fig. III-2: Structural map of S1 and S2 foliations. Location of structural profile (Fig. III-3), field photographs (Fig. III-4) and samples used for petrology are indicated. Lithological map is after Don et al. (2003).

pek *et al.*, 2011b). Peak P−T conditions subsequently attained in the superimposed subvertical fabric show a continuous increase from the chlorite to the kyanite zone from the W to the E of the dome. They are estimated at 5−9 kbar and 460−650 °C (Murtezi, 2006; Jastrzębski, 2009; Skrzypek *et al.*, 2011a; Skrzypek *et al.*, 2011b). Decompression to 2−3.5 kbar at 530−600 °C is connected with a late shallow-dipping and heterogeneously developed foliation (Skrzypek

et al., 2011b). The peak metamorphism is associated with a Sm−Nd garnet−whole-rock age of 346.5 ± 4.4 Ma for a Stronie micaschist (Jastrzębski, 2009).

In the orthogneisses around eclogite, the composition of phengitic muscovite reported by Bröcker *et al.* (2009) suggests high-pressure metamorphism. Based on garnet−zoisite−titanite−rutile−quartz thermobarometry, Bröcker & Klemd (1996) proposed ultra-high pressure metamorphism around 28 kbar. Close to the Międzygórze eclogite belt, the age of metamorphism is constrained as Carboniferous based on zircon overgrowths in the fine-grained felsic orthogneiss (342±6 Ma, Turniak *et al.*, 2000), or by leucosomes in migmatite around granulite (330−355 Ma, Štípská *et al.*, 2004; Lange *et al.*, 2005a; Lange *et al.*, 2005b; Anczkiewicz *et al.*, 2007; Bröcker *et al.*, 2009).

3. STRUCTURAL GEOLOGY

Structure was studied in the area of the Międzygórze eclogite belt, in the surrounding felsic orthogneiss, and to the east in the Stronie metasedimentary formation (Fig. III-2). Major structural patterns are shown in the map (Fig. III-2), in an interpretative profile (Fig. III-3) and documented in Figs III-4 & III-5.

3. 1. D1 deformation

The earliest structure is a shallow-dipping foliation S1 that is characterized in the felsic orthogneiss by a deformation gradient ranging from a weakly deformed coarse-grained granite, through an augen and a banded felsic orthogneiss to a fine-grained felsic orthogneiss (Fig. III-4a, b). In the augen and banded varieties, the subhorizontal S1 foliation bears a N−S trending subhorizontal L1 lineation. The foliation and the lineation are well defined by almost monomineralic recrystallized augen and layers of quartz, plagioclase and K-feldspar, and by the preferred orientation of biotite and muscovite (Fig. III-4b). In the fine-grained felsic orthogneiss, the S1 foliation is defined by biotite and/or muscovite and by rare thin monomineralic recrystallized layers of K-feldspar or quartz, although the majority of quartz and feldspar grains is randomly distributed and forms a fine-grained matrix.

The fine-grained felsic orthogneiss occurs in zones of variable thickness, ranging from several centimetres up to several tens of meters, and is volumetrically more abundant in a 2–3 km wide belt around the eclogite (Figs III-2 & III-3). Approximately 2 km to the east of the eclogite belt, the felsic augen orthogneiss with rare banded varieties occurs. In this area, the S1 foliation in the augen felsic orthogneiss is commonly very weak and ill-defined by oriented biotite and recrystallized quartz ribbons. However, the N−S trending L1 lineation is strong and marked by elongated rods of recrystallized quartz, K-feldspar and plagioclase. To the west of the eclogite belt, the majority of the felsic orthogneiss is banded, with subordinate augen and fine-grained orthogneiss types.

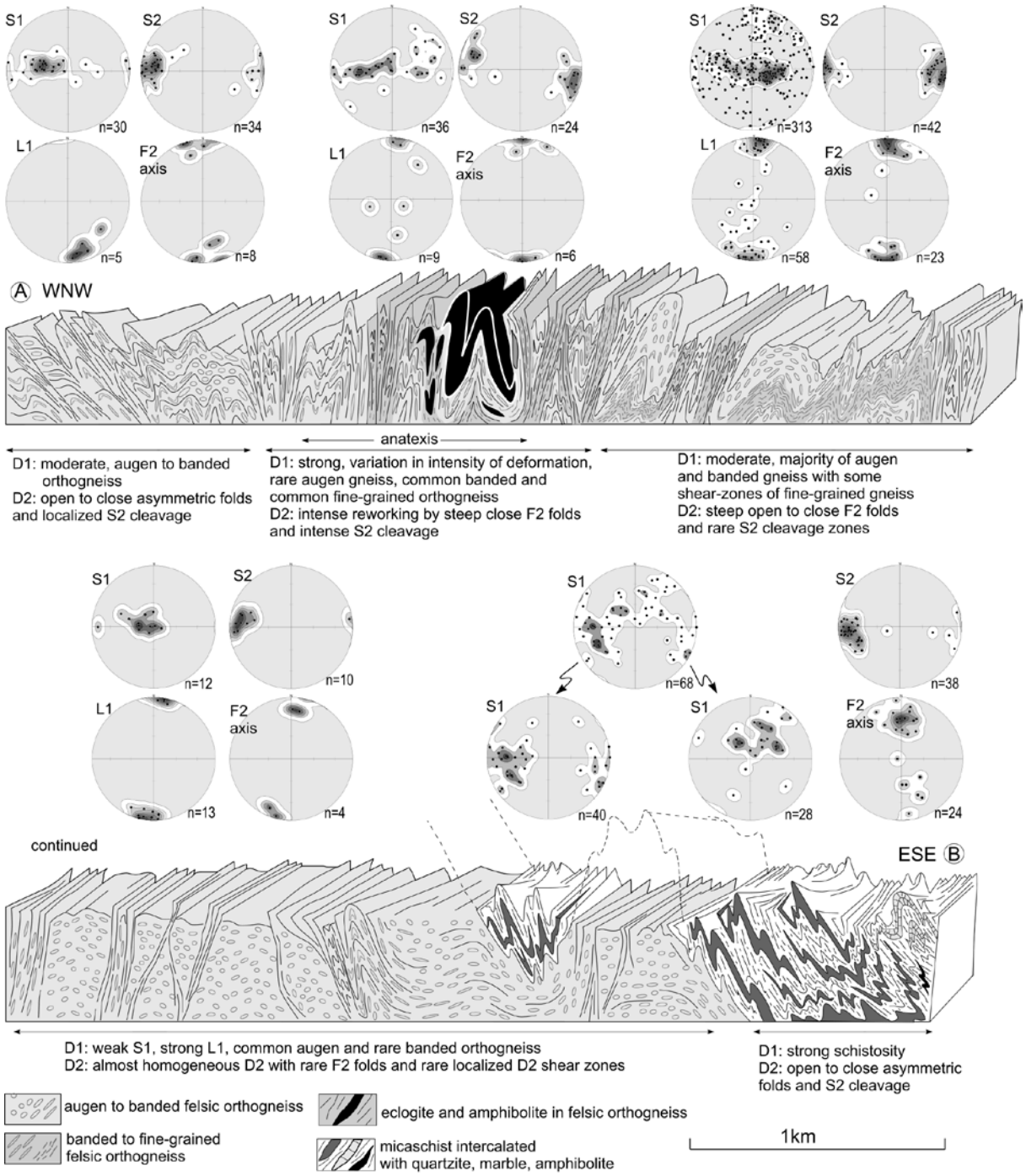

Fig. III-3: Interpretative geological cross-section showing early shallow-dipping fabric S1 and style of superimposed subvertical deformation D2 in individual parts of the studied profile. Structures associated with the S1 foliation and late D3 structures are not shown (for these structures see Figs III-4 & III-5). Equal-area, lower-hemisphere stereoplots show D1 and D2 planar and linear structures. Vertical axis not to scale.

In a 2 km wide area to the west of the eclogite near Międzygórze, the S1 foliation is folded by metre-scale N-verging open folds with subvertical short limbs and long limbs gently dipping to the south (Fig. III-5a–e, these folds are not represented in Fig. III-3). Close to isoclinal folds also occur locally. The short limbs of the N-verging folds are in places affected by tensional gashes filled with quartz (Fig. III-5b) and by an axial planar cleavage. Fold hinges are oriented E−W or SE−NW in the open to close folds, and tend to be oriented SE−NW to N−S in the close to isoclinal folds. The folds described above are attributed to the D1 deformation

where the open asymmetric folds are interpreted in terms of moderate folding of a highly anisotropic multilayer system represented by the banded and the mylonitic felsic orthogneisses in a bulk simple shear (e.g. Grocott & Watterson, 1980; Skjernaa, 1980). In such a system, the fold hinges of the progressively attenuated folds rotate towards maximum stretching direction leading to the development of the close to isoclinal folds with fold hinges parallel to the stretching lineation, the so-called sheath folds (Cobbold & Quinquis, 1980).

In the eclogite, there are no common outcrop-scale remnants of the shallow-dipping S1 foliation. An area several tens of centimetres large of the shallow-dipping S1 foliation affected by the subvertical S2 crenulation cleavage (eclogite sample JW33b2) (Fig. III-5g) was found at one place only.

In the Stronie metasedimentary belt, the S1 foliation is defined by an alternation of quartzite, garnet- and garnet−staurolite-bearing micaschist, marble and amphibolite, and by the orientation of micas and quartz ribbons in the micaschist and quartzite. Because of the strong intensity of the subsequent D2 reworking, the orientation of the S1 foliation cannot be constrained precisely. However, the F2 fold axes are variably plunging either to the north or to the south (Fig. III-2b), which suggests that before the D2 deformation, the S1 foliation was probably affected by late-stage F1 folding characterised by E–W trending hinges and variably north- or south-dipping fold limbs. This is similar to the above-described behaviour in the felsic orthogneiss located to the west of the eclogite.

3. 2. D2 deformation

In the felsic orthogneiss, where the D1 deformation led to development of the fine-grained and the banded orthogneiss varieties, the shallow-dipping S1 foliation is affected by upright metre- to several-metre-scale folding (Figs III-4c & III-5f–h). The folds are open to isoclinal, with subhorizontal N−S trending hinges and subvertical N−S striking axial planes. An axial plane cleavage is usually developed within the fold hinges, commonly showing almost complete transposition into the S2 foliation. The limbs of the tight to isoclinal folds show further attenuation, visible on the more flattened form of the augen and bands of recrystallized K-feldspar, compared to the hinge zone. In the areas with abundant N-vergent F1 folds, the steep N- or S-dipping limbs are also refolded by the F2 folds that have upright hinges and N−S striking vertical axial planes (Fig. III-5d). Locally, the S1 foliation is crosscut by localized, several cen-

Fig. III-4: Field photographs illustrating typical structural relationships. (a) Shallow-dipping foliation S1 in felsic orthogneiss showing deformational gradient from augen to banded variety. (b) Detail of shallow-dipping foliation S1 in the felsic orthogneiss with deformational gradient from augen to fine-grained variety. (c) S1 foliation of the banded felsic orthogneiss folded by upright open F2 folds. Melt-filled cleavage is subparallel to the axial plane (dashed lines). (d) Subvertical foliation S2 in the felsic orthogneiss. (e) Subvertical eclogite facies foliation S2 and amphibolite facies shear zones in the eclogite. (f) Subvertical foliation S2 in the banded felsic orthogneiss affected by S3 melt-filled shear zone (white dashed line). (g) Shallow-dipping S1 foliation in Stronie metasediments (highlighted by quartz bands) folded by open subvertical F2 folds. (h) S1 foliation in Stronie metasediments folded by close to isoclinal F2 folds leading to transposition into the subvertical S2 foliation. (i) Subvertical S2 foliation in Stronie metasediments affected by recumbent F3 folding.

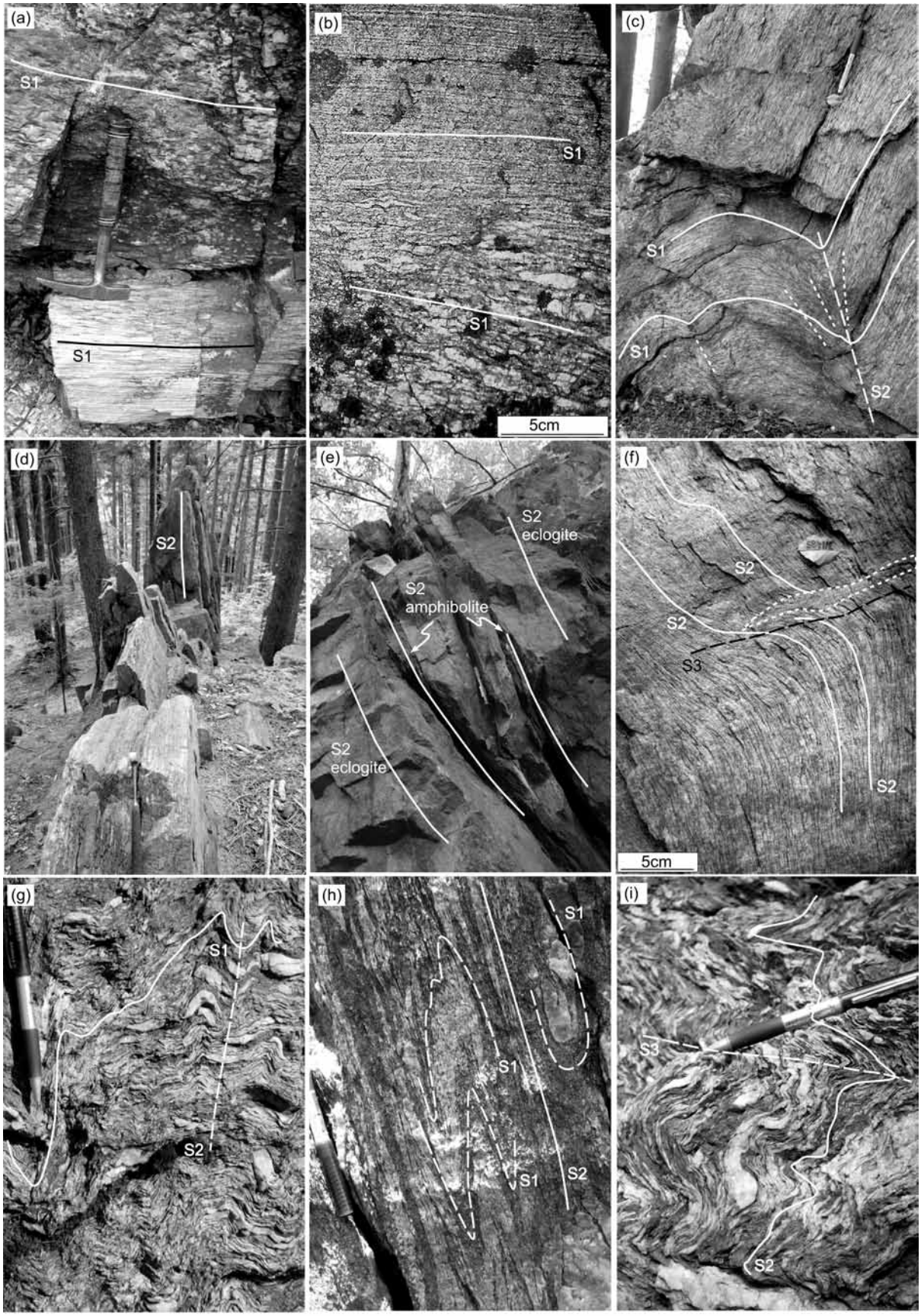
(a)
S1
S1
(b)
S1
S1
5cm
(c)
S1
S1
S2
(d)
S2
(e)
S2
eclogite
S2
amphibolite
S2
eclogite
(f)
S2
S2
S3
S2
5cm
(g)
S1
S2
(h)
S1
S1
S1
S2
(i)
S3
S2

timetres up to several metres wide subvertical N−S trending D2 shear zones. These shear zones show a sharp deformation gradient from the banded or augen felsic orthogneiss to the fine-grained felsic orthogneiss in the core of the shear zone. The S2 foliation in the felsic orthogneiss around the eclogite belt and especially to the west of the eclogite has commonly a migmatitic appearance, which is mostly visible from diffuse boundaries of the individual recrystallized bands and from the presence of quartz and plagioclase within the originally monomineralic K-feldspar layers. The migmatitic character is confirmed by the presence of centimetre-scale zones of fine-grained, macroscopically isotropic granite that occurs within the subvertical S2 cleavage (Fig. III-4c).

The F2 folding and foliation transposition into the S2 fabric is very intense in an about 2–3 km wide belt around the eclogite, leading to mostly vertical orientation of the foliations in the field (Fig. III-4d, e). To the west of the eclogite belt, the folds are open to close and overturned to the west, whereas to the east, the folds are open to close with subvertical axial planes. Further east, where augen felsic orthogneiss with very a weak S1 foliation and prolate deformation dominates, the D2 deformation can be recognized locally as millimetre-scale crenulations of S1 quartz ribbons or feldspar augen. It is suggested that the D2 deformation in this area is globally homogeneous, and leads to an intensification of the linear appearance of the augen orthogneiss. Heterogeneous N−S striking subvertical shear zones marked by the presence of the banded to fine-grained felsic orthogneiss are locally developed.

The eclogite outcrops show generally a steeply-dipping eclogite facies S1 foliation (Fig. III-5e). The subvertical eclogite foliation is crosscut by amphibolite facies fractures and affected by centimetre-scale subvertical garnet-free amphibolite facies S2 zones. Meter- to several-metre-scale bodies of amphibolite with the subvertical S2 foliation occur also around the eclogite belt within the orthogneiss.

In the Stronie metasedimentary belt, F2 folds have steep east-dipping axial planes and N−S trending fold hinges that are variably (25−65°) plunging to the north or to the south. The folds are locally open, but more commonly close to isoclinal (Fig. III-4g,h), ranging from metre-scale folds to millimetre-scale crenulations. In the micaschist, the D2 deformation leads to an almost complete transposition into the S2 foliation that contains rootless F2 folds defined by quartz ribbons or quartz-rich layers (Fig. III-4h).

3. 3. D3 deformation

Open metre- to several-metre-scale recumbent F3 folds with subhorizontal axial planes and N−S trending hinges are locally developed in the areas where the felsic orthogneiss displays an intense subvertical foliation. Shallow-dipping centimetre-scale S3 shear zones, marked by the banded or fine-grained orthogneiss variety are rarely localized in one of the limbs of the F3 folds or are crosscutting the subvertical S2 foliation. In the vicinity of the eclogite and in the area to the west of the eclogite, the D3 shear zones in the felsic orthogneiss are filled by isotro-

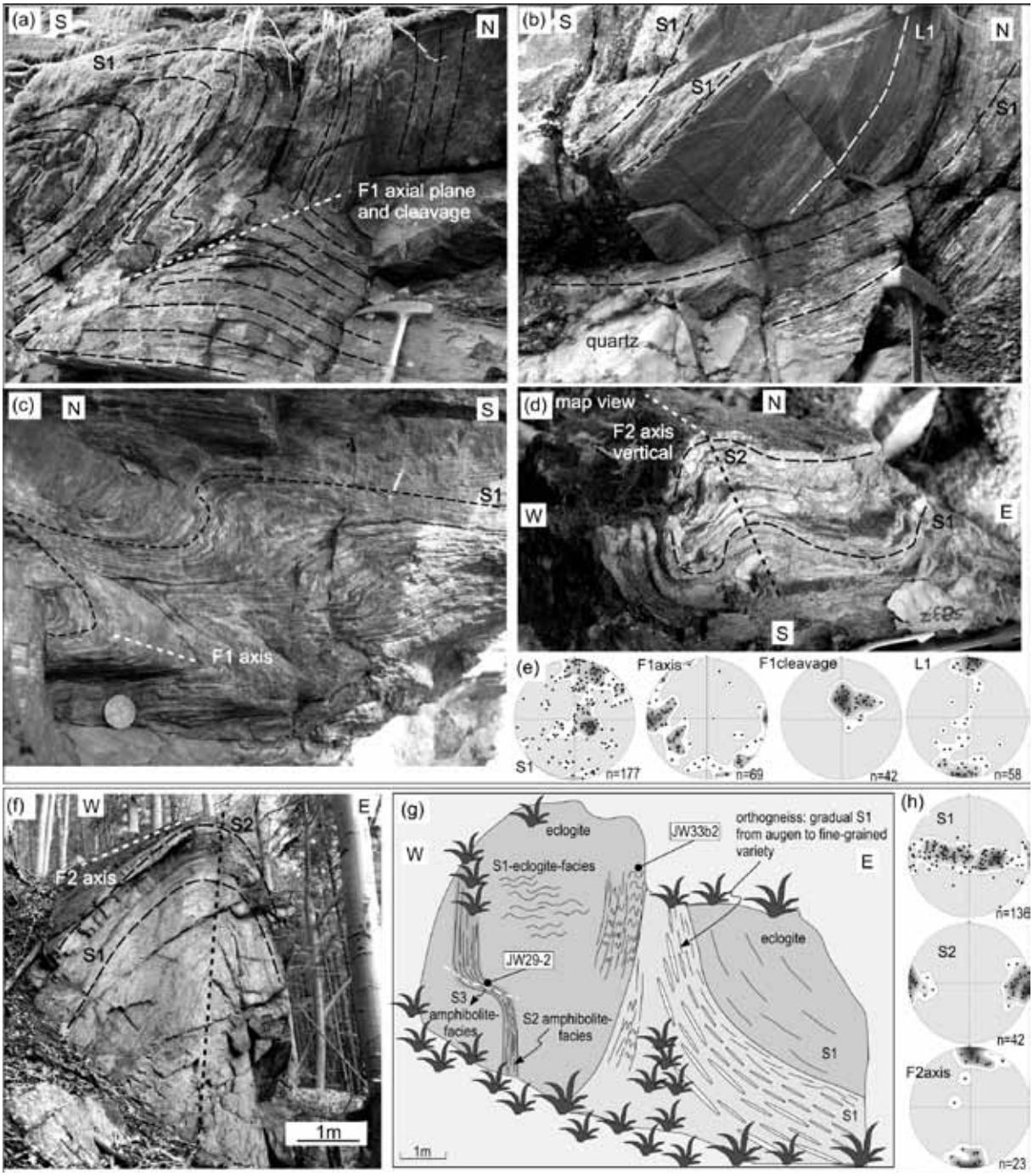

Fig. III-5: Field photographs and a drawing illustrating various structural features of the F1, F2 and F3 folds. (a) F1 fold with variable thickness of the limb and hinge region, shallowly S-dipping axial plane and cleavage and E−W trending subhorizontal axis. Asymmetry marked by long S-dipping limb and short vertical or steeply S-dipping limb indicate N-directed movement. (b) Detail of the F1 fold showing short steeply-dipping limb that bears steepened L1 lineation. Short limb is gashed with the discontinuity filled by quartz. (c) Domain of the S1 foliation with close to isoclinal F1 folds showing E−W trending axis and variable thickness in the hinge and limb regions. (d) Short subvertical limb of the F1 fold is folded by open F2 folds with subvertical N−S trending axial plane. (e) Equal-area, lower-hemisphere stereoplots show D1 planar and linear structures in a domain affected by F1 folds (E of the eclogite). (f) Upright F2 fold with horizontal N−S trending axis affects the banded foliation S1 in the felsic felsic orthogneiss. (g) Field sketch showing relations of D1, D2 and D3 in the eclogite and surrounding felsic orthogneiss and sample position. (h) Equal-area, lower-hemisphere stereoplots show D1 and D2 planar and linear structures in an area strongly affected by F2 folds (around and E of the eclogite).

pic fine-grained granite (Fig. III-4f).

Rare open F3 folds also affect the subvertical foliation in the eclogite and the steep zones of S2 amphibolite facies foliation within the eclogite. The areas of S2 amphibolite facies foliation are rarely affected by localized centimetre-scale shallow-dipping S3 shear zones (eclogite-amphibolite sample JW29-2) (Fig. III-5g).

In the Stronie metasedimentary belt, rare open to close F3 folds with subhorizontal axial planes and N−S trending subhorizontal hinges occur (Fig. III-4i). This weak folding produces crenulations on the S2 planes defining a subhorizontal L3 lineation.

4. PETROLOGY

In order to assign P−T conditions to the observed structures, oriented eclogite and metapelite samples with the S1, S2 and S3 foliations were studied.

4. 1. Analytical procedures and abbreviations

Whole-rock analyses were preformed in the Acme laboratories, Canada. Mineral analyses were performed on a scanning electron microscope VEGA\\XMU at the Strasbourg University in point beam mode at 15 kV and 10 nA.

Petrography is documented in Figs III-6 & III-7, representative mineral analyses are summarized in Tables III-1−3, and mineral chemistry is shown in Fig 8. The sign «=>» is used for a trend in mineral composition or for zoning and the sign «–» for a range of mineral compositions; p.f.u. = per formula unit. For amphibole, the variables and isopleths notations are used as in Dale *et al.* (2005) and Diener *et al.* (2007) in order to compare the chemical variability of amphibole with isopleths in pseudosections.

Mineral abbreviations: g=garnet, cpx=diopsidic clinopyroxene, o=omphacitic clinopyroxene, am=amphibole, hb=hornblende, act=actinolite, gl=glaucophane, ep=epidote, chl=chlorite, mu=muscovite, pl=plagioclase, q=quartz, ilm=ilmenite, ru=rutile, sph=sphene, mt=magnetite, bi=biotite, pa=paragonite, ky=kyanite, sill=sillimanite, and=andalusite, cd=cordierite, st=staurolite, ksp=K-feldspar; garnet: alm=Fe/(Ca + Fe + Mg + Mn), prp=Mg/(Ca + Fe + Mg + Mn), grs=Ca/(Ca + Fe + Mg + Mn), sps=Mn/(Ca + Fe + Mg + Mn), XFe=Fe/(Fe + Mg); plagioclase: an=Ca/(Ca + Na + K), ab=Na/(Ca + Na + K); clinopyroxene: jd=Na/(Na + Ca); amphibole: Z=xNa(M4)=Na(M4)/2, Y=xAl(M2)=AlVI/2, A=xNa(A)=Na(A), C=xCa(M4)=Ca/2.

The isopleth notation used in the NCKFMASHTO system is: *x*(g, cpx)=Fe/(Fe+Mg), *z*(g)=Ca/(Ca+Fe+Mg)*100, *j*(cpx)=Na/(Na+Ca)*100, *z*(am)=xNa(M4)=Na(M4)/2*100, *y*(am)=xAl(M2)=AlVI/2*100, *a*(am)=xNa(A)=Na(A)*100, Na(mu)=Na/(Na+K), y(mu)=4-Al^{IV}. The isopleth notation used in the MnNCKFMASHTO system is: x(g)=Fe/(Ca+Fe+Mg+Mn)*100, z(g)=Ca/(Ca+Fe+Mg+Mn)*100, m(g)=Mn/(Ca+Fe+Mg+Mn)*100,

x(st)=Fe/(Fe+Mg)*100.

4. 2. Eclogite and amphibolitized eclogite

The major eclogite type in the area of Międzygórze is composed of garnet (30−50 vol.%), omphacite (40−50 vol.%), epidote (0−8 vol.%), accessory muscovite, rutile, kyanite and quartz.

The shallow-dipping foliation S1 is defined by garnet-rich and omphacite-rich layers, elongated quartz ribbons, chains of rutile grains and by omphacite and muscovite preferred orientation (Fig. III-6a, sample JW33b2). Some epidote commonly occurs in the matrix. The S1 foliation is folded by open millimetre-scale upright crenulation folds (Fig. III-6a, sample JW33b2).

The dominant vertical foliation S2 in the eclogite is defined by the same features as the S1 foliation (Fig. III-6b). The vertical amphibolite facies zones D2 are composed of preferentially oriented amphibole, biotite and elongated aggregates of sphene surrounding ilmenite, with rutile locally preserved in the central area (Fig. III-6c). Plagioclase is scattered in the matrix or forms plagioclase-rich layers. Brittle cracks affecting the eclogite are filled with amphibole, plagioclase, biotite and ilmenite, indicating amphibolite facies conditions (Fig. III-6b).

The rare shallow-dipping shear-zones S3 affecting the vertical amphibolite facies foliation S2 are composed of oriented amphibole, biotite, chains of sphene aggregates located around ilmenite and rutile, and of feldspar-rich bands (Fig. III-6d). Aggregates rich in chlorite and K-feldspar with some magnetite or chlorite replacing biotite occur locally within the S3 foliation.

Eclogite sample JW33b2

The mineral assemblage is formed by garnet (40%), omphacite (45%), epidote (3%), accessory muscovite, rutile, quartz and kyanite (Figs III-6a, e−h). All minerals occur within the shallow-dipping foliation S1 (Figs III-5g & III-6a). Epidote is randomly distributed within the matrix, with areas that are richer, and areas that are almost free of epidote (Figs III-6e−g). Kyanite is commonly surrounded by garnet but contacts with matrix minerals also occur (Fig. III-6h).

The grossular content of zoned garnet in the matrix increases from around 26 mol.% in the core ($alm_{0.35}py_{0.37}grs_{0.26}sps_{0.01}$, XFe=0.47), to 29 mol.% ($alm_{0.34}py_{0.36}grs_{0.29}sps_{0.01}$, XFe=0.49) and decreases to 25−22 mol.% at the rim ($alm_{0.37}py_{0.39}grs_{0.23}sps_{0.01}$, XFe=0.48) (Fig. III-8a). The zoning is asymmetric in garnet that occurs around kyanite, with core region next to kyanite and rim next to the matrix (Fig. III-8b). The majority of garnet lacks the low grossular core, and has a flat profile with a composition that corresponds to the grossular peak ($alm_{0.34-36}py_{0.36-37}grs_{0.28-29}sps_{0.01}$, XFe=0.47−49) and lower grossular rims (Fig. III-8c). Muscovite has Si=3.26−3.31 p.f.u. and Na=0.05−0.12 p.f.u. Clinopyroxene is omphacite with 33−36 mol.% of jadeite, up to 3 mol.% of Ca-tschermak component, and XFe=0.12−0.16. Epidote has Fe^{3+} content between 0.05−0.10 p.f.u.

Amphibolitized eclogite JW29-2

Amphibolitized eclogite sample JW29-2 was collected on the same outcrop as the eclogite sample JW33b2. It is located within the steeply-dipping amphibolite facies shear zone S2 that affects the eclogite, and that is further folded by open F3 folds. The sample is taken from an attenuated limb of the F3 fold (Fig. III-5g). It contains amphibole, biotite, plagioclase, sphene, ilmenite, rutile, chlorite, K-feldspar and magnetite. Amphibole is elongated parallel to the S2 foliation and is associated with aggregates of preferentially oriented biotite. Plagioclase grains are disseminated in plagioclase-rich layers, and occasionally are associated with K-feldspar. Sphene is commonly arranged in chains parallel to the foliation, it occurs in form of elongated aggregates that surround ilmenite, which have in places rutile in the core. Aggregates with chlorite associated with K-feldspar and magnetite, and chlorite replacing biotite occur locally. Samples taken next to JW29-2 in the amphibolite facies S2 foliation that is not affected by the F3 folding are composed of amphibole, plagioclase, biotite and elongated sphene and ilmenite surrounding rutile, preferentially arranged in the S2 foliation.

Amphibole composition in the sample JW29-2 vary between tschermakitic hornblende and hornblende (Na(M4)=0.12−0.26, Al^{IV}=0.9−1.7, XFe=0.25−0.36, Y=Al^{VI}/2=0.45−0.79, Z=Na(M_4)/2=0.06−0.13, C=Ca/2=0.85−0.92, A=Na(A)=0.04−0.15) (Fig. III-8). Biotite chemistry shows XFe=0.43−0.46 and Ti=1.64−2.23 p.f.u. The anorthite content of plagioclase varies generally between 30 mol.% and 50 mol.%. However, plagioclase with lower anorthite content (up to an=0) is locally associated with chlorite.

4. 3. Metapelites

The S1 metamorphic layering is preserved rarely in the form of close to isoclinally folded alternation of quartz- and muscovite-rich bands (Fig. III-7a). Discontinuous layers rich in garnet and staurolite following the S1 foliation are commonly observed (Fig. III-7a). Garnet (1−2 mm) and staurolite (up to 1 mm) show inclusion trails parallel to the S1 foliation and containing quartz and ilmenite, with some minute crystals of staurolite in garnet. In places, larger staurolite grains are included at the outer rim of garnet porphyroblasts that show S1 inclusion trails oblique to the S2 cleavage (Fig. III-7b). Biotite parallel to the S1 foliation is scarce.

The S2 fabric ranges from a weak spaced cleavage to a continuous metamorphic schis-

Fig. III-6: Photomicrographs (plane-polarized light and BSE) of eclogite and amphibolitized eclogite showing relation of structure and mineral assemblage (a−d) and textural details of the eclogite sample JW33b2 (e−h). (a) S1 shallow-dipping foliation folded by F2 open folds. S1 defined by alternation of garnet- and clinopyroxene-rich bands. Black arrow indicates the profile in Fig. 8. (b) Subvertical S2 foliation marked by alternation of garnet- and clinopyroxene-rich bands affected by amphibolite facies fractures. (c) Subvertical S2 foliation defined by preferred orientation of amphibole, biotite, and elongated aggregates of ilmenite surrounded by sphene. (d) Attenuated limb of the F3 fold (see Fig. 5g) indicates activity of the D3 deformation, with S3 foliation marked mainly by oriented amphibole, biotite and chains of elongated aggregates of sphene. (e) Detail of matrix formed by g-cpx-ep-ru-q. (f) Clinopyroxene and muscovite oriented parallel to shallow-dipping S1 foliation. (g) Detail of epidote having net boundaries with respect to garnet, pyroxene and rutile. (h) Kyanite surrounded by coronas of garnet. Black arrow indicates profile in Fig. III-8b.

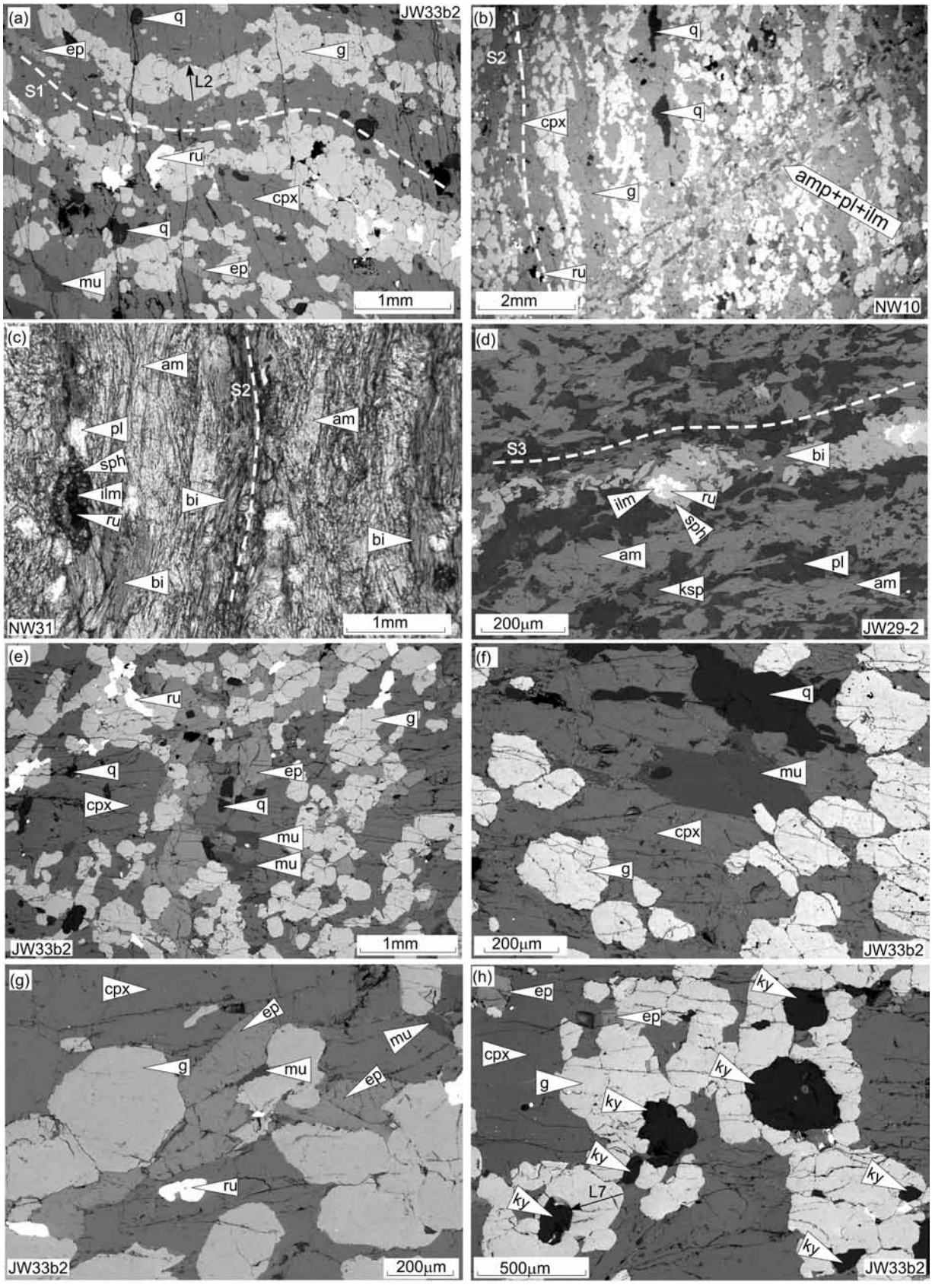
(a)
JW33b2
q
ep
g
S1
L2
ru
cpx
q
mu
ep
1mm
(b)
S2
q
q
cpx
g
amp+pl+ilm
ru
2mm
NW10
(c)
am
S2
pl
am
sph
ilm
bi
ru
bi
bi
NW31
1mm
(d)
S3
bi
ilm
ru
sph
am
pl
ksp
am
200µm
JW29-2
(e)
ru
g
q
ep
cpx
q
mu
mu
JW33b2
1mm
(f)
q
mu
cpx
g
200µm
JW33b2
(g)
cpx
ep
mu
g
mu
ep
ru
JW33b2
200µm
(h)
ep
ky
ep
cpx
ky
g
ky
ky
ky
L7
ky
ky
ky
500µm
JW33b2

Table III-1: Representative mineral analyses: eclogite JW33b2.

sample	JW33b2	JW33b2	JW33b2	JW33b2	JW33b2	JW33b2	JW33b2
mineral	g	g	g	cpx	mu	am	ep
position	core	peak	rim	mx	mx	in g	mx
analysis	A157-L2	A155-L2	A108-L1	16	A277-L4	32	12
SiO_2	39.95	40.15	39.79	55.05	50.03	43.29	39.41
TiO_2	0.12	0.26	0.14	0.20	1.10	0.26	0.08
Al_2O_3	22.93	23.01	22.58	10.82	29.14	18.05	33.29
FeO	17.03	16.32	17.87	3.18	1.34	7.31	1.63
MnO	0.48	0.40	0.44	0.16	0.10	0.07	0.12
MgO	10.15	9.69	10.42	10.10	3.61	13.51	0.23
CaO	9.92	10.41	8.59	15.42	0.05	10.23	23.38
Na_2O	0.00	0.00	0.04	5.02	0.57	3.00	0.07
K_2O	0.14	0.03	0.10	0.02	10.22	0.48	0.03
Total	100.72	100.27	99.97	99.97	96.16	96.20	98.24
Si	2.97	3.00	2.98	1.96	3.30	6.18	2.98
Ti	0.01	0.01	0.01	0.01	0.05	0.03	0.00
Al	2.01	2.03	1.99	0.46	2.27	3.04	2.97
Fe^{3+}	0.05	0.00	0.04	0.00	0.00	0.50	0.07
Fe^{2+}	1.00	1.02	1.08	0.09	0.07	0.37	0.03
Mn	0.03	0.03	0.03	0.00	0.01	0.01	0.01
Mg	1.12	1.08	1.16	0.54	0.36	2.87	0.03
Ca	0.79	0.83	0.69	0.59	0.00	1.56	1.90
Na	0.00	0.00	0.01	0.35	0.07	0.83	0.01
K	0.01	0.00	0.01	0.00	0.86	0.09	0.00
Total	8.00	8.00	8.00	4.00	7.00	15.48	8.00
XFe	0.47	0.49	0.48	0.15	0.17	0.11	
alm/an/jd/Y	0.35	0.34	0.37	0.35		0.91	
py/ab/Z	0.37	0.36	0.39			0.22	
grs/or/A	0.26	0.28	0.23			0.39	
sps/C	0.01	0.01	0.01			0.78	
Al^{IV}						1.82	

tosity (Fig. III-7b). Biotite (0.5 mm) shows preferential orientation parallel to the S2 axial plane cleavage and is more abundant than in the S1 fabric. Garnet with straight to weakly crenulated inclusion trails of the S1 fabric is overgrown by garnet with ilmenite inclusions continuous with the external S2 foliation (Fig. III-7c, e). Staurolite porphyroblasts with S1 inclusion trails are in places overgrown by rims with ilmenite inclusions parallel to the matrix S2 foliation (Fig. III-7d). Some samples exhibit widespread chlorite parallel to the S2 fabric (Fig. III-7e). Some chlorite aggregates show sharp contact with garnet rims, but clearly replace staurolite (Fig. III-7d, e). Chlorite occurs also in the axial plane of the F3 microfolds (areas highlighted in Fig. III-7f).

Metapelite sample ES95DI

Sample ES95DI was collected in the hinge of a F2 fold to study the relationship between

Table III-2: Representative mineral analyses: amphibolitized eclogite JW29-2.

sample	JW29-2	JW29-2	JW29-2	JW29-2	JW29-2	JW29-2	JW29-2	JW29-2	JW29-2
mineral	am	am	bi	pl	ksp	ab	chl	ilm	sph
position	mx	mx	mx	mx	mx	mx	mx	mx	mx
analysis	51	67	46	52	34	35	65	59	58
SiO_2	43.64	49.39	36.63	61.71	64.46	67.23	42.87	0.16	30.51
TiO_2	0.62	0.43	2.20	0.06	0.00	0.06	0.00	55.30	39.40
Al_2O_3	14.51	7.79	16.75	24.73	19.09	20.10	10.42	0.15	1.23
FeO	13.63	12.33	18.29	0.41	0.25	0.33	9.96	41.51	0.54
MnO	0.31	0.33	0.15	0.09	0.00	0.00	0.00	3.40	0.24
MgO	10.48	14.28	12.18	0.18	0.24	0.00	21.78	0.28	0.05
CaO	11.45	12.15	0.00	4.95	0.00	0.39	0.44	0.27	27.83
Na_2O	1.20	0.67	0.12	8.15	0.18	10.59	0.77	0.04	0.08
K_2O	0.64	0.40	9.09	0.16	16.35	0.09	0.29	0.06	0.12
Total	96.48	97.77	95.41	100.44	100.57	98.79	86.53	101.17	100.00
Si	6.41	7.07	2.83	2.73	2.96	2.99	8.72	0.00	0.99
Ti	0.07	0.05	0.13	0.00	0.00	0.00	0.00	1.03	0.96
Al	2.51	1.32	1.53	1.29	1.03	1.05	2.50	0.00	0.05
Fe^{3+}	0.46	0.46	0.00	0.00	0.01	0.00	0.00	0.00	0.01
Fe^{2+}	1.21	1.02	1.18	0.02	0.00	0.01	1.69	0.86	0.00
Mn	0.04	0.04	0.01	0.00	0.00	0.00	0.00	0.07	0.01
Mg	2.29	3.05	1.40	0.01	0.02	0.00	6.61	0.01	0.00
Ca	1.80	1.86	0.00	0.23	0.00	0.02	0.10	0.01	0.97
Na	0.34	0.19	0.02	0.70	0.02	0.91	0.30	0.00	0.01
K	0.12	0.07	0.90	0.01	0.96	0.01	0.08	0.00	0.00
Total	15.26	15.12	8.00	5.00	5.00	5.00	20.00	2.00	3.00
XFe	0.35	0.25	0.46				0.20		
alm/an/jd/Y	0.79	0.46		0.25	0.00	0.02			
py/ab/Z	0.10	0.07		0.74	0.02	0.97			
grs/or/A	0.14	0.05		0.01	0.98	0.01			
sps/C	0.90	0.93							
Al^{IV}	1.59	0.93							

crystallization and deformation and to assign P−T conditions to the individual deformational phases. The sample contains garnet, staurolite, biotite, muscovite, quartz, few plagioclase and accessory ilmenite, tourmaline, chlorite and apatite. The matrix displays microfolded quartz- and muscovite-rich S1 bands and S2 cleavage that is marked mostly by oriented biotite. Garnet porphyroblasts (2−4 mm) host inclusions of quartz, ilmenite, tourmaline, rare muscovite and plagioclase, which are commonly oriented at high angle to the axial plane of the F2 microfolds (similarly as in Fig. III-7a). A small curvature continuous with the external S2 foliation locally occurs at the rim. It is interpreted as garnet growth during or after the formation of the shallow-dipping S1 foliation with some garnet rims formed within the subvertical S2 fabric.

Garnet shows zoning with decreasing spessartine, grossular and XFe, and increasing

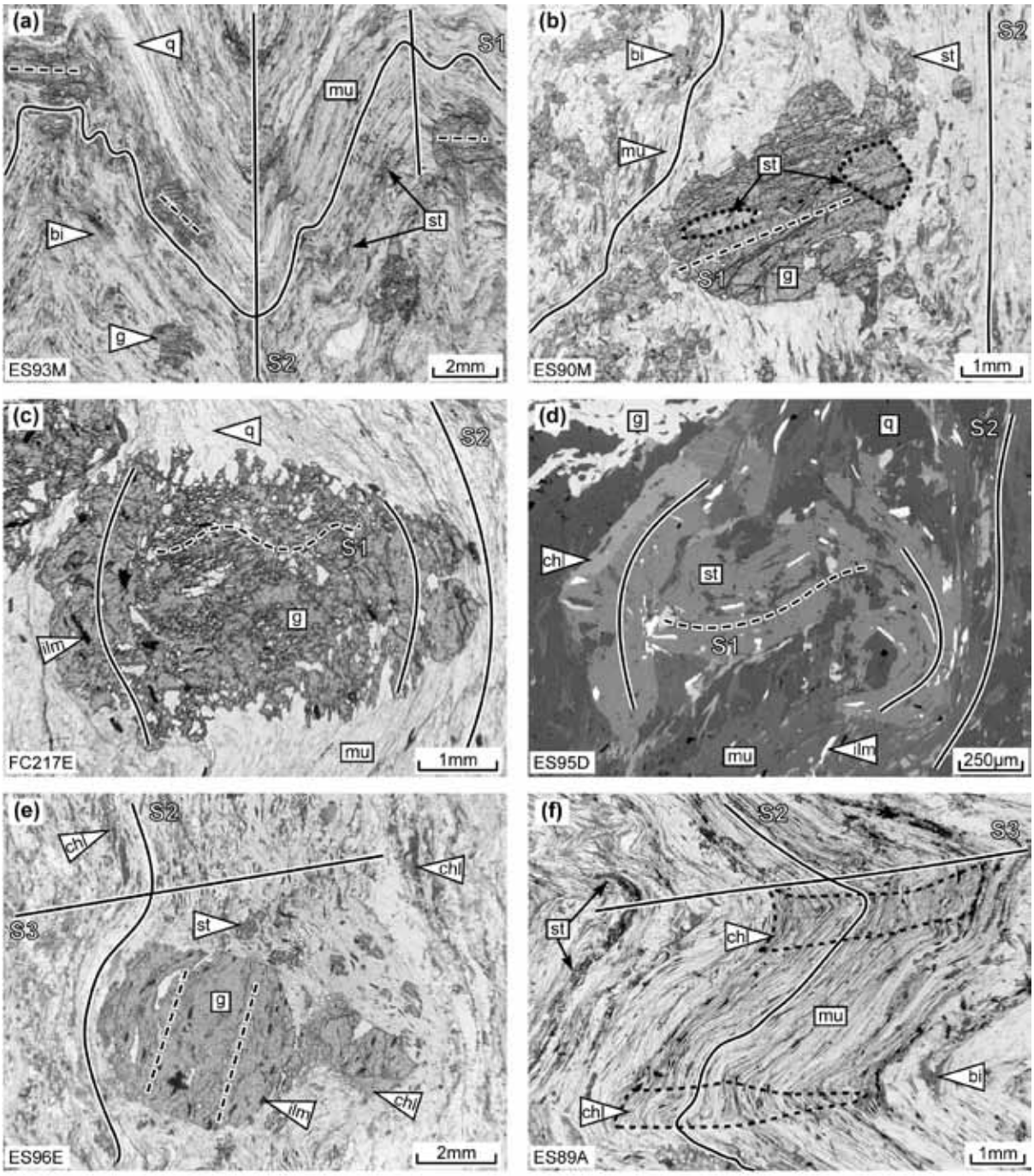

Fig. III-7: Photomicrographs (plane-polarized light and BSE) of crystallization-deformation relationships in micaschists. (a) S1 foliation containing muscovite, quartz, biotite, garnet, and staurolite affected by F2 folds. (b) Garnet with staurolite inclusions (highlighted by dashed lines) and straight inclusion trails oriented oblique to the surrounding S2 foliation. (c) Garnet with quartz inclusion trails in the core marking crenulated S1 foliation and ilmenite inclusions at the rim, continuous with external S2 foliation. (d) Staurolite with quartz and ilmenite oriented at high angle to external S2 foliation in the core and subparallel at the rim. (e) Chlorite grows parallel to S2 foliation and rarely surrounds staurolite and garnet. (f) Domains rich in chlorite (highlighted by dashed lines) located in axial planes of F3 folds.

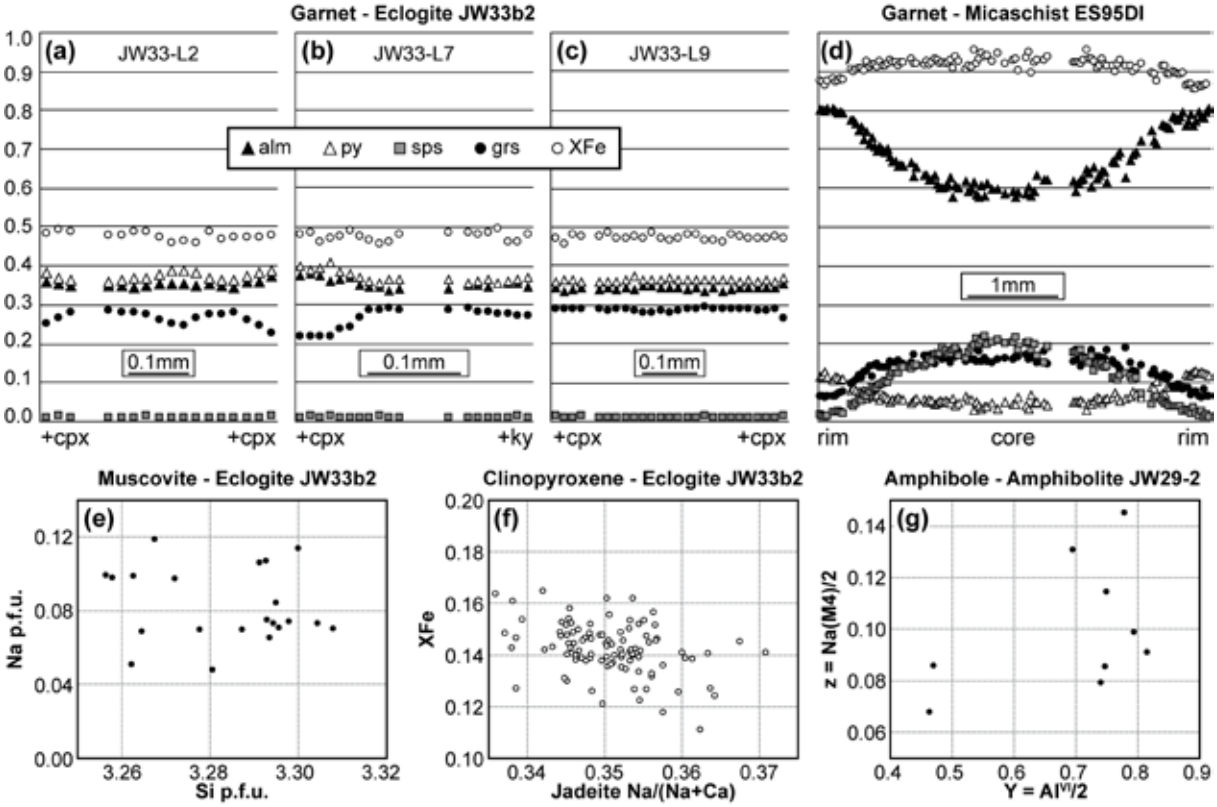

Fig. III-8: Diagrams illustrating mineral chemistry in the eclogite, in the amphibolitized eclogite and in the micaschist. For details see text.

pyrope and almandine from core to rim ($alm_{0.60=>0.75}$ $py_{0.04=>0.15}$ $grs_{0.17=>0.08}$ $sps_{0.19=>0.02}$, XFe=0.94 => 0.83) (Fig. III-8d & Table III-3). Small staurolite crystals are also partly enclosed by garnet rims. Staurolite (up to 1mm) is abundant in the matrix and includes quartz, ilmenite and tourmaline that are oriented at high angle to the external S2 fabric in the core and parallel to the S2 fabric at the rim (Fig. III-7d). This is interpreted as syn- or post-D1 staurolite growth followed by continuous growth during development of the subvertical S2 cleavage. Staurolite is not regularly zoned and its XFe varies between 0.82 and 0.86, Zn=0.07−0.14 p.f.u. and Ti=0.10−0.15 p.f.u. (Table III-3). Rare plagioclase has an=0.15−0.19, biotite has XFe=0.53−0.55 and Ti=0.07−0.10 p.f.u. Chlorite (XFe=0.56−0.60) is found mostly around garnet and staurolite.

Table III-3: Representative mineral analyses: metapelite ES95DI.

TiO_2	0.15	0.55	0.56	0.73	1.73	0.27	0.26	0.00
Al_2O_3	21.08	22.40	54.30	54.58	20.06	22.60	37.68	23.08
FeO	26.61	33.73	12.19	12.64	19.03	28.76	0.91	0.11
MnO	8.11	1.07	0.21	0.25	0.00	0.10	0.00	0.00
MgO	0.83	2.65	1.48	1.27	9.56	11.59	0.51	0.08
CaO	5.74	2.31	0.10	0.08	0.07	0.14	0.00	3.29
Na_2O	0.00	0.08	0.33	0.26	0.40	0.00	2.45	8.89
K_2O	0.00	0.16	0.00	0.00	8.61	0.03	7.33	0.00
ZnO	n.a.	n.a.	0.57	0.37	n.a.	n.a.	n.a.	n.a.
Total	98.92	99.93	97.71	97.72	95.97	86.73	93.97	99.49
Si	2.98	2.97	7.91	7.74	2.82	5.07	2.99	2.85
Ti	0.01	0.03	0.12	0.15	0.10	0.04	0.01	0.00
Al	2.03	2.12	18.09	18.03	1.83	5.81	2.96	1.21
Fe^{3+}	0.00	0.00	0.00	0.00	0.00	0.00	0.00	0.00
Fe^{2+}	1.82	2.26	2.88	3.12	1.23	5.25	0.05	0.00
Mn	0.56	0.07	0.05	0.08	0.00	0.02	0.00	0.00
Mg	0.10	0.32	0.62	0.58	1.10	3.77	0.05	0.01
Ca	0.50	0.20	0.03	0.02	0.01	0.03	0.00	0.16
Na	0.00	0.01	0.18	0.15	0.06	0.00	0.32	0.77
K	0.00	0.02	0.00	0.00	0.85	0.01	0.62	0.00
Zn	-	-	0.12	0.14	-	-	-	-
Total	8.00	8.00	30.00	30.00	8.00	20.00	7.00	5.00
X_{Fe}	0.95	0.88	0.82	0.84	0.53	0.58		
alm/an	0.61	0.79						0.83
prp/ab	0.03	0.11						0.17
grs/or	0.17	0.07						0.00
sps	0.19	0.03						

n.a. = not analyzed

5. MINERAL EQUILIBRIA MODELLING

5. 1. Calculation methods

Pseudosections were calculated using THERMOCALC 3.3 (Powell *et al.*, 1998, 2009 version) and the dataset 5.5 (Holland & Powell, 1998, November 2003 upgrade). The pseudosection for metabasic rocks (Fig. III-9) is calculated in the model system Na_2O-CaO-K_2O-FeO-MgO-Al_2O_3-SiO_2-H_2O-TiO_2-O (NCKFMASHTO) with the amphibole model from Diener *et al.* (2007), clinopyroxene from Green *et al.* (2007), garnet from White *et al.* (2007) modified by Diener *et al.* (2008), feldspar from Holland & Powell (2003), paragonite-muscovite from Coggon & Holland (2002), chlorite from Holland *et al.* (1998), epidote from Holland & Powell (1998), ilmenite from White *et al.* (2000). The pseudosection for metapelite is calculated in the model system MnO-Na_2O-CaO-K_2O-FeO-MgO-Al_2O_3-SiO_2-H_2O-TiO_2-O (MnNCKFMASHTO) (Fig. III-12). The activity-composition relationships for feldspars are from Holland & Powell (2003), white mica from Coggon & Holland (2002), silicate melt from White *et al.* (2007), epidote from Holland & Powell (1998), Mn-bearing models of staurolite, cordierite and chlorite from Mahar *et al.* (1997), Holland *et al.* (1998) and Holland & Powell (1998), and models of garnet, biotite and ilmenite as in White *et al.* (2005).

5. 2. Pseudosection for eclogite and amphibolitized eclogite

The H2O-saturated pseudosection (Figs III-9, III-10 & III-11) is calculated for the analyzed whole-rock composition of the sample JW29-2 that is an amphibolitized eclogite described above (in wt%: SiO_2=48.40, Al_2O_3=16.33, FeO=8.35, Fe_2O_3=0.90, MnO=0.16, MgO=9.53, CaO=11.28, Na_2O=2.54, K_2O=0.41, TiO_2=0.72, P_2O_5=0.01). This whole-rock composition is used also for discussion of the P−T evolution of the studied eclogite sample JW33b2 with preserved S1 foliation, due to difficulty to sample this part of the outcrop, and for discussion of the P−T evolution of the sample taken next to JW29-2 from the S2 foliation that is not affected by the F3 folding. Because the rock composition does not come from the same sample as the described thin sections of the eclogite and the amphibolite with the S2 foliation, the results should be taken only as a guide in determination of approximate P–T conditions, but should be able to allow discussion of the overall shape of the P–T path and of the relation of the P−T conditions to structural evolution. The pseudosection shows fields of mineral assemblages stable at eclogite and amphibolite facies conditions. The high-pressure and low-pressure parts of the pseudosection are contoured with the calculated compositional isopleths for muscovite, clinopyroxene, garnet, and amphibole (Figs III-10 & III-11) in order to discuss the high-pressure P−T evolution and the retrogression of the eclogite.

P−T evolution of the eclogite sample JW33b2

The minerals observed in the S1 foliation are garnet, omphacite, epidote, muscovite, quartz, rutile and kyanite. This assemblage is not stable in the pseudosection. The stability of epidote with kyanite is restricted to a very narrow field labeled 1, located between ~ 17 and 22 kbar. The calculated proportion of amphibole is between 20 and 40 mol.% in this field, which does not correlate with the absence of amphibole in the sample. The observed mineral compositions for garnet rim ($alm_{0.37}py_{0.39}grs_{0.22}sps_{0.01}$, XFe=0.47−0.49), muscovite (Si=3.26−3.31 p.f.u., Na=0.05−0.12 p.f.u.) and omphacite (jd=0.33−0.36, XFe=0.12−0.16) fit well to calculated compositional isopleths in the g−o−mu−ru−ky field that occurs in the high-pressure and high-temperature part of the diagram (Fig. III-10a−f). Therefore, it is considered that some epidote persists metastably to higher pressure than predicted by the pseudosection, up to the amphibole-free field, and that peak conditions for the eclogite S1 foliation correspond to ~ 20−23 kbar and 700−750 °C (black circle labelled S1 in Fig. III-10a−d).

Part of the prograde path may be discussed based on the garnet zoning and on the textural relation with respect to kyanite. Garnet that nucleated on kyanite has 26 mol.% of grossular at the boundary with kyanite, then grossular increases to 29 mol.% and again decreases to 22 mol.% at the rim. Such type of garnet zoning occurs in the pseudosection along a path that begins at the ky-in line and ends at the estimated peak P−T conditions, as indicated by the arrow in Figure 10d. Because this garnet is arranged in the garnet-rich bands parallel to the S1 foliation, this part of the prograde path from ~ 19.5 kbar and 640 °C to ~ 20−23 kbar and 700−750 °C is interpreted to occur during the development of the S1 fabric (black circles labelled S1 and

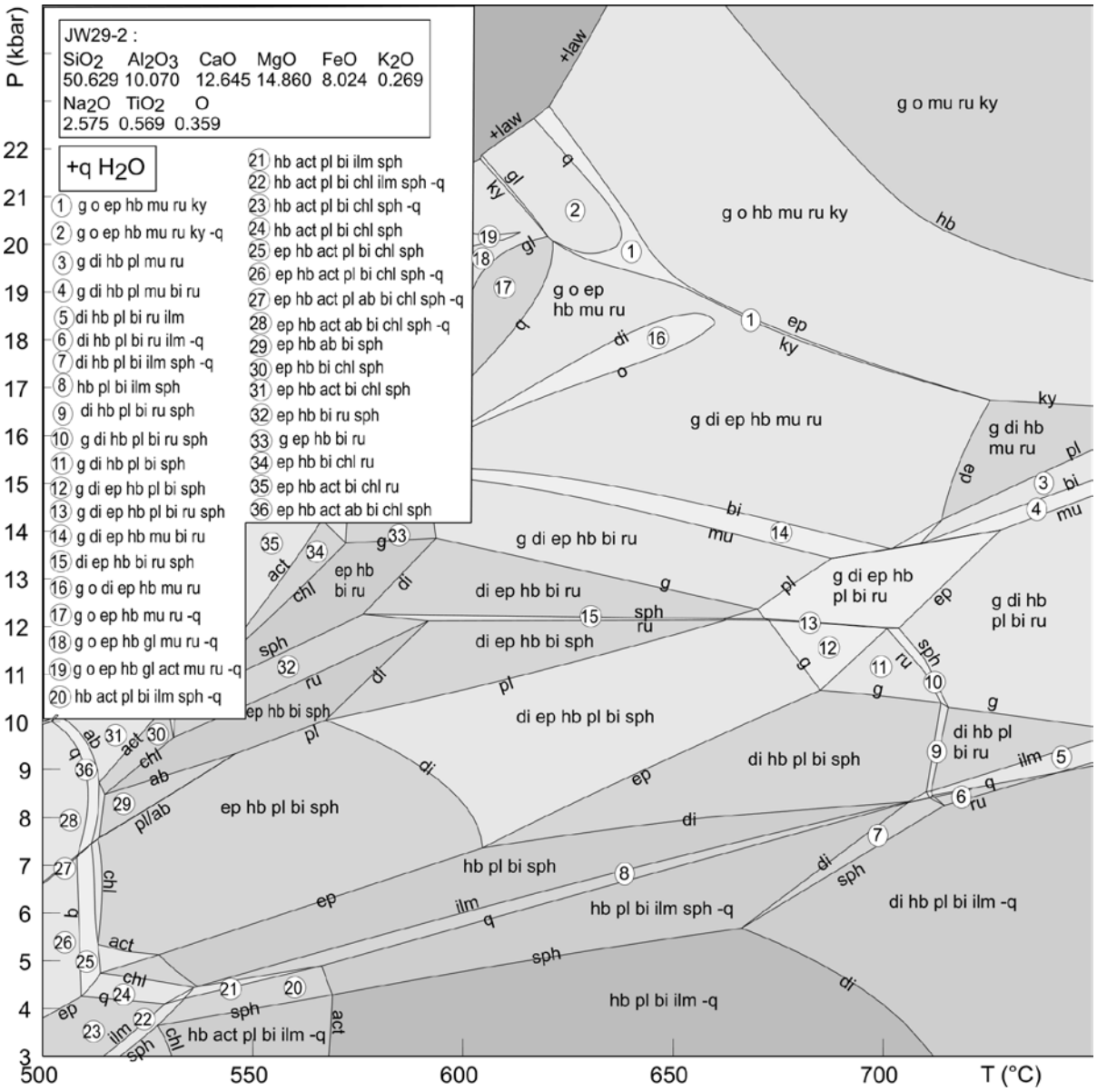

Fig. III-9: Pseudosection calculated for the rock composition of the amphibolitized eclogite sample JW29-2 (NCKFMASHTO system, whole-rock composition in moles adjusted to 100%). P−T range is chosen to discuss the high-pressure evolution and retrogression detailed in Figs III- 10 & III-11. Abbreviations on field boundaries indicate the phase that is gained or lost on this transition.

the arrow in Fig. III-10a−d).

P−T evolution of the amphibolitized eclogite sample JW29-2

The sample comprises amphibole, biotite, plagioclase, sphene, ilmenite, rutile, chlorite, K-feldspar and magnetite, quartz is absent. These minerals and the measured range of mineral compositions suggest a P−T path dominated by decompression under amphibolite and greenschist facies conditions. Absence of epidote indicates a path outside the stability of epidote, absence of muscovite and appearance of biotite indicate crossing the muscovite-out and biotite-in lines between ~ 700−750 °C and below 14−15 kbar. The overgrowth of sphene around ilmenite and rutile in the core indicates first nucleation of ilmenite on rutile and subsequent growth of sphene around ilmenite. Such succession occurs in the pseudosection along a path at tempera-

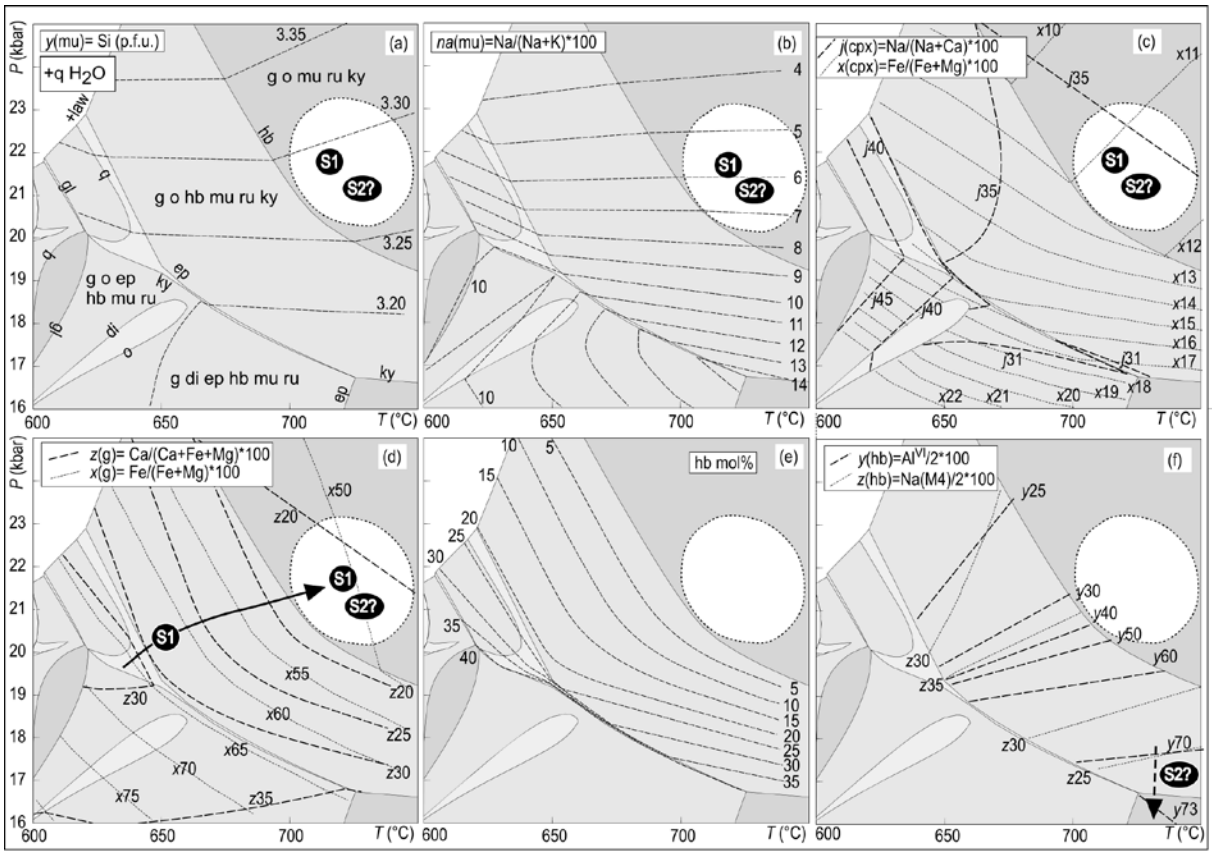

Fig. III-10: (a−f) Enlarged and simplified high-pressure part of the pseudosection from Fig. III-9. Pseudosections are contoured with calculated isopleths of mineral composition and molar proportions. Arrows and black circles indicate parts of P–T path and conditions of equilibration for individual structures, derived by comparing the modeled assemblages and isopleths with observed assemblages, chemistry and zoning of minerals. See text for details.

ture above ~ 720 °C, where the ilmenite-in line is crossed at about 9 kbar and sphene-in line is crossed during subsequent decrease of temperature at ~ 5−8 kbar and 660−710 °C (arrow in Fig. III-11). The amphibole composition corresponding to tschermakitic hornblende and hornblende (XFe=25−36, Y=Al^{VI}/2=0.45−0.79, Z=Na(M4)/2=0.06−0.13) is in agreement with the calculated isopleths along the decompression path from about ~ 16 kbar and 700−750 °C (black circle labelled S2 and arrow in Fig. III-10f) to the field hb−pl−bi−ilm−sph without quartz at ~ 4−7 kbar and 570−700 °C (Fig. III-11b). The wide range of plagioclase compositions (from an=30 mol.% to an=50 mol.%) is in agreement with the modelled isopleths along the same decompression path (Fig. 11c). Plagioclase with lower anorthite content is locally associated with chlorite. XFe of biotite and amphibole closely fit the isopleths in the hb−pl−bi−ilm−sph field without quartz (Fig. 11c). Chlorite replacing biotite, aggregates of chlorite, K-feldspar and magnetite (not shown) together with the local presence of albite are interpreted as inhomogeneous greenschist facies retrogression at lower temperature then the P−T range of the pseudosection.

The inferred P−T path is also related to the structure development (black circles labelled S2 and S3 in Fig. III-11). Tschermakitic hornblende and plagioclase with an=30−50 mol.% are interpreted as phases that may be associated with the development of the subvertical amphibole-bearing fabric S2 associated with the decompression from 16 kbar to ~ 7 kbar at 700−750

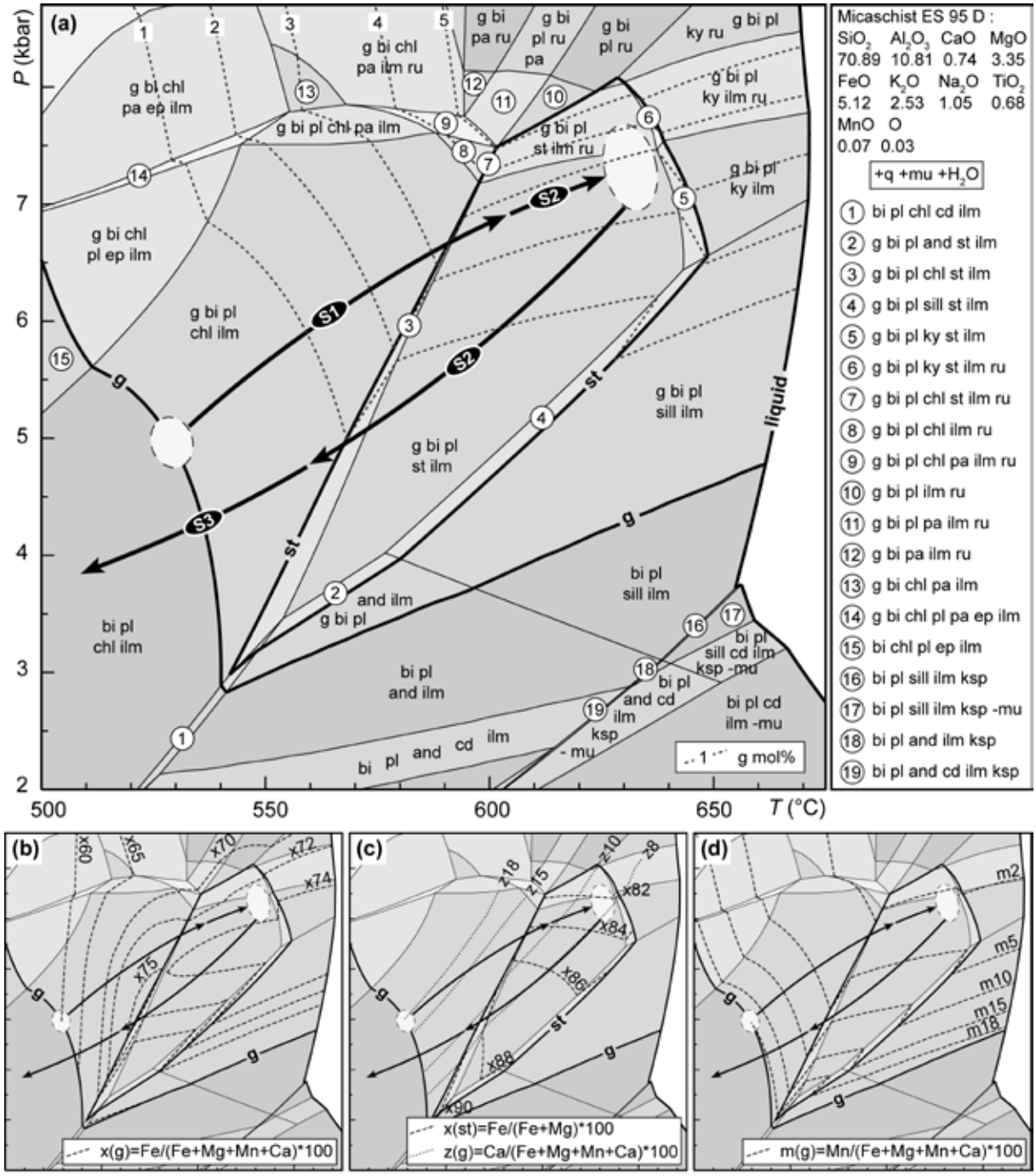

Fig. III-11: (a) Pseudosection calculated for the rock composition of the metapelite sample ES95D (Mn-NCKFMASHTO system, whole-rock composition in moles adjusted to 100%), contoured with molar proportions of garnet. (b−d) Simplified parts of the pseudosection with calculated isopleths of mineral composition. Garnet, staurolite and granitic melt stability are highlighted. White ellipses show areas corresponding to garnet core and rim compositions. Arrows and black circles indicate parts of P–T path and conditions of equilibration for individual structures, derived by comparing the modeled assemblages and isopleths with observed assemblages and chemistry of minerals. See text for details.

°C. However, the first clear microstructural indication that the steeply-dipping foliation was mechanically active during D2 is the growth of elongated aggregates of ilmenite and sphene around rutile in the samples that are not affected by the D3 foliation (several centimetres next to the sample JW29-2). Sphene started to grow still during the formation of the S2 fabric, which is correlated with the hb−pl−bi−ilm−sph field without quartz that occurs at ~ 5−7 kbar and

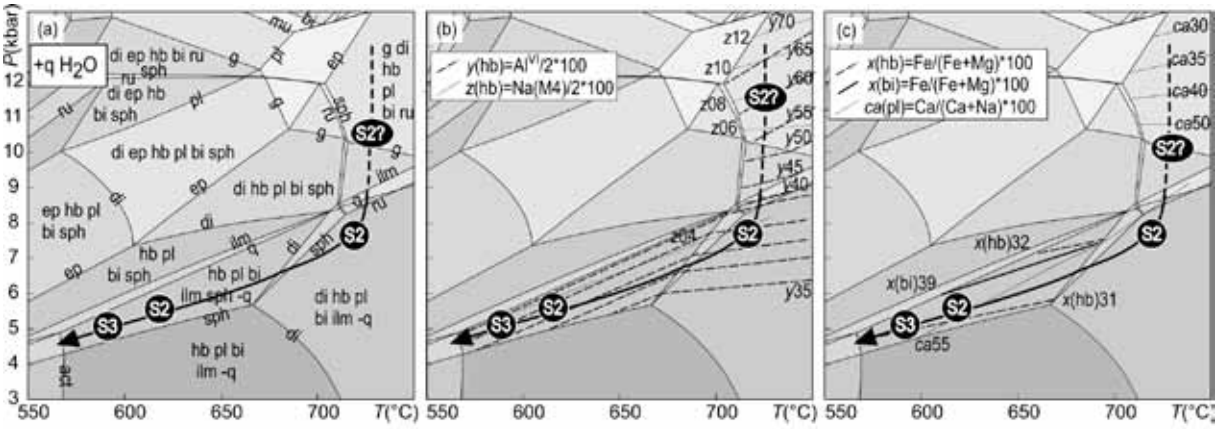

Fig. III-12: Enlarged and simplified low-pressure part of the pseudosection from Fig. III-9 contoured with calculated isopleths of mineral composition in the fields of interest. Arrows and black circles indicate parts of P–T path and conditions of equilibration for individual structures, derived by comparing the modeled assemblages and isopleths with observed assemblages and chemistry of minerals. See text for details.

560−700 °C. The S3 foliation represented by incomplete fabric transposition in the small scale shear zone (Fig. III-5g) is correlated also with the hb−pl−bi−ilm−sph field without quartz, with amphibole compositions that correspond to hornblende s.s., plagioclase with an=50 mol.%, together with XFe of the biotite and hornblende (Fig. III-11). The P−T conditions for the beginning of the S3 fabric are thus estimated to ~ 5 kbar and 600 °C. The presence of the domains with K-feldspar, chlorite, albite and magnetite suggests that the S3 fabric was mechanically active also under greenschist facies conditions.

5. 3. Pseudosection for metapelite sample ES95D

The pseudosection (Fig. III-12) is calculated for the analyzed whole-rock composition of the sample ES95D (in wt%: SiO_2=65.87, TiO_2=0.84, Al_2O_3=17.05, Fe_2O_3=7.03, MnO=0.08, MgO=2.09, CaO=0.64, Na_2O=1.01, K_2O=3.69, P_2O_5=0.34) with quartz, muscovite and H_2O in excess. The pseudosection is contoured with the calculated compositional isopleths for garnet and staurolite in order to discuss the P−T evolution of the metapelite.

P−T evolution of the micaschist sample ES95D

The stability of quartz, muscovite, garnet, staurolite, biotite and ilmenite has been documented in both the S1 and S2 foliations. The modelled compositional isopleths of garnet with values similar to garnet core ($alm_{0.60}$ $grs_{0.17}$ $sps_{0.19}$) intersect at the garnet-in line and constrain the onset of garnet growth to ~ 5 kbar and 530 °C (Fig. III-12b−d). The observed garnet zoning is compatible with prograde evolution crossing the staurolite-in line, which is in agreement with the occurrence of staurolite inclusions only close to the garnet rim. This P−T path reaches the g−bi−pl−st−ilm field (Fig. III-12a) at ~ 7 kbar and 630 °C where *x*(g), *z*(g), *m*(g) and *x*(st) values (Fig. III-12b−d) are close to staurolite (XFe=0.82) and garnet rim compositions (alm0.75 grs0.08 sps0.02). Garnet and staurolite rims (Fig. III-7c,d) are associated with the S2 fabric indicating that the transition from the shallow-dipping S1 fabric into the subvertical S2 foliation

started near the peak P−T conditions (black ellipses labelled S1 and S2 in Fig. III-12). Chlorite replacing staurolite in the S2 foliation can be correlated with a retrograde path crossing the chlorite-in line, possibly connected also with garnet rim ($alm_{0.75}$) re-equilibration below ~ 570 °C at the end of the D2 deformation (Fig. III-12b). Further evolution during the D3 deformation is associated with chlorite occurrence in the F3 fold hinges indicating temperatures lower than ~ 540 °C for the end of the retrograde path in the bi−pl−chl−ilm field (Fig. III-12a).

6. DISCUSSION AND CONCLUSIONS

6. 1. Tectonic significance of orogenic fabrics

The heterogeneous character of the D1 deformation is best expressed by the highly deformed fine-grained and the banded felsic orthogneiss types around the eclogite, by the weakly deformed augen felsic orthogneiss further away from the eclogite and by the highly foliated metasedimentary belt. In addition, structural observations show that the felsic orthogneiss records a non-coaxial top to the north shearing expressed by the metre-scale N-verging asymmetric F1 folds. Parallelism of the eclogite fabric with that of the surrounding felsic orthogneiss suggests a shared deformation history. The metasedimentary rocks also display a strong S1 schistosity, which is concordant with the structure of the adjacent orthogneiss. In summary, both the deep- and the mid-crustal tectonites experienced similar N−S oriented subhorizontal flow, but the D1 deformation was highly localized in the fine-grained and banded felsic orthogneiss and in the metasediments, leaving the augen felsic orthogneiss only weakly deformed.

The subsequent D2 deformation causes upright folding associated with the development of N−S striking foliations. This is interpreted as the result of a subhorizontal E−W shortening. A characteristic feature is the intense folding and the fabric transposition of the felsic orthogneiss around the eclogite and of the metasediments in contrast to the several-kilometres large domain of the augen felsic orthogneiss that is only moderately affected by the D2 deformation (Fig. III-3). This clearly indicates that the intensity of the F2 folding and its wavelengths are controlled by the degree of mechanical anisotropy of the individual lithologies achieved during the D1 deformation. The highly anisotropic banded felsic orthogneiss and the metasediments responded to horizontal shortening by intense folding with a common observed wavelength of several metres, while the competent augen felsic orthogneiss marked by a low degree of mechanical anisotropy responded by homogeneous flattening rarely localized into shear zones (Fig. III-3). Evaluation of the intensity of the D2 deformation in the eclogite is more difficult. The crenulation of the S1 eclogite facies fabric was observed at one place only and suggests that the eclogite is only locally affected by the F2 folding. It is proposed that the subvertical eclogite facies foliations are mostly steepened S1 fabrics, rotated in the limbs of the large F2 folds. The rare D2 amphibolite facies shear zones that affect the eclogite are thin and

heterogeneous, and probably represent the axial plane cleavage of the large-scale F2 folds.

The recumbent F3 folds and the subhorizontal S3 cleavage heterogeneously affect the S2 foliation in all the lithological types. This weak deformation reflects vertical shortening and does not influence significantly the dominant D2 pattern.

6. 2. P−T−D paths

The petrological study shows that the shallow-dipping S1 fabric in the eclogite is marked by prograde and peak mineral assemblage, for which the metamorphic P−T path is estimated from ~19.5 kbar and ~640 °C to 20−23 kbar and 700−750 °C. The S1 fabric in the felsic orthogneiss around the eclogite belt is probably co-facial with the eclogite, as indicated by the composition of white mica (Si = 3.30−3.43 p.f.u., Bröcker *et al.*, 2009). In the metapelites, minerals related to the S1 foliation show pressure and temperature increase from ~5 kbar and ~520 °C to ~7 kbar and ~630 °C (Fig. III-13). The formation of the S1 fabric is therefore related to progressive burial of both the eclogite and the metasediments, but within different crustal depths. Consequently, eclogites and adjacent felsic orthogneiss are considered as a part of an orogenic lower crust, while the metapelites as a part of an orogenic middle crust within a continental wedge structure (Fig. III-14a, inset). These crustal levels are separated by a thick layer of the augen orthogneiss for which the P−T conditions remain unknown (Fig. III-14a).

The metamorphic conditions in the eclogite at the onset of the S2 fabric are difficult to estimate. In numerous sites the subvertical eclogite foliation is affected by fractures filled by amphibolite facies assemblages and by centimetre-scale subvertical amphibolite facies shear zones (Fig. III-13a). In some places the subvertical foliation surrounding the eclogite developed entirely under amphibolite facies conditions and amphibolite bodies with a steeply-dipping foliation occur within the orthogneiss. The subsequent part of the retrograde P−T path from ~9 kbar to greenschist facies conditions is relatively well correlated with the structural development of the eclogite and the amphibolitized eclogite, but the part of the P−T path between the peak and ~ 9 kbar cannot be unambiguously correlated neither with S1 nor with S2 structures. Microstructural observations from the metapelites indicate that the P−T evolution related to the S2 fabric can be separated in two parts (Fig. III-13b). The first part is associated with the growth of garnet and staurolite rims parallel to the S2 foliation reflecting continuation of burial to ~7.5 kbar and ~630 °C (Fig. III-13b). The second part of the P−T path is related to syntectonic growth of chlorite in the S2 fabric, suggesting cooling bellow 550 °C, probably accompanied by decompression.

The petrological analysis shows that the eclogite and the metasediments were metamorphosed during the D2 deformation at different crustal levels corresponding to the orogenic lower and middle crust, respectively. The main difference is that during the F2 folding the eclogite experienced only exhumation, whereas the metapelite experienced first a burial increment (Fig. III-14b) and then exhumation (Fig. III-14c). Importantly, the coupled P−T−d paths (Fig.

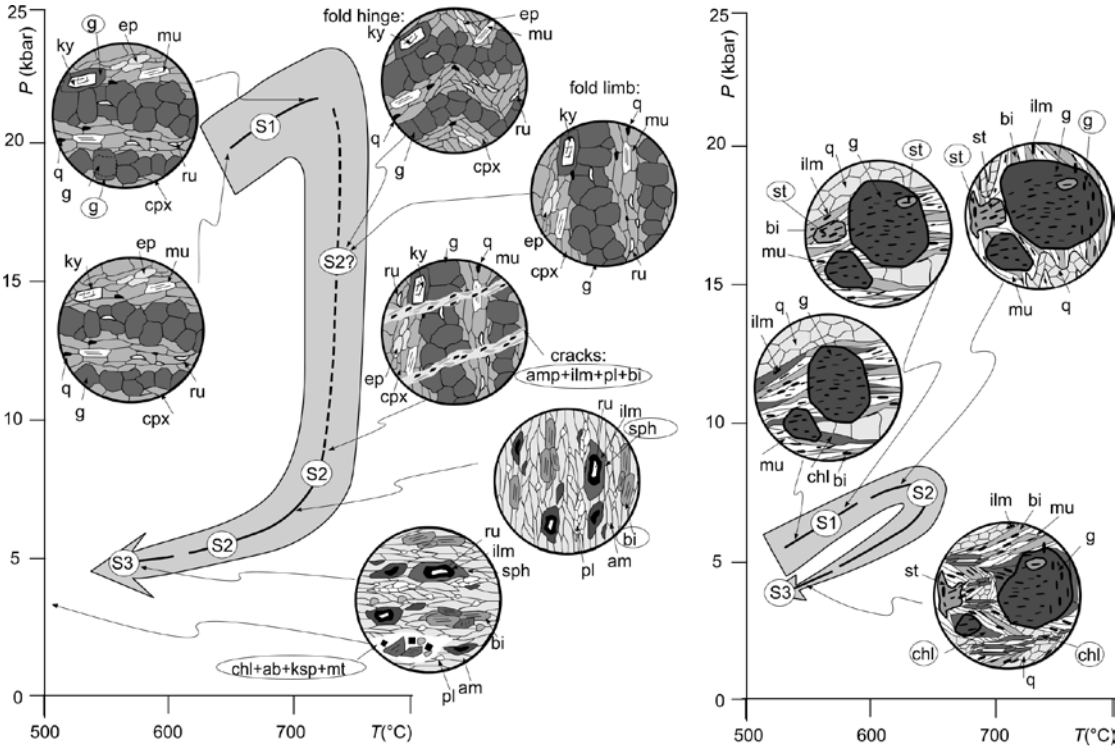

Fig. III-13: Summary of P−T data and associated microstructures. See text for discussion.

III-13) show that the F2 folding during the D2 deformation brings portions of the orogenic lower and middle crust into the same crustal level (Fig. III-14b). The subsequent metamorphic evolution of the amphibolitized eclogite and the metasediments terminates at the same pressure of ~4−5 kbar (Fig. III-13) and suggests that the final part of the exhumation was shared in the D2 fabric.

The mineral assemblages for both eclogite and metasediments in the S3 fabric are associated with temperature and pressure decrease below 550 °C and 4−5 kbar (Fig. III-13). At this stage the metamorphic evolution of the eclogite and metasediments was shared and occurred at the same crustal level (Fig. III-14d).

6. 3. Constraining the juxtaposition of eclogite and metapelites

Folding and erosion model

While the thermal evolution of folded terrains is generally a non-trivial problem, changes in pressure could be successfully correlated with changes in distance between the surface and the studied sample. Therefore, the major processes affecting pressure evolution are those responsible for the reduction (i.e. ductile thinning, detachment-related thinning and/or erosion) or the thickening of the overburden. For clarity and the purpose of our 2D kinematic model, the overburden removal is approximated by "erosion", while the vertical elongation of the modelled domain results from bulk homogeneous shortening. The pressure evolution of an originally sub-horizontal layer is governed by these bulk vertical displacements but may be modified by fold-related displacements governed by the scaled amplification equation.

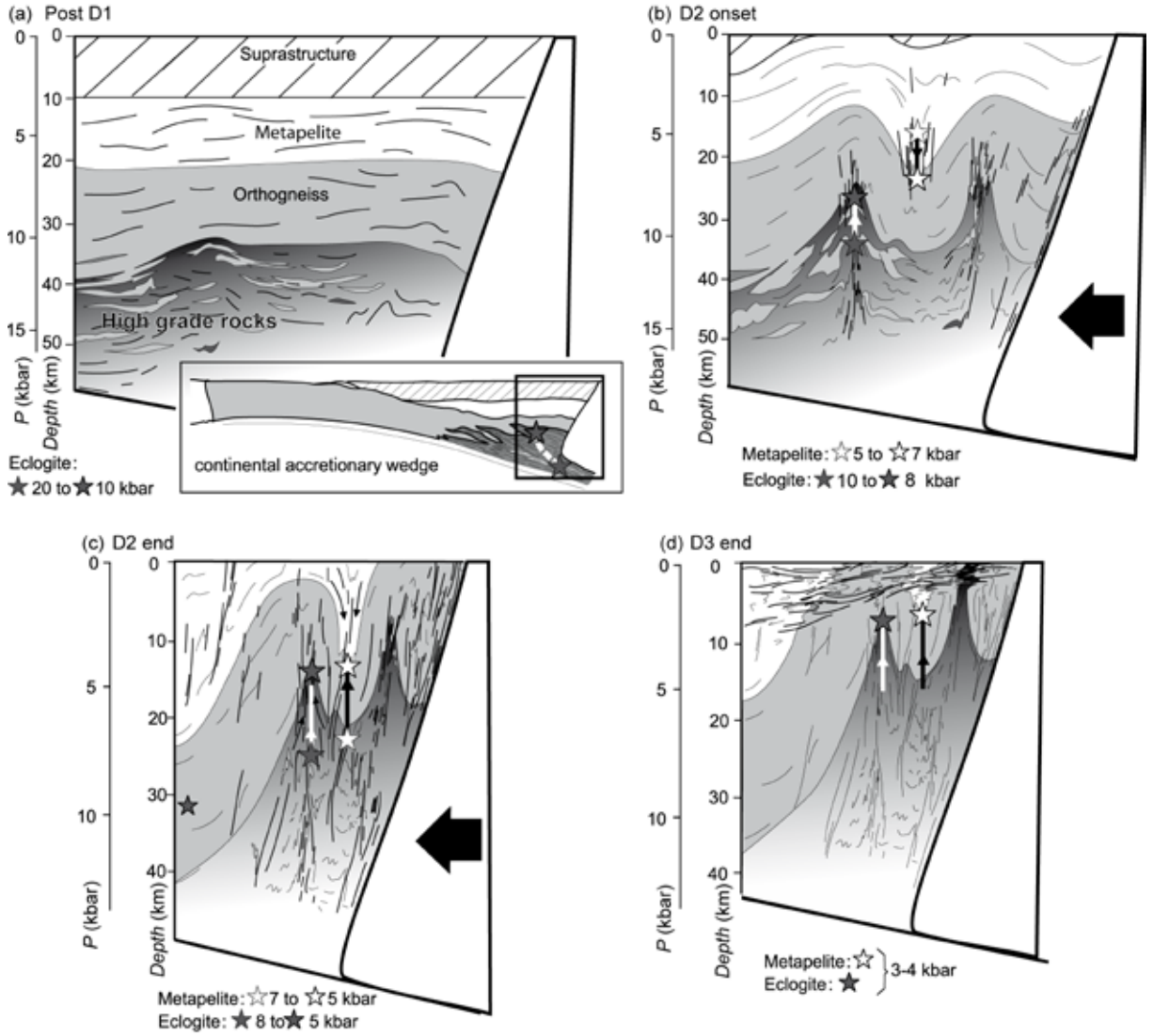

Fig. III-14: Evolutionary model permitting juxtaposition of amhibolite facies metapelites and eclogites. (a), (b) Development of two wavelength buckle folds permitting exhumation and burial of eclogites and métapélites. (c) Exhumation of both eclogites and métapélites due to the position above the inflexion line (d) Final stage of exhumation by weak ductile thinning and erosion. (e) Schematic interplay between folding, thickening and topography removing (erosion or ductile thinning) for two different wave length. See text for discussion.

In order to explain the relative contribution of erosion and the D2 folding on the complex P−T−d evolution of the metapelites in the synform and the eclogite in the antiform, we apply a kinematic model of buckling of a single layer during orogenic shortening. The single layer buckling originates from a mechanical instability developed during layer-parallel shortening and produces a lateral gradient in vertical displacement within the folded layer. The analytical results show that the growth rate of the single-layer fold amplitude is a function of the fold wavelength, where the maximum growth rate corresponds to the so-called dominant wavelength, which tends to be preferred during progressive shortening (Biot, 1961). Moreover, if the growth rate and the wavelength are non-dimensionalised by the layer-parallel shortening strain rate and the layer thickness respectively, the growth rate only depends on the wavelength and the viscosity contrast between the layer and the surrounding material (Fletcher, 1977). Schmalholz (2006) showed, that the horizontal and vertical hinge distances of many natural folds may be

well correlated with the analytical parameters of wavelength and amplitude, respectively, using the scaled amplification equation describing fold amplification during viscous single-layer folding up to high amplitudes:

$$S_S = \left(\frac{\overline{A}}{\overline{A}_0}\right)^{\frac{1}{2+\alpha_0}} \left(\frac{\overline{L}}{\overline{L}_0}\right)^{\frac{\alpha_0}{2+\alpha_0}} \left(\pi \overline{A}_0 \sqrt{2\alpha_0}\right)^{\frac{1}{2+\alpha_0}} \quad (1)$$

where S_S is scaled stretch, $\overline{A}$, $\overline{A}_0$ are dimensionless initial and final fold amplitude, $\overline{L}$, $\overline{L}_0$ are initial and final dimensionless fold arc length and $\alpha_0 = (4R/3)^{2/3}$ is the dimensionless initial maximal growth rate dependent on the viscosity contrast between layer and matrix. In summary, the scaled amplification equation (Eq. 1) together with the growth rate equation (Biot, 1961; Fletcher, 1974; Schmalholz, 2006) represent a suitable mathematical framework to describe the main mechanical characteristics of finite amplitude buckling of a single viscous layers. The results of this model are summarized in Figure 15.

Burial and exhumation paths

We studied 3 different scenarii: (i) The "no erosion" model is characterized by progressive thickening of the overburden related to bulk shortening. (ii) The "full erosion" model, the overburden removal is more effective than shortening, so that the overall thickness does not change with time. (iii) The "increasing erosion" model has a progressive increase in efficiency of the overburden removal.

The "no erosion" model shows differential burial of all the folded layers with typical exponential relation between final depth and finite strain, while deeper initial positions of the folded layer corresponds to deeper final depths (Fig. III-15a). It should be noted that final vertical displacement is partially reduced by isostatic re-equilibration due to overall thickening. The "full erosion" model shows overall exhumation of all folded layers with exception of the layers that are located very close to the bottom of the system, where synformal parts of the folded layers resist to exhumation during early stages of shortening (Fig. III-15c). The bulk rate of exhumation is slightly higher compared to burial rate in the "no erosion" model due to the absence of isostatic re-equilibration.

In the "increasing erosion" model, the early stages are characterized by a low amount of the overburden removal and an affinity to the "no erosion" model, with burial of the synformal parts of the initially shallower layer and the overall burial of the initially deeper layers (Fig. III-15b). Once the overburden removal starts to dominate, the vertical displacements progressively change and fold antiforms together with fold synforms of the initially shallower layers are exhumed.

The modelling shows that neither the "no erosion", nor the "full erosion" model satisfies the complex P−T−d evolution of the studied rocks. The 2D kinematic model indicates that in order to develop progressive burial followed by exhumation during large-scale folding, the overburden removal processes like erosion or tectonic unroofing have to be significantly involved and have to be synchronous with bulk shortening. From the three tested situations it

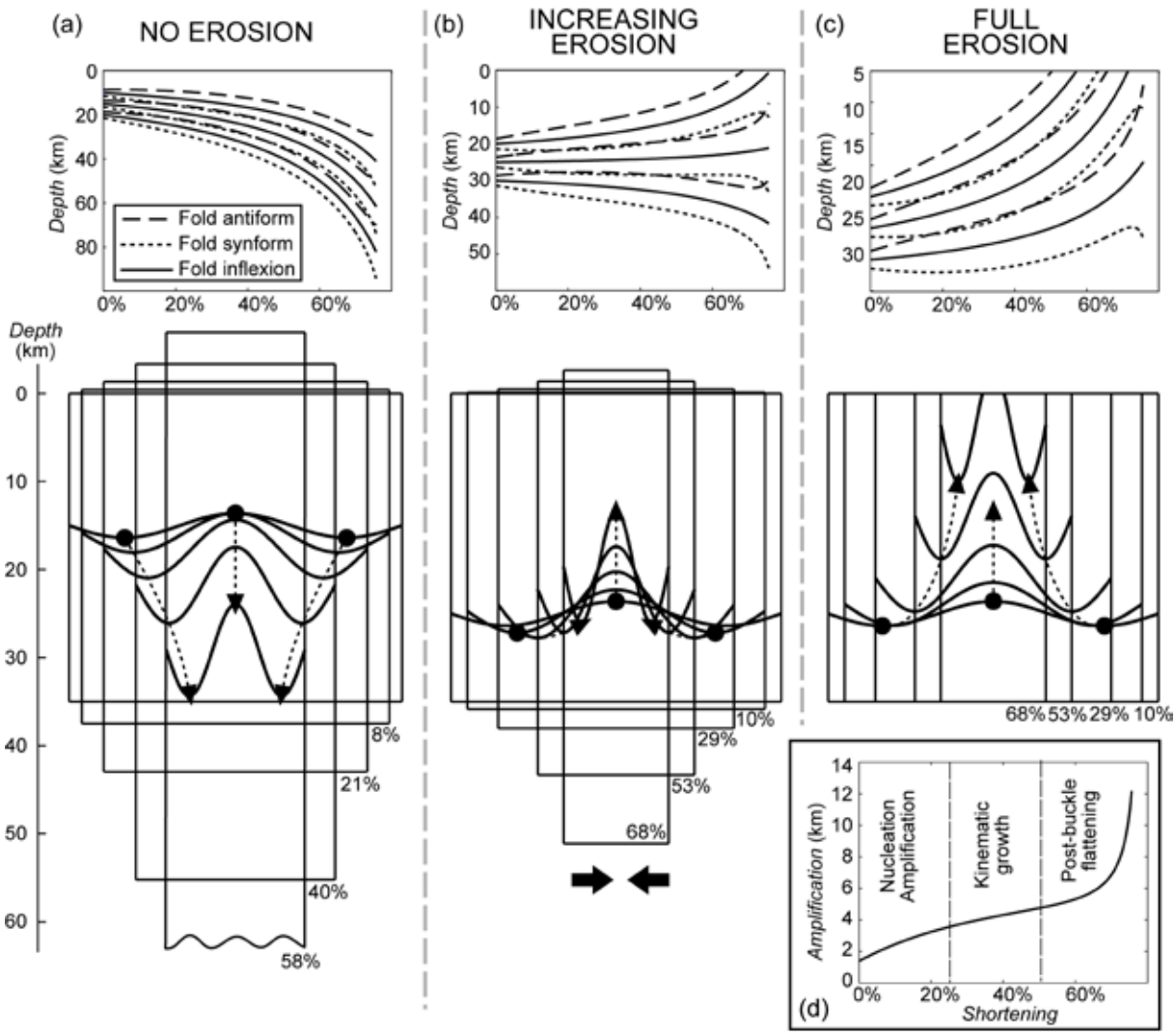

Fig. III-15: Schematic evolution of vertical displacement of folded single-layer during bulk shortening for (a) "no erosion", (b) 'increasing erosion" and (c) "full erosion" models. The differential vertical movements of fold antiform, synform and inflexion line as a function of bulk shortening are plotted in diagrams along the bottom of the figure. (d) The non-linear evolution of buckle-fold amplification is plotted in amplification vs. shortening diagram in the central inset.

is the progressively "increasing erosion rate" model that satisfies the P−T record of the studied rocks. The small burial recorded in the metapelites associated with an important exhumation in the eclogite fits well with this model (Fig. III-15). For small erosion, the burial in synforms is possible but the point at the top of the antiform shows already important exhumation (Fig. III-15b).

With increasing erosion, both antiforms and synforms exhibit an important exhumation for continuous shortening with the ongoing development of close to isoclinal folds. These modelled parameters fit well with the second stage of the P−T history where both metapelite and eclogite show important exhumation related to the development of the S2 cleavage and the decrease of the fold interlimb angle. The vertical movements of rocks located in synforms and antiforms are also associated with typical evolutionary stages of folding starting with early nucleation (active) amplification, which is rapid and effectively competes with "erosion" thereby bringing rocks quickly down or up. This stage is followed by slower kinematic amplification

where vertical movements are prevailing, followed by post-buckling stage at the late evolutionary history of fold life. The two latter fold evolutionary stages are connected with an active elevation of the whole system due to the progressively growing erosion rate.

Our model also shows that in order to simulate the simultaneous evolution of eclogite and metapelites, both rocks have to be located relatively high in the crustal column before the onset of folding. The eclogite layer located in a depth of 60 km and the metapelite at 25 km would never produce the P−T evolutions reported in this work and the juxtaposition of both lithologies. The modelling therefore suggests that both eclogite and metapelites were located close to each other before the initiation of the folding event. They were probably separated by a ~10 km thick orthogneiss layer at a depth of 25–30 km.

6. 4. P−T−D evolution in the frame of existing orogenic models

The development of the S1 subhorizontal foliations related to an increase of pressure and temperature in the different crustal levels is typical for the model of burial of the crust in a continental wedge (Fig. III-14a, inset) (Platt, 1993; Jeřábek *et al.*, 2008). The steep geometry of the D2 fabrics related to the exhumation is compatible with the corner flow circulation in the crustal wedge model (Platt, 1993; Allemand & Lardeaux, 1997). However, this model does not take into account the F2 folding reported in this work, which brings the orogenic lower and middle crustal rocks together (for similar examples see also Štípská *et al.*, 2004; Racek *et al.*, 2006; Schulmann *et al.*, 2008; Franěk *et al.*, 2011a; Franěk *et al.*, 2011b; Lexa *et al.*, 2011)(Fig. III-14b). This part of the tectono-metamorphic history of the studied rocks can be best explained by the model proposed by Burg *et al.* (2004), which is the only model that takes into account crustal-scale folding due to horizontal shortening.

Numerical modelling (Fig. III-15) shows that the juxtaposition between lower and mid-crustal rocks via crustal-scale folding can only occur if eclogite and metapelites are separated by ~10 km (Fig. III-14a). This requires a first exhumation stage of eclogitic bodies prior to the D2 deformation. We can propose that the eclogite facies fabric S1 was passively exhumed to mid-crustal depths by back-thrusting along a predisposed subduction plane (S1). This mechanism may not leave a structural trace in the exhumed eclogite as shown in other parts of the Bohemian Massif (Klápová *et al.*, 1998; Konopásek & Schulmann, 2005). In such case the F2 folding would start to deform the eclogite at amphibolite facies conditions.

The shallow-dipping amphibolite to greenschist facies fabric D3 is geometrically compatible with the horizontal spreading of rocks proposed by Koyi *et al.* (1999). However, in their model the horizontal flow occurs due to the gravitational rebound of the root and affects the whole thickened crust. In the continental wedge model, the horizontal spreading is attributed to ductile thinning mechanism and occurs only at higher crustal levels (Ring *et al.*, 1999), which is compatible with the P−T estimations of the D3 structures. In the absence of pervasive D3 deformation in the study area we favour erosion as the dominant mechanism responsible for the

removal of the overburden.

ACKNOWLEDGEMENTS

The French National Grant Agency (06-1148784 to K. Schulmann) is gratefully acknowledged. The grant MSM0021620855 of the Ministry of Education of the Czech Republic and internal research funds of CNRS UMR 7615 are acknowledged for salary and financial support of O. Lexa. J. Lehmann is thanked for helpful discussions.

CHAPITRE IV

PROGRADE DEFORMATION GRADIENT IN SUBDUCTED HP ORTHOGNEISS (ORLICA – ŚNIEŻNIK DOME, CENTRAL SUDETES): IMPLICATIONS FOR REACTION SOFTENING AND STRAIN LOCALISATION DURING CONTINENTAL SUBDUCTION

F. CHOPIN [1], K. SCHULMANN [1], J.E. MARTELAT[2], P. ŠTÍPSKÁ [1], O. LEXA [3,4] and B. PETRI [1]

[1]*Ecole et Observatoire des Sciences de la Terre, Institut de Physique du Globe – CNRS UMR7516, Université de Strasbourg, 1 rue Blessig, F-67084, Strasbourg Cedex, France*

[2]*Laboratoire des Sciences de la Terre – CNRS UMR5570, Université de Lyon 1, F-69622, Villeurbanne, France*

[3]*Institute of Petrology and Structural Geology, Charles University, Albertov 6, 128 43 Prague, Czech Republic*

[4]*Czech Geological Survey, Klárov 3, 110 00, Prague, Czech Republic*

Short title: Deformation of orthogneiss in subduction gradient

Key words: quantitative microstructural analysis, Thermocalc modeling, reaction softening, rheology, HP metamorphism

ABSTRACT

The microstructural and petrological study of a natural deformation and metamorphic gradient of MP to HP orthogneiss (Orlica-Śnieżnik Dome, Central Sudetes) allows examining the behaviour of felsic crust during progressive burial along a subduction gradient (~10°C/km). Studied finite strain gradient allows dividing rocks in three distinct structural groups, each representing an evolutionary stage of progressively deformed metagranite: Type I - augen, Type II - banded and Type III mylonitic orthogneiss. Type I orthogneiss is made of partially recrystallised K-feldspar phenocryst, fully recrystallised quartz aggregates and interconnected monomineral layers of dynamically recrystallized plagioclase. Layering defined by bands of minerals of infinite length is completed in banded orthogneiss marked by increasing proportion of interstitial phases in both plagioclase and K-feldspar rich layers. Type III orthogneiss reveal relics of quartz and K-feldspar ribbons preserved in fine polyminerallic matrix. The monotonous assemblages (q+pl+kfs+mu+bi+g+sph±ill) show variations in compositions of muscovite (from Si p.f.u.=3.16-3.28 to Si p.f.u.=3.22-3.38) and garnet (from grs=0.42-0.46 to grs=0.35-0.40) across studied deformation gradient. The deformation types thus do not represent evolutionary stages of highly partitioned deformation at constant PT conditions. Instead, variously deformed orthogneisses reflect progressive burial of continental crust from at least 12kbar and 650°C (augen orthogneiss) to 19kbar and 750°C (banded and mylonitic orthogneiss). The medium

pressure deformation is dominated by dislocation creep of quartz and K-feldspar followed by grain boundary sliding dominated diffusion creep regime at high pressure conditions. The transition from MP to HP stage is associated with progressive nucleation of interstitial phases due to continuous metamorphic reactions leading to drastic reaction weakening and strain localisation. This allows passive transport of relics of less deformed and less metamorphosed orthogneiss Types in a continental accretionary wedge to a depth of 50-60km.

1. Introduction

Quartzo-feldspathics rocks form the most important part of the continental crust and therefore the understanding of their rheological behaviour in a wide range of natural physical conditions is a goal of many microstructural studies (e.g. Gapais, 1989; Handy, 1990). Detailed studies of deformation gradients in metagranites is a common approach to evaluate the role of strain partitioning between mineral phases of contrasting rheology (Handy, 1994) and variations in mechanisms of dynamic recrystallization in progressively strained rocks (e.g. Schulmann *et al.*, 1996). Several studies shown that the quartz and feldspars in metagranites are dynamically recrystallised at dislocation creep regime at greenschist facies (Shigematsu & Tanaka, 2000; Ishii *et al.*, 2007; Menegon *et al.*, 2008) or amphibolite facies conditions (Menegon *et al.*, 2006). At granulite facies conditions and during partial melting is the dislocation creep still important deformation mechanism operating both in quartz and feldspar (Martelat *et al.*, 1999) but small fraction of melt enhances grain boundary sliding accommodated diffusion creep in feldspars (Zavada *et al.*, 2007; Schulmann *et al.*, 2008). Consequently, the bulk rock strength decreases dramatically as it has been shown experimentally by Dell'Angelo *et al.* (1987).

Studies of progressive deformation of granitoids in colder metamorphic gradient such as (U)HP eclogitic bearing orthogneiss associated with burial to great depth are almost inexistent. This is due to the fact that large bodies of metagranites did not suffered important deformation during either burial or exhumation (e.g. Dora Maira massif, Lenze & Stöckhert, 2007; Western Gneiss Region, Hacker *et al.*, 2010) even if there are some indications of plastic flow at such conditions for instance in Qinling–Dabie–Sulu orogenic belt (Zhao *et al.*, 2005). This can be explained by localisation of the strain in very narrow zones, in weaker lithologies or by low level of differential stress (Stöckhert, 2002). In the same way, metamorphic assemblages indicating (U)HP conditions (North Qaidam metamorphic belt, Menold *et al.*, 2009; Western Gneiss Region, Peterman *et al.*, 2009) are rarely found in such rocks leading to difficulties in mapping continuous (U)HP belts appart of small isolated bodies of rocks that have registered and preserved deformation and associated mineralogical changes (mafic eclogites, coesite bearing orthogneisses) (e.g. Cooke & O'Brien, 2001).

Consequently, there is a complete lack of observation allowing to understand how felsic material behaves during burial and subduction at (U)HP conditions and what can be the aspect of rocks that suffered prograde deformation in term of their microstructure and petro-

logy. In order to fill this gap we examined a deformation gradient in orthogneiss bearing (U) HP eclogites from the Orlica-Śnieżnik domes where mafic eclogites appear like large bodies in generally weakly deformed metagranites. However, the occurrence of eclogite slivers is associated with strong gradient of deformation. This allows us to perform quantitative microstructural analysis combined with detailed petrological study of a prograde deformation gradient in a HP metamorphic gradient (~10°C/km) from 12 to 20 kbar. It is shown that weakly deformed granites reveal dislocation creep deformation mechanisms in all phases which progressively pass into diffusion creep regime at high strains. The transition between the two deformation mechanisms is associated with strain localisation allowing to preserve weakly deformed metagranites. Petrological observations and thermodynamic modelling shown that the dislocation creep regime operated at 12 kbar while the diffusion creep at 20 kbar suggesting major weakening of continental crust during subduction. The shift of deformation mechanisms is therefore enhanced by chemical reactions along the prograde PTd path. Finally, we position the petrological and deformation mechanisms evolution into a conceptual model of influx of material in a continental accretionary wedge.

2. Geological setting

The Orlica-Śnieżnik Dome (OSD - Central Sudetes) is situated in the north-eastern termination of the Bohemian Massif at the contact of the Moldanubian-Lugian Variscan deep crust and the Brunovistulian microcontinent (Mazur *et al.*, 2006, Fig. IV-1a). The OSD (Fig. IV-1b) is made of belts of high grade orthogneiss, sometimes cored by (U)HP rocks (Bröcker & Klemd, 1996; Štípská *et al.*, 2004), and surrounded by amphibolite facies metasediments altogether forming the Lugian root of the Variscan orogen (Skrzypek *et al.*, 2010b). The dome is mantled by supracrustal units of supposed Neo-Proterozoic age in the south (the Nové Město and Zábřeh Units) and by relics of Cambro-Ordovician rift sequences (Staré Město formation, Parry *et al.*, 1997; Štípská *et al.*, 2001) in the east. Protolith of orthogneisses, and metapelites have a coeval Cambro-Ordovician origin (Jastrzębski *et al.*, 2010) whereas protolith of (U)HP rocks remain still unknown (Bröcker *et al.*, 2010). ^{40}Ar-^{39}Ar cooling ages of hornblende and micas (Schneider *et al.*, 2006) and metamorphic zircons (e.g. Bröcker *et al.*, 2009) from both gneisses and metasediments cluster around 340Ma. Recent studies have highlighted the succession of three main episodes of deformations: the remnants of early Variscan flat fabrics related to crustal thickening, followed by steep structures associated with E-W lateral shortening and ubiquitous flat supracrustal fabrics connected to ductile thinning and unroofing of thickened crustal root (Chopin *et al.*, this volume; Štípská *et al.*, this volume).

The area of this study is located in surroundings of the Międzygórze town, at the eastern vicinity of the eclogitic belt described by Štípská *et al.* (Štípská *et al.*, this volume) (Fig. IV-1c). In this area, early flat fabrics S1 are well preserved in orthogneiss that show various macroscopic textural varieties ranging from augen orthogneiss (referred to Śnieżnik group in

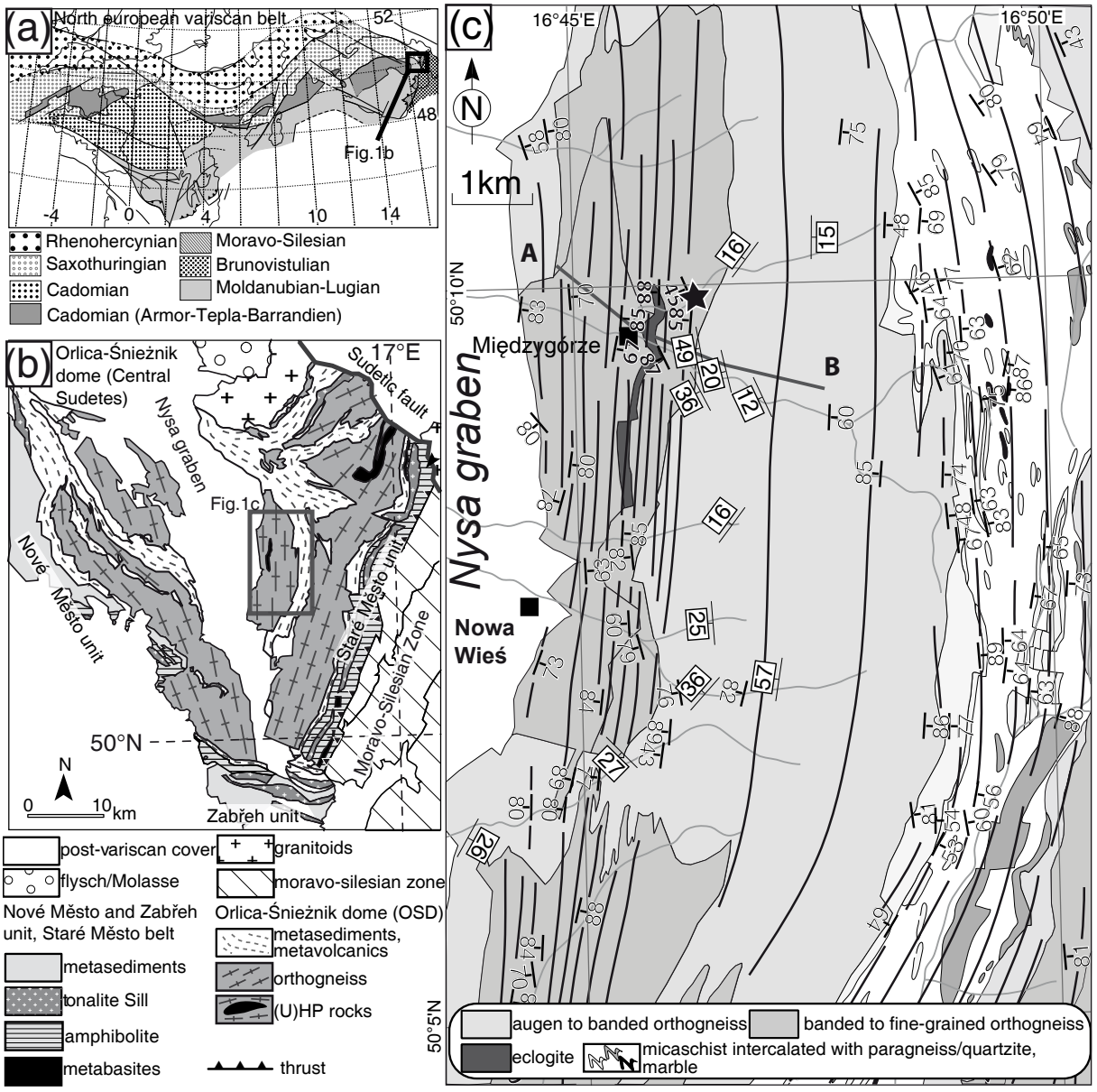

Fig. IV-1: Tectonic setting and geology of the studied area. (a) Position of the Orlica-Śnieżnik dome in the Variscan belt of Europe (modified after Edel et al., 2003). (b) Geological map of the Orlica-Śnieżnik dome (modified after Aleksandrowski et al., 1997; Don et al., 2003; Żelaźniewicz et al., 2006). (c) Structural map of the studied area (lithology after Don et al., 2003).

the literature e.g. Fisher, 1936) to banded and fine grained mylonitic orthogneiss (Gierałtów group). It has been shown that Śnieżnik and Gierałtów orthogneiss represents different degree of deformation derived from the same protolith (Lange *et al.*, 2005). These textural types form belts parallel to eclogite bearing zone cored by ultramylonites and banded gneiss which became progressively less frequent away from eclogites. The rock suffered a late lateral shortening leading to steepening of metamorphic fabrics mainly in the vicinity of HP rocks (Štípská *et al.*, this volume). In this work, we study textural transition from the Śnieżnik augen orthogneiss to the Gierałtów mylonitic orthogneiss accompanied with thermodynamic modelling to understand the physical conditions, mechanism of formation and geodynamic significance of these spectacular rocks.

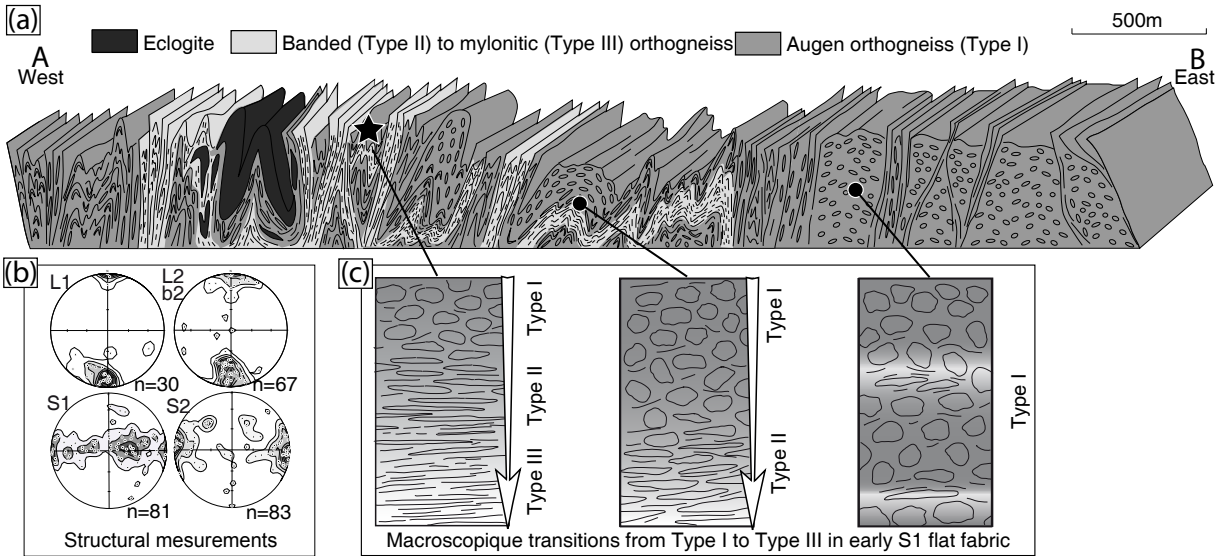

Fig. IV-2: (a) Geological cross-section of the Międzygórze Massif (A–B) showing principal structural features (modified after Štípská et al., this volume). (b) Equal-area, lower-hemisphere projections of D1 and D2 planar and linear structures (contoured at regular multiples of distribution). (c) Spatial and macroscopic evolution of metagranite with increasing strain and corresponding types in S1 fabric (Type I augen orthogneiss, Type II banded gneiss and Type III mylonite).

3. Definition of structural types according to finite strain gradient

All samples were taken in one outcrop (UTM coordinates X=626626 Y=5566086), close to the Międzygórze town (Fig. IV-1c) which show well preserved decimetre scale to meter scale finite D1 strain gradients mostly close to the eclogitic belt (Fig. IV-2). The N-S sub horizontal macroscopic lineation is marked by rodding of Qtz and feldspars and alignment of micas. Here, this deformation gradient is affected by tens of metre scale open to close F2 folds that are not associated with the development of new cleavage. In agreement with macroscopic appearance we recognize three types of rocks representing different degree of deformation: Type I of weakly deformed porphyric granite/augen gneiss (Śnieżnik orthogneiss, samples mzgA, mzg02, mzg14, fc019A), intermediate Type II banded orthogneiss (mzgD, mzg03, mzg04, mzg12, mzg11 and fc19C), and Type III mylonitic orthogneiss (Gierałtów orthogneiss, samples mzg05, mzg10 and fc19D) (Fig. IV-3a-g). Representative samples mzgA, mzgD and mzg05 have been cut parallel to XZ and YZ section of finite strain ellipsoid in order to evaluate the evolution of deformation intensity form the Type I to Type III by using Rf/phif method of finite strain analysis for K-feldspar only (Ramsay & Huber, 1983). Results of shape analysis are presented in a Flinn's diagram (Flinn, 1965) (Fig. IV-3h,i). Type I and type II samples show a significant increase of bulk strain intensity from D=1 to D= 6, associated with weak variations in of strain symmetry from plane strain to oblate shapes. Type III sample (mzg05) reveals dramatic increase of finite strain intensity up to D value = 25 associated with oblate shape. In general, the early stages of deformation can be interpreted as a result of strain partitioning in plane strain and flattening components while the highly deformed ultramylonites show absence of lineation and reflect bulk flattening only.

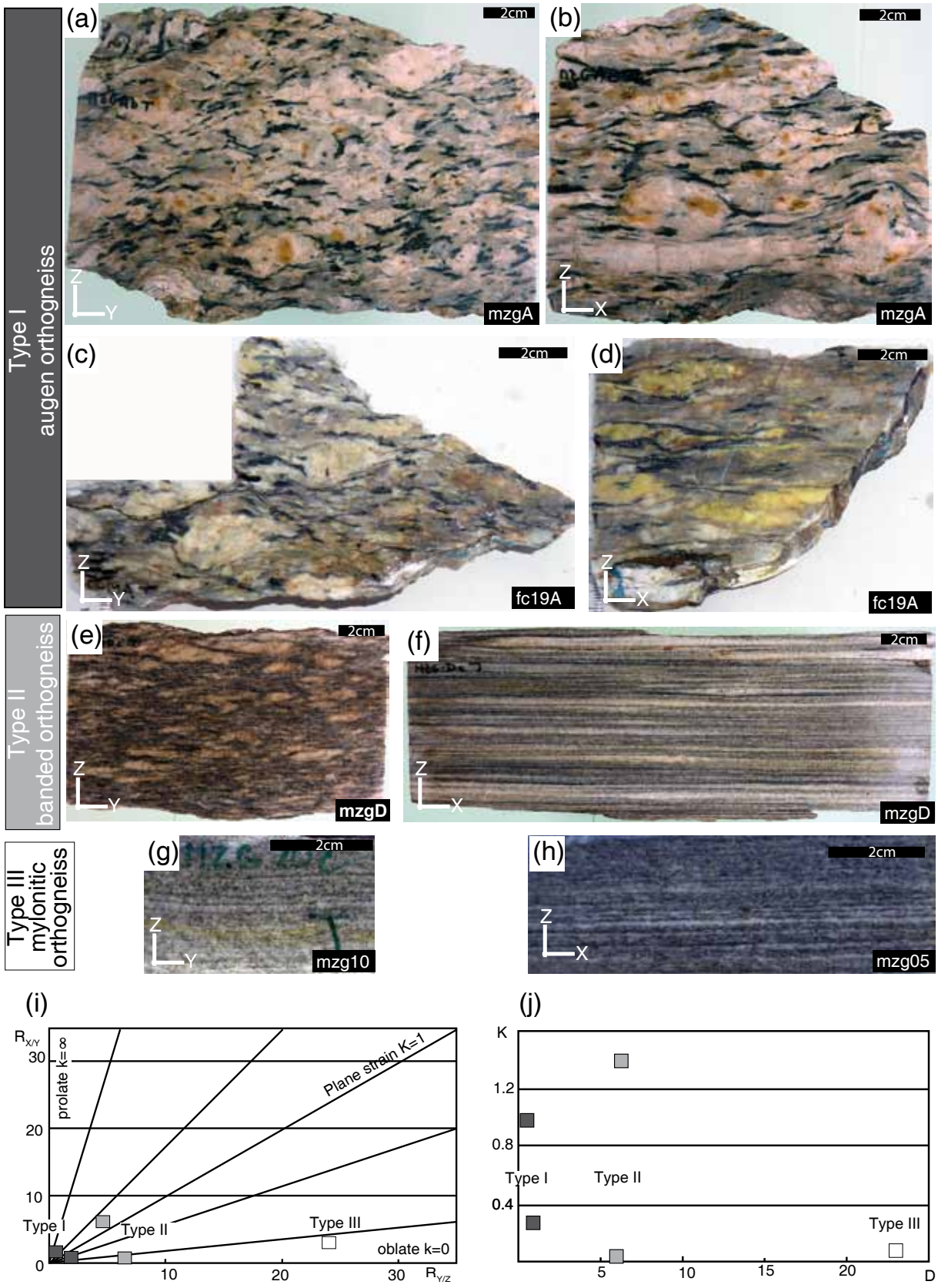

Fig. IV-3: Illustration of the three metagranite types defined macroscopic pattern and deformation intensity. X, Y, and Z refer to the axes of the finite strain ellipsoid. (a-d) Type I augen gneiss. (e, f) Type II banded gneiss. (h) Type III mylonite. Scale bar is 2mm. (i) Flinn's diagram after Flinn (1965) showing the shapes of deformation ellipsoids. (j) Diagram showing strain intensity expressed by the shape parameter K as a function of bulk strain intensity parameter D.

4. Whole rocks composition

The whole rock ICP-MS analyses were performed in the Acme laboratories (Canada). Results are summarized in Table IV-1 and presented in a Grant's isocon diagram (Grant, 1986) (Fig. IV-4a) and Chondrite-normalized REE patterns (Fig. IV-4b). Isocon diagram show a constant composition without major losses or gains of major elements in the rocks sequence (i.e. no deviation from the reference line). No measurement of densities have been done in the frame of this work but our results are consistent with those carried out in the same rock sequences and in the same area by Lange *et al.* (2002). In agreement with the latter authors we conclude that there are no indications for deformation-and/or fluid-enhanced element mobility and redistribution in progressively deformed rocks. Slight enrichment iron, magnesium and titanium in sample mzg2 can be attributed to a higher proportion of biotite in this particular sample. REE pattern shows a constant composition of REE except for Type III mylonitic rocks that are slightly depleted in LREE (samples mzg05 and mzg10) compared to Type I and Type II rocks.

Table IV-1: Representative whole-rock analyses of samples from the deformation sequence.

Rock type	Augen orthogneiss (Type I)			Banded orthogneiss (Type II)		Mylonitic orthogneiss (Type III)	
Sample	mzg02	mzg15	mzg14	mzg04	mzg12	mzg05	mzg10
wt%							
SiO2	70.80	69.59	71.10	70.43	70.05	71.29	69.69
TiO2	0.37	0.37	0.36	0.49	0.35	0.32	0.36
Al2O3	14.86	15.45	14.71	14.67	15.37	14.68	15.27
Fe2O3	2.55	2.80	2.70	3.18	2.55	2.57	2.63
MnO	0.03	0.03	0.03	0.04	0.03	0.03	0.03
MgO	0.70	0.66	0.68	0.85	0.64	0.66	0.70
CaO	1.75	1.73	1.74	1.85	1.74	1.75	1.65
Na2O	3.40	3.26	3.34	3.44	3.37	3.48	3.50
K2O	4.30	4.98	3.97	3.72	4.62	4.08	4.81
P2O5	0.18	0.18	0.15	0.17	0.16	0.17	0.18
Sum	99.87	99.84	99.86	99.80	99.83	99.87	99.85
Xfe	0.65	0.68	0.67	0.65	0.67	0.66	0.65

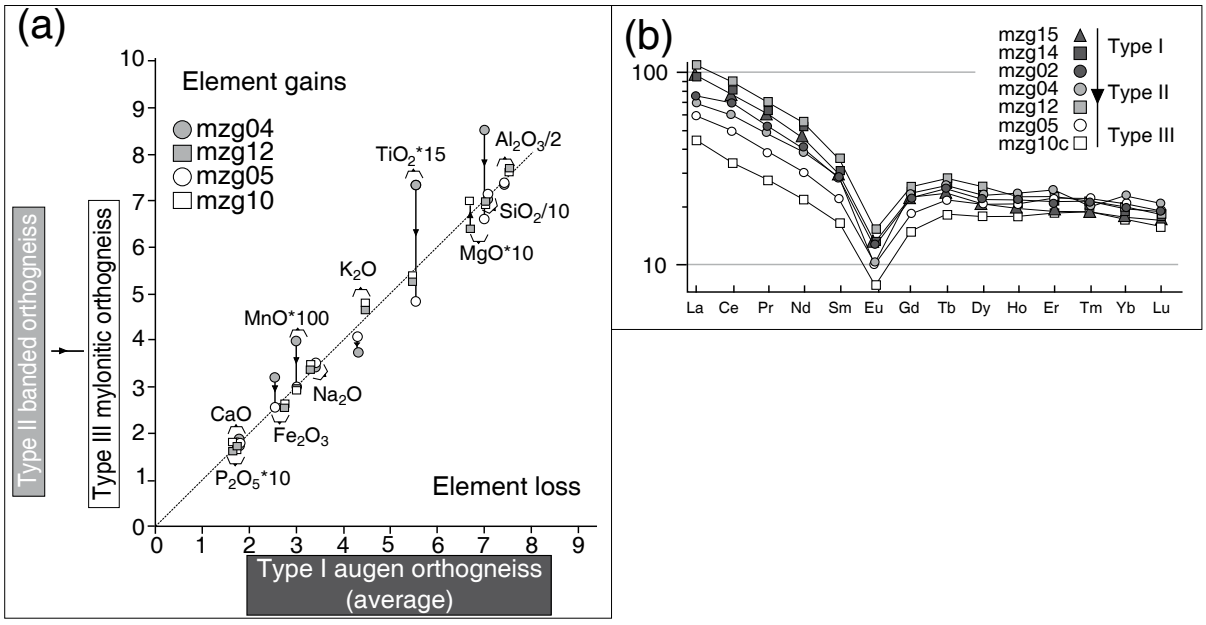

Fig. IV-4: (a) Isocon diagram after Grant (1986) using average bulk rock compositions of augen orthogneiss vs. banded (gray) and mylonitic (white) orthogneiss. This diagram show loss and/or gain of elements with respect to the reference line. Concentrations are scaled to fit in the plot. (b) REE patterns of the rocks sequences normalized to chondrites (Envensen et al. 1978).

5. Microstructural and petrological characteristics of rock types

The qualitative characterization of rock Types has been carried out using classical optical microscope study, back scattered electron images (Figs IV-5-7) and microprobe analysis of feldspars, micas and garnets (Fig. IV-8, Tables 2 & 3). BSE images have been acquired with a TESCAN VEGA XMU electron microscope at the EOST laboratory (University of Strasbourg). Mineral analyses were performed on a EPMA JEOL 8200 microprobe at the University of Lausanne. Operating conditions were a 15-kV acceleration voltage, a 10-nA beam current, a spot diameter of 5 µm and a counting time of 20–30 s. All studied samples show constant modal proportions of major phases in the whole sequences (30-35% of quartz, 25-30% of K-feldspar, 30-35% of plagioclase and 10% of micas).

5. 1. Type I: Augen gneiss

This rocks type is made of K-feldspar augens and quartz ribbons (1-5mm wide) alternating with contiguous layers of plagioclase and micas (1-3 mm wide) (Fig. IV-5a). Limits between feldspar aggregates and quartz are straight whereas limit between plagioclase and K-feldspar layers is more irregular (Fig. IV-6a). From original magmatic structure are preserved only feldspar phenocrysts, whereas neither relic of primary plagioclase nor quartz has been found in studied samples.

Quartz exhibits form of augens (Fig. IV-5a) or highly elongated completely recrystallised monomineral ribbons made of large grains ~150-300µm in size with highly lobated boundaries (Fig. IV-5a). Relics of primary K-feldspar phenocrysts up to 10 cm size are internally

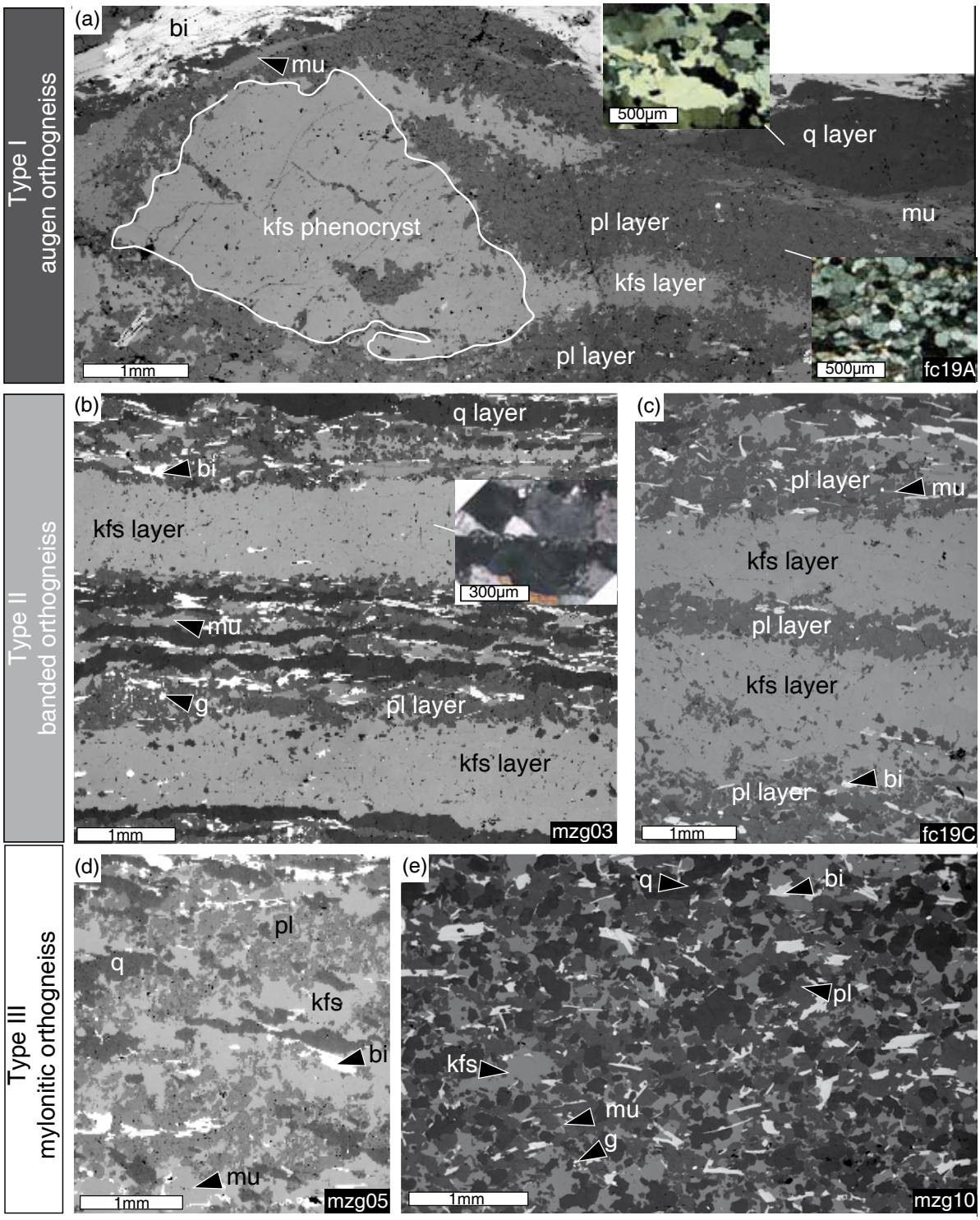

Fig. IV-5: Back scattered electron (BSE) images showing evolution of layering in the deformation gradient. (a) Type I augen gneiss with K-feldspar phenocryst with recrystallized tail, recrystallized quartz augen, and plagioclase layer. (b, c) Well-developped ribbons of feldspar and quartz in Type II banded orthogneiss. Plagioclase-rich layers are enriched in micas and accessories minerals (e.g. garnet). (c, d) Weak layering and mixing of quartz and feldspar in an homogeneous matrix. Scale bar is 1 mm.

Table IV-2: Representative analyses of plagioclases.

Rock type	Augen orthogneiss (Type I)								Banded orthogneiss (Type II)								Mylonite (Type III)	
Sample	MZG02				fc19A				mzg11				fc19C				mzg05	
Analysis n°	364	365	384	379	777	793	805	781	485	478	501	491		756	763	766	447	432
Mineral	pl1 core	pl1 rim	pl2 core	pl2 rim	pl chain	pl1 core	pl1 rim	pl2	pl1 core	pl1 rim	pl2 core	pl2 rim	pl1 core	pl1 rim	pl2 core	pl2 rim	pl core	pl rim
Wt%																		
SiO2	62.91	67.58	62.34	73.29	63.90	62.97	64.48	68.08	63.08	63.41	64.10	65.53	63.77	64.17	64.58	68.34	62.65	63.54
TiO2	0.05	0.05	0.04	0.00	0.03	0.00	0.01	0.02	0.01	0.02	0.01	0.00	0.00	0.02	0.00	0.00	0.05	0.00
Al2O3	23.40	20.93	23.63	16.82	23.23	23.31	22.13	19.77	22.71	23.01	22.79	21.79	22.80	21.70	22.58	20.45	23.35	22.76
FeO	0.01	0.00	0.03	0.04	0.01	0.01	0.12	0.08	0.02	0.02	0.01	0.11	0.01	0.15	0.00	0.01	0.03	0.00
MgO	0.00	0.01	0.00	0.00	0.01	0.00	0.00	0.01	0.01	0.01	0.00	0.05	0.00	0.00	0.00	0.03	0.00	0.00
CaO	4.91	1.51	4.88	0.72	4.19	4.70	2.24	0.53	4.14	2.99	4.17	1.52	4.14	1.69	3.73	1.47	4.78	4.31
Na2O	9.08	10.99	8.99	9.21	9.56	9.14	10.00	11.93	9.32	9.20	9.26	10.54	9.43	10.02	9.83	9.91	9.02	9.54
K2O	0.27	0.04	0.11	0.28	0.19	0.23	0.43	0.11	0.25	0.91	0.23	0.61	0.20	0.92	0.19	0.55	0.28	0.25
Sum	100.63	101.10	100.02	100.35	101.12	100.37	99.41	100.52	99.55	99.57	100.57	100.16	100.36	98.66	100.90	100.76	100.16	100.40
Structural formulae calculated on the basis of 5 cations																		
Cations																		
Si	2.77	2.93	2.76	3.27	2.79	2.77	2.85	2.95	2.80	2.81	2.82	2.87	2.81	2.86	2.82	3.00	2.77	2.79
Al	1.21	1.07	1.23	0.88	1.19	1.21	1.15	1.01	1.19	1.20	1.18	1.12	1.18	1.14	1.16	1.06	1.22	1.18
Ca	0.23	0.07	0.23	0.03	0.20	0.22	0.11	0.02	0.20	0.14	0.20	0.07	0.20	0.08	0.17	0.07	0.23	0.20
Na	0.77	0.92	0.77	0.80	0.81	0.78	0.86	1.00	0.80	0.79	0.79	0.89	0.80	0.86	0.83	0.84	0.77	0.81
K	0.02	0.00	0.01	0.02	0.01	0.01	0.02	0.01	0.01	0.05	0.01	0.03	0.01	0.05	0.01	0.03	0.02	0.01
Sum	5.00	5.00	5.00	5.00	5.00	5.00	5.00	5.00	5.00	5.00	5.00	5.00	5.00	5.00	5.00	5.00	5.00	5.00
an	0.23	0.07	0.23	0.04	0.19	0.22	0.11	0.02	0.19	0.14	0.20	0.07	0.19	0.08	0.17	0.07	0.22	0.20
ab	0.76	0.93	0.76	0.94	0.80	0.77	0.87	0.97	0.79	0.80	0.79	0.89	0.80	0.87	0.82	0.89	0.76	0.79
or	0.01	0.00	0.01	0.02	0.01	0.01	0.02	0.01	0.01	0.05	0.01	0.03	0.01	0.05	0.01	0.03	0.02	0.01

An = Ca/(Ca + Na + K); Ab = Na/(Ca + Na + K); Or = K/(Ca + Na + K)

recrystallised along crystallographic planes forming chains of fine grained K-feldspar, plagioclase (An_{20}) and quartz (Fig. IV-5a) crosscutting the parental grins. Limits of K-feldspar augens are formed by wide zones of myrmekites (Fig. IV-6b) forming the mixture of K-feldspar, quartz and plagioclase. Newly formed and dynamically recrystallized K-feldspar grains (~80-150µm) are present in form of almost monomineral aggregates tails smeared out from the primary phenocrysts (Fig. IV-5a). The dynamic recrystallisation is achieved in those parts of samples where

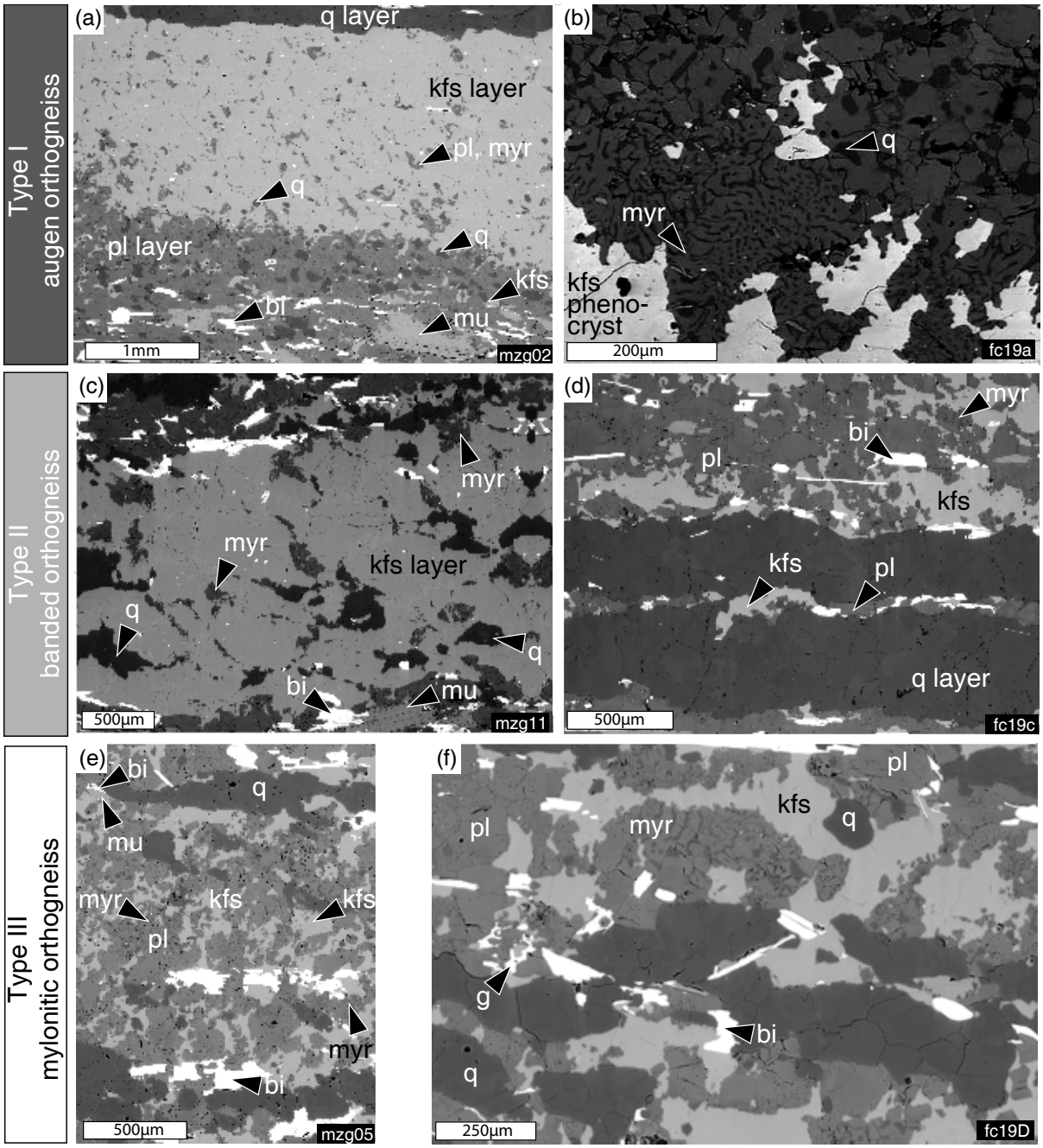

Fig. IV-6: Back scattered electron (BSE) images showing progressive mixing of phases. (a) Straight boundaries between K-feldspar- and quartz-rich layers, irregular boundaries between feldspar and plagioclase layers with rounded quartz at the interface. Micas and accessories mineral preferentially occur in plagioclase layers. (b) From bottom to top: kfs phenocryst, myrmekite zone with progressive coalescence and growth of rounded quartz, sub-equant foam structure in plagioclase-rich layer. (c) Irregular growth of plagioclase and quartz at grain boundaries in a K-feldspar-rich layer. (d) Two small quartz ribbons and irregular K-feldspar in pl rich layer. (e, f) Relics of quartz and feldspar ribbon. Scale bar is 1 mm.

we observe only feldspar layers without relics of phenocryst (Fig. IV-6a). Plagioclase (An_{0-05}) is present in recrystallized K-feldspar layers in form of less than 10µm wide and highly elongated grains rimming feldspar grains or as irregular crystals in triple point sites. Large quartz grains (~20-100µm) form also an interstitial phase located in between K-feldspar grains, preferentially along margins of recrystallized layers (Figs IV-6a & 7b).

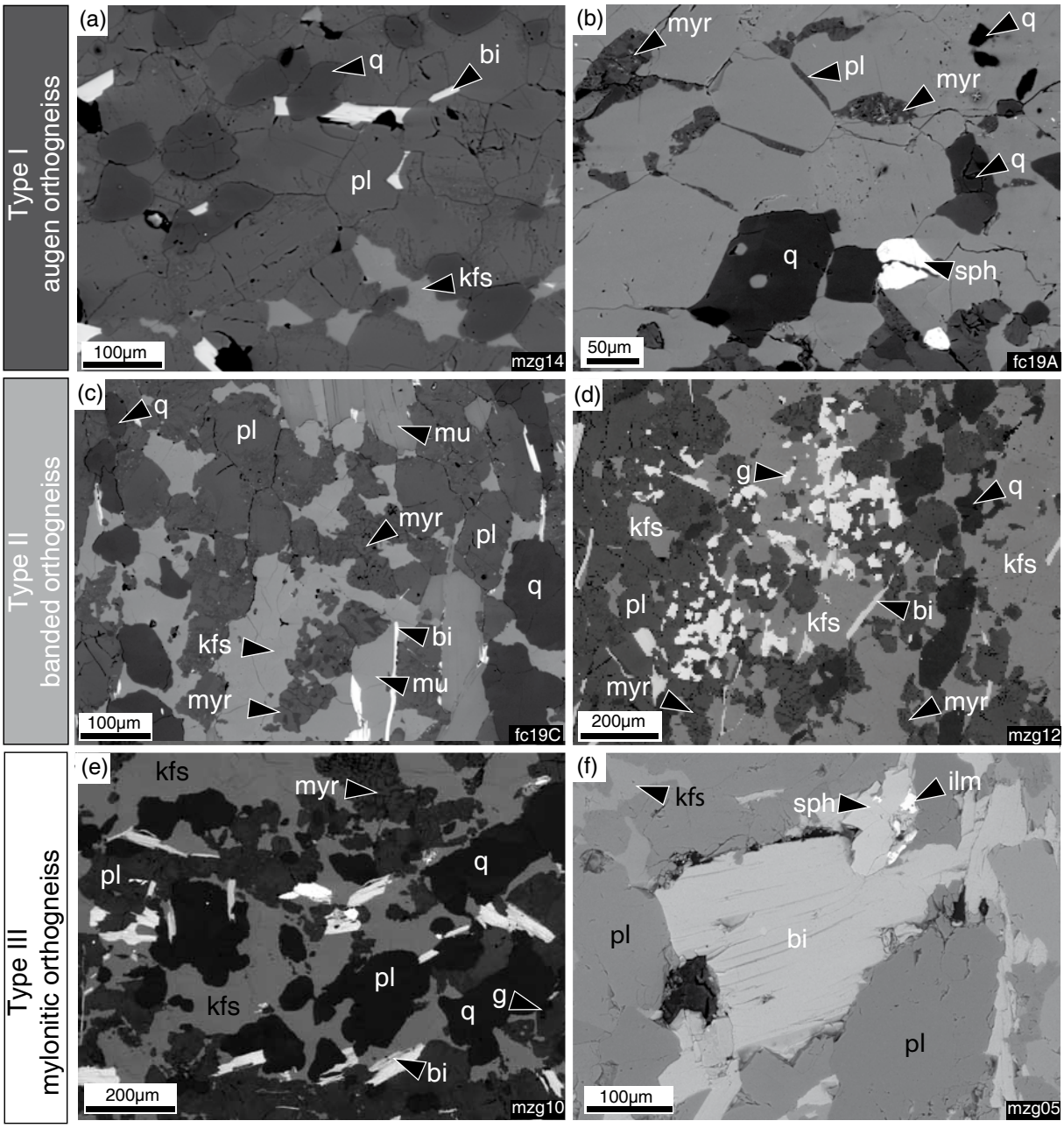

Fig. IV-7: Detailed back scattered images (BSE) showing growth of interstitial phases in originally monomineralic layers. (a) Rounded quartz and cuspate K-feldspar at triple points of plagioclase foam structure. (b) Interstitial plagioclase film and small rounded quartz in K-feldspar-rich layer (c) Relics of equilibrated pl, rounded quartz and K-feldspar embayment in a plagioclase-rich layer. (d) Garnet growth and interpenetration of K-feldspar- and plagioclase-rich layers. (e) Final mixing of all phases. (f) Sphene mantled by ilmenite.

Table IV-3: Representative analyses of muscovite, biotite and garnet

Representative analyses of muscovite, biotite and garnet

Rock type	Augen orthogneiss (Type I)					Banded orthogneiss (Type II)						Mylonitic orthogneiss (Type III)		
Sample	mzg02			fc19A		mzg11			fc19C			mzg05		
Analysis n°	350	516	339	815	825	515	520	455	705	702	726	420	257	408
Mineral	mu	bi	g	mu	bi	mu	bi	g	mu	bi	g	mu	bi	g
Wt%														
SiO2	47.19	36.05	37.36	47.25	35.96	48.94	35.93	38.08	49.07	34.67	37.40	49.29	35.66	37.45
TiO2	0.54	2.97	0.02	0.59	4.18	0.53	2.97	0.04	0.66	1.81	0.03	0.51	2.00	0.017
Cr	0.00	0.04	0.00	0.04	0.01	0.00	0.05	0.01	0.01	0.00	0.00	0.04	0.07	0.00
Al2O3	29.90	17.27	21.35	30.29	17.58	28.48	17.08	21.42	29.48	17.36	21.02	27.64	17.26	21.32
FeO	3.28	22.91	24.55	3.15	21.62	3.18	22.78	23.02	2.58	25.66	25.05	3.41	25.13	22.94
MnO	0.01	0.31	0.53	0.03	0.28	0.00	0.30	3.72	0.03	0.37	2.73	0.03	0.36	4.07
MgO	1.99	6.53	0.43	1.86	6.57	2.12	6.93	0.79	1.54	5.98	0.75	2.11	6.02	0.74
CaO	0.00	0.01	15.46	0.00	0.01	0.00	0.00	12.78	0.22	0.02	13.10	0.00	0.00	12.82
Na2O	0.27	0.11	0.00	0.31	0.10	0.13	0.00	0.00	0.72	0.04	0.00	0.17	0.04	0.00
K2O	10.70	9.57	0.00	10.85	9.35	10.98	9.65	0.00	10.03	8.51	0.00	10.92	8.91	0.00
Sum	93.87	95.78	99.70	94.38	95.65	94.37	95.68	99.86	94.35	94.41	100.09	94.12	95.45	99.35
Structural formulae calculated on the basis of 12 oxygens for garnet. 22 for biotite and muscovite														
Cations														
Si	3.22	2.88	2.97	3.20	2.88	3.33	2.87	3.03	3.33	2.87	2.97	3.36	2.87	2.99
Ti	0.03	0.18	0.00	0.03	0.25	0.03	0.18	0.00	0.03	0.18	0.00	0.03	0.12	0.00
Cr	0.00	0.00	0.00	0.00	0.00	0.00	0.00	0.00	0.00	0.00	0.00	0.00	0.01	0.00
Al	2.40	1.62	2.00	2.42	1.66	2.28	1.61	2.01	2.36	1.61	1.97	2.22	1.64	2.01
Fetot	0.19	1.53	1.63	0.18	1.45	0.18	1.52	1.53	0.15	1.52	1.67	0.20	1.69	1.53
Mn	0.00	0.02	0.04	0.00	0.02	0.00	0.02	0.25	0.00	0.02	0.18	0.00	0.02	0.28
Mg	0.20	0.78	0.05	0.19	0.78	0.22	0.82	0.09	0.16	0.82	0.09	0.22	0.72	0.09
Ca	0.00	0.00	1.32	0.00	0.00	0.00	0.00	1.09	0.02	0.00	1.12	0.00	0.00	1.10
Na	0.04	0.02	0.00	0.04	0.02	0.02	0.00	0.00	0.10	0.00	0.00	0.02	0.01	0.00
K	0.93	0.97	0.00	0.94	0.95	0.95	0.98	0.00	0.87	0.98	0.00	0.95	0.92	0.00
Sum	7.00	8.00	8.00	7.00	8.00	7.00	8.00	8.00	7.00	8.00	8.00	7.00	8.00	8.00
X Fe	0.48	0.663	0.97	0.49	0.65	0.46	0.649	0.94	0.48	0.65	0.95	0.48	0.70	0.95
Prp			0.02					0.03			0.04			0.03
Alm			0.50					0.49			0.51			0.51
Grs			0.42					0.35			0.36			0.37
Sps			0.01					0.08			0.06			0.09

XFe = Fe/(Fe + Mg); Prp = Mg/(Fe +Mg+Ca+Mn); Alm = Fe/(Fe + Mg + Ca + Mn); Grs = Ca/Fe + Mg + Ca + Mn); Sps = Mn/(Fe + Mg + Ca + Mn).

Plagioclases layers (Fig. IV-5a) are made of subequant plagioclase grains 60-80µm in size with foam like appearance and excellent triple point network (Figs IV-5a & 6b). Their compositions change from the core (An_{05-10}) to the rim (An_{0-05}) (Fig. IV-8a & Table IV-2). They contain interstitial phases in form of small rounded quartz (20-100µm, Fig. IV-6a) and highly cuspate K-feldspar grains (10-50µm) located at triple point junctions (Fig. IV-7b). Garnet form clusters 500µm wide made of small isolated garnet ($alm_{0.48-0.53}py_{0.012-0.022}grs_{0.42-0.46}sps_{0.01-0.02}$, Fig. IV-8b & Table IV-3) grains 5-50µm in size. Muscovites laths occur either in biotite rich aggregates or as small grains inside plagioclase layers. They show Si content spreading between

Fig. IV-8: (a) Ternary diagrams showing the composition of plagioclase grains in plagioclase-rich layer and interstitial plagioclase in K-feldspar- and quartz-rich layers in the different metagranite types. Plagioclase in K-feldspar phenocryst (pl chain) is shown for sample fc19A (Type I). No distinction between plagioclases has been done for sample mzg05 (Type III) (see text for explanation). Representative analyses are listed in Table IV-2. ((b, c) Composition of muscovite and biotite for the different metagranite types. Note the increase in Si p.f.u. content in muscovite from Type II to III. Representative analyses are listed in Table IV-3. (d) Garnet composition trends of spessartine, grossular, almandine and pyrope throughout the rock sequence. The data are summarized in box-and-whiskers plots of individual component content (mol.%) vs. rock type. Individual box-and-whiskers plots show median and first and third quartile of the component content. The whiskers represent a statistical estimate of the data range, where outliers are not plotted. The number of analyses is marked. Representative analyses are listed in Table IV-3.

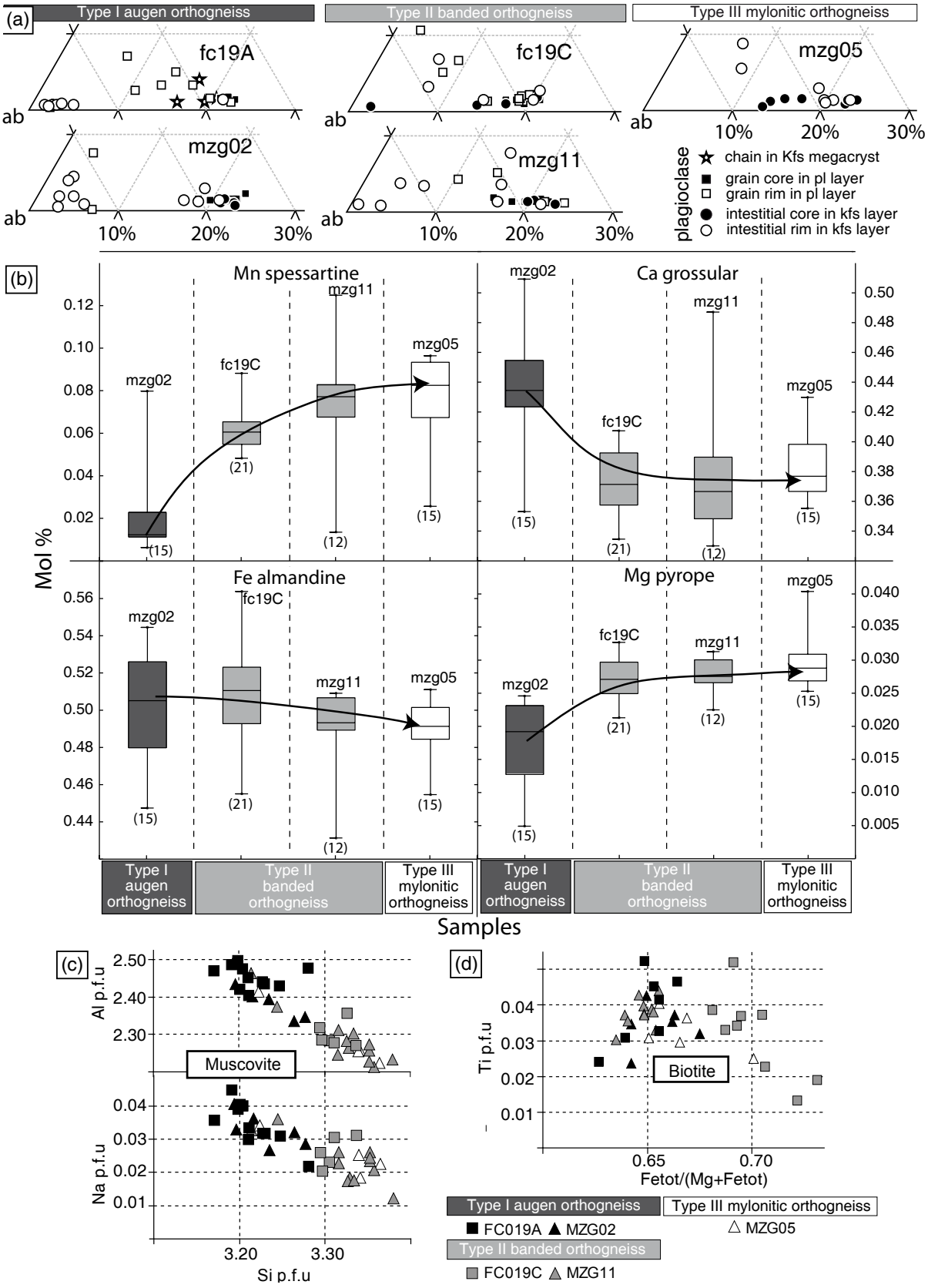
(a)
Type I augen orthogneiss
Type II banded orthogneiss
Type III mylonitic orthogneiss
fc19A
fc19C
mzg05
mzg02
mzg11
ab
10%
20%
30%
plagioclase
chain in Kfs megacryst
grain core in pl layer
grain rim in pl layer
intestitial core in kfs layer
intestitial rim in kfs layer
(b)
Mn spessartine
Ca grossular
Fe almandine
Mg pyrope
Mol %
Type I augen orthogneiss
Type II banded orthogneiss
Type III mylonitic orthogneiss
Samples
(c)
Al p.f.u
Muscovite
Na p.f.u
Si p.f.u
(d)
Ti p.f.u
Biotite
Fetot/(Mg+Fetot)
FC019A MZG02
MZG05
FC019C MZG11

3.18 to 3.28 and Na content 0.02 to 0.04 p.f.u (Fig. IV-8c & Table IV-3). Biotites form large micaceous aggregates or single grains in plagioclase matrix and exhibit XFe values comprised between 0.63 to 0.67 with Ti values of 0.02-0.05 p.f.u (Fig. IV-8d & Table IV-3). Sphene, illmenite, apatite are frequent in plagioclase rich layers.

5. 2. Type II: Banded orthogneiss gneiss

Type II banded orthogneiss is characterized by alternation of interconnected ribbons of quartz (0.3-2 mm wide), plagioclase and K-feldspar (1-5mm wide) (Fig. IV-5b). Boundaries between feldspar layers are poorly defined and interlobed with adjacent minerals (Fig. IV-5c), whereas limits between quartz and feldspar aggregates are straight (Fig. IV-5b).

Quartz monomineral ribbons (Fig. IV-5b) are thinner, composed of smaller grains ~50-100µm in size with less serrated boundaries compared to the Type I augengness (Fig. IV-6d).

K-feldspar rich layer are free of relics K-feldspar phenocrysts (Fig. IV-5b,c). They are made of completely recrystallised sub-equant new K-feldspar grain (50-80µm) which show almost straight boundaries covered by numerous interstitial phases represented by 10µm wide films or irregular grains of plagioclase of albitic composition (An_{0-05}, Fig. IV-8a & Table IV-2) and isolated small rounded quartz grains (~20-50µm) or quartz aggregates up to 100µm in diameter mostly located at triple junction points (Fig. IV-6c).

Ribbons of plagioclase are mixed with quartz, K-feldspar, micas and accessory minerals (Fig. IV-5b,c). Relictual foam structure of subequant plagioclase is disintegrated by numerous highly cuspate K-feldspar intergrowths (Fig. IV-6d) that line plagioclase which became rounded and lobated (Fig. IV-7c). Plagioclases shows a weak compositional zoning from core (An_{15-20}) to rim (An_{10-20}, Fig. IV-8a & Table IV-2). Small interstitial rounded quartz grains (~50µm) are also present (Fig. IV-7c). Compared to Type I augen gneiss, the small garnets (Fig. IV-7d) are enriched in spessartine and pyrope (samples fc19C: $alm_{0.49-0.52}py_{0.025-0.030}grs_{0.36-0.40}sps_{0.05-0.06}$ & Sample mzg11: $alm_{0.49-0.51}py_{0.027-0.030}grs_{0.36-0.40}sps_{0.07-0.08}$, Fig. IV-8b & Table IV-3). No variations from core to rim have been observed. Muscovites show an increase in Si p.f.u. content (3.22 – 3.37 p.f.u.) correlated with lower Na content (0.01 – 0.035 p.f.u.) compared to Type I augengneiss (Fig 8c & Table IV-3. There is no clear compositional evolution in biotite (Fig. IV-8d & Table IV-3). Sphene, illmenite, apatite are still frequent in plagioclase rich layers, mostly associated with biotite occurrences.

5. 3. Type III: Mylonitic gneiss

In Type III mylonitic orthogneiss, relics of ribbons of feldspars and quartz are very narrow (less than 1mm wide and 200µm, respectively) and not continuous (few thousand µm long) (Fig. IV-5d). Feldspar and quartz are mixed with plagioclase and micas (Fig. IV-6e,f). In some places the quartz and feldspar ribbons are almost absent (sample mzg10, Fig. IV-5e). Boundaries between K feldspar (~50µm) and plagioclases (~50µm) are highly irregular with cuspate K feldspar

and lobate plagioclase boundaries whereas relictual boundaries between plagioclase grains are almost straight (Fig. IV-7e). Small aggregates or isolated grain of quartz (50µm) show rounded boundaries. Micas are completely dispersed. Composition of small garnets which are associated with micas and plagioclase is stable compared to Type I and II orthogneiss, with a weak increase in spessartine content ($alm_{0.48\text{-}0.50}py_{0.027\text{-}0.031}grs_{0.37\text{-}0.40}sps_{0.07\text{-}0.09}$, Fig. IV-8b & Table IV-3). White micas show high Si content values around 3.35 p.f.u. associated with low Na contents close to 0.02 p.f.u. (Fig. IV-7c & Table IV-3). Biotite exhibits absence of compositional variations compared to those measured in Type I and II orthogneiss (Fig. IV-8d & Table IV-3). Sphene and illmenite are generally isolated but sphene is locally mantled by illmenite (Fig. IV-7e).

6. Petrological modelling

The pseudosection was calculated using THERMOCALC (ref) and the dataset 5.5 (Holland & Powell, 1998; November 2003 upgrade), in the system Na2O-CaO-K2O-FeO-MgO-Al2O3-SiO2-H2O-TiO2-O (NCKFMASHTO) with the biotite and melt models from White *et al.* (2007), garnet from Holland and Powel (1998), ilmenite from White *et al.* (2000), feldspars from Holland & Powell (Holland & Powell, 2003), white mica from Coggon & Holland (2002). The analysed rock composition of sample MZG5 in wt% SiO_2=71.29, TiO_2=0.32, Al_2O_3=14.68, FeO=2.57, MnO=0.03, MgO=0.66, CaO=1.75, Na_2O=3.48, K_2O=4.08, P_2O_5=0.17), was used for calculations. The mineral abbreviations used are mu = muscovite, qtz = quartz, g = garnet, bi = biotite, mu = muscovite, ksp = K-feldspar, pl = plagioclase, liq = liquid; ilm = ilmenite; ru = rutile; sph = sphene, ky = kyanite, ep = epidote. A stable pseudosection shows omphacite line running approximately from 11kbar and 650°C to 17kbar and 850°C and no sphene stability at high pressure (not shown). Because omphacite is not observed in the samples and sphene is present systematically, we calculated equilibria metastable with respect to omphacite (Fig. IV-pseu], and these involve also stability of sphene at high pressure. Mineral composition isopleths, *z*(g)=Ca/(Ca+Fe+Mg) and *y*(mu)=Si p.f.u. were plotted for garnet and muscovite. The amount of H_2O is chosen to allow the H2O-undersaturated and melt-absent assemblages on a prograde P−T path and at peak P−T conditions, as is indicated by quartz exudations filling the S1-syntectonic structures (Štípská *et al.*, this volume), that indicate absence of melt during D1 deformation. The major features of the pseudosection involve melt being stable above the line heading approximately from 11kbar and 650°C to 20kbar and 810°C, biotite stability up to 19−20kbar in the melt-absent field and up to 800−850°C in the melt-persent fields, muscovite out and kyanite-in line heading from 750 °C and 9kbar to 830°C and 16kbar. Ilmenite is stable in the LP part of the psudosection, whereas sphene is stable in the LT and HP part of the pseudosection, in opposite to rutile along a line from 670°C and 10kbar to 800°C and 20kbar.

The textural features indicate that the observed assemblage, muscovite, biotite, garnet, plagioclase, K-feldspar, sphene, ilmenite and quartz are stable minerals in the S1 mylonitic fo-

liation. However, there are chemical differencies, because least deformed Type I shows different garnet (until grs=0.50 to 0.42-0.46) and muscovite (Si p.f.u.=3.16-3.28) compositions then more deformed Types II and III (garnet grs=0.37-0.40, muscovite: Si p.f.u.=3.22-3.38).

This assemblage (but without rutile) occurs in the pseudosection in the g-mu-bi-sph fields that occurs in the HP part of the pseudosection, between 10 and 20kbar. The compositional isopleths for garnet and muscovite correspond well to the measured values for the Types II and III at around 19kbar and 730°C, while for the Type I fit better in the lower pressure conditions, at about 12kbar and 650°C. It is interpreted as incomplete equilibration of the

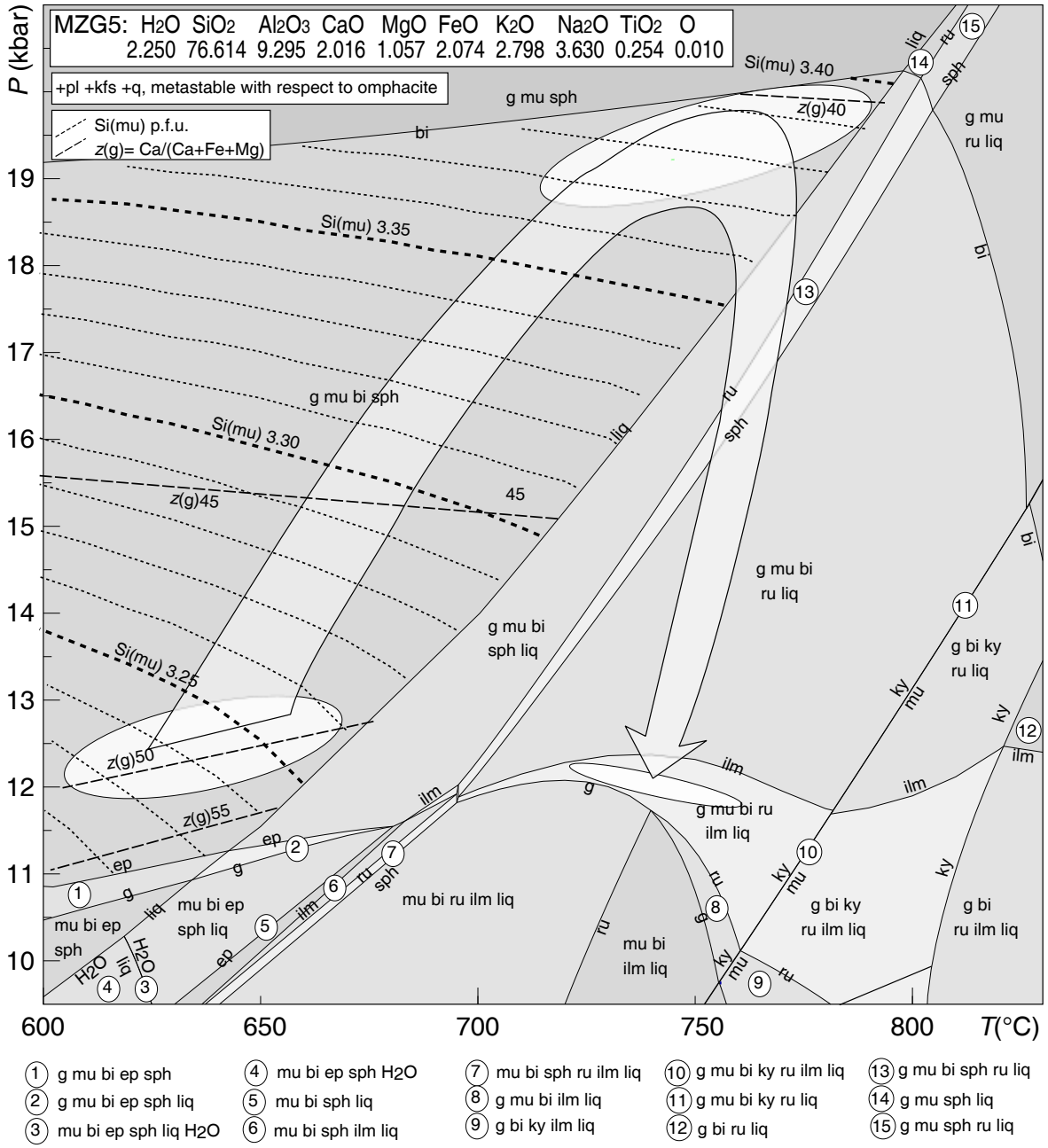

Fig. IV-9: Pseudosection calculated for the rock composition of the sample mzg05 (NCKFMASHTO system, in moles adjusted to 100%). with calculated isopleths of muscovite (Si p.f.u.) and garnet z(g). P-T evolution from Type I to type III is shown.

mineral assemblage in least deformed orthogneiss Type I at high-pressure, and preservation of the equillibria corresponding to P-T conditions attained on the prograde path. The assemblage and chemistry of the phases in penetratively deformed Types II and II shows equilibration at high pressure, around 18−21kbar and 700−750°C. This peak P-T estimate is close to the peak estimated for the eclogites by Štípská *et al.* (this volume), and shows shared HP history of both eclogites and surrounding orthogneisses in the S1 flat fabric. The decompression path is not documented in the studied samples, but involves likely crossing the liq-in line that is compatible with presence of structures filled by melt during development of the S2 and S3 fabrics in the orthogneisses around the eclogite belt. Likely point on the retrograde P−T path is within the field g-mu-bi-ru-ilm-liq, as is indicated by ilmenite overgrowths on sphene. These P−T estimates of retrogression are not connected with specific structure development in the studied samples.

7. Quantitative microstructural analysis

Quantitative microstructural analysis is the statistical study of grain size, shape and spatial distribution of grain and their boundaries. Theses microstructural parameters are sensitive to variations in physical conditions, strain intensity and mineral reactions allowing to define rock microstructure using quantitative values. This approach permits to follow microstructural trends and better constrain processes like grain coarsening, annealing, nucleation and syn-deformational growth.

In order to evaluate quantitatively the above described microstructural sequence of rock type, we evaluate the grain size, the crystal size distribution (CSD), the grain shape preferred orientation (SPO), the grain boundary preferred orientation (GBPO) and the grain contact frequency (GCF). For this, we manually digitized 9 portions of XZ sections of representative thin section (3 per Type) with ESRI ArcMap desktop Gis using superposition of BSE and classical optical images (Fig. IV-10). Shapefiles .shp outup, i.e. maps of grains with ful topology (between 2000-5000 grains per map), were carried out using the MATLAB™ PolyLX toolbox V2.0. (Lexa, 2003; http://petrol.natur.cuni.cz/ ondro/). Except for the sample mzg10 (Type III) which show complete mixing of phases, we also separated aggregates (mono phase rich layer) from interstitial phases.

7. 1. Grain size statistics and Crystal Size Distribution (CSD)

The evolution of the crystal size has been first evaluated using the grain size (Ferret diameter) in aggregates and interstitial phases. Results are presented for each sample in box-whisker plot (Fig. IV-11a), which shows median value and the grain size spread as third and first quartile. From Type I augen orthogneiss to Type III mylonite, quartz aggregates show a decrease of mean grain size from 110 to 50 µm in conjunction to decrease of grain size spread. A similar trend is visible for both grain size mean (from 150 to 50 µm) and spread of K-feldspars. Plagioclase

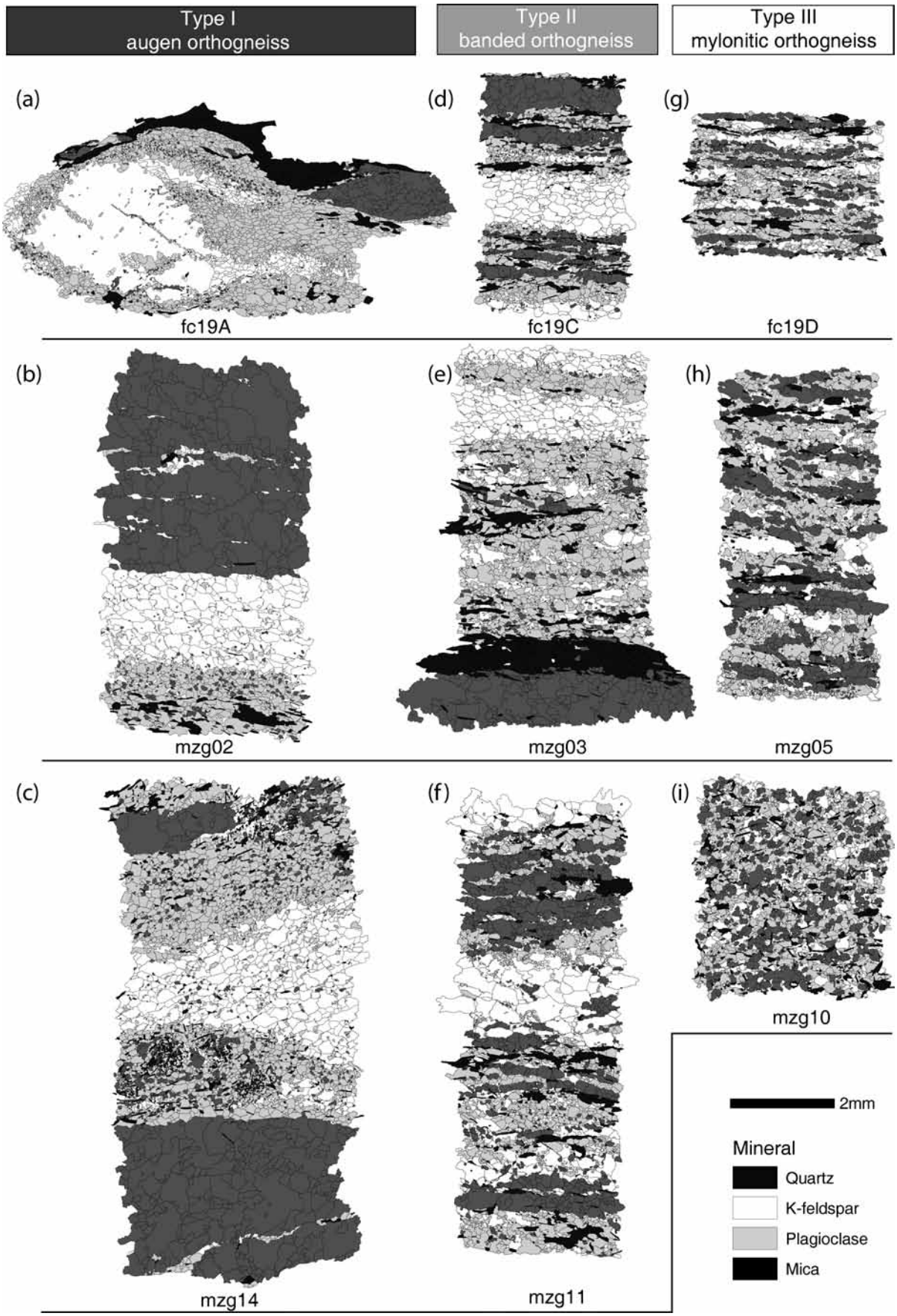

Fig. IV-10: Representative digitalized microstructures of the different metagranite types that have been used for quantitative microstructural analysis (see text for method). Same scale for each samples. (a, b, c) Type I augen orthogneiss. (d, e, f) Type II banded gneiss. (g, h, i) Type III mylonitic orthogneiss.

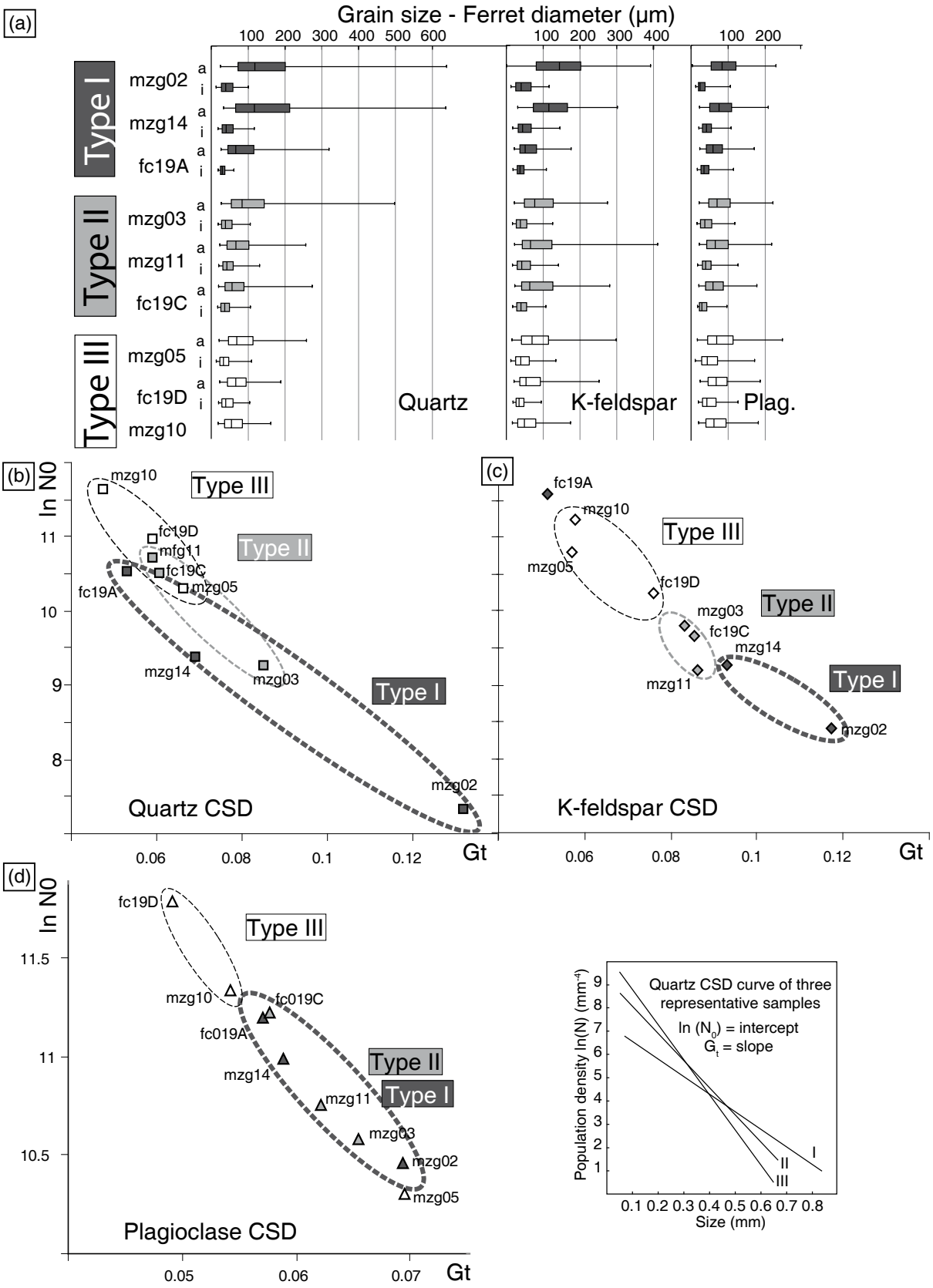

Fig. IV-11: Evolution of grain size diameter and crystal size distribution (CSD) in the deformation gradient. (a) Grain size diameter (i.e. Ferret diameter, or equivalent area diameter) presented in box-and-whiskers plot for aggregates ("a") and for interstitial phases ("i") from type I to type III. No distinction between aggregates and interstitial phases for sample mzg10 (Type III). Plot of crystal size distribution (CSD) parameters N0 and Gt of (b) quartz, (c) K-feldspar and (d) plagioclase. Inset shows examples of linearized CSD curves used for Gt and N0 estimates. See text for explanation.

grains in aggregates are more equant with a stable mean grain size of 90 to 50µm in all rocks types. Interstitial plagioclase in K-feldspar rich layers shows a weak increase of the grain size from 30 to 50µm with increasing finite strain, whereas grain size of interstitial quartz in feldspar layers and interstitial K-feldspar in plagioclase rich layers remain constant (~10-50µm).

The crystal nucleation and crystal growth can be revealed using the technique of Crystal Size distribution (CSD, Randolph & Larson, 1971). This method was initially developped for metallurgical studies and permits to evaluate the nucleation density (N_0) and growth rate multiplied by time (G_t). The following equation shows a log linear relationship between grain size (L) and population density (N, i.e the number of crystals per size per volume) (Higgins, 1998)

$$N=N_0e^{-L/Gt}$$

This technique has been also used for metamorphic rocks by Cashman & Ferry (1988) and more recently by Lexa *et al.* (2005) Hasalová *et al.* (2008b) and Schulmann *et al.* (2008). The latter authors apply the method not to determine kinetics of crystal growth and nucleation but to obtain numerical values which may compare individual grain size distributions. This method allows to find subtle trends in growth and nucleation histories compared to simple visual inspection of grain size histograms. We used the method of Peterson (1996) where construction of linear regression by plotting L in function of ln (N) give access to constant ln N_0 (intercept) and G_t (slope). Each sample has been plotted separately using method of Lexa *et al.* (2005) (Fig. IV-11b-d).

Quartz, K-feldspar and plagioclase show a systematic decrease of Gt associated with an increase of N_0 values from Type I to Type III microstructure. Exceptional are sample fc19A (Type I) that shows high value of N_0 for K-feldspar and sample mzg05 (Type III) with a low N_0 value for plagioclase compared to samples of the same group.

7. 2. Grain Shapes and Shape Preferred Orientation (SPO)

The aspect ratio, i.e ratio between long and short axis of best fit ellipse, characterise the shape of grain (Panozzo, 1984). The Shape Preferred Orientation (SPO) is calculated using the eigne-value ratio of Scheidegger-Watson orientation tensor of individual linear segments of grain boundaries of each phase (Lexa *et al.*, 2005). In dynamically recrystallised rocks, a high SPO is interpreted to reflect a recrystallisation by dislocation creep, whereas low SPO can be related to diffusion creep regime or annealing postdating deformation.

In "mono" mineral aggregates (Fig. IV-12), a constant and low aspect ratio of each phase is observed for all orthogneiss Types. Except for the quartz aggregates where no clear variation is visible (not shown), shape preferred orientation increases from Type I to Type II and

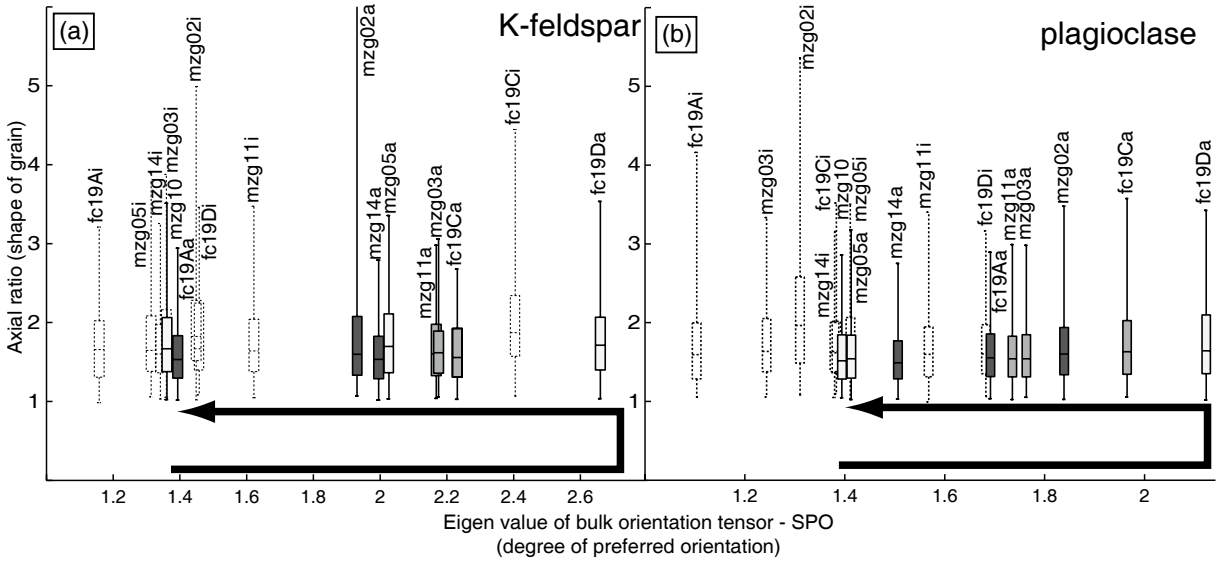

Fig. IV-12: Plot of the shape and shape preferred orientation of (a) K-feldspar and (b) plagioclase grains. Box-and-whiskers plots display axial ratio (representing the shape of grains) vs. eigenvalue of bulk preferred orientation (showing the degree of preferred orientation of grains). Full lines correspond to aggregates while dashed lines stand for interstitial phases. For the aggregates, note the constant axial ratio in all types and the first increase and final decrease of SPO. Note also the weak SPO of interstitial phases.

decrease from Type II to Type III. Interstitial feldspar (plagioclase and K-feldspar in k-feldspar and plagioclase rich layer respectively) show slightly higher aspect ratio associated with a weaker shape preferred orientation compared to aggregate grains.

7. 3. Grain Contact Frequency (GCF) and Grain Boundary Preferred Orientation (GBPO)

The grain contact frequency method (Kretz, 1994) allows to study the statistical deviation from random spatial distribution of grains. Random distribution corresponds to rocks with the same proportion of like-like contact (contact between grains of the same phases) and unlike contact (contact between grains of different phases). In aggregates distribution, quantity of like-like contacts is higher than unlike contacts whereas regular distribution shows preferentially unlike contact. The degree of deviation from random distribution is measured by using the following the equation:

$$\chi = \frac{Observed - Expected}{\sqrt{Expected}}$$

For like-like contact, McLellan (1983) interprets random distribution (i.e. χ=0) to be a result of rapid quenching of granitic melt. Regular distribution (i.e. χ negative) is expected with process of extensive solid-state annealing (Flinn, 1969; Vernon, 1976; McLellan, 1983; Lexa *et al.*, 2005) in order to reduce the surface energy (Seng, 1936; DeVore, 1959), and also by mechanical mixing, and heterogeneous nucleation (Kruse & Stünitz, 1999; Baratoux *et al.*, 2005). Aggregate distribution (i.e. χ positive) is formed by solid-state differentiation mostly by dynamic recrystallisation of rheologicaly different phases (Vernon, 1976; McLellan, 1983;

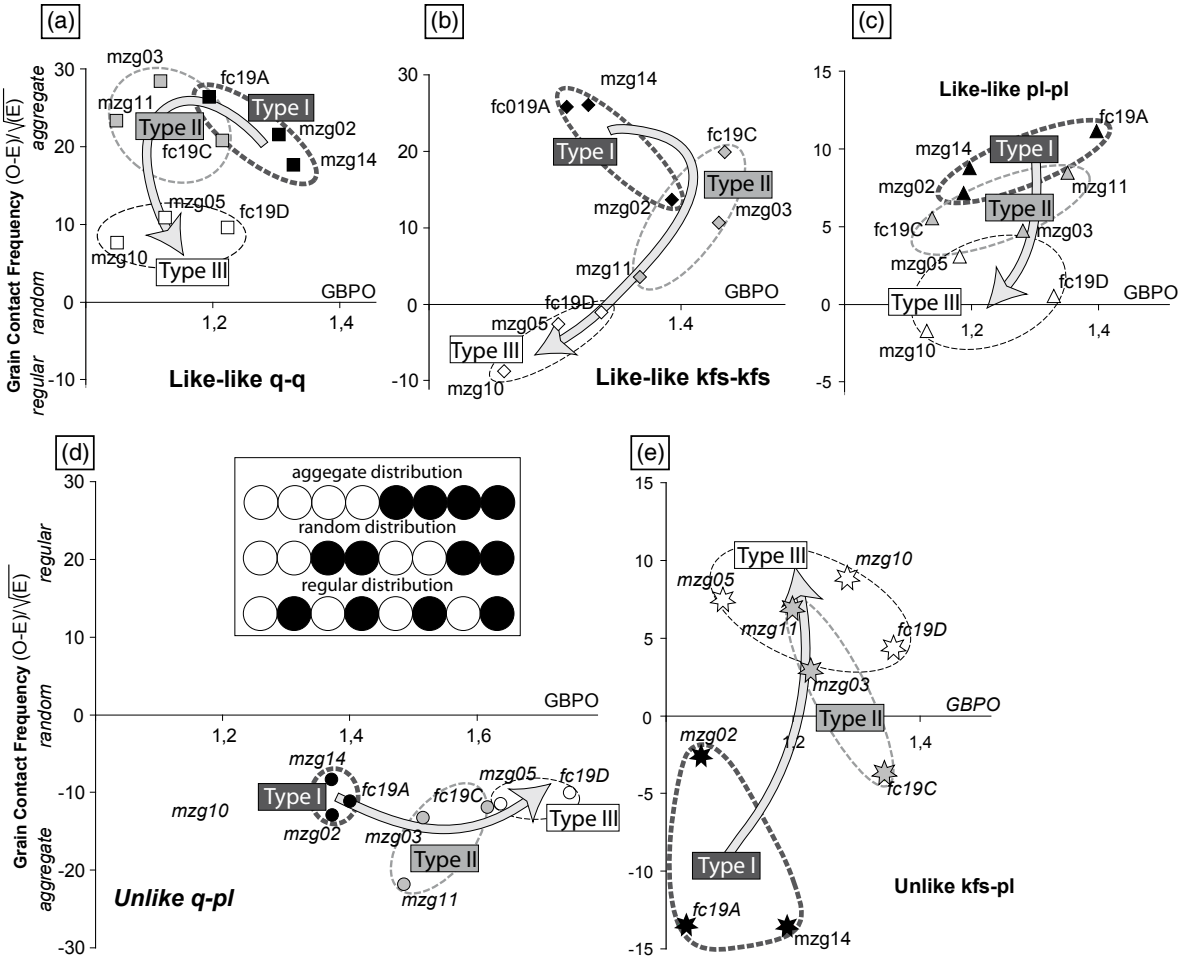

Fig. IV-13: Plot of the grain boundaries statistics for (a) quartz, (b) K-feldspar and (c) plagioclase. Deviation from random spatial distribution vs. degree of grain boundary preferred orientation (GBPO) is calculated using grain contact frequency method and ratio of eigenvalues of the bulk matrix of inertia (see text for details). Aggregates and intersticial phases have not been distinguished for this statistic. Like-Like statistics for quartz show a decrease of GBPO and a loose of aggregate distribution in rocks sequences, whereas like-like contacts in feldspar show a small increase followed by a decrease of GBPO associated to the transition from aggregates to random distribution. Unlike K-feldspar – plagioclase contacts mirror this late evolution.

Schulmann *et al.*, 1996).

As it have been proposed by Lexa *et al.* (2005), the results are presented in plots of Grain Contact Frequency (GCF) against Grain Boundary Preferred Orientation (ratio of eigenvalues of bulk matrix of inertia, length-weighted) showing the spatial evolution of grains from Type I to Type III (Fig. IV-13). For like-like contacts, quartz show an increase of aggregate distribution from Type I to Type II associated with a decrease of GBPO terminated with a decrease of aggregate distribution towards the Type III (Fig. IV-13a). Both K-Feldspar and plagioclase show a decrease of aggregate distribution from Type I to Type III towards random to slightly regular distribution. GBPO of K-feldspar increases from Type I to Type II and de-

creases towards Type II orthogneiss whereas GBBO of plagioclase monotonously decreases (Fig. IV-13b,c). Distribution of quartz-plagioclase contacts remains constant but their GBPO values increase with increasing degree of deformation (Fig. IV-13d). In contrast, number of K-feldspar-plagioclase contacts is increasing continuously with slightly increasing GBPO (Fig. IV-13e).

8. Lattice Preferred Orientation (LPO)

The Lattice Preferred Orientation (LPO) or Crystallographic Preferred Orientation (CPO) have been measured in aggregates (except in sample mzg10 where no ribbon is visible) of representative thin sections of each type for quartz and K-feldspar. Acquisition of data has been done in manual mode using electron back-scattered diffraction technique (Prior *et al.*, 1999; Bascou *et al.*, 2001; Prior *et al.*, 2009) on a scanning electron microscope TESCAN Véga 2 XMU in the EOST laboratory (University of Strasbourg). Direct visualisation of kikuchi bands patterns associated with comparison of back scattered and optical images permit to plot only one measurement per grain. Output .ang data files (TSL ASCII) have been transformed into .ctf file using HKLtechnology in order to be read and plot using PFch5 software (ftp://ftp.dstu.univ-montp2.fr/pub/TPHY/david/pc/). The results are presented in lower hemisphere equal area stereographic projection in homogeneous sample coordinates (Z direction up directed, and X in horizontal right direction. LPO of quartz is presented in the pole Figure IV-of the crystallographic direction < c > (001) and < a > (100) (Fig. IV-14). For the K-feldspars, we only plot plane and directions that fit with main axes of the finite strain ellipsoid (Fig. IV-15).

8. 1. LPO of quartz

LPO of quartz c axis in Type I microstructures aggregates (sample mzg02) show a strong maxima in an intermediate position close to YZ plane and weaker sub-maxima at the periphery of the diagram forming an asymmetric incomplete single girdle. This suggest a mean activity of rhomb <a + c> and sub-ordinate basal <a> slip system in a top-to-the north non-coaxial shearing. Quartz c axis in type II microstructures aggregates is similar for the sample mzg03 with activity of rhomb <a + c> and basal <a> slip system in a single asymmetric cross girdle whereas sample mzg04 suggest addition of prism <a> activity and development of incomplete asymmetric crossed girdle (Lister & Paterson, 1979; Lister & Hobbs, 1980). For Type III microstructures, activities of above mentioned slip systems decrease, but maxima are still visible in the periphery (sample mzg05) or in intermediate part of the diagram (sample mzg10), with development of either crossed or single asymmetric girdle in samples mzg05 and mzg10, respectively, corresponding to a weak activity of basal <a>, rhomb <a+c> and prism <a> slip systems (Schmid & Casey, 1986). The characteristic feature of all diagrams is the constant kinematics of non-coaxial shearing towards north.

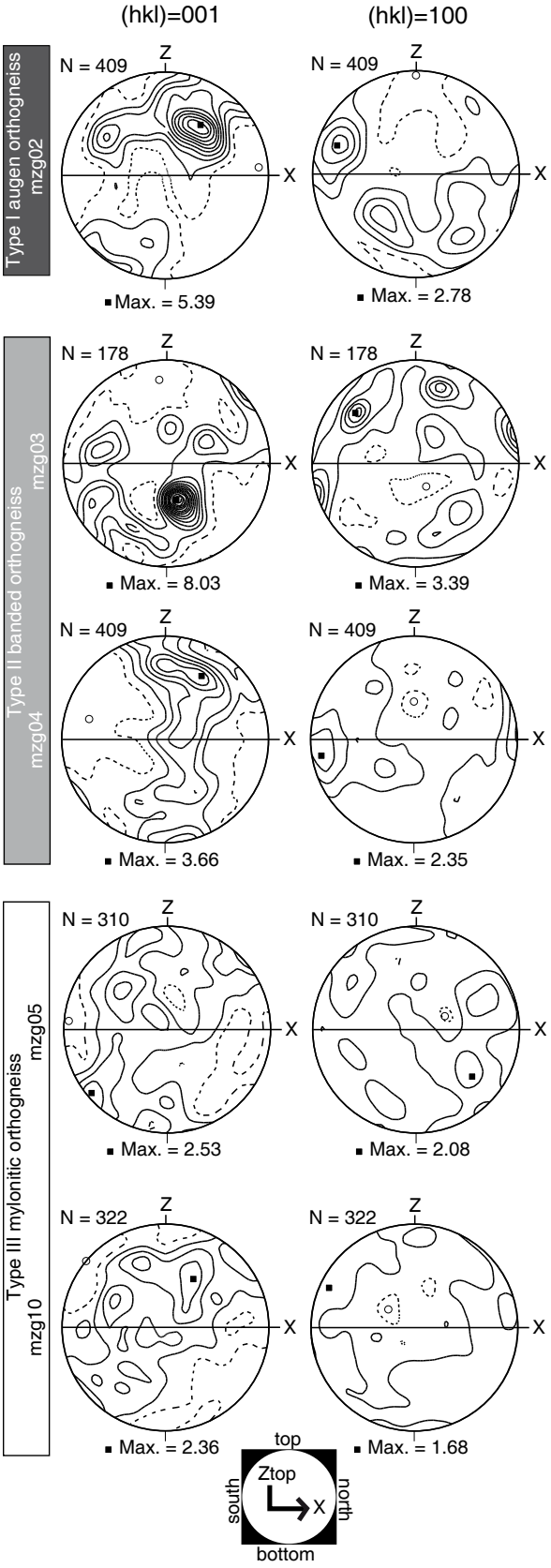

Fig. IV-14: Crystallographic preferred orientation of quartz ribbons from electron backscattered diffraction in situ measurements. Pole diagrams are represented in equal area, lower hemisphere projection, contoured at intervals of 0.5 times uniform distribution. X and Z refer to the direction of lineation and pole to the foliation, respectively. Quartz shows activity of basal <a>, rhomb <a> and weak prism <a> slip systems in Type I and II decreasing in Type III rocks.

8. 2. LPO of Kfeldspar

LPO of K-feldspar in mono-mineral aggregates in Type I microstructures (sample mzg02) show a strong preferred orientation of the (010) plane parallel to the sample foliation plane. This planar preferred orientation is associated with a strong preferred orientation of the [001] axes parallel to the lineation. This suggest a activation of classic [001](010) slip system reported for K-feldspar (Willaime *et al.*, 1979; Sacerdoti *et al.*, 1980; Schulmann *et al.*, 1996; Franěk *et al.*, 2006). In Type II aggregates (sample mzg04), the activity of [001](010) is still visible but with a weaker maxima compared to the Type I microstructure. This trend further continues in the feldspar from poly-mineral matrix of the sample mzg10 (Type III microstructure) where distribution of wide and weak maxima may suggest minor activity of [001](010) slip system.

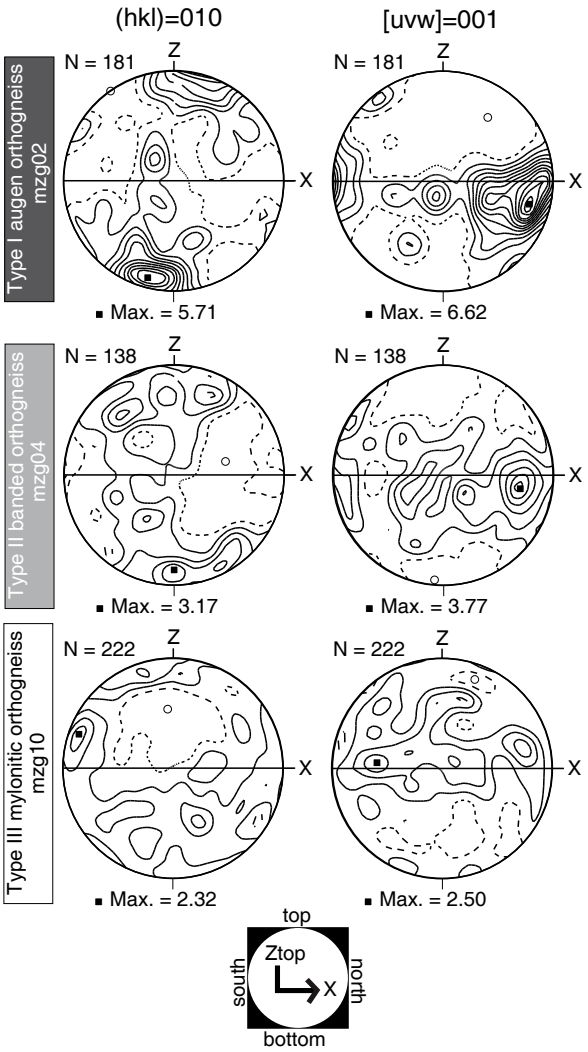

Fig. IV-15: Crystallographic preferred orientation of K-feldspar ribbons using electron backscattered diffraction in situ measurements. Pole diagrams are represented in equal area, lower hemisphere projection, contoured at intervals of 0.5 times uniform distribution. X and Z refer to the direction of lineation and pole to the foliation, respectively. K-Feldspar shows strong activity of (010)[001] glide system in Type I and II, whereas this pattern decreases in the Type III mylonite.

9. Discussion

In this work, we performed a detailed microstructural study of progressively deformed eclogite bearing orthogneiss (peak conditions ~18kbar at ~740°C) from the Orlica Śnieżnik Dome (Central Sudetes). Based on macroscopical and finite strain analysis the studied orthogneisses sequence was divided into three rock types that correspond to an increase of the finite stain associated with major microstructural transformation of original metagranite, i.e. augen orthogneiss (Type I), banded orthogneiss (Type II), mylonitic orthogneiss (Type III). We discuss variations in deformation mechanisms of individual minerals in terms of rheological behaviour of felsic crust during continental subduction. The studied finite strain gradient is proposed to develop along subduction path as a result of an isochemical and prograde metamorphic – deformation process. The variations in mineral compositions of garnet and micas reflect significant pressure increase from the Type I augen gneiss to the Type III mylonitic orthogneiss indicating that three orthogneiss types originated in different crustal depths. Finally, based on this microstructural and petrological study a model of burial of deeply subducted felsic crust in a continental accretionary wedge is proposed.

9. 1. Interpretation of deformation mechanisms and rheology of orthogneiss across finite strain gradient

In the Type I augen orthogneiss, recrystallized augens of quartz and relics of primary feldspars are still present whereas plagioclase forms elongated but poorly connected layers. This indicates that plagioclase is at this stage certainly the weakest phase whereas K-felspar +/- quartz made a rigid framework. Increasing deformation allows the formation of layering that is associated to a decrease of grain size of quartz and feldspar that culminates in the Type II banded orthogneiss. The quartz-feldspar mixture is developed in the Type III mylonitic orthogneiss where relictual ribbons are small or totally absent.

The Type I orthogneiss reveals combination of localized deformation marked by development of narrow recrystallized zones cross-cutting feldspar phenocrysts accompanied with chemically driven developments of myrmektic fronts on porphyroclasts margins (Hanmer, 1982; Simpson, 1985). These processes are accompanied by dynamic recrystallization of both K-feldspar and adjacent plagioclase into medium-grained matrix. Relatively large mean grain size is associated with large grain size spread which cannot result from equilibrium between stress and dynamically recrystallized grain size (e.g. Baratoux *et al.*, 2005; Schulmann *et al.*, 2008). The grain size measurements took place in relatively large distance away from poprhyroclasts to avoid the grain size inheritance of parental grains. Therefore, the grain size distribution has to reflect an important component of syn-to post-deformational crystal growth at this stage. This is compatible with quartz microstructure which can be interpreted as a result of grain boundary migration recrystallization mechanisms while K-feldspar recrystallized mosaic reveals signs of post-recrystallization annealing (Fig. IV-5). The growth of recrystallized matrix

grains can be favoured by well developed aggregate distribution Fig. IV-13 precluding pinning of growing phases by interstitial phases. This microstructure is characterized by strongest LPO of both recrystallized quartz and K-feldspar from all rock types, which indicate intense plastic deformation (Heilbronner & Tullis, 2006) which may be enhanced by post-deformational annealing (Park *et al.*, 2001; Heilbronner & Tullis, 2002).

The Type II banded orthogneiss shows development of contiguous quasi monomineral layers composed of fully recrystallized grains of feldspars and quartz. This evolution is connected with decreasing mean grain size (Fig. IV-11a) and spread which is manifested by decreasing Gt parameter and increasing N0 values in Gt-N0 diagram (Fig. IV-11b-d). This trend is accompanied with destruction of aggregate distribution and increase of volume of interstitial phases in feldspar dominated layers (Fig. IV-13). In progressively recrystallized and deformed metagranite sequence, the mean grain size decrease associated with decrease of standard deviation would be interpreted as a result of grain size equalization due to progressive re-equilibration to applied stress (Shimizu, 1998, 2008). However, the increase of volume of interstitial phases in feldspars dominated layers indicates a dominant nucleation process associated with removal of large crystal grain suggesting suppressed crystal growth. Therefore, the large crystals which were present in Type I orthogneiss were either recrystallized or dissolved and reprecipitated elsewhere. This kind of dissolution and precipitation is supported by presence of higly lobated boundaries between interstitial k-feldspar and plagioclase. The cuspate – lobate relationships suggest extreme mobility of grain boundaries (Gower & Simpson, 1992) which cannot be explained by conservative recrystallization models. In addition, the form of interstitial phases is not compatible with mechanical mixing model (Kruse & Stünitz, 1999). Instead, the mineral mixing observed here is due to continuous mineral reactions responsible for precipitation of new phases and corrosion of reactants (e.g. Franěk *et al.*, 2006). The Type II orthogneiss reveal distinct but weaker LPO of quartz and feldspars compared to Type I rock (Figs IV-14 & 15). However, the decrease of quartz and feldspar LPO strength is incompatible with increasing strain intensity determined by strain measurements (Heilbronner & Tullis, 2006). The mineral LPO's thus document activity of dislocation creep importance of which is however decreasing compared to Type I orthogneiss. Therefore, microstructural observations and quantitative microstructural data can be interpreted as a result syndeformation metamorphic reactions contributing to strain weakening and partial reduction of grain size (Holyoke Iii & Tullis, 2006a, b) . The prevailing deformation mechanism of quartz and K-feldspar is still dislocation creep but diffusion creep component cannot be excluded.

The Type III orthogneiss is characterized by entire destruction of aggregate distribution resulting in complete mixing of all mineral phases (Fig. IV-13), further decrease of grain size (Fig. IV-11) and loss of lattice preferred orientation of all mineral phases (Figs IV-14 & 15). The crystal size distribution diagram reveals increase of No values associated with vigorous decrease of Gt values. This means that the grain size is shifted towards higly lognormal distribution marked by predominance of small grains and removal of all large grains (Fig.

IV-13). This process would be normally interpreted as a result of increased equilibration of grain size to applied higher stress (e.g. Ulrich *et al.*, 2002). However, the increase of interstitial phases together with strongly lobated grain boundaries of K-feldspar and plagioclase (Fig. IV-7) suggest reaction origin of this microstructure compatible with new garnet microstrutures typical for nucleation process. The strain reaches extreme values in Type III orthogneiss suggesting maximum weakening and strain localization associated to a major change of deformation mechanism. The absence of LPO, complete mixing of mineral phases and significant reduction of grain size are compatible with transition from dislocation creep to grain boundary sliding deformation mechanism (Holyoke Iii & Tullis, 2006a). Our observations are compatible with experimental and natural rock studies suggesting extreme weakening of deformed rocks due to syndeformational reactions (e.g. Berger & Stünitz, 1996; Handy & Stünitz, 2002; Oliot *et al.*, 2010).

9. 2. Open or close system?

Recent studies of Hasalová *et al.* (2008a; 2008b) show that a range of microstructures of interstitial minerals described in this work can be attributed to arrival of external fluids or highly corrosive external melts. This is valid for cuspate – lobate relationships of feldspars (Figs5d, 6e & 7e) lining of large K feldspar by albite grains (Fig. IV-7b), development of complete mineral mixture at high strains and nucleation dominated CSD patterns (Fig. IV-11b-d). However, the influx of external fluids has to be associated with major modification of bulk rock chemistry and REE patterns as shown by Hasalová *et al.* (2008c). This was not observed by our study (Fig. IV-4) indicating that there is no or very limited influx of external fluids/melts and that the system can be considered as chemically closed or that fluids were in complete chemical equilibrium with parental rock, which is unlikely. Therefore, unlike the microstructural sequence studied by Hasalová et al. (2008a; 2008b; 2008c) the studied gradient results from closed system metamorphic reactions and deformation.

9. 3. HP character of studied orthogneiss sequence

Despite the poor assemblages (e.g. lack of omphacite) that has been found in studied orthogneiss sequence, there are many indications that these rocks were metamorphosed at eclogites facies as for example high Si content in muscovite and presence of Ca-rich garnet (Proyer, 2003). The absence of omphacite in the orthogneisses can be explained by kinetic arguments (Oberhänsli *et al.*, 1983; Koons *et al.*, 1987) suggesting that in natural HP metagranites clinopyroxene is less stable than garnet (Proyer, 2003). The pseudosection modelling (Fig. IV-9) shows that sphene can be stable up to 18 kbar if the omphacite is not present in the HP assemblage. Another important consequence is the decrease of Ca content in garnet with increasing pressure (Fig. IV-9). Consequently, the evolution of composition of garnet (decrease of Ca from Type I to Type III orthogneiss) and increase of Si content in muscovite in studied rock sequence (Fig.

IV-8b-d) show that with increasing strain increases also pressure and less importantly temperature from at least 12kbar and 650°C (Type I microstructure) to 19kbar and 730°C (Type II and III microstructure). Therefore, Type III mylonitic microstructure and mineral assemblage were stable in terms of rheology and petrology at depth of ~50-60 km, whereas Type I microstructure is probably an unstable relic of rocks that was passively transported into depth. Due to the absence retrograde minerals, we emphasize that burial was followed by rapid exhumation of the whole rock sequence, that is in agreement with petrological observations of adjacent mafic eclogites which show isothermal cooling during exhumation (Štípská *et al.*, this volume) .

9. 4. Model of strain localisation and reaction weakening in a continental accretionnary wedge

Regarding the microstructral and petrological evolution of the studied sequences and its position in Central Sudetes (Chopin *et al.*, this volume; Štípská *et al.*, this volume), we propose that the studied orthogneiss sequence registered a continuous progressive and prograde deformation along a cold metamorphic gradient (~10°C/km). This event is related to burial of continental crust during continental subduction and influx of rocks into apex of a continental accretionary wedge, before fast extrusion close to the rigid buttress indentor (Fig. IV-16)

Origin of the protolith of studied rock sequence is unknown but we assume subduction of Cambro-Ordovician granite rich crust underneath upper plate autochthonous Proterozoic sequences resulting in formation of studied HP orthogneisses. Because our studied rocks are intimately associated with mafic eclogites that registered similar PTd paths, we proposed that the granitoids were originally intruded by mafic dykes that were eclogitized and deformed together with surrounding felsic gneisses (Lange *et al.*, 2002). This interpretation may be in conflict with MORB composition of eclogites which may suggest their oceanic origin (Bakun-Czubarow, 1998).

Experimental works of Holyoke Lii and Tullis (2006a, b) suggest that the reaction softening is a mechanism responsible for strain partitioning and strain localisation in sample scale. In this work we show an important example of crustal scale strain partitioning which is induced also by continuous reaction softening which leads to extreme strain localisation. While the Śnieżnik orthogneiss was deformed at conditions of 12 - 13 kbar at 620°C the Gierałtów banded and mylonitic orthogneisses reveal pressures of 18 – 19 kbar at 750°C. This indicates that the strain partitioning did not occur at constant PT conditions as it was shown in other natural examples (Schulmann *et al.*, 1996; Zavada *et al.*, 2007; Schulmann *et al.*, 2008). In our example the Śnieżnik orthogneiss were vertically buried 20 km along shear zone few km wide. For an inclination of subduction zone 30° the Śnieżnik orthogneiss was passively transported 40 km into depth 50 – 60 km where the mylonitic orthogneiss was finally reequilibrated. The shear strain along the zone may vary between 20 to 40 γ in function of the width of zone of active deformation (2 to 1 km). This kind of strain localisation requires extremely efficient weakening mechanism and transition from dislocation creep to efficient diffusion dominated grain

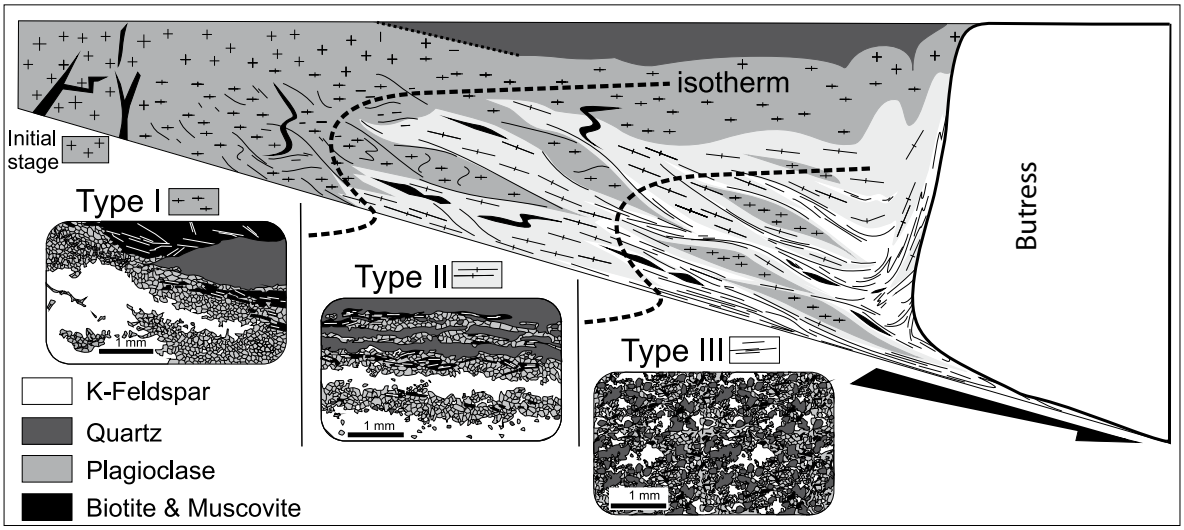

Fig. IV-16: Model of progressive evolution from Type I augen orthogneiss to Type II banded orthogneiss and Type III orthogneiss during corner flow in a continental accretionnary wedge. Further late D2 extrusion is shown. During burial, porphyritic granite is progressively transformed into Type I orthogneiss. Increasing strain triggers the formation of Type II orthogneiss at the expense of Type I orthogneiss. At this stage, the already deformed Type I orthogneiss is passively transported. Ongoing burial and deformation leads to the development of the Type III mylonitic orthogneiss at the expense of both Type I and II orthogneisses which are passively buried in the apex of the corner forming the root. Mafic dyke intrusions could represent the protolith of mafic eclogites found inside orthogneissic bodies.

boundary sliding mechanism.

10. Conclusion

This study reveals three major results which improve our knowledge of rheological behaviour, strain localisation and petrological evolution of deeply subducted continental crust in crustal scale wedges:

1) The development of HP orthogneiss is marked by narrow finite strain gradient indicating important strain localisation. The microstructural study shows that weakly deformed Type I augen orthogneiss is deformed in dislocation creep regime accompanied with dynamic recrystallization and subordinate metamorphic transformations. Type II and III banded and mylonitic orthogneisses show features of syndeformational continuous reactions responsible for major weakening of rocks and transition to grain boundary sliding mode.

2) Petrological study and thermodynamic modelling show that the Type I orthogneiss microstructure originated at 12 kbar and 620°C while Type II and III orthogneiss at 19 kbar and 750°C. Increase of Si content in muscovite and nucleation of Ca-rich garnets, decrease of Ca component in garnet in conjunction with increase of Ca component in plagioclase indicates that all microstructures developed along cold 10°C/km subduction type gradient and that they originated in contrasting crustal depths.

3) A dynamic model of influx of felsic material in a continental accretionnary wedge has been established in order to understand the prograde evolution of the rock sequences. This

model shows importance of prograde continuous metamorphic reactions on softening of granitic crust and localisation of deformation during continental subduction.

Acknowledgments

Financial support of the French National Grant Agency (06-1148784 to K. Schulmann) is acknowledged. We thank James Alibon (University of Lausanne) for microprobe analysis Assistance. Karim Malamoud (University of Grenoble) provided the .ang (TSL ASCII) to .ctf (HKLtechnology) conversion which was used in this work.

CHAPITRE V

RHEOLOGY OF HIGH GRADE MIGMATITES DURING LATERAL SHORTENING AND ASSOCIATED EXHUMATION (ORLICA ŚNIEŻNIK DOME - BOHEMIAN MASSIF)

F. CHOPIN[1], K. SCHULMANN[1], J.E. MARTELAT[2], P.PITRA[3], O.LEXA[4,5], J. HALODA[6]

[1]Ecole et Observatoire des Sciences de la Terre, Institut de Physique du Globe - CNRS UMR7516, Université de Strasbourg, 1 rue Blessig, F-67084 Strasbourg Cedex, France
[2]Observatoire des Sciences de l'Univers de Grenoble, Laboratoire de Géodynamique des Chaînes Alpines - UMR5025, Université Joseph Fourier, BP 53, F-38041 Grenoble Cedex 9, France
[3]Geosciences Rennes - CNRS UMR6118, Université Rennes 1, Campus de Beaulieu, F-35042 Rennes Cedex, France
[4]Institute of Petrology and Structural Geology, Charles University, Albertov 6, CZ-12843 Praha, Czech Republic
[5]Czech Geological Survey, Albertov 3, CZ-11000, Praha, Czech Republic
[6]Czech Geological Survey, Geologická 6, CZ-15200, Praha, Czech Republic

Abstract

In order to constrain the rheology of high grade migmatite orthogneisses that form the central part of an anticlinal shape gneiss dome, we performed a microstructural and petrological study of a natural deformation gradient from Augen (Type I), stromatitic (Type II) to nebulitic orthogneiss migmatites (Type III). This transition is characterized by a decrease of grain size of all phases and disintegration of monomineral aggregates of all phases. The high nucleation rate of interstitial phases associated with high mobility of grain boundaries is the consequence of partial melting and high temperature dynamic recrystallisation processes. Petrological modelling (not shown) suggest presence of at least 2 %mol of melt in the late deformation stage which is probably a lower estimate assuming unknown amount of released water during melt crystallization. Quartz recrystallises by dislocation creep mechanism together with K-feldspar at the early stage of deformation and melting. The unusual strong [001](100) "apparent" slip system recorded by K-feldspar and plagioclase can be interpreted as reflecting activity of so far unknown slip system in feldspar, anisotropic growth by dissolution-precipitation creep mechanism or rigid body rotation of the [001] long axis parallel to the X direction. Lack of mineral fabrics of all phases during Type III microstructures is concordant with a melt-enhanced grain-boundary sliding process of deformation. The inferred granular-flow is a likely mechanism of softening of felsic orogenic lower crust. This process probably facilitates the growth of the migmatitic dome during lateral shortening.

1. Introduction

Microstructural investigations of naturally deformed migmatitic orthogneisses have been recently matter of numerous studies in order to constrain the rheology of lower to middle crust during orogenic processes (e.g. Zavada *et al.*, 2007; 2008b; Schulmann *et al.*, 2008). The main problem related to understanding of microstructural deformation – partial melting trends is seen in polyphase nature of parental metagranites that are composed of aggregated or mixed minerals of contrasting rheology which change with modification of physical parameters (e.g. temperature, strain rate, confining pressure) (Rutter & Elliott, 1976; Handy, 1990; Stipp *et al.*, 2002; Rybacki & Dresen, 2004; Toy *et al.*, 2008). Small amount of melt or fluid is an important factor responsible for significant decrease of rock strength (e.g. Renner et al., 2001). Therefore, shape, topology and quantification of melt relics in rocks are regarded as a major tool to understand rheological properties of quartzo feldspatic rocks (e.g. Sawyer, 1999; Hasalová *et al.*, 2008b).

In the Orlica Śnieżnik Dome (OSD), several kilometre scale anticlines are cored by migmatitic orthogneiss and HP granulite that suffered partial melting before and during exhumation. Here, a natural deformation gradient in migmatitic orthogneisses is related to lateral shortening and associated exhumation. Our first aim is to characterize the microstructural and petrological evolution involved in progressive deformation and synchronous melting of porphyric metagranite. We describe exceptionally strong crystal plastic deformation of quartz and feldspars active during progressive deformation-melting process. Finally we extrapolate these results to a regional scale to better understand the rheology of gneiss during growth of crustal scale migmatitic dome.

2. Geological setting

The Orlica Śnieżnik Dome (OSD) form a part of crystalline basement of Central Sudetes at the N-E termination of the Bohemian massif (Mazur *et al.*, 2006, Fig. 1a). The dome has been formed as a result of interplay between SE directed continental subduction and indentation of westerly Brunovistulian plunger (Chopin *et al.*, this volume-b). The OSD is made by alternations of amphibolite facies metasediments with various orthogneisses locally cored by (U)HP rocks (Fig. 1b). Protolith of metasediments (Jastrzębski *et al.*, 2010) and orthogneiss (Bröcker *et al.*, 2009 and references herein) is of Cambro-Ordovician age whereas origin of (U)HP rocks is still unknown (Bröcker *et al.*, 2010). UHP metamorphism have been proposed for eclogites (Bröcker & Klemd, 1996) and HP-granulites (Bakun-Czubarow, 1992; Klemd & Bröcker, 1999), nevertheless, recent petrological studies suggest lower peak PT conditions of 18-22 kbar at 800-1000°C (Štípská *et al.*, 2004) for the granulites and 18-22 kbar at 700-800°C for the eclogites (Štípská *et al.*, this volume). The metamorphic ages of (U)HP rocks and surrounding orthogneiss and metapelites cluster at 340-350Ma (Bröcker *et al.*, 2009 and references herein).

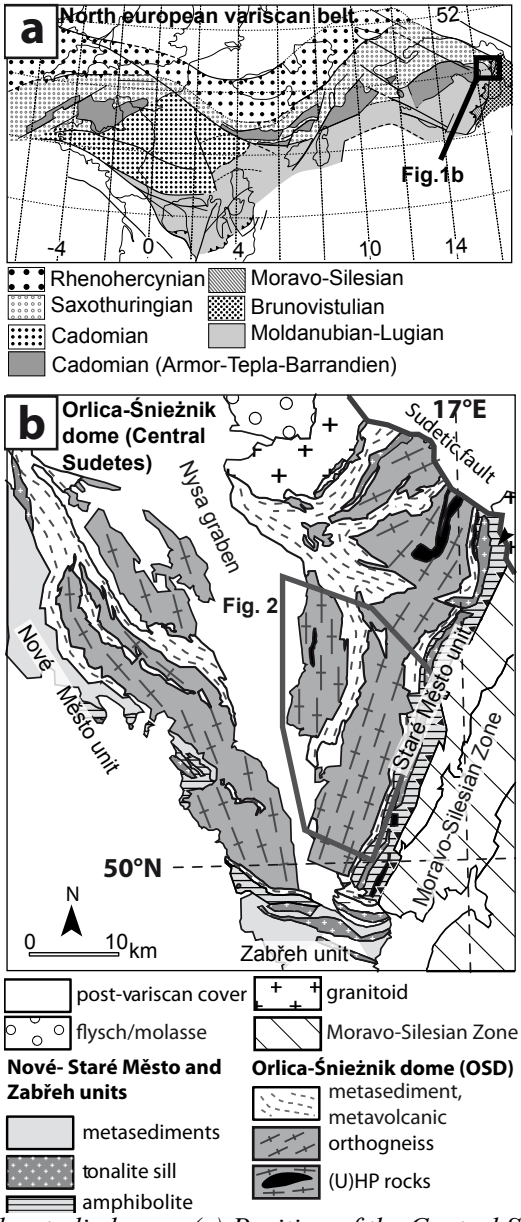

Fig. V-1: Tectonic setting of the studied area. (a) Position of the Central Sudetes in the European Variscides (modified after Aleksandrowski et al., 1997; Don et al., 2003, Zelaziewicz et al., 2006).

In the studied area, Chopin *et al.* (this volume-a) shows that a part of the orthogneiss adjacent to the mafic eclogites suffered PTD evolution similar to that of adjacent eclogites. It was suggested both lithologies shared the same process of burial and exhumation by crustal scale folding in front of a continental buttress (Štípská *et al.*, this volume). It is lateral E-W D2 shortening that allowed juxtaposition and exhumation of eclogites bearing orthogneiss in the core of anticline, syncline of mid-crustal metapelites and migmatitic anticline (Figs 2 & 3). We focussed this study on an outcrop in the core of the latter anticline (Fig. 2) which shows well preserved D2 deformation gradient in partially melted orthogneiss.

Fig. V-2: Lithological (modified after Don et al., 2003) and structural map of the studied area, samples used for microstructural and petrological investigations are indicated.

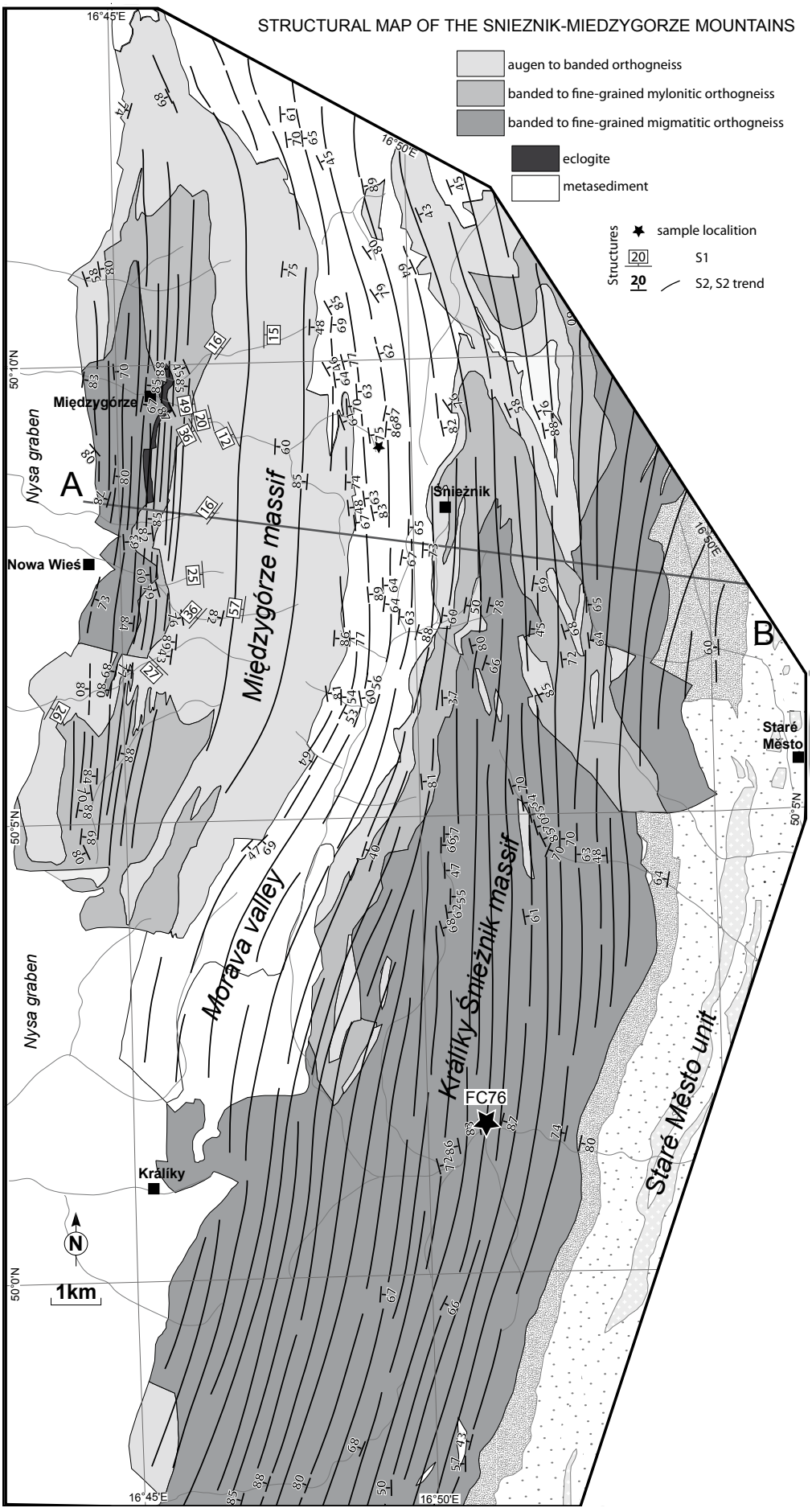
STRUCTURAL MAP OF THE SNIEZNIK-MIEDZYGORZE MOUNTAINS
augen to banded orthogneiss
banded to fine-grained mylonitic orthogneiss
banded to fine-grained migmatitic orthogneiss
eclogite
metasediment
sample localition
Structures
S1
S2, S2 trend
16°45'E
16°50'E
50°10'N
50°5'N
50°0'N
Międzygórze
Nysa graben
A
B
Śnieżnik
Nowa Wieś
Międzygórze massif
Morava valley
Králíky Śnieżnik massif
Staré Město
Staré Město unit
FC76
Králíky
N
1km

3. Macroscopic structural trend

Samples have been carried out in a single outcrop situated of the central part of Králicky Śnieżnik massif, along the Morava river (UTM WGS84 coordinates X=632590 and Y= 5550699; Fig. 2). Here, the main foliation S2 is steeply dipping to the west (261/83) and bears nearly sub-horizontal lineation (Fig. 3). It shows rare relics of previous fabrics S1 foliation (Fig. 4a, c) that locally attest for an early episode of partial melting (Chopin et al., this volume). This early fabric is mostly transposed by dominant S2 foliation (Fig. 4b). Numerous decimetre scale transitions from an apparently weakly deformed partially molten porphyritic augen orthogneiss (Type I) sample fc76A) passing through stromatitic-banded migmatite (Type II, sample fc76B and fc76D) to 'nebulitic' fine grained leucocratinc migmatite (Type III, sample fc76C). This textural trend may indicate an increase of the melt fraction from Type I to Type III according to Brown (1995) classification (Fig. 4b). This type of transition, from "augen" to "fine grained" orthogneiss is referred as the so-called Śnieżnik augengneiss – Gieraltów gneiss transition in the whole OSD (Lange *et al.*, 2005 and references therein). However, this distinction is descriptive and did not take into account the process leading to the gradual development of rock types (Chopin *et al.*, this volume-a; Chopin *et al.*, this volume-b; Štípská *et al.*, this volume). Augen-orthogneiss Type I is made of elongated centimetre scale quartz and feldspar augens, with diffuse boundary between plagioclase and K-feldspar rich domains. The lineation is marked by the sub-horizontal elongation of augens and by alignment of biotite and muscovite clusters. Type II rocks shows highly elongated quartz and feldspars aggregates with more pronounced diffuse boundaries compared to the Type I orthogneiss. Alternation of leucocratic and melanocratic bands is forming ubiquitous planar fabric while the subhorizontal mineral lineation is less pronounced. Finally, the Type III nebulitic migmatite is a fine grained almost isotropic leucocratic rock marked by faint foliation and lineation defined by orientation of micas.

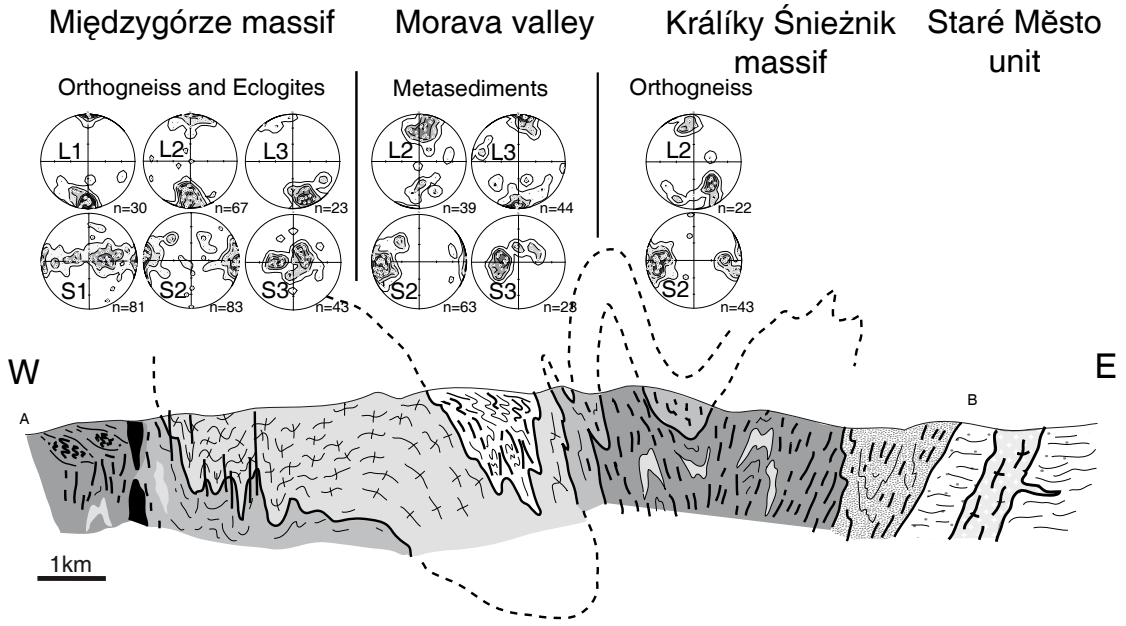

Fig. V-3: Cross section through the eastern part of the OSD (see fig 2 for legend and profile location).

Fig. V-4: Field photographs of the rock sequence from augen (Type I), to stromatitic (Type II) and to nebulitic migmatite. (a) Typical Type I rock with relics of S1 fabric. (b) Decimeter-scale deformation gradient from Type I to III. (c) Superposition of deformation and localized development of Type II migmatite. (d-f) Typical pattern of Type I, II and III migmatites.

4. Whole rock chimistry

The whole rock ICP-MS analyses were performed in the Acme laboratories (Canada). Results are summarized in the Tab. 1 and presented in an isocon diagram (Fig. 5, Grant, 1986). This diagram point out to a similar composition of major elements for all textural orthogneiss types (I, II and III) described above suggesting lack of loses and gains elements during the process of deformation and melting supposing that there were no variations in volume (Marquer & Burkhard, 1992). Compared to orthogneiss bearing eclogites (Lange *et al.*, 2002; Lange *et al.*, 2005; Chopin *et al.*, this volume-a), this rock sequence is depleted in MgO and TiO_2.

Table II-1: Whole rock chemistry of Type I, II and III migmatites.

Whole-rock compositions (ICP-MS)			
Rock type	Augen orth. migmatite (Type I)	Stromatitic migmatite (Type II)	Nebulitic migmatite (Type III)
Sample	fc76A	fc76D	fc76C
wt%			
SiO2	74.38	73.36	73.80
TiO2	0.15	0.17	0.18
Al2O3	13.46	13.85	13.49
Fe2O3	2.15	2.02	2.09
MnO	0.03	0.03	0.03
MgO	0.31	0.33	0.34
CaO	0.78	1.06	0.89
Na2O	3.11	3.06	2.98
K2O	4.47	4.92	4.97
P2O5	0.19	0.19	0.19
Sum	99.96	99.95	99.96
Xfe	0.78	0.75	0.75

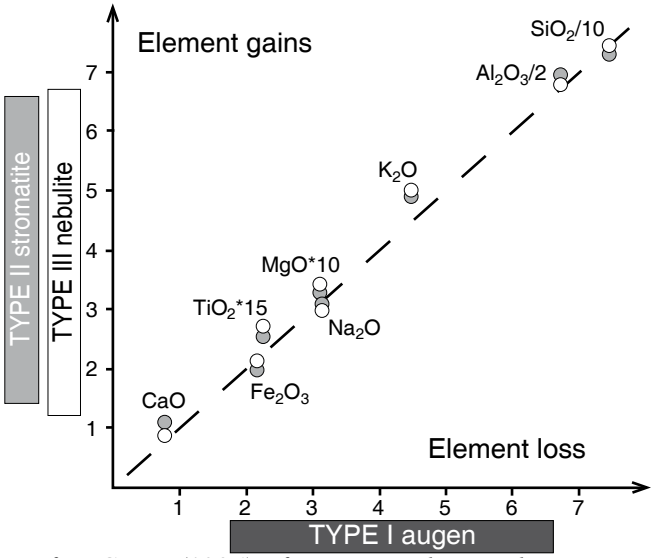

Fig. V-5: Isocon diagram after Grant (1986) of Type II and III with respect to Type I migmatite. This diagram shows loss and/or gain of elements with respect to Type I chemistry (reference line). Concentrations are scaled to fit on the plot.

5. Microstructural and Mineral chemistry evolution

BSE images have been acquired with a TESCAN VEGA XMU electron microscope at the EOST laboratory (University of Strasbourg). Mineral analyses were performed on a JEOL82000 microprobe at the University of Lausanne. Operating conditions were a 15-kV acceleration voltage, a 10-nA beam current, a spot diameter of 5 μm and a counting time of 20–30 s. Representative analyses of micas and garnet are presented in Tab. 2.

The mineralogy of all orthogneiss Type is rather monotonous and consists of quartz + K-feldspar + plagioclase + biotite + muscovite + garnet + apatite. However, the grain size, grain shape and grain boundary geometry of theses phases as well as geometry of quartz and feldspar aggregate is changing throughout the rock sequences. In all rock types, the Ti bearing phases are represented by rutile needless (20-50μm large) enclosed in biotites.

5. 1. Type I microstructure: augen orthogneiss (sample fc76A)

This rock type is in XZ section of finite strain ellipsoid made of alternations of recrystallised quartz, K-feldspar and plagioclase 3 to 10 mm wide ribbons (Fig. 6a, c), whereas in YZ sections these aggregates reveal elliptic shapes(Fig. 6b, d). Boundaries between ribbons are diffuse and interdigitized. Coarse biotites ± muscovite 1mm in length form aggregates commonly lining quartz ribbons (Fig. 7a).

Quartz form completely recrystallised aggregates composed of large grains 30-2000 µm in size with highly lobated (Fig. 7a). They show a weak shape preferred orientation. Numerous small quartz grains occur at the K-feldspar grain boundaries inside feldspar aggregates (Fig. 7a & Fig. 8a).

K-feldspar aggregates are made of fully recrystallised grains 50-1000 µm grain size. Large grains show a well developed shape preferred orientation parallel to macroscopic linea-

Table II-1: Representative analyses of muscovite, biotite and garnet. For sample fc76C (Type III - nebulite), core and rim compositions of garnet are distinguished.

Rock type	Ophtalmitic migmatite (Type I)			Schlieren migmatite (Type II)			Nebulitic migmatite (Type III)			
Sample	fc76A			fc76B			fc76C			
Mineral	mu	bi	g	mu	bi	g	mu	bi	g rim	g core
Wt%										
SiO2	45.77	32.94	36.14	47.24	33.26	35.89	47.18	33.97	35.55	36.63
TiO2	0.48	1.979	0.00	0.68	1.59	0.016	0.76	2.50	0.08	0.10
Cr	0.00	0.024	0.00	0.01	0.05	0.00	0.01	0.06	0.00	0.02
Al2O3	31.40	17.79	20.34	31.18	18.31	20.53	31.07	17.94	20.25	20.81
FeO	2.79	27.11	30.85	2.92	27.09	31.04	3.29	26.99	32.30	29.25
MnO	0.01	0.314	8.63	0.01	0.38	7.45	0.03	0.27	6.57	2.46
MgO	1.11	4.58	0.60	1.18	4.17	0.58	1.10	4.61	0.73	0.62
CaO	0.00	0.05	2.47	0.02	0.06	2.90	0.00	0.00	3.18	9.11
Na2O	0.33	0.09	0.00	0.31	0.04	0.00	0.35	0.06	0.00	0.00
K2O	10.61	7.97	0.00	10.53	7.12	0.00	10.37	9.17	0.00	0.00
Sum	92.52	92.88	99.06	94.13	92.11	98.44	94.18	95.57	98.68	98.60
Structural formulae calculated on the basis of 12 oxygens for garnet. 22 for biotite and muscovite										
Cations										
Si	3.162	2.757	2.987	3.216	2.815	2.980	3.215	2.758	2.945	2.955
Ti	0.025	0.125	0.000	0.035	0.102	0.001	0.039	0.153	0.005	0.006
Cr	0.000	0.002	0.000	0.001	0.003	0.000	0.001	0.004	0.000	0.001
Al	2.557	1.755	1.982	2.503	1.827	2.009	2.496	1.717	1.978	2.000
Fetot	0.161	1.897	2.132	0.166	1.918	2.155	0.188	1.832	2.238	1.995
Mn	0.001	0.022	0.605	0.001	0.028	0.524	0.002	0.019	0.461	0.170
Mg	0.114	0.571	0.074	0.120	0.527	0.073	0.112	0.558	0.091	0.076
Ca	0.000	0.005	0.219	0.002	0.006	0.258	0.000	0.000	0.282	0.000
Na	0.045	0.015	0.000	0.042	0.007	0.000	0.046	0.010	0.000	0.000
K	0.936	0.852	0.000	0.915	0.769	0.000	0.901	0.950	0.000	0.000
Sum	7.000	8.000	8.000	7.000	8.000	8.000	7.000	8.000	8.000	8.000
X Fe	0.585	0.769	0.966	0.582	0.785	0.967	0.626	0.766	0.961	0.963
Prp			0.024			0.024			0.028	0.024
Alm			0.681			0.698			0.660	0.613
Grs			0.072			0.085			0.088	0.254
Sps			0.197			0.172			0.144	0.054

XFe = Fe/(Fe + Mg); Prp = Mg/(Fe +Mg+Ca+Mn); Alm = Fe/(Fe + Mg + Ca + Mn); Grs = Ca/Fe + Mg + Ca + Mn); Sps = Mn/(Fe + Mg + Ca + Mn).

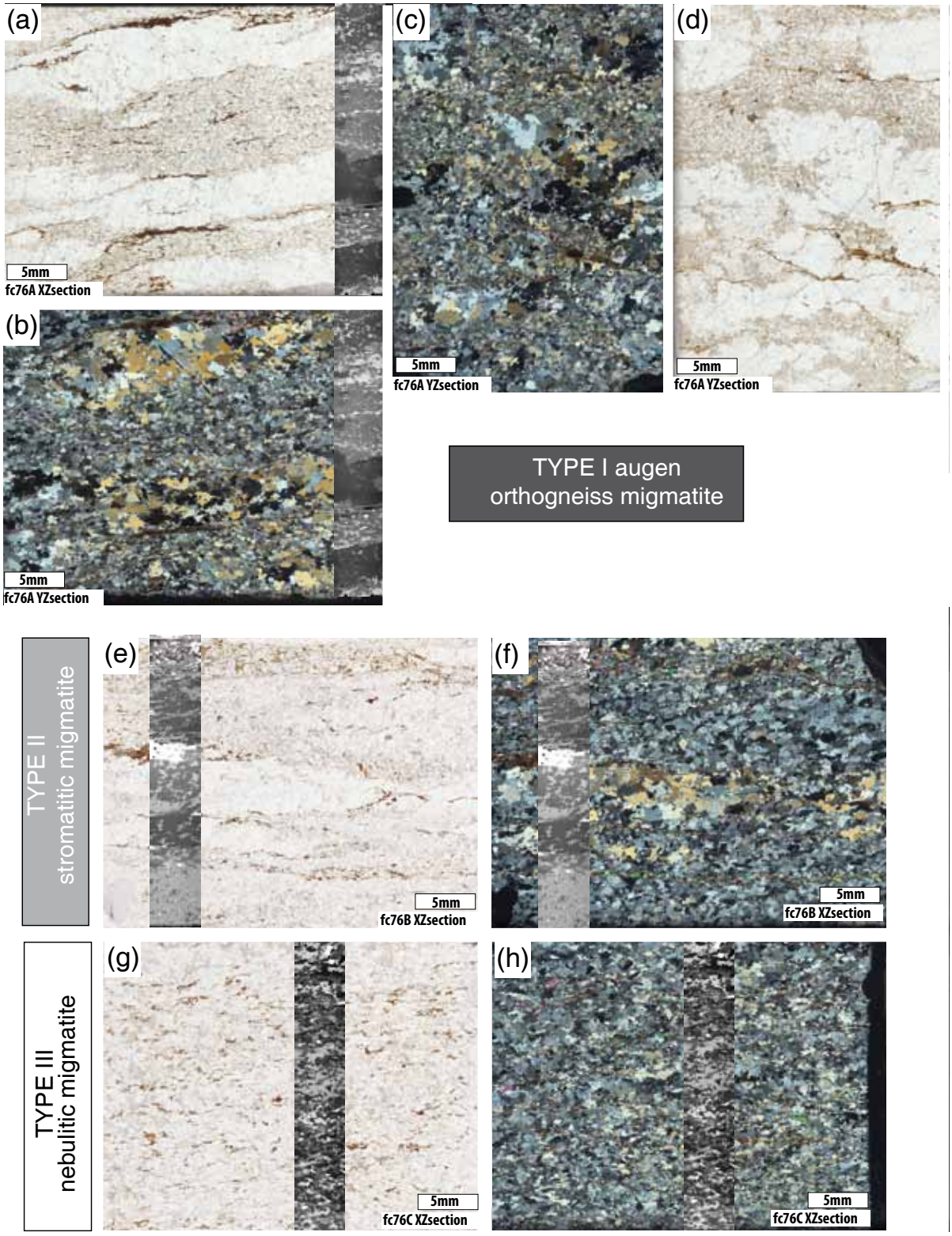

Fig. V-6: Large photomicrographs of representative thin sections from the rock sequence (plane and plane-polarized light). (a, b) XZ and (c, d) YZ sections of augen migmatite (Type I). (e, f) XZ section of the stromatitic migmatite (Type II). (g, h) XZ section of the nebulitic migmatite (Type III). BSE images enlarged in Fig 7 are indicated. All pictures are at the same scale.

tion (Fig. 6), whereas preferred orientation of smaller grains is less developed. The boundaries between K-feldspar grains are highly serrated and lined by irregular 10-30µm wide films and irregular albite An_{0-15} crystals of 10-300µm in size) and rounded quartz intergrowth 10-200 µm in size.

Plagioclase aggregates are made of equigranular oligoclase An_{08-18} grains 50-800 µm in size that forms a granoblastic to foam microstructure (Fig. 8b). The plagioclase grains do not display a visible shape preferred orientation. Triple junctions are frequently filled with rounded and isolated quartz (10-100µm) and cuspate K-feldspars (10-50µm in size; Or_{88-96}) that coat the straight boundaries of adjacent plagioclases. Partially chloritized, tiny garnet (50-200µm in size; $alm_{0.63-0.70}py_{0.019-0.029}grs_{0.067-0.105}sps_{0.13-0.22}$, Fig. 9a) with dispersed small muscovite (50-300µm; Si = 3.09-3.29, Al = 2.38-2.72, Fig. 10a) and biotite (50-500µm; X_{Fe} = 0.74-0.78, Ti = 0.01-0.04 p.f.u., Fig. 10b) are frequent in plagioclase dominated layers (Fig. 7a). The proportion of muscovite is higher compared to biotite (70% and 30% of all micas respectively). Secondary biotite is often visible either as fine overgrowth of muscovite or as lamellae partial replacing host muscovite parallel to cleavage planes.

5. 2. Type II microstructure: stromatitic - banded migmatite (samples fc76B and fc76D)

This rock type is made of alternations of quartz, K-feldspar and plagioclase 1 to 4 mm thick ribbons (Fig. 6e, f). Limits between layers are highly diffused and interdigitized (Figs 7b & 8d, e).

Quartz layers are made of irregular grains (30-1000µm in size) that display amoeboid to highly lobated boundaries. Feldspar crystals penetrate heterogeneously in quartz aggregates along mutually lobated boundaries (Fig. 8e). As in previous microstructural type, quartz grains did not display shape preferred orientation and aggregates are often lined by coarse biotite±muscovite aggregates.

K-feldspar aggregates exhibit irregular grains (50-600 µm in size; Or_{84-92}) with large grains strongly preferentially oriented in the X direction. The proportion of interstitial quartz and plagioclase (core An_{09-16}, rim An_{03-10}) is also high (Fig. 8d).

The foam texture of plagioclase aggregates is less pronounced in this type and display a decrease of their grains size. Boundaries between plagioclase grains (core An_{08-17}, rim An_{03-17}) are mostly irregular and the presence of numerous cuspate K-feldspar (Or_{87-95}) and isolated rounded quartz grains is more important compared to Type I microstructure (Fig. 8c). Regularly dispersed small muscovite (50-300µm; Si = 3.12-3.33, Al = 2.38-2.72, Fig. 10a), biotite (50-400µm; X_{Fe} = 0.77-0.78, Ti = 0.020-0.025 p.f.u., Fig. 10b) and partially chloritized elongated tiny garnet occur (until 500µm long, Fig. 8g; $alm_{0.65-0.71}py_{0.021-0.028}grs_{0.064-0.105}sps_{0.13-0.20}$, Fig. 7b & 9a). The mutual proportion between these muscovite and biotite is approximately 70% and 30%, respectively. As in Type I microstructure the muscovites are still often replaced and overgrown by new biotite.

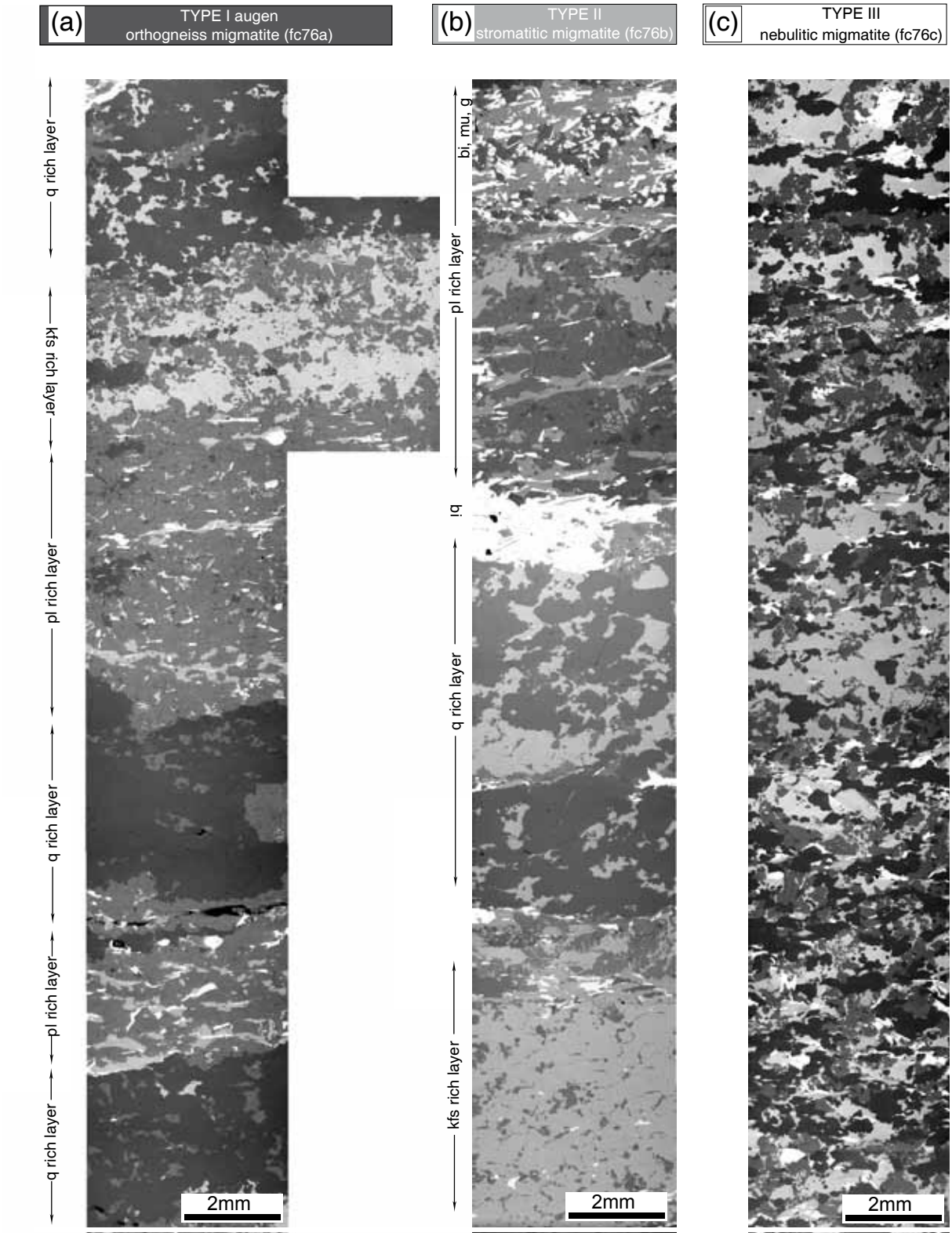

Fig. V-7: Compilation of back scattered electron (BSE) images of the rock sequence. Gray color scale corresponds to variation in chemical components, i.e with increasing white intensity: void, quartz, plagioclase, K-feldspar, muscovite and biotite/garnet (not distinguished). All pictures are at the same scale. Location of images is shown in Fig. 6.

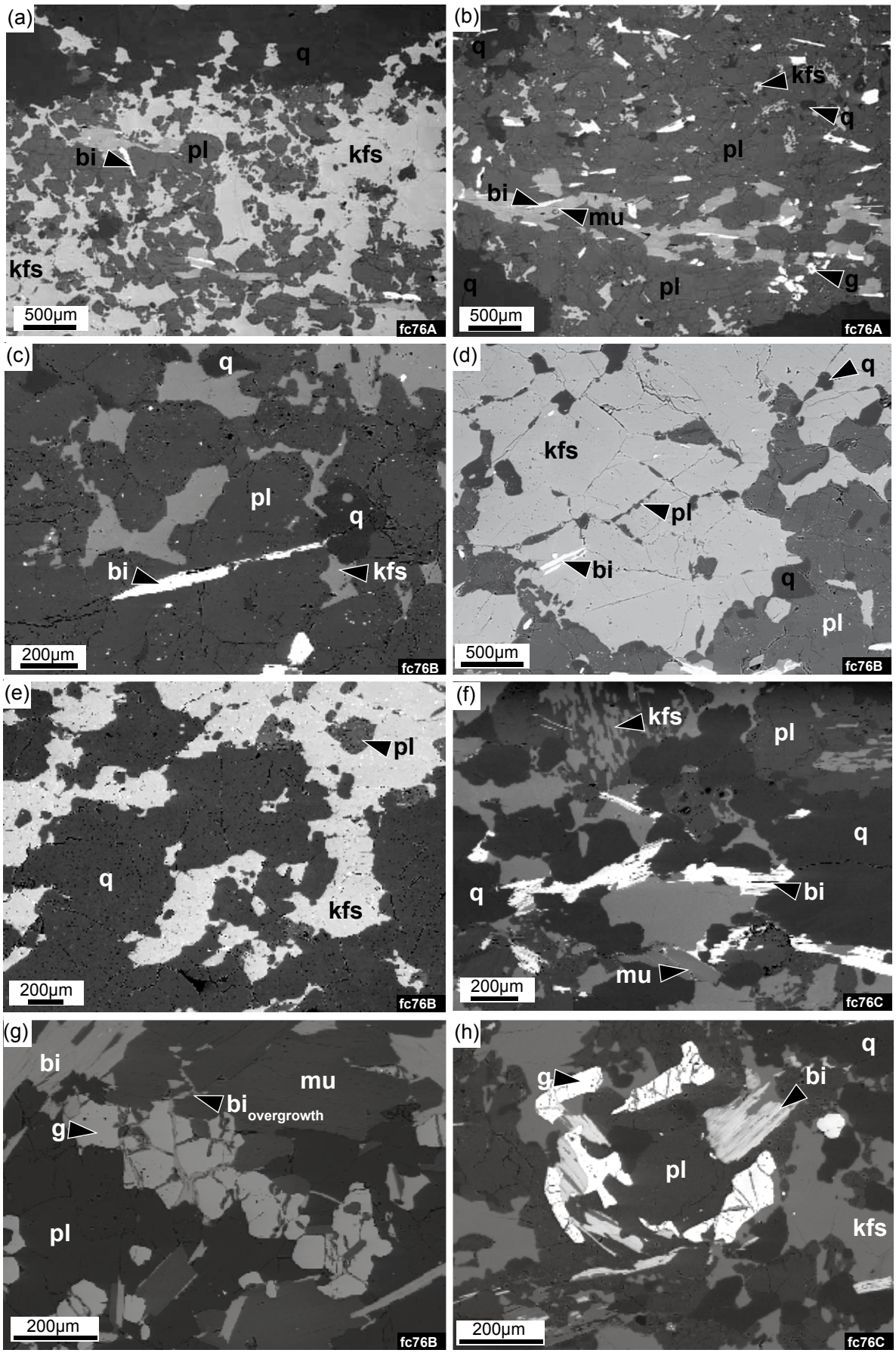
(a)
q
bi
pl
kfs
kfs
500µm
fc76A
(b)
q
kfs
q
pl
bi
mu
q
pl
g
500µm
fc76A
(c)
q
pl
q
bi
kfs
200µm
fc76B
(d)
q
kfs
pl
bi
q
pl
500µm
fc76B
(e)
pl
q
kfs
200µm
fc76B
(f)
kfs
pl
q
q
bi
mu
200µm
fc76C
(g)
bi
mu
bi overgrowth
g
pl
200µm
fc76B
(h)
q
g
bi
pl
kfs
200µm
fc76C

5. 3. Type III microstructure: nebulitic migmatite (sample fc76A)

In this rock type modal proportions are 36% of quartz, 26% of K-feldspar, 26% of plagioclase, 6% of muscovite, 4% of biotite and 2% of garnet. Ribbons of feldspars and quartz are missing and the microstructures show a weakly developed fabric (Figs 6g, h & 7b). The quartz and feldspar grains have similar grain size that range from 50 to 400 µm with weakly developed shape preferred orientation in the X direction. The boundaries between quartz, K-feldspar (Or_{87-93}) and plagioclase (core An_{10-18}; rim An_{02-13}) grains are highly lobated to amoeboid. Coarse biotites are rare and small crystals of dispersed biotite and muscovite emphasize the foliation (50-300µm long; Si = 3.09-3.31, Al = 2.30-2.71 for muscovite, Fig. 10a; and 50-300µm long; X_{Fe} = 0.76-0.78, Ti = 0.020-0.040 p.f.u., Fig. 10b). Tiny and partially chloritized dispersed garnets are still present (200µm in size, Fig. 8h) some coarser garnets (400µm) are zoned form the core (until $alm_{0.58}py_{0.030}grs_{0.36}sps_{0.05}$ Fig. 9b) to the rim (until $alm_{0.69}py_{0.030}grs_{0.28}sps_{0.20}$ Fig. 9a, b). Compared to Type I and II microstructures, the proportion of biotite is higher reaching 40% of the total amount of the micas. Similarly, to previously described rock types the muscovite is often destabilized and replaced by new biotite.

5. 4. Microstructural evidences of melting

As reported by Sawyer (2001), grain scale evidences of melting in rapidly quenched rocks can be represented by melt pools with cuspate – lobated margins (Jurewitz & Watson, 1984), thin melt films along grains boundaries (Daines & Kohlstedt, 1997) or rounded and corroded minerals (Büsch *et al.*, 1974). In partially molten felsic rocks thin films, corroded grains or triple junction intergrowths of quartz, K-feldspar or albite are interpreted as reflecting the presence of melt (e.g. Zavada *et al.*, 2007; Hasalová *et al.*, 2008b; Schulmann *et al.*, 2008). In this studies, the increasing amount of small cuspate K-feldspar in plagioclase layer, as well as quartz and albite rich plagioclases intergrowths in K-feldspar ribbons, amoeboid grains of K-feldspar in quartz bands and diffuse boundaries between layers can be interpreted as reflecting presence of quenched melt in the rock sequence (Rosenberg & Riller, 2000).

Preliminary results from petrological modelling using thermocalc (not shown) suggest maximum P-T conditions of 14 bbar – 660-680°C followed by decompression until 7-8 kbar at 630-650°C for the sample fc76c (Type III). It suggest a melt production during retrograde path of about 2% mol.

Fig. V-8: Detailed back scattered electron (BSE) images of the rock sequence. (a) Diffuse boundary between a quartz-rich and K-feldspar-rich layer with high density of plagioclase intergrowth in Type I sample. (b) Plagioclase-rich layer with micas and garnet intergrowths in Type II sample. (c) Cuspate K-feldspar and rounded quartz as interstitial phases in plagioclase band from Type II sample. (d) Film and blebs of plagioclase and quartz between K-feldspar grains in Type II sample. (e) Highly amoeboid and penetrative boundaries between K-feldspar and quartz. (f) Mixing in nebulitic migmatite. (g) Tiny, elongated garnet aggregates surrounded by plagioclase, biotite and muscovite overgrown by minute biotite. (h) Tiny garnet cluster associated with matrix of mixed micas, quartz and feldspar.

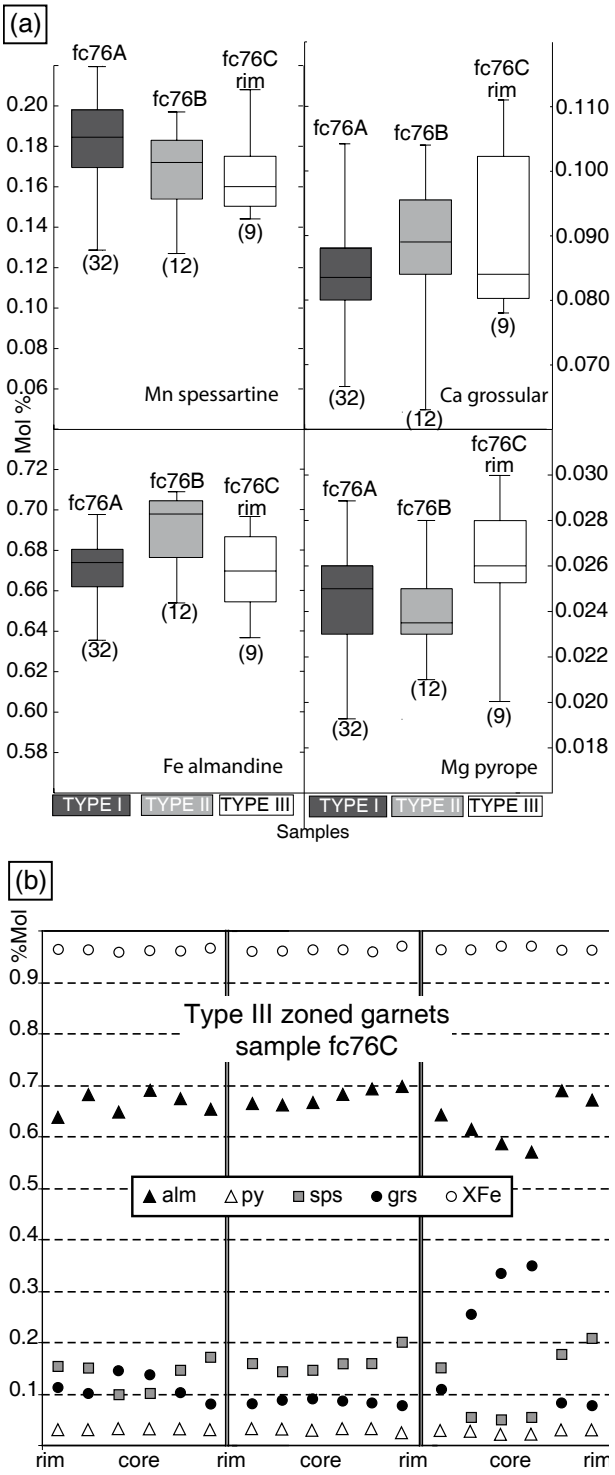

Fig. V-9: Garnet compositional trends of (a) spessartine grossular, almandine and pyrope within the whole rock sequence. The data are presented in a box-and-whiskers plot of individual component (mol.%). Individual boxes show median and first and third quartiles of the component content. The whiskers represent a statistical estimate of the data range. Number of microprobe analyses is shown. For the sample fc76C, only garnet rim compositions have been used for the statistic. (b) Compositional profiles of three zoned garnets from sample fc76C (Nebulite – Type III).

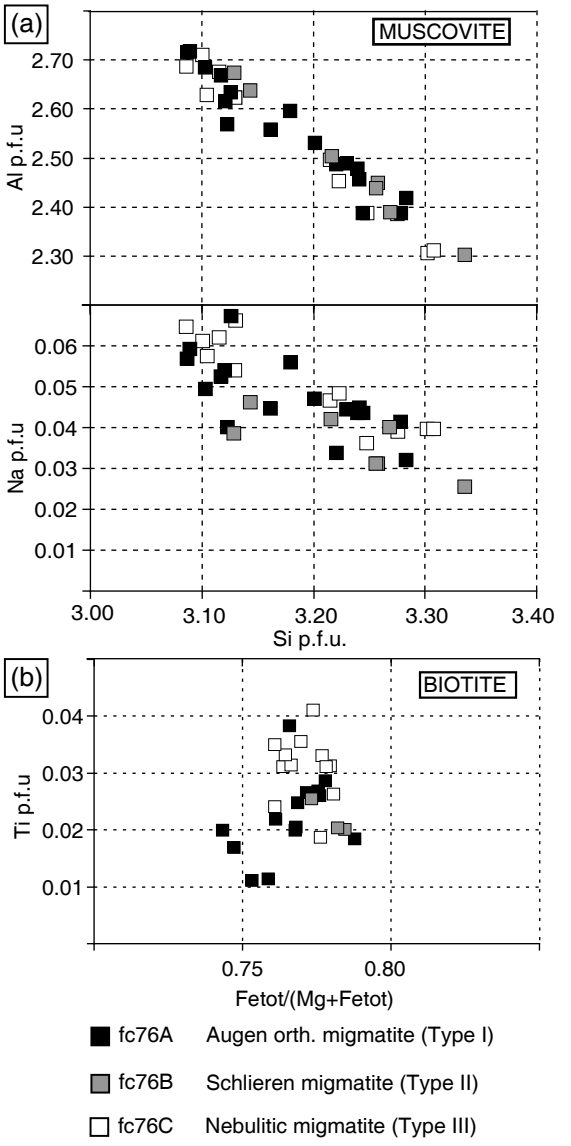

Fig. V-10: Muscovite and biotite composition for the different rock Types. Representative analyses are listed in Tab. 2.

6. Latice preffered orientation

In order to examine the dynamic mode of recrystallisation and plastic deformation in the rock sequences, we performed electron back-scattered diffraction measurement of quartz, K-feldspar and plagioclase in ribbons/aggregates in XZ sections of the samples fc76A (Type I), fc76B (Type II), and fc76C (Type III). Measurements have been done on a scanning electron microscope CamScan3200 in the Czech Geological Survey in Prague (HKL technology). Diffraction patterns were measured at 20kV accelerating voltage, 5nA probe current and a working distance ranging from 21 to 42 mm. The procedure was carried out in manual mode in order to avoid multiple measurements on a single grain and only well-fitted data were used (Bascou *et al.*, 2001; Prior *et al.*, 2009). Lattice Preferred Orientation (LPO) of quartz is presented in the pole figure of the crystallographic direction < c > (001) and < a > (001) (Fig. 11). For the feldspars, planes and directions were plotted that fit with main axes of the finite strain ellipsoid (Fig. 11).

6. 1. LPO of quartz

LPO of quartz from Type I microstructures (sample fc76A) is strong with a well defined maxima close to the X direction of D2 finite strain ellipsoid and sub-maxima in the centre and at the periphery of the pole figure forming incomplete asymmetric crossed girdle with high opening angle (Fig. 11). This pattern suggests an activity of the prism <c> and, prism <a> slip systems in a non-coaxial regime. The Type II rock reveals weak maximum close to lineation (sample fc76B), absence of central sub-maximum, and development of sub-maximum parallel to Z direction This c-axis pattern is interpreted as a result of combined activity of prism <c> and basal <a> slip systems whereas activity of prism <a> slip system becomes reduced. The Type III microstructure shows a rather dispersed c axis pattern and therefore it is interpreted as a reduction of crystal plasticity of quartz.

6. 2. LPO of K-feldspar

In Type I microstructures (sample fc76A), the (010) lattice plane is preferentially oriented parallel to the XY plane of the finite strain ellipsoid, and the [001] direction is parallel to the X direction (Fig. 11). This indicates the activity of the [001](010) slip system. This classical slip system is reported in experimentally (Willaime *et al.*, 1979; Scandale *et al.*, 1983) or naturally deformed K-feldspar (Sacerdoti *et al.*, 1980; Schulmann *et al.*, 1996; Franěk *et al.*, 2006). The Type II microstructures (sample fc76B) exhibit a very strong preferred orientation of the (001) lattice plane and [001] direction parallel to foliation and lineation respectively. This can

Fig. V-11: Crystallographic preferred orientation of quartz, K-feldpar and plagioclase from electron backscattered diffraction in situ measurements. Pole diagrams are represented in equal area, lower hemisphere projection, contoured at intervals of 0.5 times uniform distribution. X and Z refer to the direction of lineation and pole to the foliation, respectively. Numbers of analysis and maximum density are indicated.

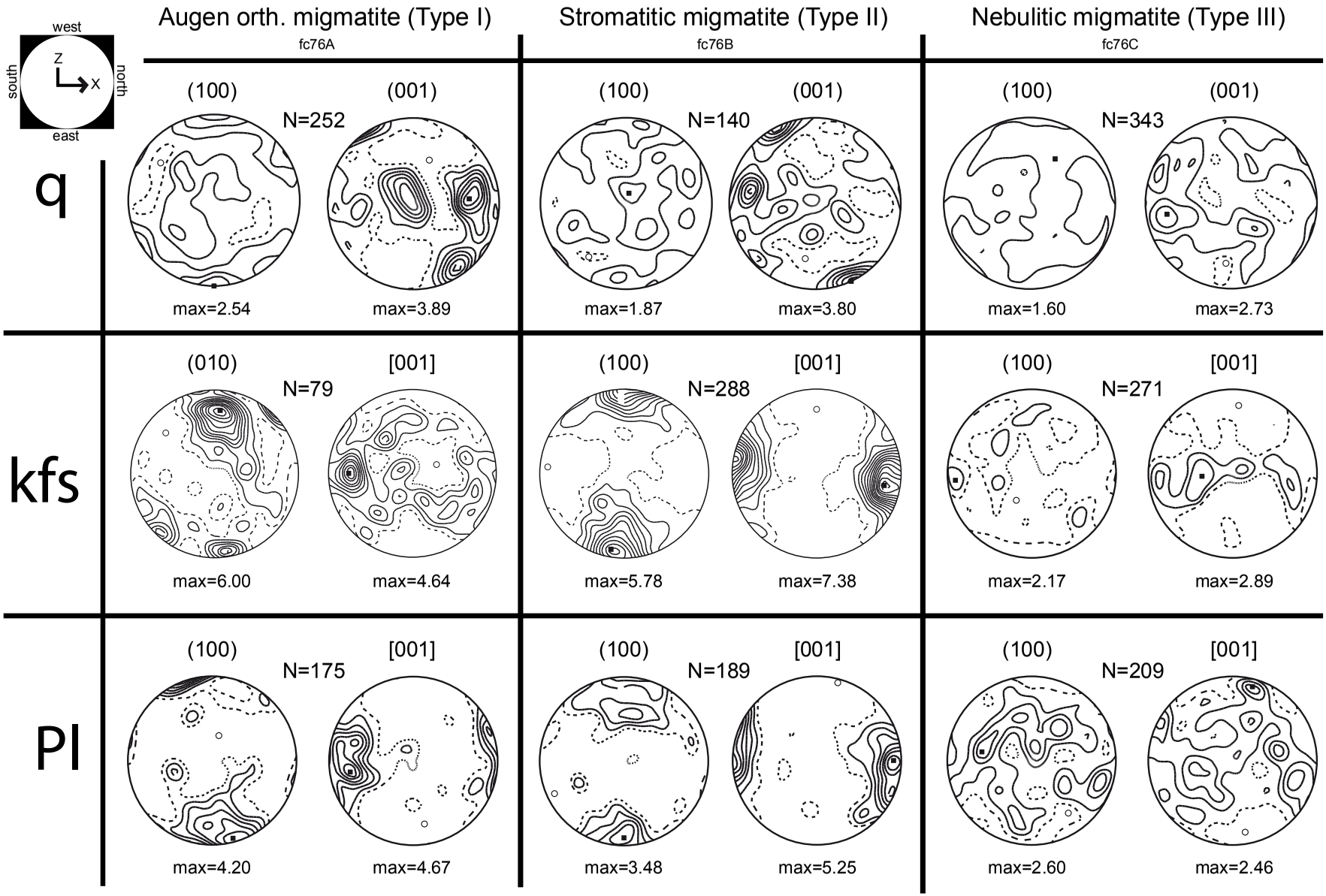
west
south
north
east
Z
X
Augen orth. migmatite (Type I)
fc76A
Stromatitic migmatite (Type II)
fc76B
Nebulitic migmatite (Type III)
fc76C
q
kfs
Pl
(100)
(001)
(010)
[001]
N=252
N=140
N=343
N=79
N=288
N=271
N=175
N=189
N=209
max=2.54
max=3.89
max=1.87
max=3.80
max=1.60
max=2.73
max=6.00
max=4.64
max=5.78
max=7.38
max=2.17
max=2.89
max=4.20
max=4.67
max=3.48
max=5.25
max=2.60
max=2.46

suggest an unusual activity of the [001](100) slip system but it has never been reported in the literature (Menegon *et al.*, 2008). K-feldspar in type III nebulite (sample fc76C) does not show distinct crystallographic preferredl orientation.

6. 3. LPO of plagioclase

As reported for K-feldspar, plagioclases in Type I (fc76A) and II (fc76C) show LPO marked by [001] directions forming strong maxima close to the lineation associated with a well oriented (100) plane showing maximum in the XY plane (Fig. 11). This can suggest the existence of the activity of so far not reported glide system [001](100) (see for instance compilation of Kruse et al., 2001). We observe a lack of LPO in the Type III rock (fc76C).

7. Discussion

In this study, we present the microstructural, petrological and LPO's of three types of migmatites from the Orlica Śnieżnik Dome. To understand the mechanism of development of the rock sequences, we first discuss the microstructural evidences of melting associated with increasing strain. Then, we discuss the evolution of microstructures associated lattice preferred orientation of quartz and feldspars and in particular the strong apparent unknown [001](100) slip system. We finally discuss the rheology of the rock sequence with respect to estimated PT evolution and tectonic model proposed for adjacent lithologies.

7. 1. Migmatite origin

The destruction of layering and mixing of phases in the rock sequences form Type I to Type III can be explained either by mechanical or chemical (enhanced by melt) process. Regarding the increasing amount of interstitial phases in all layers, their chemistry, the interdigitized boundaries between quartz and feldspar as well as calculated isopleths in PT pseudosection (not shown), we can expect a minimum proportion of 2% of melt in these rocks. But this can be underestimated because we do not know the exact amount of water that has been released during melt crystallisation. This estimation is also insufficient to explain the nebulitic macroscopic character of the last Type III migmatites. Because the whole rock and mineral composition is very similar throughout the whole rock sequences, there is no evidence that theses nebulitic migmatites originated by progressive melt infiltration as it have been proposed for similar rock sequence by Hasalova et *al.* (2008a) for orthogneiss migmatites from the Gföhl unit. We therefore propose an in-situ origin of the melt similarly to Zavada *et al.* (2007) and Schulmann *et al.* (2008). Also, even if film of supposed melt relics are present at grain boundaries in K-feldspar layers, their orientations does not show apparent preferential shape orientation perpendicular to the foliation which is a evidence of melt-enhanced creep failure in partially melted orthogneiss (Kassner & Hayes, 2003; Zavada *et al.*, 2007; Schulmann *et al.*, 2008). Therefore, we suggest

that these processes did not operated in studied rocks.

7. 2. Significance of lattice preferred orientation and associated microstructures

Quartz show high mobility of grain boundaries that can be interpreted to a result of grain boundary migration dynamic recrystallisation process (Stipp *et al.*, 2002). This is associated with a well developed activity of prism <c> and <a> glide system that corresponds to high temperature dislocation creep mechanism during stage I and II in quartz (e.g. Gapais & Barbarin, 1986). In the same way, the boundaries between K-feldspar grains are strongly lobated, which is only possible at high temperatures to allow rapid movements of grains boundaries. The observed [001](010) slip system yields no information about the conditions of plastic deformation because it has been reported for various conditions of deformations ranging from lower greenschist (Sacerdoti *et al.*, 1980) to granulite facies (Franěk *et al.*, 2006). No classical slip system has been found in plagioclase in the studied rock sequence. However, a very strong preferred orientation of the [001] direction parallel to the lineation and of the (001) crystal plane parallel to the foliation is observed in Type I and II microstructures. The inferred [001](001) slip system has never been reported in the literature (Kruse *et al.*, 2001; Menegon *et al.*, 2008) and there is no information about the hypothetic original preferred orientation of crystal mother grains. Therefore, we, we can postulate that this unknown slip system was active in studied rocks. This implies a high plastic crystal deformation of both feldspars that can only happen at very high temperature and at the presence of melt. Alternatively, this type of LPO can be interpreted as a result of rigid body rotation and alignment of grains in a viscous matrix during magmatic deformation (i.e [001] in the X directionfor amphibole, see Berger & Stünitz, 1996). Such an unusal LPO can be also produced by anisotropic growth by dissolution-precipitation creep on preferential plane as it has been proposed by Menegon *et al.* (2008) to explain unusual apparent slip system in K-feldspar. This late proposition involves high mobility of elements and vacancies during diffusion creep mechanism. In all cases theses strong LPO's in quartz and feldspars disappear in type III microstructure. This may be possible, if the grain boundary sliding is active which fits well with increasing amount of interstitial phases and diffuse contact between monomineralic layers. At this stage, the amount of melt was certainly sufficient to reduce the field of power-law creep and at the same time decrease the viscosity of feldspar aggregates (Rybacki & Dresen, 2004). The grain boundary sliding results in an almost total mixing of all mineral phases in conjunction with decrease of mean grain size as it has been shown in deformation map for feldspar (Rybacki & Dresen, 2004) or quartz (Rutter & Elliott, 1976).

7. 3. Correlation with adjacent units

Field observations in the Králiky Śnieżnik massifs have shown that orthogneiss was at least locally already partially molten during development of the first flat lying S1 foliation which

preceded lateral D2 shortening and associated crustal folding. This has been also observed in other places around high grade eclogite and HP-granulite bearing cores of anticlines at the scale of the whole OSD (Don, 1982; Štípská *et al.*, 2004; Chopin *et al.*, this volume-b; Štípská *et al.*, this volume). This study focused on a deformation gradient from rarely preserved augen gneiss to the migmatite in the anticline where the D2 lateral shortening results in pervasive reworking of previous structures (Fig. 3.) compared to more heterogeneneous D2 deformation around westerly eclogite bearing orthogneiss. Therefore, this study yields information about the rheology of orthogneisses in deeper section of the accretionnary wedge close to continental indentor where deep seated rocks were exhumed by crustal scale folding. Increase of partial melting decreased considerably the rheology of the deeper part of the felsic lower crust thereby allowing pervasive deformation of metagranite. This softening mechanism is accompanied with reduction of crystal plasticity of quartz and both feldspars suggesting activity of granular type flow in partially molten rocks.

CONCLUSION

Ce travail est une approche multiméthode sur l'évolution du flux de matière, de l'architecture et de la rhéologie d'un prisme d'accrétion crustal et d'un dôme orogénique associé (Orlica-Śnieżnik, Sudètes, République Tchèque / Pologne).

Les résultats obtenus dans le **chapitre II** ont permis de développer un modèle d'évolution géodynamique à l'échelle du prisme de cette partie de l'orogène hercynienne.

Les structures D1, rarement préservées, sont liées au flux d'entrée dans le prisme d'accrétion continental formant progressivement une croûte épaissie (50-60 km). Les fabriques plates ainsi formées enregistrent une évolution prograde jusqu'au faciès éclogite ou de granulite de HP pour les roches de plus haut degré métamorphique (19-22 kbar). Cette nouvelle croûte inférieure, associée à des orthogneiss mylonitiques à migmatitique passe progressivement à des orthogneiss rigides peu déformés et peu fondus. La croûte moyenne est constituée de métasédiments et métavolcanites du faciès amphibolite.

Les structures D2 sont liées à une compression latérale de cette croûte anisotrope entraînant la formation de fabriques verticales parallèles au butoir. La formation de plis crustaux associée permet l'exhumation des roches de hauts degrés jusqu'au faciès amphibolite dans le cœur d'anticlinaux proches du butoir où cette phase de déformation est la plus intense. L'évolution prograde et/ou rétrograde dans les synclinaux adjacents de croûte moyenne est expliquée par la présence de plis à plus grande longueur d'onde sur lesquels ces plis « parasites » sont enfouis et/ou exhumés suivant leur position par rapport à la ligne d'inflexion. Cette plus grande longueur d'onde peut s'expliquer par le caractère rigide des orthogneiss. La présence de ces plis non visibles en surface explique la répartition des âges de refroidissement et des isogrades qui sont fortement influencés par la présence d'une large portion de migmatite dans leur cœur. La suprastructure enregistre cette même convergence qui s'exprime au plus proche du butoir par une déformation transpressive. Cet épisode est daté à 340-350 Ma.

La dernière phase de déformation en liaison avec l'amincissement ductile de l'infrastructure est plus hétérogène et n'est pas visible dans tous le dôme, elle se caractérise par des fabriques plates à l'arrière du dôme alors que les zones proches du butoir semblent mieux préservées. Ce stade est associé avec le détachement de la suprastructure permettant l'exhumation finale du dôme dans son ensemble vers 330-340 Ma.

Le modèle géodynamique proposé prend en compte toutes ces conclusions et les replace dans le cadre des sudètes, à l'échelle du prisme d'accrétion continental. Les structures D1 sont directement issues de la subduction et du sous-placage sous la croûte Tepla-Barandienne de matériel felsique provenant de la marge Saxo-Thuringienne. Le blocage de la subduction entraine la formation de plis d'échelle crustale D2 au front du butoir qui, associé à des plis de plus petites amplitudes, entraîne des échanges de matière verticaux au sein de l'infrastructure. L'exhumation finale de l'ensemble du dôme d'Orlica Snieznik résulte d'un amincissement ductile de l'infrastructure et du décoiffement de sa suprastructure alors qu'il se produit des bassins sédimentaires supportant l'érosion massive des reliefs.

La structure du dôme d'Orlica-Śnieżnik est donc expliquée en termes d'exhumation au

front du butoir rigide d'un prisme d'accrétion orogénique par plissement crustal de différentes longue d'ondes dans l'infrastructure se terminant par un amincissement ductile et un décoiffement de celle-ci.

Le **chapitre III** met en valeur d'une façon plus précise comment les plis crustaux au front du butoir sont responsables des échanges de matière verticaux dans l'infrastructure. Il amène des données quantitatives au modèle précédemment décrit et permet de détailler le mode de plissement de l'infrastructure dans une zone où l'on retrouve actuellement des éclogites juxtaposées à des métapélites du faciès amphibolite. Le pic métamorphique dans les fabriques plates précoces est enregistré à 22 kbar et 730°C dans les éclogites et 6 kbar à 550-650°C dans les métapélites. Ce pic est associé au flux de matière dans le coin du prisme. L'exhumation quasi adiabatique des éclogites est contemporainement associée à un léger enfouissement puis à une exhumation des métapélites jusqu'à 5kbar. Ce phénomène est expliqué par l'influence d'un anticlinal de 1er ordre permettant une exhumation finale aussi bien dans les anticlinaux et synclinaux de 2ème ordre, au dessus de la ligne d'inflexion primaire. Cette exhumation est finalement associée à une érosion importante dont témoigne la chute rapide de pression et de température dans les deux lithologies. L'amincissement ductile semble négligeable dans cette zone.

Dans le **chapitre IV**, l'étude détaillée d'un gradient de déformation dans les orthogneiss bordant les éclogites a permis de révéler la rhéologie de la croûte felsique (orthogneiss) lors de son enfouissement dans le prisme d'accrétion crustal le long d'un gradient géothermique froid typique d'une zone de subduction (~10°C/km). Les différents types d'orthogneiss étudiés (augen gneiss, gneiss lité et mylonite) montrent que le gradient observé reflète l'enfouissement progressif d'une portion de croûte continentale à partir d'au moins 12 kbar à 650°C vers 19 kbar à 750°C. Les mécanismes de déformation par fluage dislocation disparaissent pour laisser place à une déformation par glissement de joints de grains et transfert de matière. Cette transition, initiée par les réactions métamorphiques (croissance de phases interstitielles) est responsable de la localisation de la déformation permettant le transport passif des orthogneiss les moins déformés dans le prisme jusqu'à 50-60 km. Cette évolution prograde est directement liée à l'enfouissement des éclogites que l'on retrouve dans ces orthogneiss.

Enfin le **chapitre V** permet d'étudier la rhéologie des migmatites lors de leur exhumation au cœur d'un anticlinal situé au front du butoir. Par rapport aux mylonites précédemment décrites, on décrit ici un trajet rétrograde depuis le faciès granulite. Les mécanismes de déformation sont dominés par une forte recrystallisation par fluage dislocation du quartz et des feldspaths, bien qu'un système de glissement non répertorié dans ces derniers puisse suggérer un autre mode de recrystallisation pour ces derniers. L'intensité croissante de la déformation est associée à un flux granulaire, associé à une mobilité accrue des limites de phases ainsi qu'à une proportion de liquide silicaté probablement plus importante aux joints de grains. Ceci est en accord avec la faible viscosité des ces migmatites formant la majeure partie de l'anticlinal migmatitique au front du butoir orogénique.

REFERENCES

Aleksandrowski, P., Kryza, R., Mazur, S. & Zaba, J., 1997. Kinematic data on major Variscan strike-slip faults and shear zones in the Polish Sudetes, northeast Bohemian Massif. *Geological Magazine*, **134**(5), 727-739.

Allemand, P. & Lardeaux, J. M., 1997. Strain partitioning and metamorphism in a deformable orogenic wedge: Application to the Alpine belt. *Tectonophysics*, **280**(1-2), 157-169.

Anczkiewicz, R., Szczepanski, J., Mazur, S., Storey, C., Crowley, Q., Villa, I. M., Thirlwall, M. E. & Jeffries, T. E., 2007. Lu-Hf geochronology and trace element distribution in garnet: Implications for uplift and exhumation of ultra-high pressure granulites in the Sudetes, SW Poland. *Lithos*, **95**(3-4), 363-380.

Andersen, T. B. & Fossen, H., 1993. The role of extensional tectonics in the Caledonides of south Norway-discussion and reply. *Journal of Structural Geology*, **15**, 1379-1383.

Bakun-Czubarow, N., 1991. On the possibility of occurence of quartz pseudomorph after coesite in the eclogite-granulite rock series of the Zlote Mountains in the Sudetes (SW Poland). *Archiwum Mineralogiczne*, **47**(1), 5-16.

Bakun-Czubarow, N., 1992. Quartz pseudomorphs after coesite and quartz exsolutions in eclogitic omphacites of the Zlote Mountains in the Sudetes (SW Poland). *Archiwum Mineralogiczne*, **48**(1-2), 3-25.

Bakun-Czubarow, N., 1998. Ilmenite-bearing eclogites of the West Sudetes – their geochemistry and mineral chemistry. *Archiwum Mineralogiczne*, **51**(1-2), 29-110.

Baratoux, L., Schulmann, K., Ulrich, S. & Lexa, O., 2005. Contrasting microstructures and deformation mechanisms in metagabbro mylonites contemporaneously deformed under different temperatures (c. 650°C and c. 750°C). In: *Deformation Mechanisms, Rheology and Tectonics: from Minerals to Lithosphere.* (ed Gapais, D., Brun, J. P., Cobbold, P. R.), pp. 97–125, Geological Society Special Publications, London.

Bascou, J., Barruol, G., Vauchez, A., Mainprice, D. & Egydio-Silva, M., 2001. EBSD-measured lattice-preferred orientations and seismic properties of eclogites. *Tectonophysics*, **342**(1-2), 61-80.

Beaumont, C., Jamieson, R. A., Butler, J. P. & Warren, C. J., 2009. Crustal structure: A key constraint on the mechanism of ultra-high-pressure rock exhumation. *Earth and Planetary Science Letters*, **287**(1-2), 116-129.

Beaumont, C., Jamieson, R. A., Nguyen, M. H. & Lee, B., 2001. Himalayan tectonics explained by extrusion of a low-viscosity crustal channel coupled to focused surface denudation. *Nature*, **414**(6865), 738-742.

Beaumont, C., Nguyen, M. H., Jamieson, R. A. & Ellis, S., 2006. Crustal flow modes in large hot orogens. Channel flow, ductile extrusion and exhumation in continental collision zones. *Geological Society Special Publications*, **268**, 91-145.

Berger, A. & Stünitz, H., 1996. Deformation mechanisms and reaction of hornblende: Examples from the Bergell tonalite (Central Alps). *Tectonophysics*, **257**(2-4 SPEC. ISS.), 149-174.

Białek, D. & Werner, T., 2004. Geochemistry and Geochronology of the Javornik Granodiorite and its Geodynamic Significance in the Eastern Variscan Belt. *Geolines*, **17**, 22-23.

Biot, M. A., 1961. Theory of folding of stratified viscoelastic media and its implications in tectonics and orogenesis. *Geological Society of America Bulletin*, **72**, 1595-1620.

Blay, P., Cosgrove, J. W. & Summers, J. M., 1977. An experimental investigation of the development of structures in multilayers under the influence of gravity. *Journal of the Geological Society*, **133**(4), 329-342.

Borkowska, M., Choukroune, P., Hameurt, J. & Martineau, F., 1990. A geochemical investigation of the age, significance and structural evolution of the Caledonian-Variscan granite-gneisses of the Snieznik metamorphic area (Central Sudetes, Poland). *Geologia Sudetica*, **15**, 1-27.

Bott, M. H. P. & Dean, D. S., 1973. Stress diffusion from plate boundaries. *Nature*, **243**(5406), 339-341.

Bröcker, M. & Klemd, R., 1996. Ultrahigh-pressure metamorphism in the Snieznik Mountains (Sudetes, Poland): P-T constraints and geological implications. *Journal of Geology*, **104**(4), 417-433.

Bröcker, M., Klemd, R., Cosca, M., Brock, W., Larionov, A. N. & Rodionov, N., 2009. The timing of eclogite facies metamorphism and migmatization in the Orlica-Snieznik complex, Bohemian Massif: constraints from a multimethod geochronological study. *Journal of Metamorphic Geology*, **27**(5), 385-403.

Bröcker, M., Klemd, R., Kooijman, E., Berndt, J. & Larionov, A., 2010. Zircon geochronology and trace element characteristics of eclogites and granulites from the Orlica-Snieznik complex, Bohemian Massif. *Geological Magazine*, **147**(3), 339-362.

Brown, M., Averkin, Y. A. & McLellan, E. L., 1995. Melt segregation in migmatites. *Journal of Geophysical Research*, **100**(B8), 15,655-15,679.

Brueckner, H. K., Medaris, L. G. & Bakun-Czubarow, N., 1991. Nd and Sr age and isotope patterns from Variscan eclogites of the eastern Bohemian Massif. *Neues Jahrbuch für Mineralogie, Abhandlungen*, **163**, 169-196.

Brun, J. P., 1983. (The origin of gneiss domes: models and tests). *L' origine des domes gneissiques: modeles et tests.*, **25**(2), 219-228.

Brun, J. P. & Van Den Driesshe, J., 1994. Extensional gneiss domes and detachment faults - structure and kinematics. *Bulletin de la Société Géologique de France*, **165**(519-530).

Burg, J.-P., Kaus, B. J. P. & Podladchikov, Y. Y., 2004. Dome structures in collision orogens: Mechanical investigation of the gravity/compression interplay. *Geological Society of America Special Papers*, **380**, 47-66.

Burg, J. P., Nievergelt, P., Oberli, F., Seward, D., Davy, P., Maurin, J. C., Diao, Z. & Meier, M., 1998. The Namche Barwa syntaxis: evidence for exhumation related to compressional crustal folding. *Journal of Asian Earth Sciences*, **16**, 239-252.

Buriánek, D., Verner, K., Hanžl, P. & Krumlová, H., 2009. Ordovician metagranites and migmatites of the Svratka and Orlice-Sněžník units, northeastern Bohemian Massif. *Journal of Geosciences*, **54**(2), 181-200.

Büsch, W., Schneider, G. & Mehnert, K. R., 1974. Initial melting at grain boundaries. Part II: Melting in rocks of granodioritic, quartz dioritic and tonalitic composition *Neues Jahrbuch Für Mineralogie Monatshefte*, **8**, 345–370.

Buslov, M. M., Saphonova, I. Y., Watanabe, T., Obut, O. T., Fujiwara, Y., Iwata, K., Semakov, N. N., Sugai, Y., Smirnova, L. V. & Kazansky, A. Y., 2001. Evolution of the Paleo-Asian Ocean (Altai-Sayan Region, Central Asia) and collision of possible Gondwana-derived terranes with the southern arginal part of the Siberian continent. *Journal of Asian Earth Sciences*, **3**, 203-224.

Cashman, K. V. & Ferry, J. M., 1988. Crystal size distribution (CSD) in rocks and the kinetics and dynamics of crystallization; 3 Metamorphic crystallization *Contributions to Mineralogy and Petrology*, **99**(4), 401–415.

Chemenda, A. I., Burg, J. P. & Mattauer, M., 2000. Evolutionary model of the Himalaya-Tibet system: geopoem based on new modelling, geological and geophysical data. *Earth and Planetary Science Letters*, **174**(3-4), 397-409.

Chemenda, A. I., Mattauer, M., Malavielle, J. & Bokun, A. N., 1995. A mechanism for syn-collisional rock exhumation and associated normal faulting: Results from physical modelling. *Earth and Planetary Science Letters*, **132**, 225-232.

Chopin, F., Schulmann, K., Martelat, J. E., Štípská, P., Lexa, O. & Petri, B., 2010a. Quantitative microstructural and petrological study of a prograde deformation gradient in HP-eclogite

bearing orthogneiss (Orlica - Snieznik Dome, Central Sudetes). *This volume*.

Chopin, F., Schulmann, K., Skrzypek, E., Lexa, O., Martelat, J. E., Lehmann, J., Corsini, M., Dujardin, J. R., Edel, J. B., Stipska, P. & Pitra, P., 2010b. Growth and collapse of mantled gneiss dome during Variscan Orogeny (Orlica Snieznik Dome, Bohemian Massif). *This volume*.

Cloos, M., 1982. Flow melanges - numerical modeling and geologic constraints on their origin in the Franciscan Subduction Complex, California. *Geological Society of America Bulletin*, **93**(4), 330-345.

Cobbold, P. R. & Quinquis, H., 1980. Development of sheath folds in shear regimes. *Journal of Structural Geology*, **2**(1-2), 119-126.

Coggon, R. & Holland, T. J. B., 2002. Mixing properties of phengitic micas and revised garnet-phengite thermobarometers. *Journal of Metamorphic Geology*, **20**(7), 683-696.

Cooke, R. A. & O'Brien, P. J., 2001. Resolving the relationship between high P-T rocks and gneisses in collisional terranes: an example from the Gföhl gneiss-granulite association in the Moldanubian Zone, Austria. *Lithos*, **58**(1-2), 33-54.

Cosgrove, J. W., 2007. The use of shear zones and related structures as kinematic indicators: A review, pp. 59-74.

Cowan, D. S. & Silling, R. M., 1978. A dynamic, scaled model of accretion at trenches and its implications for the tectonic evolution of subduction complexes. *Journal of Geophysical Research*, **83**, 5389-5396.

Culshaw, N., 2005. Buckle folding and deep-crustal shearing of high-grade gneisses at the junction of two major high-strain zones, Central Gneiss Belt, Grenville Province, Ontario. *Canadian Journal of Earth Sciences*, **42**(10), 1907-1925.

Culshaw, N. G., Beaumont, C. & Jamieson, R. A., 2006. The orogenic superstructure-infrastructure concept: Revisited, quantified, and revived. *Geology*, **34**(9), 733-736.

Cymerman, Z., 1997. Structure, kinematics and evolution of the Orlica - Snieznik dome, Sudetes. *Prace Panstwowego Instytutu Geologicznego*, **156**, 1-120.

Cymerman, Z., Piasecki, M. & Seston, M., 1997. Terranes and terrane boundaries in the Sudetes, NE Bohemian Massif. *Geological Magazine*, **134**(5), 717-725.

Daines, M. J. & Kohlstedt, D. L., 1997. Influence of deformation on melt topology in peridotites. *Journal of Geophysical Research*, **102**, 10257–10271.

Dale, J., Powell, R., White, R. W., Elmer, F. L. & Holland, T. J. B., 2005. A thermodynamic model for Ca-Na clinoamphiboles in Na_2O-CaO-FeO-MgO-Al_2O_3-SiO_2-H_2O-O for petrological calculations. *Journal of Metamorphic Geology*, **23**(8), 771-791.

Dell'Angelo, L. N., Tullis, J. & Yund, R. A., 1987. Transition from dislocation creep to melt-enhanced diffusion creep in fine-grained granitic aggregates *Tectonophysics*, **139**, 325–332.

DeVore, G. W., 1959. Role of minimum interfacial free energy in determining the macroscopic features of minerals assemblages. *Journal of Geology*, **67**, 211–227.

Dewey, J. F., 1988. Extensional collapse of orogens. *Tectonics*, **7**(6), 1123-1139.

Diener, J. F. A., Powell, R., White, R. W. & Holland, T. J. B., 2007. A new thermodynamic model for clino- and orthoamphiboles in the system Na_2O-CaO-FeO-MgO-Al_2O_3-SiO_2-H_2O-O. *Journal of Metamorphic Geology*, **25**(6), 631-656.

Diener, J. F. A., White, R. W. & Powell, R., 2008. Granulite facies metamorphism and subsolidus fluid-absent reworking, Strangways Range, Arunta Block, central Australia. *Journal of Metamorphic Geology*, **26**(6), 603-622.

Don, J., 1964. The Zlote and Krowiarki Mountains as structural elements of the Snieznik metamorphic massif. *Geologia Sudetica*, **1**, 79-117.

Don, J., 1982. The Sienna synform and the relationship of gneisses to the deformational stages

distinguished in the Snieznik metamorphic massif (Sudetes). *Geologia Sudetica*, **17**, 130-124.

Don, J., Dumicz, M., Wojciechowska, I. & Zelazniewicz, A., 1990. Lihology and tectonics of the Orlica-Snieznik Dome, Sudetes: recent state of knowledge. *Neues Jahrbuch für Geologie und Paläontologie, Abhandlungen*, **179**(2/3), 159-188.

Don, J., Skácel, J. & Gotowała, R., 2003. The boundary zone of the East and West Sudetes on the 1:50 000 scale geological map of the Velké Vrbno, Staré Město and Śnieznik Metamorphic Units. *Geologia Sudetica*, **35**(1), 25-59.

Don, J., Skácel, J. & Gotowała, R., 2004. The boundary zone of the East and West Sudetes on the 1:50 000 scale geological map of the Velké Vrbno, Staré Město and Śnieznik Metamorphic Units. *Geologia Sudetica*, **35**(1), 25-59.

Don, J. & Zelazniewicz, A., 1990. The Sudetes - boundaries, subdivisions and tectonic position. *Neues Jahrbuch für Geologie und Paläontologie, Abhandlungen*, **179**, 121-127.

Duchene, S., Lardeaux, J. M. & Albarede, F., 1997. Exhumation of eclogites: insights from depth-time path analysis. *Tectonophysics*, **280**, 125-140.

Dudek, A., 1980. The crystalline basement block of the Outher Carpathians in Moravia - Brunovistulicum. *Rozpravy Československé Akademie Věd*, **90**(8), 1-85.

Dumicz, M., 1964. Geology of the crystalline massif of the Bystrzyckie Mts. *Geologia Sudetica*, **1**, 169-208.

Dumicz, M., 1979. Tectogenesis of the metamorphosed series of the Klodzko district: a tentative explanation. *Geologia Sudetica*, **14**, 29-44.

Dziedzic, K. & Teisseyre, A. K., 1990. The Hercynian mollase and younger deposits in the Intra-Sudetic Basin, SW Poland. *N. Jb. Geol. Paläont. Abh.*, **197**, 285-305.

Edel, J. B., 2003. Magnetic overprints in granitoids and metamorphic rocks from Limousin (France): evidence for Late Variscan rotations, crustal folding and tilting. *Tectonophysics*, **363**(3-4), 225-241.

Edel, J. B., Schulmann, K. & Holub, F. V., 2003. Anticlockwise and clockwise rotations of the Eastern Variscides accommodated by dextral lithospheric wrenching: palaeomagnetic and structural evidence. *Journal of the Geological Society*, **160**, 209-218.

Fajst, M., 1976. New discordance in the pre-Cambrian of the Bohemian massif (in Czech). *Èasopis pro Mineralogii a Geologii*, **21**(3), 257-275.

Faure, M., Be Mezeme, E., Cocherie, A., Melleton, J. & Rossi, P., 2009. The South Millevaches Middle Carboniferous crustal melting and its place in the French Variscan belt. *Bulletin de la Société Géologique de France*, **180**(6), 473-481.

Feehan, J. G. & Brandon, M. T., 1999. Contribution of ductile flow to exhumation of low-temperature, high-pressure metamorphic rocks: San Juan-Cascade nappes, NW Washington State. *Journal of Geophysical Research B: Solid Earth*, **104**(B5), 10883-10902.

Finger, F., Hanzl, P., Pin, C., von Quadt, A. & Steyrer, H. P., 2000. The Brunovistulian: Avalonian Precambrian sequence at the eastern end of the Central European Variscides? *Geological Society, London, Special Publications*, **179**(1), 103-112.

Fisher, G., 1936. Der Bau des Glatzer Schneegebirges. *Jahrbuch der Preußischen Geologischen Landesanstalt*, **56**, 712-732.

Fletcher, R. C., 1974. Wavelength selection in the folding of a single layer with power-law rheology. *American Journal of Science*, **274**, 1029-1043.

Flinn, D., 1965. On the symmetry principle and the deformation ellipsoid. *Geological Magazine*, **102**(1), 36-45.

Flinn, D., 1969. Grain contacts in crystalline rocks. *Lithos*, **2**(4), 361–370.

Forbes, C. J., Betts, P. G. & Lister, G. S., 2004. Synchronous development of Type 2 and Type

3 fold interference patterns: Evidence for recumbent sheath folds in the Allendale Area, Broken Hill, NSW, Australia. *Journal of Structural Geology*, **26**(1), 113-126.

Franěk, J., Schulmann, K. & Lexa, O., 2006. Kinematic and rheological model of exhumation of high pressure granulites in the Variscan orogenic root: example of the Blanský les granulite, Bohemian Massif, Czech Republic. *Mineralogy and Petrology*, **86**(3-4), 253-276.

Franěk, J., Schulmann, K., Lexa, O., Tomek, Č. & Edel, J. B., 2010a. Model of syn-convergent extrusion of orogenic lower crust in the core of the Variscan belt: implications for exhumation of HP rocks in large hot orogens. *Submitted to Journal of Metamorphic Geology*.

Franěk, J., Schulmann, K., Lexa, O., Ulrich, S., Štípská, P., Haloda, J. & Týcová, P., 2010b. Origin of felsic granulite microstructure by heterogeneous decomposition of alkali feldspar and extreme weakening of orogenic lower crust during the Variscan orogeny. *Submitted to Journal of Metamorphic Geology*.

Franke, W. & Zelazniewicz, A., 2000. The eastern termination of the Variscides: terrane correlation and kinematic evolution. In: *Orogenic processes: Quantification and Modelling in the Variscan belt* (eds Franke, W., Haak, V., Oncken, O. & Tanner, D.), pp. 63-86, Geological Society, London, Special publications, 179.

Gapais, D., 1989. Shear structures within deformed granites: Mechanical and thermal indicators. **17**, 1144-1147.

Gapais, D. & Barbarin, B., 1986. Quartz fabric transition in a cooling syntectonic granite (Hermitage massif, France). *Tectonophysics*, **125**, 357-370.

Gapais, D., Cagnard, F., Gueydan, F., Barbey, P. & Ballèvre, M., 2009. Mountain building and exhumation processes through time: Inferences from nature and models. *Terra Nova*, **21**(3), 188-194.

Gapais, D. & Cobbold, P. R., 1987. Slip system domains. 2. Kinematic aspects of fabric development in polycrystalline aggregates. *Tectonophysics*, **138**(2-4), 289-309.

Gerya, T. & Stöckhert, B., 2006. Two-dimensional numerical modeling of tectonic and metamorphic histories at active continental margins. *International Journal of Earth Sciences*, **95**(2), 250-274.

Gerya, T. V., Perchuk, L. L., Maresch, W. V. & Willner, A. P., 2004. Inherent gravitational instability of hot continental crust: Implications for doming and diapirism in granulite facies terrains. Geological Society of America Special Papers 380, 97-115.

Gerya, T. V., Perchuk, L. L., Maresch, W. V., Willner, A. P., Van Reenen, D. D. & Smit, C. A., 2002. Thermal regime and gravitational instability of multi-layered continental crust: implications for the buoyant exhumation of high-grade metamorphic rocks. European Journal of Mineralogy, 14, 687-699.

Gordon, S. M., Schneider, D. A., Manecki, M. & Holm, D. K., 2005. Exhumation and metamorphism of an ultrahigh-grade terrane: geochronometric investigations of the Sudete Mountains (Bohemia), Poland and Czech Republic. *Journal of the Geological Society*, **162**, 841-855.

Gower, R. J. W. & Simpson, C., 1992. Phase boundary mobility in naturally deformed, high-grade quartzofeldspathic rocks: evidence for diffusional creep. *Journal of Structural Geology*, **14**(3), 301–313.

Grant, J. A., 1986. The isocon diagram-a simple solution to Gresens' equation for metasomatic alteration. *Economic Geology*, **81**(8), 1976-1982.

Green, E., Holland, T. & Powell, R., 2007. An order-disorder model for omphacitic pyroxenes in the system jadeite-diopside-hedenbergite-acmite, with applications to eclogitic rocks. *American Mineralogist*, **92**(7), 1181-1189.

Grocott, J. & Watterson, J., 1980. Strain profile of a boundary within a large ductile shear zone. *Journal of Structural Geology*, **2**(1-2), 111-117.

Guy, A., Edel, J.-B., Schulmann, K., Tomek, C. & Lexa, O., 2010. A geophysical model of the Variscan orogenic root (Bohemian Massif): Implications for modern collisional orogens. *Lithos*, **in press**.

Handy, M., 1990a. The solid state flow of polymineralic rocks. *Journal of Geophysical Research*, **95**, 8647-8661.

Handy, M., 1994. Flow laws for rocks containing two non-linear viscous phases: a phenomenological approach. *Journal of Structural Geology*, **16**, 287-301.

Handy, M. R., 1990b. The Solid-State Flow of Polymineralic Rocks. *Journal of Geophysical Research-Solid Earth and Planets*, **95**(B6), 8647-8661.

Handy, M. R. & Stünitz, H., 2002. Strain localization by fracturing and reaction weakening -A mechanism for initiating exhumation of subcontinental mantle beneath rifted margins, pp. 387-407.

Hanmer, S. K., 1982. Microstructure and geochemistry of plagioclase and microcline in naturally deformed granite. *Journal of Structural Geology*, **4**(2), 197-213.

Hasalová, P., Janoušek, V., Schulmann, K., Štípská, P. & Erban, V., 2008a. From orthogneiss to migmatite: geochemical assessment of the melt infiltration model in the Gföhl Unit (Moldanubian Zone, Bohemian Massif). *Lithos*, **102**, 508-537.

Hasalová, P., Schulmann, K., Lexa, O., Štípská, P., Hrouda, F., Ulrich, S., Haloda, J. & Týcová, P., 2008b. Origin of migmatites by deformation-enhanced melt infiltration of orthogneiss: a new model based on quantitative microstructural analysis. *Journal of Metamorphic Geology*, **26**, 29-53.

Hasalová, P., Štípská, P., Powell, R., Schulmann, K., Janoušek, V. & Lexa, O., 2008c. Transforming mylonitic metagranite by open-system interactions during melt flow. *Journal of Metamorphic Geology*, **26**(1), 55-80.

Heilbronner, R. & Tullis, J., 2002. The effect of static annealing on microstructures and crystallographic preferred orientations of quartzites experimentally deformed in axial compression and shear, pp. 191-218.

Heilbronner, R. & Tullis, J., 2006. Evolution of c axis pole figures and grain size during dynamic recrystallization: Results from experimentally sheared quartzite. *Journal of Geophysical Research B: Solid Earth*, **111**(10).

Higgins, M. D., 1998. Origin of anorthosite by textural coarsening: quantitative measurements of a natural sequence of a textural development. *Journal of Petrology*, **39**(7), 1307–1323.

Hodges, K. V., Hurtado, J. M. & Whipple, K. X., 2001. Southward extrusion of Tibetan crust and its effect on Himalayan tectonics. *Tectonics*, **20**(6), 799-809.

Holland, T. J. B., Baker, J. & Powell, R., 1998. Mixing properties and activity-composition relationships of chlorites in the system MgO-FeO-Al_2O_3-SiO_2-H_2O. *European Journal of Mineralogy*, **10**(3), 395-406.

Holland, T. J. B. & Powell, R., 1998. An internally consistent thermodynamic data set for phases of petrological interest. *Journal of Metamorphic Geology*, **16**(3), 309-343.

Holland, T. J. B. & Powell, R., 2003. Activity-composition relations for phases in petrological calculations: an asymmetric multicomponent formulation. *Contributions to Mineralogy and Petrology*, **145**, 492-501.

Holyoke Iii, C. W. & Tullis, J., 2006a. The interaction between reaction and deformation: An experimental study using a biotite + plagioclase + quartz gneiss. *Journal of Metamorphic Geology*, **24**(8), 743-762.

Holyoke Iii, C. W. & Tullis, J., 2006b. Mechanisms of weak phase interconnection and the

effects of phase strength contrast on fabric development. *Journal of Structural Geology*, **28**(4), 621-640.

Hrouda, F. & Chlupáčová, M., 1993. Geologický model západní části Českého masívu ve vazbě na ultrahluboký VRT (KTB-1) V SRN. Zpráva za dílčí úkol 04: Petrofyzikální výzkum v západních Čechách ve vazbě na ultrahluboký vrt (KTB-1) v SRN. MS Geofyzika, a.s., Brno.

Ibrmajer, 1981. Geological interpretation of gravity maps of Czechoslovakia. In: A. Zapotek (Editor), Geophysical synthesis in Czechoslovakia. Veda, Bratislava. *In: A. Zapotek (Editor), Geophysical synthesis in Czechoslovakia. Veda, Bratislava*, 135-148.

Indares, A., Dunning, G. & Cox, R., 2000. Tectono-thermal evolution of deep crust in a Mesoproterozoic continental collision setting: The Manicouagan example. *Canadian Journal of Earth Sciences*, **37**(2-3), 325-340.

Ishii, K., Kanagawa, K., Shigematsu, N. & Okudaira, T., 2007. High ductility of K-feldspar and development of granitic banded ultramylonite in the Ryoke metamorphic belt, SW Japan. *Journal of Structural Geology*, **29**(6), 1083-1098.

Jamieson, R. A., Beaumont, C., Nguyen, M. H. & Lee, B., 2002. Interaction of metamorphism, deformation and exhumation in large convergent orogens. *Journal of Metamorphic Geology*, **20**(1), 9-24.

Jastrzębski, M., 2005. The tectonometamorphic evolution of the marbles in the Lądek- Śnieżnik Metamorphic Unit, West Sudetes. *Geologia Sudetica*, **37**, 1-26.

Jastrzębski, M., 2009. A Variscan continental collision of the West Sudetes and the Brunovistulian terrane: a contribution from structural and metamorphic record of the Stronie Formation, the Orlica-Snieznik Dome, SW Poland. *International Journal of Earth Sciences*, **98**(8), 1901-1923.

Jastrzębski, M., Żelaźniewicz, A., Nowak, I., Murtezi, M. & Larionov, A. N., 2010. Protolith age and provenance of metasedimentary rocks in Variscan allochthon units: U-Pb SHRIMP zircon data from the Orlica-Snieznik Dome, West Sudetes. *Geological Magazine*, **147**(3), 416-433.

Jeřábek, P., Faryad, W. S., Schulmann, K., Lexa, O. & Tajčmanová, L., 2008. Alpine burial and heterogeneous exhumation of Variscan crust in the West Carpathians: Insight from thermodynamic and argon diffusion modelling. *Journal of the Geological Society*, **165**(2), 479-498.

Ježek, J., Schulmann, K. & Thompson, A. B., 2002. Strain partitioning parametres in front of an obliquely convergent indenter. In: *Continental collision and the tectonosedimentary evolution of forelands* (eds Bertotti, G., Schulmann, K. & Cloethingh, S.), pp. 145-165, European Geophysical Society, Stephan Mueller Special Publication Series.

Jolivet, L., Raimbourg, H., Labrousse, L., Avigad, D., Leroy, Y., Austrheim, H. & Andersen, T. B., 2005. Softening trigerred by eclogitization, the first step toward exhumation during continental subduction. *Earth and Planetary Science Letters*, **237**(3-4), 532-547.

Jurewitz, S. R. & Watson, E. B., 1984. Distribution of partial melt in a felsic system -the importance of surface energy. *Contributions to Mineralogy and Petrology*, **85**(1), 25–29.

Kadziałko-Hofmokl, M., Mazur, S., Werner, T. & Kruczyk, J., 2004. Relationships between magnetic and structural fabrics revealed by Variscan basement rocks subjected to heterogeneous deformation - A case study from the Kłodzko Metamorphic Complex, Central Sudetes, Poland, pp. 475-491.

Kassner, M. E. & Hayes, T. A., 2003. Creep cavitation in metals. *Int. J. Plasticity*, **19**(10), 1715-1748.

Klápová, H., Konopásek, J. & Schulmann, K., 1998. Eclogites from the Czech part of the Erzgebirge: multi-stage metamorphic and structural evolution. *Journal of the Geological*

Society, 155, 567-583.

Klemd, R. & Bröcker, M., 1999. Fluid influence on mineral reactions in ultrahigh-pressure granulites: a case study in the Snieznik Mts. (West Sudetes, Poland). *Contributions to Mineralogy and Petrology*, **136**(4), 358-373.

Klemd, R., Bröcker, M. & Schramm, J., 1995. Characterization of amphibolite-facies fluids of Variscan eclogites from the Orlica-Snieznik Dome (Sudetes, SW Poland). *Chemical Geology*, **119**(1-4), 101-113.

Konopásek, J. & Schulmann, K., 2005. Contrasting Early Carboniferous field geotherms: evidence for accretion of a thickened orogenic root and subducted Saxothuringian crust (Central European Variscides). *Journal of the Geological Society*, 162, 463-470.

Koons, P. O., Rubie, D. C. & Fruehgreen, G., 1987. The Effects of Disequilibrium and Deformation on the Mineralogical Evolution of Quartz Diorite During Metamorphism in the Eclogite Facies. *Journal of Petrology*, **28**(4), 679-700.

Koppers, A. A. P., 2002. ArArCALC-software for $^{40}Ar/^{39}Ar$ age calculations. *Computers and Geosciences*, **28**(5), 605-619.

Kossmatt, F., 1927. Gliederung des varistischen Gebirgsbaues. *Abhandlungen des Sachsischen geologischen Landesamts*, **1**, 1-39.

Košuličová, M. & Štípská, P., 2007. Variations in the transient prograde geothermal gradient from chloritoid-staurolite equilibria: a case study from the Barrovian and Buchan-type domains in the Bohemian Massif. *Journal of Metamorphic Geology*, **25**(1), 19-35.

Koyi, H. A., Milnes, A. G., Schmeling, H., Talbot, C. J., Juhlin, C. & Zeyen, H., 1999. Numerical models of ductile rebound of crustal roots beneath mountain belts. *Geophysical Journal International*, **139**(2), 556-562.

Kozłowska-Koch, 1973. Polimetamorfity strefy tektonicznej Złoty Stok – Skrzynka w Sudetach. *Geol. Sudetica*, **8**, 121-155.

Kozłowski, 1961. Kompleks granulitowy Starego Gieraltowa w Górach Złlotych (The granulitic complex of Stary Gierałtow—East Sudetes). *Archiwum Mineralogiczne* **25**, 5–123.

Kretz, R., 1994. *Metamorphic Crystallization*. Wiley, New York.

Kröner, A., Jaeckel, P., Hegner, E. & Opletal, M., 2001. Single zircon ages and whole rock Nd isotopic systematics of early Palaeozoic granitoid gneisses from the Czech and Polish Sudetes (Jizerské hory, Krkonoše Mountains and Orlice-Sneznik Complex). *International Journal of Earth Sciences*, **90**(2), 304-324.

Kröner, A., Štípská, P., Schulmann, K. & Jaeckel, P., 2000. Chronological constraints on the pre-Variscan evolution of the northeastern margin of the Bohemian Massif, Czech Republic. In: *Orogenic processes; quantification and modelling in the Variscan Belt.* (eds Franke, W., Haak, V., Oncken, O. & Tanner, D.) *Geological Society of London Special Publications*, pp. 175-197, Geological Society of London. London, United Kingdom, 179, 175-197.

Kruse, R. & Stünitz, H., 1999. Deformation mechanisms and phase distribution in mafic high-temperature mylonites from the Jotun Nappe, southern Norway. *Tectonophysics*, **303**, 223–249.

Kruse, R., Stunitz, H. & Kunze, K., 2001. Dynamic recrystallization processes in plagioclase porphyroclasts. *Journal of Structural Geology*, **23**(11), 1781-1802.

Kryza, R., Pin, C. & Vielzeuf, D., 1996. High-pressure granulites from the Sudetes (south-west Poland): evidence of crustal subduction and collisional thickening in the Variscan Belt. *Journal of Metamorphic Geology*, **14**, 531-546.

Lange, U., Bröcker, M., Armstrong, R., Trapp, E. & Mezger, K., 2005a. Sm-Nd and U-Pb dating of high-pressure granulites from the Zlote and Rychleby Mts (Bohemian Massif, Poland and Czech Republic). *Journal of Metamorphic Geology*, **23**(3), 133-145.

Lange, U., Bröcker, M., Armstrong, R., Zelazniewicz, A., Trapp, E. & Mezger, K., 2005b. The orthogneisses of the Orlica-Snieznik complex (West Sudetes, Poland): geochemical characteristics, the importance of pre-Variscan migmatization and constraints on the cooling history. *Journal of the Geological Society*, **162**, 973-984.

Lange, U., Bröcker, M., Mezger, K. & Don, J., 2002. Geochemistry and Rb-Sr geochronology of a ductile shear zone in the Orlica-Snieznik dome (West Sudetes, Poland). *International Journal of Earth Sciences*, **91**(6), 1005-1016.

Lardeaux, J. M., Ledru, P., Daniel, I. & Duchene, S., 2001. The Variscan French Massif Central - a new addition to the ultrahigh pressure metamorphic 'club': exhumation processes and geodynamic consequences. *Tectonophysics*, **332**(1-2), 143-167.

Lee, J., Hacker, B. R., Dinklage, W. S., Wang, Y., Gans, P., Calvert, A., Wan, J. L., Chen, W. J., Blythe, A. E. & McClelland, W., 2000. Evolution of the Kangmar Dome, southern Tibet: Structural, petrologic, and thermochronologic constraints. *Tectonics*, **19**(5), 872-895.

Lee, J. Y., Marti, K., Severinghaus, J. P., Kawamura, K., Yoo, H. S., Lee, J. B. & Kim, J. S., 2006. A redetermination of the isotopic abundances of atmospheric Ar. *Geochimica et Cosmochimica Acta*, **70**(17), 4507-4512.

Lehmann, J., 2009. *Mécanismes de déformation dans les systèmes d'accrétion paléozoïques*. Unpub. PhD Thesis Thesis, Université de Strasbourg, Strasbourg.

Lexa, O., 2003. *Numerical approaches in structural and microstructural analyses*, Unpublished PhD Thesis, Charles University, Prague.

Lexa, O., Cosgrove, J. & Schulmann, K., 2004. Apparent shear-band geometry resulting from oblique fold sections. *Journal of Structural Geology*, **26**(1), 155-161.

Lexa, O., Schulmann, K., Janoušek, V., Štípská, P., Guy, A. & Racek, M., 2010. Heat sources and trigger mechanisms of exhumation of HP granulites in Variscan orogenic root (submitted to Journal of Metamopthic Geology). *Journal of Metamorphic Geology*, **in press**.

Lexa, O., Schulmann, K. & Jezek, J., 2003. Cretaceous collision and indentation in the West Carpathians: View based on structural analysis and numerical modeling. *Tectonics*, **22**(6).

Lexa, O., Stipska, P., Schulmann, K., Baratoux, L. & Kroner, A., 2005. Contrasting textural record of two distinct metamorphic events of similar P-T conditions and different durations. *Journal of Metamorphic Geology*, **23**(8), 649-666.

Lister, G. S. & Hobbs, B. E., 1980. The simulation of fabric development during plastic deformation and its application to quartzite: the influence of deformation history. *Journal of Structural Geology*, **2**(3), 355-370.

Lister, G. S. & Paterson, M. S., 1979. The simulation of fabric development during plastic deformation and its application to quartzite: fabric transitions. *Journal of Structural Geology*, **1**(2), 99-115.

Mahar, E. M., Baker, J. M., Powell, R., Holland, T. J. B. & Howell, N., 1997. The effect of Mn on mineral stability in metapelites. *Journal of Metamorphic Geology*, **15**(2), 223-238.

Majdański, M., Kozlovskaya, E. & Grad, M., 2007. 3D structure of the Earth's crust beneath the northern part of the Bohemian Massif. *Tectonophysics*, **437**(1-4), 17-36.

Maluski, H. & Patoèka, F., 1997. Geochemistry and 40Ar-39Ar geochronology of the mefic metavolcanic rocks from the Rýchory Mountains complex (west Sudetes, Bohemian Massif): palaeotectonic significance. *Geological Magazine*, **134**(5), 703-716.

Maluski, H., Rajlich, P. & Souèek, J., 1995. Pre-Variscan, Variscan and early Alpine thermo - tectonic history of the northeastern Bohemian Massif: An $^{40}Ar/^{39}Ar$ study. *Geologische Rundschau*, **84**, 345-358.

Marheine, D., Kachlík, V., Maluski, H., Patočka, F. & Zelaźniewicz, A., 2002. The $^{40}Ar/^{39}Ar$ ages from the West Sudetes (NE Bohemian Massif): Constraints on the Variscan polyphase tectonothermal development, pp. 133-155.

Marquer, D. & Burkhard, M., 1992. Fluid circulation, progressive deformation and mass-transfer processes in the upper crust: the example of basement-cover relationships in the External Crystalline Massifs, Switzerland. *Journal of Structural Geology*, **14**(8-9), 1047-1057.

Martelat, J. E., Schulmann, K., Lardeaux, J. M., Nicollet, C. & Cardon, H., 1999. Granulite microfabrics and deformation mechanisms in southern Madagascar. *Journal of Structural Geology*, **21**(6), 671-687.

Matte, P., Maluski, H., Rajlich, P. & Franke, W., 1990. Terrane boundaries in the Bohemian Massif: Result of large-scale Variscan shearing. *Tectonophysics*, **177**, 151-170.

Mazur, S. & Aleksandrowski, P., 2001. The Tepla(?)/Saxothuringian suture in the Karkonosze-Izera massif, western Sudetes, central European Variscides. *International Journal of Earth Sciences*, **90**(2), 341-360.

Mazur, S., Aleksandrowski, P., Kryza, R. & Oberc-Dziedzic, T., 2006. The Variscan Orogen in Poland. *Geological Quarterly*, **50**(1), 89-118.

Mazur, S., Aleksandrowski, P. & Szczepański, J., 2005. The presumed Teplá-Barrandian/ Moldanubian terrane boundary in the Orlica Mountains (Sudetes, Bohemian Massif): Structural and petrological characteristics. *Lithos*, **82**(1-2 SPEC. ISS.), 85-112.

Mazur, S., Kröner, A., Szczepański, J., Turniak, K., Hanžl, P., Melichar, R., Rodionov, N. V., Paderin, I. & Sergeev, S. A., 2010. Single zircon U-Pb ages and geochemistry of granitoid gneisses from SW Poland: Evidence for an Avalonian affinity of the Brunian microcontinent. *Geological Magazine*, **147**(4), 508-526.

McLellan, E. L., 1983. Contrasting textures in metamorphic and anatectic migmatites - an example from the Scottish Caledonides. . *Journal of Metamorphic Geology*, **1**(3), 241–262.

Menegon, L., Pennacchioni, G., Heilbronner, R. & Pittarello, L., 2008a. Evolution of quartz microstructure and c-axis crystallographic preferred orientation within ductilely deformed granitoids (Arolla unit, Western Alps). *Journal of Structural Geology*, **30**(11), 1332-1347.

Menegon, L., Pennacchioni, G. & Spiess, R., 2008b. Dissolution-precipitation creep of K-feldspar in mid-crustal granite mylonites. *Journal of Structural Geology*, **30**(5), 565-579.

Menegon, L., Pennacchioni, G. & Stünitz, H., 2006. Nucleation and growth of myrmekite during ductile shear deformation in metagranites. *Journal of Metamorphic Geology*, **24**(7), 553-568.

Murtezi, M., 2006. The acid metavolcanic rocks of the Orlica-Śnieżnik Dome (Sudetes): Their origin and tectono-metamorphic evolution. *Geologia Sudetica*, **38**, 1-38.

Oberhänsli, R., Hunziker, J. C., Martinotti, G. & Stern, W. B., 1983. Geochemistry, geochronology and petrology of Monte Mucrone: an example of eo-Alpine eclogitization of Permian granitoids in the Sesia –Lanzo zone, Western Alps, Italy. *Chemical Geology*, **52**, 165-184.

Oliot, E., Goncalves, P. & Marquer, D., 2010. Role of plagioclase and reaction softening in a metagranite shear zone at mid-crustal conditions (Gotthard Massif, Swiss Central Alps). *Journal of Metamorphic Geology*, no-no.

Oliver, G. J. H., Corfu, F. & Krogh, T. E., 1993. U-Pb ages from SW Poland: evidence for a Caledonian suture zone between Baltica and Gondwana. *Journal of the Geological Society, London*, **150**, 355-369.

Ondra, P. & Hanák, J., 1984. Densities of principal rock types of the Moldanubicum on Czechoslovak territory. *Časopis pro Mineralogii a Geologii*, **29**, 19-28.

Panozzo, R., 1984. Two-Dimensional Strain from the Orientation of Lines in a Plane. *Journal of Structural Geology*, **6**(1-2), 215-221.

Park, Y., Ree, J.-H. & Kim, S., 2001. Lattice preferred orientation in deformed-then-annealed material: observations from experimental and natural polycrystalline aggregates. *International Journal of Earth Sciences*, **90**(1), 127-135.

Parry, M., Štípská, P., Schulmann, K., Hrouda, F., Ježek, J. & Kröner, A., 1997. Tonalite sill emplacement at an oblique plate boundary: northeastern margin of the Bohemian Massif. *Tectonophysics*, **280**(1-2), 61-81.

Pauk, F. R., 1953. Poznámky ke geologii Orlických hor a Králického Sniěniku. *Véstnik Ústředniho ústavu Geologickiho*, **28**, 193-212.

Pavlis, T. L. & Bruhn, R. L., 1983. Deep-seated flow as a mechanism for the uplift of broad forearc ridges and its role in the exposure of high P/T metamorphic terranes. *Tectonics*, 473-497.

Platt, J. P., 1987. The uplift of high-pressure low-temperature metamorphic rocks. *Philosophical Transactions of the Royal Society of London*, **A321**, 87-103.

Platt, J. P., 1993. Exhumation of high-pressure rocks; a review of concepts and processes. *Terra Nova*, **5**(2), 119-133.

Plaumann, S., 1983. Die Schwerekarte 1:500 000 der Bundesrepublik Deutschland (Bouguer-Anomalien), Blatt Nord. *Geologischen Jahrbuch*, **27**, 3-16.

Plaumann, S., 1987. Karte der Bouguer-Anomalien in der Bundesrepublik Deutschland 1:1 500 000. *Geologischen Jahrbuch*, **40**, 3-7.

Plesch, A. & Oncken, O., 1997. Reconstructing the growth of a fossil orogenic wedge: The Rhenohercynian, pp. 139-142.

Plesch, A. & Oncken, O., 1999. Orogenic wedge growth during collision - constraints on mechanics of a fossil wedge from its kinematic record (Rhenohercynian FTB, Central Europe). *Tectonophysics*, **309**(1-4), 117-139.

Polanský, J. & Škvor, V., 1975. Structural-tectonic problems of north-western Bohemia (Summary of Czech. Text). *Sborník geologických Věd. – Užitá geofyzika*, **13**, 47-64.

Pouba, Z., Padìra, K. & Fiala, J., 1985. Omphacite granulite from the NE margin of the Bohemian Massif (Rychleby Mts). *Neues Jahrbuch für Mineralogie, Abhandlungen*, **151**, 29-52.

Powell, R., Holland, T. & Worley, B., 1998. Calculating phase diagrams involving solid solutions via non- linear equations, with examples using THERMOCALC. *Journal of Metamorphic Geology*, **16**(4), 577-588.

Pressler, R. E., Schneider, D. A., Petronis, M. S., Holm, D. K. & Geissman, J. W., 2007. Pervasive horizontal fabric and rapid vertical extrusion: Lateral overturning and margin sub-parallel flow of deep crustal migmatites, northeastern Bohemian Massif. *Tectonophysics*, **443**(1-2), 19-36.

Přikryl, R., Schulmann, K. & Melka, R., 1996. Perpendicular fabrics in the Orlické hory orthogneisses (western part of the Orlice-Sněžník Dome, Bohemian Massif) due to high temperature E-W deformational event and late lower temperature N-S overprint. *Journal of the Czech Geological Society*, **41**(3-4), 156-166.

Prior, D. J., Mariani, E. & Wheeler, J., 2009. EBSD in the Earth Sciences: Applications, Common Practice, and Challenges. In: *Electron Backscatter Diffraction in Materials Science* (eds Schwartz, A. J., Kumar, M., Adams, B. L. & Field, D. P.), pp. 345-360, Springer US.

Proyer, A., 2003. The preservation of high-pressure rocks during exhumation: metagranites and metapelites. *Lithos*, **70**(3-4), 183-194.

Racek, M., Štípská, P., Pitra, P., Schulmann, K. & Lexa, O., 2006. Metamorphic record of burial

and exhumation of orogenic lower and middle crust: a new tectonothermal model for the Drosendorf window (Bohemian Massif, Austria). *Mineralogy and Petrology*, **86**(3-4), 221-251.

Ramsay, J. G., 1967. *Folding and fracturing of rocks*. McGraw-Hill Book Company.

Ramsay, J. G. & Huber, M. I., 1983. *The techniques of modern structural geology.Volume 1: Strain Analysis.* Academic Press, London.

Randolph, A. D. & Larson, M. A., 1971. *Theory of Particle Processes* Academic Press, New York.

Rey, P., Vanderhaeghe, O. & Teyssier, C., 2001. Gravitational collapse of the continental crust: definition, regimes and modes. *Tectonophysics*, **342**(3-4), 435-449.

Ring, U. & Brandon, M. T., 1999. Ductile deformation and mass loss in the Franciscan Subduction Complex: implications for exhumation processes in accretionary wedges. *Geological Society Special Publication*, **154**, 55-86.

Ring, U., Brandon, M. T., Lister, G. S. & Willett, S. D., 1999. Exhumation processes: normal faulting, ductile flow and erosion. *Geological Society Special Publication*, **154**, 1-27.

Rolland, Y., Maheo, G., Guillot, S. & Pecher, A., 2001. Tectono-metamorphic evolution of the Karakorum Metamorphic complex (Dassu-Askole area, NE Pakistan): exhumation of mid- crustal HT-MP gneisses in a convergent context. *Journal of Metamorphic Geology*, **19**(6), 717-737.

Rosenberg, C. L. & Riller, U., 2000. Partial-melt topology in statically and dynamically recrystallized granite. *Geology*, **28**(1), 7–10.

Rutter, E. H. & Elliott, D., 1976. The Kinetics of Rock Deformation by Pressure Solution [and Discussion]. *Philosophical Transactions of the Royal Society of London. Series A, Mathematical and Physical Sciences*, **283**(1312), 203-219.

Rybacki, E. & Dresen, G., 2004. Deformation mechanism maps for feldspar rocks. *Tectonophysics*, **382**(3-4), 173-187.

Rychtár, J. & Rybák., V., 1987. Gravimetrical mapping of the Jesenik Mts. Region Ostružná-Mikulovice. Unpublished report in Czech, Geophysical Institute, Brno.

Sacerdoti, M., Labernardiere, H. & Gandais, M., 1980, 1980. Transmission electron microscope (TEM) study of geologically deformed potassic feldspars. *Bulletin de Minéralogie*, **103**, 148-155.

Sawyer, E. W., 1999. Criteria for the recognition of partial melting. *Physics and Chemistry of the Earth*, **24**(3), 269–279.

Sawyer, E. W., 2001. Melt segregation in the continental crust: distribution and movement of melt in anatectic rocks. *Journal of Metamorphic Geology*, **19**(3), 291–309.

Scandale, E., Gandais, M. & Willaime, C., 1983. Transmission electron microscopic study of experimentally deformed k-feldspar single crystals - The (010) [001], (001) ½[110], (110) ½[112] and (111) ½[110] slip systems. *Physics and Chemistry of Minerals*, **9**(3-4), 182-187.

Schmalholz, S. M., 2006. Scaled amplification equation: a key to the folding history of buckled viscous single-layers. *Tectonophysics*, **419**, 41-53.

Schmid, S. M. & Casey, M., 1986. Complete fabric analysis of some commonly observed quartz c-axis patterns. In: *Mineral and Rock Deformation: Laboratory Studies* (eds Hobbs, B. E. & Heard, H. C.) *Geophys. Monograph*, pp. 263-286.

Schmid, S. M., Fügenschuh, B., Kissling, E. & Schuster, R., 2004. Tectonic map and overall architecture of the Alpine orogen. *Eclogae Geologicae Helvetiae*, **97**(1), 93-117.

Schneider, D. A., Zahniser, S. J., Glascock, J. M., Gordon, S. M. & Manecki, M., 2006. Thermochronology of the West Sudetes (Bohemian Massif): Rapid and repeated eduction in the Eastern Variscides, Poland and Czech Republic. *American Journal of*

Science, **306**(10), 846-873.

Schulmann, K. & Gayer, R., 2000. A model for a continental accretionary wedge developed by oblique collision: the NE Bohemian Massif. *Journal of the Geological Society, London*, **157**, 401-416.

Schulmann, K., Konopásek, J., Janousek, V., Lexa, O., Lardeaux, J. M., Edel, J. B., Stipska, P. & Ulrich, S., 2009. An Andean type Palaeozoic convergence in the Bohemian Massif. *Comptes Rendus Geoscience*, **341**(2-3), 266-286.

Schulmann, K., Kröner, A., Hegner, E., Wendt, I., Konopásek, J., Lexa, O. & Štípská, P., 2005. Chronological constraints on the pre-orogenic history, burial and exhumation of deep-seated rocks along the eastern margin of the Variscan orogen, Bohemian Massif, Czech Republic. *American Journal of Science*, **305**, 407-448.

Schulmann, K., Lexa, O., Štípská, P., Racek, M., Tajčmanová, L., Konopásek, J., Edel, J. B., Peschler, A. & Lehmann, J., 2008a. Vertical extrusion and horizontal channel flow of orogenic lower crust: key exhumation mechanisms in large hot orogens? *Journal of Metamorphic Geology*, **26**, 273–297.

Schulmann, K., Martelat, J. E., Ulrich, S., Lexa, O., Stipska, P. & Becker, J. K., 2008b. Evolution of microstructure and melt topology in partially molten granitic mylonite: Implications for rheology of felsic middle crust. *Journal of Geophysical Research-Solid Earth*, **113**(B10).

Schulmann, K., Mlcoch, B. & Melka, R., 1996. High-temperature microstructures and rheology of deformed granite, Erzgebirge, Bohemian Massif. *Journal of Structural Geology*, **18**(6), 719-733.

Seng, H., 1936. Die Migmatitfrage und der Mechanismus parakristalliner Prägung. *Geologische Rundschau*, **27**, 471–492.

Seyferth, M. & Henk, A., 2004. Syn-convergent exhumation and lateral extrusion in continental collision zones - Insights from three-dimensional numerical models. *Tectonophysics*, **382**(1-2), 1-29.

Shigematsu, N. & Tanaka, H., 2000. Dislocation creep of fine-grained recrystallized plagioclase under low-temperature conditions. *Journal of Structural Geology*, **22**(1), 65-79.

Shimizu, I., 1998. Stress and temperature dependence of recrystallized grain size: A subgrain misorientation model. *Geophysical Research Letters*, **25**(22), 4237-4240.

Shimizu, I., 2008. Theories and applicability of grain size piezometers: The role of dynamic recrystallization mechanisms. *Journal of Structural Geology*, **30**(7), 899-917.

Simpson, C., 1985. Deformation of granitic rocks across the brittle-ductile transition. *J. Struct. Geol.*, **7**(5), 503-511.

Skjernaa, L., 1980. Rotation and deformation of randomly oriented planar and linear structures in progressive simple shear. *Journal of Structural Geology*, **2**(1-2), 101-109.

Skrzypek, E., Schulmann, K., Štípská, P., Chopin, F., Lehmann, J., Lexa, O. & Haloda, J., 2010a. Garnet porphyroblast growth in collisional orogens: insight from EBSD inclusion trails study and thermodynamic modelling. *Submitted to Journal of Metamorphic Geology*.

Skrzypek, E., Štípská, P., Lexa, O., Schulmann, K. & Lexova, M., 2010b. Prograde and retrograde metamorphic fabrics - a key for understanding burial and exhumation in orogens (Bohemian massif). *Submitted to Journal of Metamorphic Geology*.

Smulikowski, K., 1967. Eklogity Gór Śnieznickich w Sudetach (Eclogites of the Snieznik Mts in the Sudetes). *Geologia Sudetica*, **3**, 157-174.

Smulikowski, K., 1979. Polymetamorphic evolution of the crystalline complex of Snieznik and Gory Zlote Mts in the Sudetes. *Geologia Sudetica*, **14**, 7-76.

Smulikowski, K. & Smulikowski, W., 1985. On the porphyroblastic eclogites of the Śnieżnik Mountains in the Polish Sudetes. *Chemical Geology*, **50**(1-3), 201-222.

Smulikowski, W., 1995. Evidence of glaucophane-schist facies metamorphism in the East Karkonosze complex, West Sudetes, Poland. *Geologische Rundschau*, **84**(4), 720-737.

Steiger, R. H. & Jäger, E., 1977. Subcommission on geochronology: Convention on the use of decay constants in geo- and cosmochronology. *Earth and Planetary Science Letters*, **36**(3), 359-362.

Steltenpohl, M. G., Cymerman, Z., Krogh, E. J. & Kunk, M. J., 1993. Exhumation of eclogitized continental basement during Variscan lithospheric delamination and gravitational collapse, Sudety Mountains, Poland. *Geology*, **21**, 1111-1114.

Stipp, M., Stunitz, H., Heilbronner, R. & Schmid, S. M., 2002. The eastern Tonale fault zone: a 'natural laboratory' for crystal plastic deformation of quartz over a temperature range from 250 to 700 degrees C. *Journal of Structural Geology*, **24**(12), 1861-1884.

Štípská, P., Pitra, P. & Powell, R., 2006. Separate or shared metamorphic histories of eclogites and surrounding rocks? An example from the Bohemian Massif. *Journal of Metamorphic Geology*, **24**(3), 219-240.

Štípská, P. & Powell, R., 2005. Constraining the P-T path of a MORB-type eclogite using pseudosections, garnet zoning and garnet-clinopyroxene thermometry: an example from the Bohemian Massif. *Journal of Metamorphic Geology*, **23**(8), 725-743.

Štípská, P., Schulmann, K. & Kröner, A., 2004. Vertical extrusion and middle crustal spreading of omphacite granulite: a model of syn-convergent exhumation (Bohemian Massif, Czech Republic). *Journal of Metamorphic Geology*, **22**(3), 179-198.

Štípská, P., Schulmann, K. & Powell, R., 2008. Contrasting metamorphic histories of lenses of high-pressure rocks and host migmatites with a flat orogenic fabric (Bohemian Massif, Czech Republic): a result of tectonic mixing within horizontal crustal flow? *Journal of Metamorphic Geology*, **26**, 623-646.

Štípská, P., Schulmann, K., Thompson, A. B., Ježek, J. & Kröner, A., 2001. Thermo-mechanical role of a Cambro-Ordovician paleorift during the Variscan collision: the NE margin of the Bohemian Massif. *Tectonophysics*, **332**(1-2), 239-253.

Štípská, P., Chopin, F., Skrzypek, E., Schulmann, K., Lexa, O., Pitra, P., Martelat, J. E. & Bolinger, C., 2010. The role of large-scale folding and erosion on juxtaposition of eclogite and mid-crustal rocks (Orlica-Śnieżnik Dome, Bohemian Massif). *This volume*

Stöckhert, B., 2002. Stress and deformation in subduction zones: Insight from the record of exhumed metamorphic rocks, pp. 255-274.

Stöckhert, B. & Gerya, T. V., 2005. Pre-collisional high pressure metamorphism and nappe tectonics at active continental margins: A numerical simulation. *Terra Nova*, **17**(2), 102-110.

Suess, F. E., 1926. *Intrusionstektonik und Wandertektonik im variszichen Grundgebirge*. Verlag Bornttrager, Berlin.

Švancara, J. & Chlupáčová, M., 1994. Hustotní model geologické stavby podél geotraverzu 9HR a nadstavbové zpracování tíhového pole západní části Českého masívu. Zpráva za úkol: Geologický model západní části Českého masívu ve vazbě na ultrahlubokývrt KTB v SRN. MS Geofyzika, a.s., Brno.

Teisseyre, A. K., 1968. The Lower Carboniferous of the Intra-Sudetic Basin; Sedimentary petrology and basin analysis. *Geologia Sudetica*, **4**, 221-298.

Teisseyre, A. K., 1975. Sedimentology and paleogeography of the Kulm alluvial fans in the western Intrasudetic Basin (central Sudetes, SW Poland). *Geologia Sudetica*, **9**(2), 5-135.

Teyssier, C. & Whitney, D. L., 2002. Gneiss domes and orogeny. *Geology*, **30**(12), 1139-1142.

Thompson, A. B., Schulmann, K. & Ježek, J., 1997. Thermal evolution and exhumation in obliquely convergent (transpressive) orogens. *Tectonophysics*, **280**(1-2), 171-184.

Toy, V. G., Prior, D. J. & Norris, R. J., 2008. Quartz fabrics in the Alpine Fault mylonites: Influence of pre-existing preferred orientations on fabric development during progressive uplift. *Journal of Structural Geology*, **30**(5), 602-621.

Turniak, K., Mazur, S. & Wysoczanski, R., 2000. SHRIMP zircon geochronology and geochemistry of the Orlica-Snieznik gneisses (Variscan belt of Central Europe) and their tectonic implications. *Geodinamica Acta*, **13**, 1-20.

Ulrich, S., Schulmann, K. & Casey, M., 2002. Microstructural evolution and rheological behaviour of marbles deformed at different crustal levels. *Journal of Structural Geology*, **24**(5), 979-995.

van Breemen, O., Aftalion, M., Bowes, D. R., Dudek, A., Mísař, Z., Povondra, P. & Vrána, S., 1982. Geochronological studies of the Bohemian Massif, Czechoslovakia, and their significance in the evolution of Central Europe. *Transactions of the Royal Society of Edinburgh, Earth Sciences*, **73**, 89-108.

Vanderhaeghe, O., 1999. Pervasive melt migration from migmatites to leucogranite in the Shuswap metamorphic core complex, Canada: control of regional deformation. *Tectonophysics*, **312**(1), 35–55.

Vanderhaeghe, O., 2009. Migmatites, granites and orogeny: Flow modes of partially-molten rocks and magmas associated with melt/solid segregation in orogenic belts. *Tectonophysics*, **477**(3-4), 119-134.

Vanderhaeghe, O. & Teyssier, C., 2001. Partial melting and flow of orogens. *Tectonophysics*, **342**(3-4), 451-472.

Verner, K., Buriánek, D., Vrána, S., Vondrovic, L., Pertoldová, J., Hanžl, P. & Nahodilová, R., 2009. Tectonometamorphic features of geological units along the northern periphery of the Moldanubian Zone (Bohemian Massif). *Journal of Geosciences*, **54**(2), 87-100.

Vernon, R. H., 1976. *Metamorphic Processes: Reactions and Microstructure Development*. Wiley, New York.

Warren, R. G. & Ellis, D. J., 1996. Mantle underplating, granite tectonics, and metamorphic P-T-t paths. *Geology*, **24**(7), 663-666.

White, R. W., Pomroy, N. E. & Powell, R., 2005. An in situ metatexite-diatexite transition in upper amphibolite facies rocks from Broken Hill, Australia. *Journal of Metamorphic Geology*, **23**, 579-602.

White, R. W., Powell, R. & Baldwin, J. A., 2008. Calculated phase equilibria involving chemical potentials to investigate the textural evolution of metamorphic rocks. *Journal of Metamorphic Geology*, **26**(2), 181-198.

White, R. W., Powell, R. & Holland, T. J. B., 2007. Progress relating to calculation of partial melting equilibria for metapelites. *Journal of Metamorphic Geology*, **25**(5), 511-527.

White, R. W., Powell, R., Holland, T. J. B. & Worley, B. A., 2000. The effect of TiO_2 and Fe_2O_3 on metapelitic assemblages at greenschist and amphibolite facies conditions: mineral equilibria calculations in the system K_2O-FeO-MgO-Al_2O_3-SiO_2-H_2O-TiO_2-Fe_2O_3. *Journal of Metamorphic Geology*, **18**(5), 497-511.

Whitney, D. L., Teyssier, C. & Heizler, M. T., 2007. Gneiss domes, metamorphic core complexes, and wrench zones: Thermal and structural evolution of the Niğde Massif, central Anatolia. *Tectonics*, **26**(5).

Whitney, D. L., Teyssier, C. & Vanderhaeghe, O., 2004. Gneiss domes and crustal flow. *Geological Society of America Special Papers*, **380**, 15-33.

Willaime, C., Christie, J. M. & Kovacs, M.-P., 1979. Experimental deformation of K-feldspar single crystals. *Bulletin de Minéralogie*, **102**, 168-177.

Žáčková, E., Konopásek, J., Jeřábek, P., Finger, F. & Košler, J., 2010. Early Carboniferous blueschist facies metamorphism in metapelites of the West Sudetes (Northern

Saxothuringian Domain, Bohemian Massif). *Journal of Metamorphic Geology*, **28**(4), 361-379.

Zavada, P., Schulmann, K., Konopasek, J., Ulrich, S. & Lexa, O., 2007. Extreme ductility of feldspar aggregates - Melt-enhanced grain boundary sliding and creep failure: Rheological implications for felsic lower crust. *Journal of Geophysical Research-Solid Earth*, **112**.

Żelaźniewicz, A., 1988. Orthogneisses due to irrotational extension, a case from the Sudetes, Bohemian Massif. *Geologische Rundschau*, **77**(3), 671-682.

Żelaźniewicz, A., Nowak, I., Larionov, A. & Presnyakov, S., 2006. Syntectonic Lower Ordovician migmatite and post-tectonic Upper Viséan syenite in the western limb of the Orlica-Śnieżnik Dome, West Sudetes: U-Pb SHRIMP data from zircons. *Geologia Sudetica*, **38**, 63-80.

Zhao, Z. Y., Wei, C. J. & Fang, A. M., 2005. Plastic flow of coesite eclogite in a deep continent subduction regime: Microstructures, deformation mechanisms and rheologic implications. *Earth and Planetary Science Letters*, **237**(1-2), 209-222.

ANNEXE

Déformation plastique & recristallisation

Les dislocations, les défauts ponctuels, les sous-grains ainsi que les limites de grains constituent l'énergie interne d'un cristal (Drury & Urai, 1990) à laquelle s'ajoute l'enthalpie libre générée par les différences de compositions chimiques entre des cristaux de mêmes phases. Le cristal recristallise afin de minimiser ces deux types d'énergie par migration des défauts ponctuels (fluage de matière ou fluage-diffusion) ou par migration des défauts linéaires (fluage-dislocation).

DÉFAUTS CRISTALLINS ET DÉFORMATION PLASTIQUE

Les cristaux comportent des défauts au sein de leur structure géométrique régulière (Fig. 1), i.e. les défauts ponctuels (e.g. un atome ou molécule intersticiel, lacune ou impureté) et les défauts linéaires (e.g. demi-plan réticulaire supplémentaire ou dislocation). C'est la migration de ces défauts qui permet la déformation plastique des cristaux (*crystal plastic deformation*).

Le mouvement des défauts peut se faire au cours d'une déformation (recristallisation dynamique) ou lors de la relaxe du matériel (recristallisation statique)

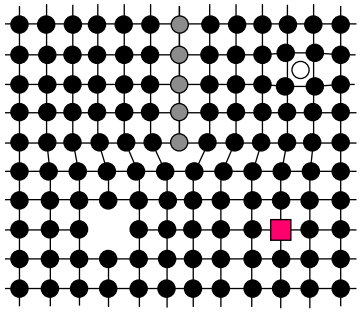

*Fig. 1: Défauts ponctuels (**point defects**) et linéaire (**line defect**) dans un réseau cristallin (**crystal lattice**)*

RECRISTALLISATION DYNAMIQUE

Déformation par glissement des dislocations et fluage-dislocation (dislocation glide & dislocation creep).

La recristallisation dynamique est définie comme « un réarrangement de la taille, de la forme et des orientations des grains induit par une déformation, sans ou avec très peu d'échanges chimiques » (Guillope & Poirier, 1979). Celle-ci peut se faire grâce à l'activation d'un système de glissement, c'est-à-dire le déplacement d'un demi-plan réticulaire le long d'un plan de glissement dans une direction donnée (Fig. 2). On parle de déformation plastique.

Son activation dépend de la valeur de la contrainte cisaillante résolue appliquée sur ce plan ou cette famille de plan. Si la contrainte dépasse une valeur critique (contrainte cisaillante critique résolue, CRSS - *Critical Resolved Shear Strees*) le système de glissement plan-direction est activé : le plan de glissement tendra à s'orienter selon le plan XY de l'ellipsoïde de déformation, la direction de glissement selon X. Ce processus est appelé glissement des disloca-

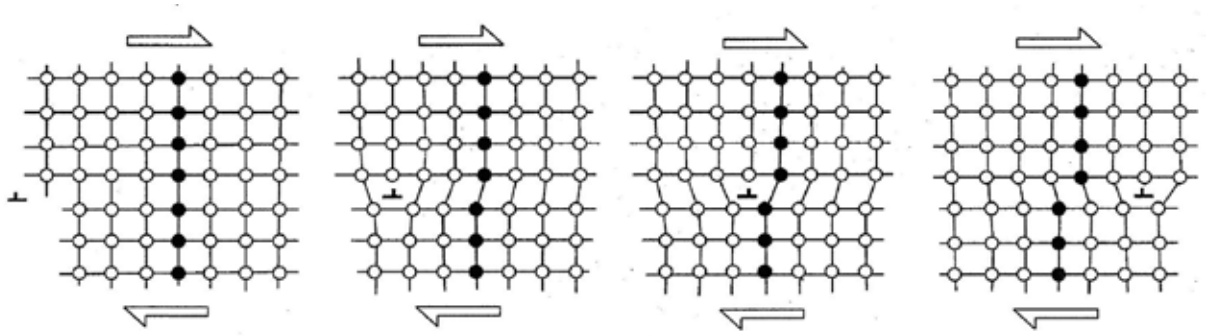

Fig. 2: Migration d'une dislocation coin (dessin d'aprèsPasschier & Trouw, 1996)

tions ou *dislocation glide*. Le mouvement des dislocations est le principal facteur influençant la recristallisation dynamique, qui implique une compétition entre le taux de dislocation générée et la vitesse à laquelle elles sont évacuées du minéral.

Les paramètres influençant le flux des dislocations, c'est-à-dire l'activation préférentielle d'un système de glissement sont notamment la température, la vitesse de déformation, la fugacité de l'eau f(H20), la pression de confinement, la contrainte appliquée, l'héritage textural primaire ou secondaire … (e.g. Ralser *et al.*, 1991; Mei & Kohlstedt, 2000a, b; Stipp *et al.*, 2002; Rybacki & Dresen, 2004; Mainprice *et al.*, 2005; Toy *et al.*, 2008; Oliot *et al.*, 2010)

La migration des dislocations peut aboutir à un enchevêtrement de celles-ci (*dislocation tangle*) et donc à un durcissement du cristal : c'est le phénomène d'écrouissage (*work-hardening*). Le glissement des dislocations peut tout de même se faire par montée des dislocations (ou fluage-dislocation, *dislocation creep*, Hirth & Tullis, 1992) c'est-à-dire par ajout de lacunes ou d'atomes au demi-plan réticulaire, permettant ainsi de contourner les « obstacles ».

Remarque : Le processus de restauration (*Recovery)* va tendre à diminuer la densité de dislocation (énergie interne) par annihilation et réarrangement des défauts cristallins. Il s'oppose en ce sens au phénomène d'écrouissage. Il en résulte une baisse de la densité des dislocations (quantité, longueur..) par formation de sous-grains et de bandes de déformations.

Déformation par transfert de matière (Diffusion creep)

Ici, la recristallisation se fait par diffusion des défauts ponctuels à travers l'ensemble du réseau cristallin (fluage de Nabarro-Herring) ou bien par diffusion aux joints de grains (fluage de Cobble) (Knipe, 1989; Wheeler, 1992). Il en résulte un flux d'atomes vers les zones où la contrainte compressive est minimale. La vitesse de déformation par fluage diffusion est directement liée au coefficient de diffusion propre au minéral considéré ou à son interface et est inversement proportionnelle à la taille des grains (très efficace pour une taille de grain très faible). Ce type de fluage est prépondérant à HT et faible contrainte déviatorique.

RECRISTALLISATION STATIQUE PAR RECUIT

Le processus de recuit (*Annealing*) est un processus de restauration statique (relaxation post déformation). Il tend à augmenter la stabilité des cristaux par une diminution de l'énergie interne par élimination des dislocations (recristallisation primaire) et une diminution de l'éner-

gie de surface par migration des limites de grains vers les grains à forte densité de dislocation et diminution de l'aire de surface (GBAR-Grain boundary area reduction). Il en résulte des structures à l'équilibre en mosaïques (*foem structure*) comme par exemple les fabriques polygonales à 120° dans les agrégats de qtz (grains automorphes).

MISE EN ÉVIDENCE DE LA DÉFORMATION PLASTIQUE : MICROSTRUCTURES

La déformation plastique peut être mise en évidence par de nombreuses microstructures associées à différents types de mode de recristallisation. Tout d'abord, **l'extinction ondulante**, qui se produit à relativement basse température, correspond à une déformation par « plissement » du réseau cristallin. La désorientation (*misorientation*) est progressive et ne tend pas à priori à l'apparition de sous-grains. Les **macles de déformation** (*twin gliding*), sont semblables aux structures macroscopiques de type kink-band et de la même manière, ne tendent pas à recristalliser le grain primaire. Les **bandes de déformation** et les **structures en damiers** (ou *Chess-board structure)* se forment par processus de restauration : les défauts accumulés dans des plans préférentiels tendent à augmenter la désorientation et ainsi faire apparaître des sous-grains.

Les processus de « *bulging* » (BLG), de rotation des sous-grains (SGR - *Sub Grain Rotation*) et de migration des joints de grain (GBM - *Grain Boundary Migration*) sont trois processus de recristallisation dynamique par fluage-dislocation (dislocation creep) (Stipp et al., 2002) où l'interface entre deux grains de densité de dislocation différente va être modifiée de façon à minimiser l'énergie interne élastique (Fig.3), soit par migration de limites préexistantes, soit par la création de nouvelles limites. Le processus de **bulging** apparaît généralement à basse température : de petites parties du grain le plus stable vont interpénétrer par bombement dans le grain adjacent à plus forte densité de dislocation (le réseau cristallin s'homogénéisant par cannibalisme). Progressivement, il va en résulter la nucléation de petits sous-grains puis de grains en bordure du cristal ou au sein même de celui-ci, si un nucleus de faible densité s'y trouve initialement inclus. Les dislocations sont produites, mais leur mouvement n'est pas rapide. Les nouveaux grains créés sont très petits et présentent des limites équantes, formant une structure dite de « *core-and-mantle* ». La **rotation des sous-grains** (SGR) consiste en une désorientation progressive des sous-grains par accumulation continue de dislocations à leurs limites produisant une force élastique de distorsion qui, si elle est trop importante, se transforme en déformation plastique. Cette accumulation progressive par migration rapide des dislocations (*dislocation climb*) va augmenter la désorientation entre deux sous-grains adjacents et permettre ainsi l'apparition d'un « nouveau grain ». C'est cette désorientation progressive qui est appelée rotation des sous-grains. Ce type de recristallisation dynamique affecte le cristal dans son ensemble bien qu'il en résulte souvent une structure de type « *core & mantle* » caractéristique avec un grain originel relique entouré par de nouveaux grains et sous-grains à forte

orientation cristallographique préférentielle. Enfin, la **migration des joints de grains** (GBM) apparaît à haute température. Elle correspond à une mobilité accrue des joints de grains faisant chuter rapidement la densité des dislocations. Les bordures de grains deviennent extrêmement suturées donnant une structure amiboïde-loboïde caractéristique ; Les nouveaux grains formés sont de taille plus importante que ceux créés par rotation des sous-grains.

À plus haute température, on note l'apparition de **glissements aux joints de grains** (GBS - *Grain Boundary Sliding*). Ce processus implique une recristallisation par transfert de matière (diffusion creep) qui accommode les interstices créés par la rotation des grains (flux granulaire), le fluage-dislocation est dans ce cas négligeable. Ce processus est souvent considéré comme responsable de la perte de l'orientation préférentielle de réseau précédemment acquise par fluage-dislocation dans le cas d'une déformation progressive. Il est normalement associé à une réduction majeure de la taille des grains (ultramylonite).

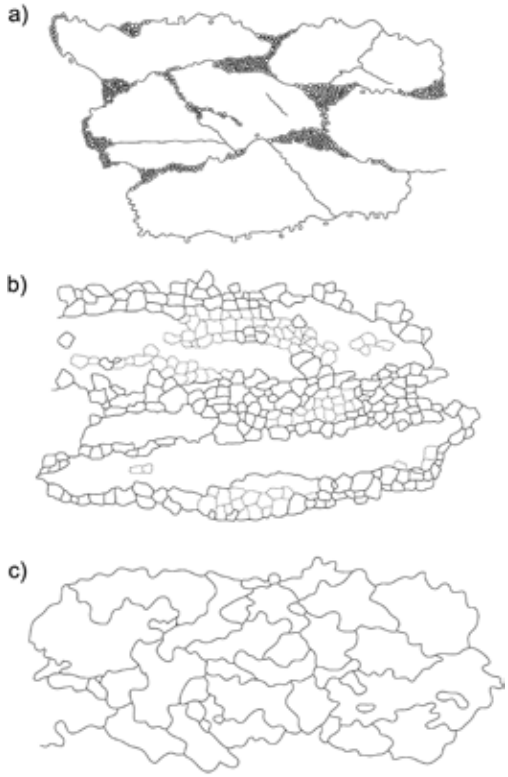

Fig. 3: Figure 3 Mécanismes de recristallisation : a) « Bulging », b) Rotation des sous-grains et c) migration des joints de grains (Stipp et al., 2002).

DÉFORMATION PLASTIQUE DU QUARTZ ET DES FELDSPATHS

Orientation Préférentielle de réseau : (OPR ou CPO - *Cristal Preferred Orientation,* et LPO - *Latice Preferred Orientation*) :

Le quartz est un minéral de structure cristalline trigonale (Fig. 4). Dans la classification de bravais, il est considéré comme un système rhomboédrique pseudo hexagonal. On note *prism* <*c*>, pour un glissement sur le *plan prismatique* dans la *direction c* du cristal. Pour le quartz, les principaux systèmes de glissement répertoriés sont *basal* <*a*>, *rhomb* <*a* >, *prism* <*a*> et *prism* <*c*> (Fig. 5)

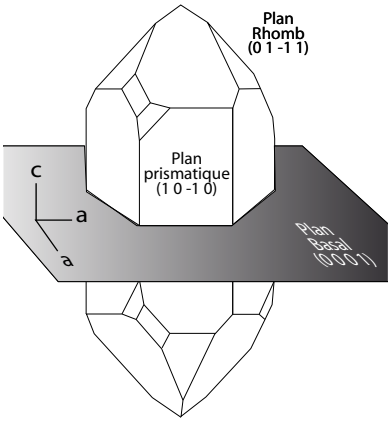

Fig. 4: Cristal de quartz et principaux plans de glissements

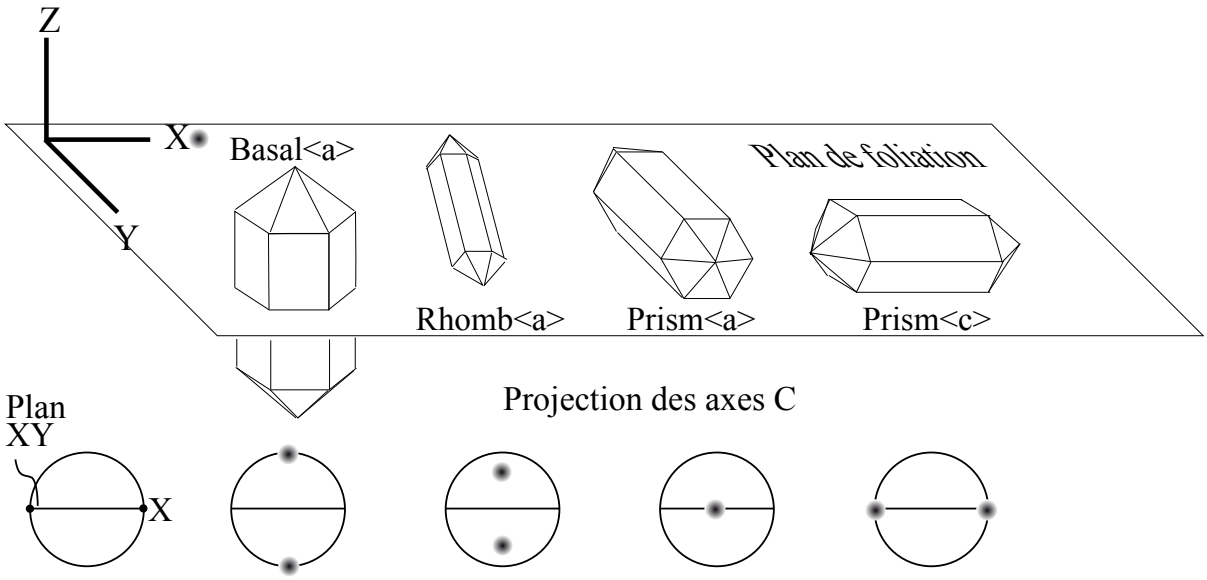

Fig. 5: Figure 5 Orientation des cristaux qtz et projection des axes c (plan de glissement selon XY, direction de glissement suivant X).

Les feldspaths sont classés dans les systèmes monocliniques (orthose) ou tricliniques (plagioclase). Les études des processus de recristallisation des feldspaths ont mis en exergue l'existence de nombreux systèmes de glissements. D'un point de vu terminologique, le système de glissement *[0 0 1](0 1 0)* correspond au glissement de la dislocation sur le *plan (0 1 0)* dans la *direction [0 0 1]*. S'il existe un ensemble de plans symétriquement équivalents, ils seront notés par des crochets puis des parenthèses angulaires pour la direction: <direction>. Les principaux systèmes de glissements des plagioclases ont été répertoriés par Kruse *et al.* (2001) (Fig. 6). Les systèmes de glissement observés dans les feldspaths potassiques ont eux été compilés par Menegon et al. (2008) (Table 1).

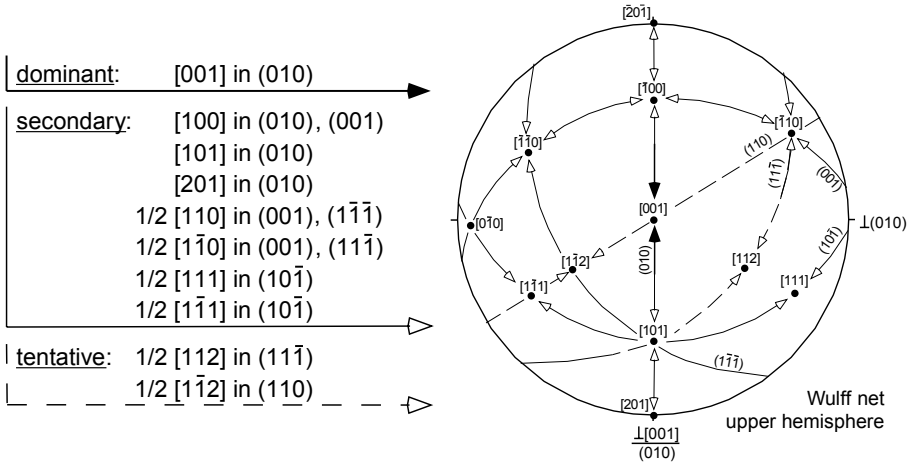

Fig. 6: Principaux systèmes de glissement dans les plagioclases projetés dans le référentiel du cristal (hémisphère supérieur). Ce type de projection peut être utilisé pour trouver plus facilement l'activation de systèmes de glissement préférentiels par projection de la linéation et de la foliation de l'échantillon dans ce référentiel (« inverse pole figure »).

Table 1: Systèmes de glissements actifs pour les feldspaths potassiques (Modifié d'après Menegon et al., 2008) : les analyses de Tullis and Yund (1977) ont été éffectué à sec sur le granite de Westerly (avec du microcline); les analyses de Willaime et al. (1979) et Scandale et al. (1983) ont été éffectué sur un monocrystale de sanidine (Or80). TEM : microscope électonique à transmission, OM : microscopie optique, U-stage : platine universelle, EBSD : imagerie en diffraction d'électrons rétrodiffusés.

Reference	Conditions	Slip plane	Slip direction	Method of observation
Experimental deformation:				
Tullis and Yund (1977)	900-1000°C, 10-15 kb, 10^{-6}/s	(010)	Not determined	TEM
Willaime et al. (1979) and Scandale et al. (1983)	700°C, 15 kb, 10^{-6}/s	(010)	[101]	TEM
		(001)	½[110]	
		(1-2-1)	[101]	
	900°C, 15 kb, 10^{-6}/s	(010)	[001]	
		(110)	½[1-12]	
		(1-11)	½[110]	
		(010)	[101]	
		(001)	½[110]	
		(1-2-1)	[101]	
		(010)	[100]	
Natural deformation:				
Debat et al. (1978)	550°C, 2 kb	(010)	Not determined	OM
		(110)	Not determined	
		(12-1)	[101]	
Sacerdoti et al. (1980)	500°C, 2 kb	(010)	[101]	TEM
		(010)	[100]	
		(010)	[001]	
		(010)	½[1-12]	
Schulmann et al. (1996)	550-600°C, 4-8 kb	(010)	[001]	U-stage
		(010)	[100]	
Martelat et al. (1999)	700-800°C, 4-10 kb	(010)	[100]	U-stage
		(001)	[100]	
Franek et al. (2006)	700-800°C, 5-8 kb	(010)	[001]	EBSD
Ishii et al. (2007)	Upper green-schist facies	(100)	[010]	EBSD
		(101)	[010]	
Zavada et al. (2007)	700°C, 10 kb	(001)	[110]	EBSD
		(010)	[100]	
		(120)	[001]	
Hasalova et al. (2008)	750-650°C, 8-4 kb	(001)	½[110]	EBSD
		(010)	[100]	
		(001)	[100]	
Schulmann et al. (2008)	670°C, 8 kb	(001)	½[110]	EBSD
		(1-10)	½[110]	
		(10-1)	[101]	

Dans un agrégat polycristallin sous contrainte, on obtiendra progressivement une orientation préférentielle de réseau des monograins fonction du système de glissement activé. L'étude de la CPO dans un échantillon pourra nous renseigner sur les mécanismes de déformations (dislocation creep, diffusion creep...), le(s) système(s) de glissement activé(s) (fonction de la température, pression...) ainsi que le régime de déformation (cisaillement simple, compression axiales, ellipsoïde de déformation...). Remarque : plusieurs processus peuvent amener à la destruction d'une orientation préférentielle de réseau comme la recristallisation statique (recuit ou annealing) et le glissement de joints de grains (voir ci-dessous).

L'étude des orientations préférentielles est donc un outil utile pour caractériser le mode déformation des cristaux. Par exemple, l'un des facteurs les plus importants pour le quartz est la température de déformation. A basse température, le fluage-dislocation est quasi inexistant, les structures de déformations prépondérantes sont les fractures, l'extinction onduleuse et les kinks-bands. À relativement plus haute température, le fluage-dislocation (déformation plastique) devient dominant : les systèmes de glissement basal <a> et sur le plan rhomb sont activés, souvent associés à une recristallisation de type « bulging » (BLG), les bandes de cristallisations sont communes. A plus haute température, le système de glissement prism <a> est préférentiellement activé, et le mécanisme de recristallisation se fait majoritairement par rotation des sous-grains (SGR). Encore à plus haute température, l'activité du système de glissement prism <c> domine, et la migration des joints de grains (GBM) est le processus de recristallisation majeur. Les structures en damier (chessboard extinction) sont interprétés comme une combinaison des systèmes basal <a> et prism <c> à HT.

Cependant, si la température semble être le paramètre majeur régissant l'activation des différents systèmes de glissement et les processus de recristallisation, de nombreux paramètres doivent être également pris en compte comme la fugacité de l'eau, la contrainte différentielle, la vitesse de déformation etc...

ANALYSE DE L'ORIENTATION CRISTALLOGRAPHIQUE

Une des méthodes utilisées pour connaître l'orientation cristalline d'un minéral en lame mince est l'utilisation de l'imagerie en diffraction d'électrons rétrodiffusés (Electron BackScatter Diffraction ou EBSD, voir Prior *et al.*, 1999; Bascou *et al.*, 2001; Prior *et al.*, 2009). Sous vide, un faisceau d'électron est envoyé sur l'échantillon (lame mince), les électrons diffractés selon la loi de braggs sont détectés par un écran phosphorescent lui-même situé dans la chambre. Un capteur CCD (Charge-Coupled Device, ou dispositif à transfert de charge) permet d'obtenir un cliché composé d'un enchevêtrement de bandes appelées bandes de Kikuchi, chaque bande représentant un plan réticulaire (Fig. 7). Si la structure théorique du cristal est connu, son orientation dans l'échantillon peut être retrouvée automatiquement à l'aide du cliché : les bandes sont tout d'abord localisée à l'aide de transformé de Fourrier : l'intensité et la largeur des bandes sont directement liées à l'espace interatomique du plan considéré, et l'angle entre deux bandes est fonction de l'angle entre les deux plans réticulaires. Le cliché est donc indexé en utilisant

la géométrie des bandes pour obtenir l'orientation correspondante. Un indice de confiance est donné pour chaque nouveau cliché.

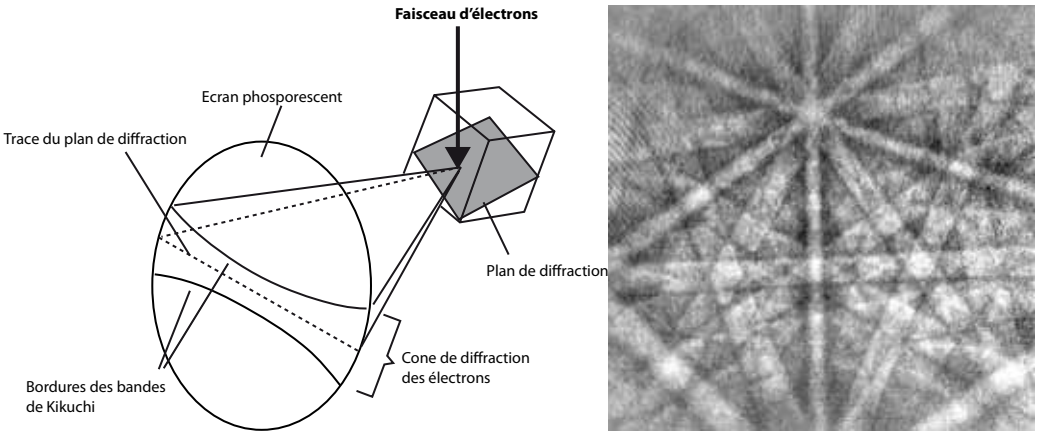

Fig. 7: Formation des bandes de Kikuchi (Dessin EDAX©) et Cliché montrant les bandes de Kikuchi issue de la diffraction d'un faisceau d'électrons sur un cristal de quartz.

Références

Bascou, J., Barruol, G., Vauchez, A., Mainprice, D. & Egydio-Silva, M., 2001. EBSD-measured lattice-preferred orientations and seismic properties of eclogites. *Tectonophysics*, **342**(1-2), 61-80.

Debat, P., Soula, J. C., Kubin, L. & Vidal, J. L., 1978. Optical studies of natural deformation microstructures in feldspars (gneiss and pegmatites from Occitania, southern France). *Lithos*, **11**(2), 133-145.

Drury, M. R. & Urai, J. L., 1990. Deformation-related recrystallization processes. *Tectonophysics*, **172**(3-4), 235-253.

Franěk, J., Schulmann, K. & Lexa, O., 2006. Kinematic and rheological model of exhumation of high pressure granulites in the Variscan orogenic root: example of the Blanský les granulite, Bohemian Massif, Czech Republic. *Mineralogy and Petrology*, **86**(3-4), 253-276.

Guillope, M. & Poirier, J. P., 1979. Dynamic recrystallization during creep of single-crystalline halite: an experimental study. *Journal of Geophysical Research*, **84**, 5557-5567.

Hasalová, P., Schulmann, K., Lexa, O., Štípská, P., Hrouda, F., Ulrich, S., Haloda, J. & Týcová, P., 2008. Origin of migmatites by deformation-enhanced melt infiltration of orthogneiss: a new model based on quantitative microstructural analysis. *Journal of Metamorphic Geology*, **26**, 29-53.

Hirth, G. & Tullis, J., 1992. Dislocation Creep Regimes in Quartz Aggregates. *Journal of Structural Geology*, **14**(2), 145-159.

Ishii, K., Kanagawa, K., Shigematsu, N. & Okudaira, T., 2007. High ductility of K-feldspar and development of granitic banded ultramylonite in the Ryoke metamorphic belt, SW Japan. *Journal of Structural Geology*, **29**(6), 1083-1098.

Knipe, R. J., 1989. Deformation mechanisms - recognition from natural tectonites. *Journal of Structural Geology*, **11**(1-2), 127-146.

Kruse, R., Stunitz, H. & Kunze, K., 2001. Dynamic recrystallization processes in plagioclase porphyroclasts. *Journal of Structural Geology*, **23**(11), 1781-1802.

Mainprice, D., Tommasi, A., Couvy, H., Cordier, P. & Frost, D. J., 2005. Pressure sensitivity of olivine slip systems and seismic anisotropy of Earth's upper mantle. *Nature*, **433**(7027), 731-733.

Martelat, J. E., Schulmann, K., Lardeaux, J. M., Nicollet, C. & Cardon, H., 1999. Granulite microfabrics and deformation mechanisms in southern Madagascar. *Journal of Structural Geology*, **21**(6), 671-687.

Mei, S. & Kohlstedt, D. L., 2000a. Influence of water on plastic deformation of olivine aggregates 1. Diffusion creep regime. *Journal of Geophysical Research B: Solid Earth*, **105**(B9), 21457-21469.

Mei, S. & Kohlstedt, D. L., 2000b. Influence of water on plastic deformation of olivine aggregates 2. Dislocation creep regime. *Journal of Geophysical Research B: Solid Earth*, **105**(9).

Menegon, L., Pennacchioni, G. & Spiess, R., 2008. Dissolution-precipitation creep of K-feldspar in mid-crustal granite mylonites. *Journal of Structural Geology*, **30**(5), 565-579.

Oliot, E., Goncalves, P. & Marquer, D., 2010. Role of plagioclase and reaction softening in a metagranite shear zone at mid-crustal conditions (Gotthard Massif, Swiss Central Alps). *Journal of Metamorphic Geology*, in press.

Passchier, C. W. & Trouw, R. A. J., 1996. Microtectonics. *Microtectonics*.

Prior, D. J., Boyle, A. P., Brenker, F., Cheadle, M. C., Austin, D., Lopez, G., Peruzzo, L., Potts, G. J., Reddy, S., Spiess, R., Timms, N. E., Trimby, P., Wheeler, J. & Zetterström, L., 1999. The application of electron backscatter diffraction and orientation contrast imaging in the SEM to textural problems in rocks. *American Mineralogist*, **84**(11-12), 1741-1759.

Prior, D. J., Mariani, E. & Wheeler, J., 2009. EBSD in the Earth Sciences: Applications, Common Practice, and Challenges. In: *Electron Backscatter Diffraction in Materials Science* (eds Schwartz, A. J., Kumar, M., Adams, B. L. & Field, D. P.), pp. 345-360, Springer US.

Ralser, S., Hobbs, B. E. & Ord, A., 1991. Experimental deformation of a quartz mylonite. *Journal of Structural Geology*, **13**(7), 837-850.

Rybacki, E. & Dresen, G., 2004. Deformation mechanism maps for feldspar rocks. *Tectonophysics*, **382**(3-4), 173-187.

Sacerdoti, M., Labernardiere, H. & Gandais, M., 1980, 1980. Transmission electron microscope (TEM) study of geologically deformed potassic feldspars. *Bulletin de Minéralogie*, **103**, 148-155.

Scandale, E., Gandais, M. & Willaime, C., 1983. Transmission electron microscopic study of experimentally deformed k-feldspar single crystals - The (010) [001], (001) ½[110], (110) ½[112] and (111) ½[110] slip systems. *Physics and Chemistry of Minerals*, **9**(3-4), 182-187.

Schulmann, K., Martelat, J. E., Ulrich, S., Lexa, O., Stipska, P. & Becker, J. K., 2008. Evolution of microstructure and melt topology in partially molten granitic mylonite: Implications for rheology of felsic middle crust. *Journal of Geophysical Research-Solid Earth*, **113**(B10).

Schulmann, K., Mlcoch, B. & Melka, R., 1996. High-temperature microstructures and rheology of deformed granite, Erzgebirge, Bohemian Massif. *Journal of Structural Geology*, **18**(6), 719-733.

Stipp, M., Stunitz, H., Heilbronner, R. & Schmid, S. M., 2002. The eastern Tonale fault zone: a 'natural laboratory' for crystal plastic deformation of quartz over a temperature range from 250 to 700 degrees C. *Journal of Structural Geology*, **24**(12), 1861-1884.

Toy, V. G., Prior, D. J. & Norris, R. J., 2008. Quartz fabrics in the Alpine Fault mylonites: Influence of pre-existing preferred orientations on fabric development during progressive uplift. *Journal of Structural Geology*, **30**(5), 602-621.

Tullis, J. & Yund, R. A., 1977. Deformation-enhanced fluid distribution in feldspar aggregates and implications for ductile shear zones. *Geology*, **24**, 63-66.

Wheeler, J., 1992. Importance of pressure solution and coble creep in the deformation of polymineralic rocks. *Journal of Geophysical Research*, **97**(B4), 4579-4586.

Willaime, C., Christie, J. M. & Kovacs, M.-P., 1979. Experimental deformation of K-feldspar single crystals. *Bulletin de Minéralogie*, **102**, 168-177.

Zavada, P., Schulmann, K., Konopasek, J., Ulrich, S. & Lexa, O., 2007. Extreme ductility of feldspar aggregates - Melt-enhanced grain boundary sliding and creep failure: Rheological implications for felsic lower crust. *Journal of Geophysical Research-Solid Earth*, **112**.